Title
Plasma-Thermal Atomic Layer Etching of Metals

Author
Sang, Xia

Publication Date
2022

Peer reviewed|Thesis/dissertation

UNIVERSITY OF CALIFORNIA

LOS ANGELES

Plasma-Thermal Atomic Layer Etching of Metals

A dissertation submitted in partial satisfaction of the requirements for the degree Doctor of Philosophy in Materials Science and Engineering

by

Xia Sang

2022

ABSTRACT OF THE DISSERTATION

Plasma-Thermal Atomic Layer Etching of Metals

by

Xia Sang

Doctor of Philosophy in Materials Science and Engineering

University of California, Los Angeles, 2022

Professor Jane P. Chang, Chair

This work demonstrated a generalizable approach for patterning metals on the nanometer scale. As the complexity of device structures keeps evolving, corresponding etching techniques need to be developed to accommodate the integration of new materials on ever-shrinking scales. The contrast in chemical reactivity is explored and leveraged as the source of etching selectivity in the illustrated atomic layer etching (ALE) process to meet the increasingly stringent dimension requirements on etch-resistant metals.

Thermodynamic assessments are performed on Ni to screen and predict the potential solution and gas-phase etchants. Organic etchants such as acetic acid, formic acid, acetylacetone, and hexafluoro-acetylacetone were screened to etch Ni and NiO in the solution phase. In concentrated solutions of formic acid, NiO was observed to etch selectively over metallic Ni at values up to 30. Such selectivity is further explored in the gas-phase via a sequential oxidation-etch process. Cyclic oxygen plasma and gas phase formic acid exposures resulted in an etch rate

of 2.3 nm/cycle. A high (>100) gas-phase etch selectivity of NiO over Ni by this cyclic process is achieved, fulfilling the self-limiting requirement of an Atomic Layer Etching (ALE) process. Anisotropic etch profile for Ni thin film with SiO_2 hard mask was achieved through this cyclic process and the final feature sidewall was measured to be close to 90°. This ALE approach is further facilitated by a prior RIE chemistry to realize highly directional removal at a high throughput. Density Functional Theory (DFT) simulation was conducted, and Ni thin film with an oxygen underlayer was calculated to be the configuration that enables favorable etching reaction with the presence of formic acid vapor.

A similar cyclic approach was applied to the patterning of Cu thin film and directional removal was also achieved. An average etch rate of 2.4 nm/cycle was determined experimentally. LMM Auger signal was used to confirm the change in Cu surface states from Cu dominant (as deposited) to CuO dominant (after oxidation) to $Cu(OH)_2$ dominant (after etching). DFT based simulation was established with the most energetically stable Cu, CuO and $Cu(OH)_2$ configurations. The most favorable etch product was determined to be $Cu_2(HCOO)_4$ dimer with a formic acid exposure partial pressure window of 150 Torr ~ 250 Torr. Experimental verification of the gas phase etching products was attempted, and Cu was detected in the etch product.

Manipulating atoms to form desired structures on an atomic scale has long been the ultimate goal of the semiconductor industry, as it would open up infinite possibilities for device innovation and manufacturing. The new ALE chemistry introduced in this work adds an essential piece of the puzzle to the bigger picture and brings the goal one step closer. It is believed that with the implementation and further optimization of the demonstrated ALE process, atomistic subtraction of metals would be eventually realized.

The dissertation of Xia Sang is approved.

Yu Huang

Suneel Kodambaka

Philippe Sautet

Jane P. Chang, Committee Chair

University of California, Los Angeles

2022

Table of Contents

List of Figures

List of Tables

ACKNOWLEDGEMENTS

First and foremost, I would like to express my deepest gratitude to Prof. Jane Chang, who brought me into her lab, provided me with a plethora of research opportunities, and trained me to become the researcher I am today. None of the achievements would be possible without her guidance, and I am forever grateful.

I would also like to thank all my committee members, Prof. Yu Huang, Prof. Suneel Kodambaka, and Prof. Philippe Sautet. Thank you for the insightful comments and constructive advice. I owe a special debt of gratitude to Prof. Sautet and his student Yantao for their input on the simulation part of the work. I also learned a lot from talking to other UCLA members such as Dr. John Mark Martirez and Prof. Louis Bouchard. Brian, Tom, and Noah at Nanolab; Adam, Mike, and Paul at CNSI are my mentors in tool operation and troubleshooting, thank you all.

This work would not be able to materialize without the funding support from our industry sponsors. I would like to thank Semiconductor Research Corporation (SRC), Center of Design Enabled Nanofabrication (C-DEN), and Intel Corporation. Special thanks to Dr. Changju Choi at Intel for his monthly feedback over a three-year period, the professional interaction with the industry gave me a sneak peek of my future career.

I am fortunate to work with my lab mates at Chang lab. Postdocs that I have worked with, Hamid and Katie; and students before me, Nick, Ernest, and Ryan, all provided priceless help to make the journey possible. The younger generation of students, Taylor, Owen, Brian, and Coco have grown rapidly and already started to bear great responsibilities. To Taylor, who joined the lab in the middle of the pandemic and need to learn everything from the ground up, you are doing

a much better job than I did back then, and you are presented with even better opportunities than I had, I am confident that you would be very successful. And, of course, my cohort Adrian, I enjoyed our countless times walking to lunch and you sharing your view on recent events along the way. Friends from other labs also companied me over these years providing much-needed mental support. Jin, Sicong, and Peter, wish you all the best with your future career.

Numerous collaborators outside of UCLA also instilled valuable insights. Dr. Jean-Francois de Marneffe and Dr. Vicky Philipsen at IMEC are extremely kind in providing samples and exchanging ideas, I wish our paths would cross again in the future. Dr. Scott Walton at Naval Research Lab and Dr. Ethan Crumlin at Lawrence Berkeley National Lab both offered their facilities for experiments, I believe future students would make the best of them. Big thank you to Prof. Miroslav Peric at CSUN and Dr. Shamon Walker at UCSB, who helped me with EPR measurements.

The support from my family and loved ones is the cornerstone of things I have built upon, and the pandemic made that even clearer. To my mom and dad, thank you for the unconditional love. Also thank you to my extended families in Shanghai and Zhuji for their emotional support. To Lynn and David here at LA, thank you, LA feels like home with your helping hands.

Lastly, please allow me to take a moment and pat myself on the back. The journey ended up quite rockier than I had expected, with uncertainties and turbulences outside of the academic realm. I am glad that I crossed the finish line with a positive heart and a stable mind. There would be greater challenges in the future, and I can’t wait to see what would happen next.

Chapter 1 consists of sections from ***X. Sang*** *and J. P. Chang, Journal of Physics D: Applied Physics 53, 183001 (2020).*

Chapter 3 is an adaptation of ***X. Sang****, E. Chen and J. P. Chang, Journal of Vacuum Science & Technology A: Vacuum, Surfaces, and Films 38 (4), 042603 (2020),* ***X. Sang*** *and J. P. Chang, Journal of Vacuum Science & Technology A: Vacuum, Surfaces, and Films 38 (4), 042604 (2020),* and ***X. Sang****, Y. Xia, P. Sautet and J. P. Chang, Journal of Vacuum Science & Technology A: Vacuum, Surfaces, and Films 38 (4), 043005 (2020).* DFT simulation of the Ni etch process is conducted by Yantao Xia.

Chapter 4 is an adaptation of *R. Sheil, J. M. P. Martirez,* ***X. Sang****, E. A. Carter and J. P. Chang, The Journal of Physical Chemistry C 125 (3), 1819-1832 (2021).* DFT simulation of the Cu etch process is conducted by J. Mark P. Martirez.

VITA

2017	B.S. Nuclear, Plasma and Radiological Engineering University of Illinois, Urbana - Champaign Champaign, IL
2017-2022	Graduate Student Researcher Department of Materials Science and Engineering University of California, Los Angeles Los Angeles, CA

AWARDS

2013-2017	Dean's List University of Illinois, Urbana - Champaign
2021	Atomic Layer Etching Best Student Paper Award ALD/ALE 2021 Virtual Meeting
2021	John Coburn and Harold Winters Student Award in Plasma Science and Technology Division AVS 67 Virtual Symposium

PUBLICATIONS

Christenson, M., S. Stemmley, S. Jung, J. Mettler, **X. Sang**, D. Martin, K. Kalathiparambil, and David N. Ruzic. "*Determining the ion temperature and energy distribution in a lithium-plasma interaction test stand with a retarding field energy analyzer.*" Rev. Sci. Instrum. 88, no. 8 (2017): 083501.

Sang, Xia, and Jane P. Chang. "*Physical and chemical effects in directional atomic layer etching.*" J. Phys. D 53, no. 18 (2020): 183001.

Sang, Xia, Ernest Chen, and Jane P. Chang. "*Patterning nickel for extreme ultraviolet lithography mask application I. Atomic layer etch processing.*" J. Vac. Sci. Technol. A 38, no. 4 (2020): 042603. (Editor's Pick)

Sang, Xia, and Jane P. Chang. "*Patterning nickel for extreme ultraviolet lithography mask application. II. Hybrid reactive ion etch and atomic layer etch processing.*" J. Vac. Sci. Technol. A 4 (2020): 042604. (Editor's Pick)

Sang, Xia, Yantao Xia, Philippe Sautet, and Jane P. Chang. "*Atomic layer etching of metals with anisotropy, specificity, and selectivity*." J. Vac. Sci. Technol. A: 4 (2020): 043005. (Editor's Pick)

Sheil, Ryan, J. M. P. Martirez, **X. Sang**, E. A. Carter, and Jane P. Chang. "*Precise Control of Nanoscale Cu Etching via Gas-Phase Oxidation and Chemical Complexation.*" J. Phys. Chem. C 125, no. 3 (2021): 1819-1832.

Liu, Yichen, N. Lim, T. Smith, **X. Sang**, and Jane P. Chang "*Thermochemical Prediction of Runaway Energetic Reactions Involving Organometallic (Al, In) and Silane Precursors in Deposition Tools.*" J. Vac. Sci. Technol. B 40, 012201 (2022). (Editor's Pick)

PRESENTATAIONS

X. Sang, E. Chen, and J. P. Chang, "Surface Chemistry Controlled Patterning of Cobalt & Palladium", 5th CDEN Workshop, San Diego, CA, November 16th, 2018.

X. Sang, E. Chen, and J. P. Chang, "*Surface Functionalization Enabling Selective Etching of Metals*", 6th C-DEN Workshop, San Jose, CA, June 7th, 2019.

X. Sang, and J. P. Chang, "*Effective Patterning of Ni for EUV Masks*", SRC Nano-manufacturing Materials and Processes Annual Research Review, Austin, TX, September 11th, 2019.

X. Sang, E. Chen, and J. P. Chang, "*Chemically Enhanced Patterning of Nickel for Next Generation EUV Mask*", AVS 66th International Symposium & Exhibition, Columbus, OH, October 23rd, 2019.

X. Sang, E. Chen, and J. P. Chang, "*Hybrid RIE-ALE on Ni for EUV mask absorber*", 7th C-DEN Workshop, Dublin, CA, November 8th, 2019.

X. Sang, and J. P. Chang, "*Directional and Selective Patterning of Ni for Next Generation EUV Absorber*", SPIE Advanced Lithography, San Jose, CA, February 26th, 2020.

X. Sang, E. Chen and J. P. Chang, "*Thermal-Plasma ALE on Selected Metals for EUV and Integration Processes*", ALD/ALE 2020 Virtual Meeting, June 28th, 2020 (Best student paper award finalist).

X. Sang, and J. P. Chang, "*Effective Patterning of Metals for EUV and Integration Applications*", SRC Nano-manufacturing Materials and Processes Annual Research Review, November 19th, 2020.

X. Sang, J. M. P. Martirez, T. Smith, E. A. Carter and Jane P. Chang, "*Reaction Pathways Leading to Anisotropic Patterning of Cu*", ALD/ALE 2021 Virtual Meeting, June 28th, 2021 (Atomic Layer Etching Best Student Paper Award).

X. Sang, J. M. P. Martirez, L-S. Bouchard, E. A. Carter and Jane P. Chang, "*Characterization of Plasma-Thermal Cu ALE Processes and Etch Products*", AVS 67th Virtual Symposium, October 25th, 2021 (Coburn & Winters Student Award).

Chapter 1 Motivation and Background

This chapter serves as an introduction to the importance of metal patterning in the hyper-scaling era to extend Moore's Law. An overview of the mainstream metal patterning techniques is presented, with the highlight of their respective limitations. Atomic layer etching (ALE) is introduced as a promising candidate of nanometer-scale metal patterning and the applications of plasma ALE and thermal ALE are discussed. The importance of electron configuration and material composition and its implication is reviewed. Based on the overview and comparison of the existing techniques, a generalizable patterning scheme, plasma-thermal ALE, is proposed.

1.1 The Need to Pattern Metals at Nanometer Scale

In the past decades, the physical dimensions of computing devices have shrunk from room size to palm size, while their computing power surged exponentially. Smartphones these days are much more powerful than computers used in the Apollo missions, while only consuming a fraction of the power. As of 2022, the most cutting-edge supercomputers are reaching exascale (10^{18} calculations per second) levels of performance, making weather forecasting more reliable, aerodynamic simulations more accurate, and pharmaceutical developments more efficient. On the other end of the spectrum, consumer electronics also fundamentally changed how people interact with the world, fully functional computers are now available on the wrist, offering non-stop cardiac monitoring while tracking daily motion and calorie consumption. The concept of Metaverse is recently proposed, which would only be possible with the adaptation of more subtle and personal devices. This generation is witnessing the most rapid increase of calculating capability in human

history. Such trend, often referred to as Moore's Law (Moore 1965), has been proven valid for the past several decades.

Keeping up with the projection proposed almost 60 years ago requires constant innovations and revolutions, as the continuous device scaling imposes significant challenges in both design and manufacturing processes, and the industry has been actively looking for means to uplift the computational capabilities. The invention of the Fin field-effect transistor (FinFET) switched the scaling process from geometric scaling to equivalent scaling and has been the cornerstone for integrated circuit (IC) advancement in the past 20 years (Clark 2018). Now, another major transition point is on the horizon: going into the hyper-scaling era (Figure 1.1). The hyper-scaling era is an overhaul from the top-down, introducing new changes on the system (heterogeneous integration), design (contact over active gate), device (gate-all-around transistors), materials (functional materials), and lithography (extreme ultra-violet lithography) levels (Salahuddin 2018). Among all these changes, materials incorporation plays a vital role, as new materials would be ubiquitous throughout the system, and their compatibilities would fundamentally affect the overall performance.

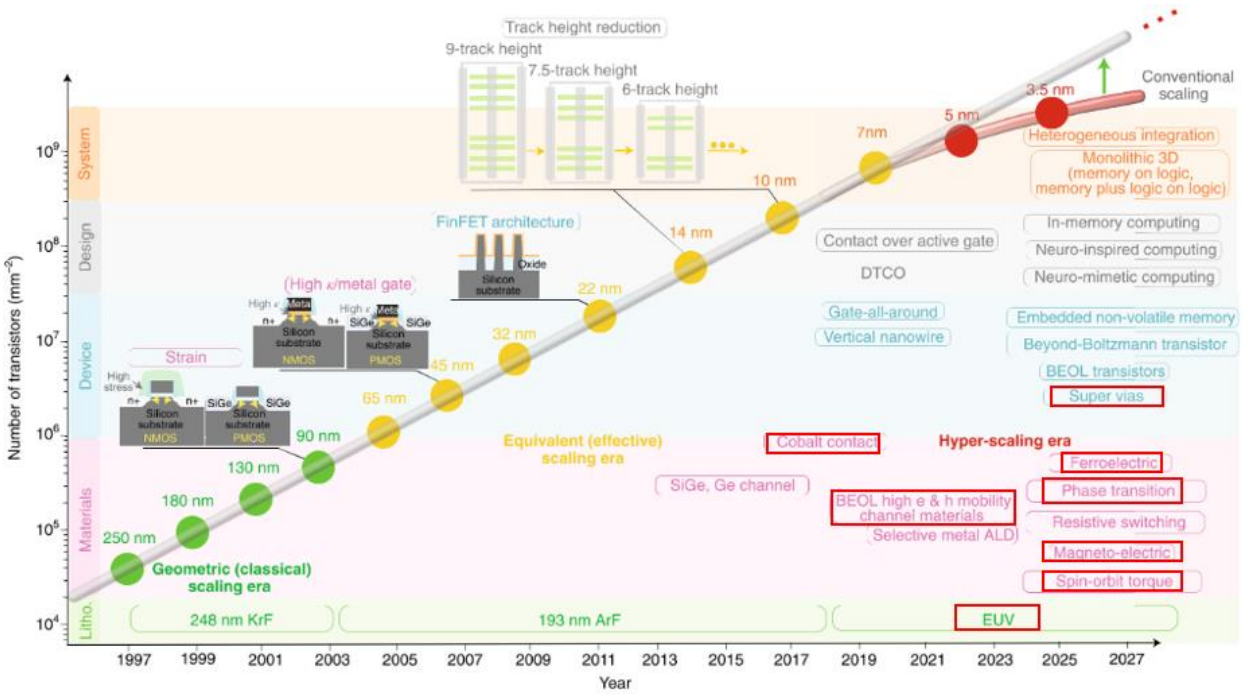

Figure 1.1 Transistor scaling history and projection, with the need of metal etch highlighted. (Salahuddin 2018)

Among the surge in new materials integrations, functional materials such as metals, metal oxides, and metal alloys gain significant interest as they offer unique properties like ferroelectricity (Setter 2006), magnetism (Falicov 1990), and even phase-change (Shen 2020). They are getting increasingly more attention for being the foundations of new applications, a couple of which are highlighted in Figure 1.1. Naturally, the need for patterning these materials on nanometer scales has rapidly increased in recent years (Neisser 2013, Deloitte 2017, ASML 2019), both the bottom-up (deposition) and top-down (etch) of aforementioned materials are actively discussed and reported.

Among the burgeoning integration of new materials, metal is considered to be the most difficult to pattern, as previous knowledge of metal etch predominately originated from metallurgy

and refinement, which impose zero requirements on the microscopic reaction location. Controlled etching of metals on a nanometer level is a very difficult task, as their novel properties come with new processing constraints, and the possible combinations of materials would further complicate the processing conditions as factors such as selectivity would need to be considered. Additionally, some of the electric and magnetic properties are inherently associated with the inertness of the metals, making them etch-resistant. All these difficulties call for a systematic investigation of metal etch process.

1.1.1 Patterning Nickel (Ni) for Extreme Ultraviolet (EUV) Lithography Absorber

Ni is an element that could be found from dental fillings to space shuttles. It is traditionally valued for its corrosion resistance, i.e., as a common additive in stainless steel to promote mechanical properties in harsh environments. For the same reason, mints introduce Ni in coins to prevent depreciation in monetary values during circulation. Its chemical stability and economic affordability also make it a competitive catalyst for many hydrogenation reactions. It also exists in batteries in the form of nickel cadmium (NiCd) and nickel metal hydride (NiMH). Its optical, electrical, and magnetic properties are further explored and leveraged in recent times. Nickel silicide (Ni_xSi_y), for example, is a family of important intermetallic materials for reducing contact resistance at Ni-Si interfaces in microelectronics (Lavoie 2003). Co/Ni multilayers is widely used for spintronic devices (Andrieu 2018). Among the various advantageous traits, its potential application as a candidate material for next-generation extreme ultraviolet (EUV) absorbing layer is the focus in this work.

The constant shrinkage of transistors has been partially enabled by the steady advancement in photolithography, which uses light to change the chemical properties of photoresists on designed

regions, thus transferring patterns to layers underneath. Photolithography resolution limit is given by the Rayleigh criterion:

$$CD = \frac{k\lambda}{n \sin \theta} = \frac{k\lambda}{NA} \tag{1.1}$$

where CD stands for critical dimension, the size of smallest feature differentiable; λ stands for the wavelength of light used; n stands for the refractive index of the medium in which light travels through; θ is the half of the angle subtended by the lens at its focus and NA is the numerical aperture. As feature size started to approach nanometer scale, traditional lithography ran into physical limitations. To compensate for the stagnancy imposed by lithography, other innovations like double and even quadruple patterning have been implemented to further extend the validity of Moore's Law. Table 1.1 summarizes critical dimensions achievable using various patterning techniques from a 193 nm deep ultraviolet (DUV) system, the most advanced DUV system.

Table 1.1 Critical dimension achievable by 193 nm DUV light source.

Method		Critical Dimension (nm)
Rayleigh criterion (n = 1, k = 0.61)		115
Immersion lithography (water, NA = 1.35)		40
Immersion lithography (higher n-fluid, NA > 1.35)		32
Multi-patterning &	Double patterning	22
Immersion lithography	Quadruple patterning	15

As shown above, by implementing techniques such as immersion lithography and multi-patterning, feature size about one order of magnitude smaller than that predicted by the Rayleigh criterion could be achieved. Impressive as it is, it only postpones the come of limitation. Now that the 5 nm node is in production, the industry embraced another groundbreaking advancement in

lithography technology to push Moore's Law forward. Light with a wavelength of 13.5 nm has been chosen in the next-generation lithography system. Since 13.5 nm falls in the extreme ultra-violet range, the next generation lithography gets the name EUV lithography.

The transition from DUV to EUV is much more complicated than changing the light source for a shorter wavelength. Unlike traditional lithography, which could be done in atmospheric pressure, EUV lithography needs to be performed in a high vacuum environment, since the light at the wavelength of 13.5 nm could be easily absorbed by air. Similarly, masks used in DUV systems are no longer applicable since EUV could not transmit through these materials, new reflection optics needs to be designed. The decrease in wavelength also requires modifications in other aspects of the system, such as cleaning and inspection. A comparison of some key parameters of EUV and DUV systems is listed in

Table 1.2, while a visual comparison of transmission optics and reflection optics is shown in Figure 1.2.

Table 1.2 Comparison of EUV and DUV systems.

	Item	EUV	DUV
System	Wavelength	13.5 nm	193 nm
	Critical dimension	5 nm	15 nm
	Optics	Reflection	Transmission
	Ambient pressure	High vacuum (~1 mTorr)	Atmospheric
Mask	Multilayer deposition	Yes, with good periodicity	Not required
	Metal etch	Constrained by surrounding	No constraint
	Uniformity	Concern on pattern shift	Concern on defocus
	Thickness	Must be precise	Less concern

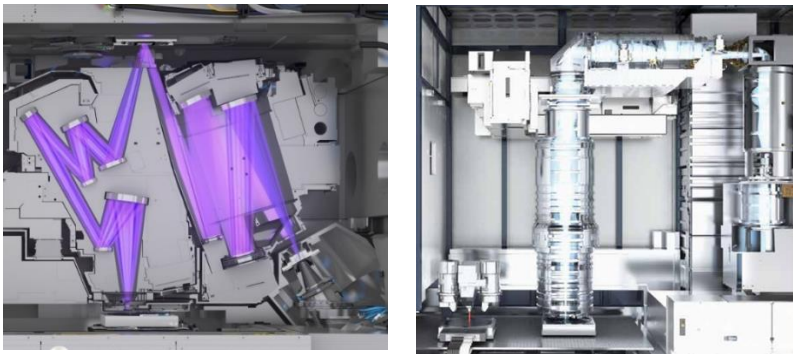

Figure 1.2 (Left) reflection-based optics for EUV system (right) transmission-based optics for DUV system. (Fu 2019)

These stringent requirements make the design and manufacturing of EUV lithography systems even more difficult and costly compared to its predecessor. A state-of-the-art EUV system is about the size of a classroom, with a fully automated stepper and maintenance system, and cost around 1 billion dollars. Nevertheless, EUV lithography is booming, with ASML shipped 42 systems in 2021, and the demand is never greater with the surge in remote communication need and recent semiconductor supply chain challenges. The burgeoning market calls for further workflow streamlining and process improvements.

Like other parts of the system, photomasks for the EUV lithography system needs to be redesigned. A conventional mask is made of a patterned layer of Cr on top of quartz, openings of Cr defines features on wafers as light transmits through. The absorbable nature of EUV requires a reflection-based mask for pattern transferring at a specific wavelength range.

Figure 1.3 shows a cross-sectional view of a EUV lithography mask, thicknesses of each layer is not to scale.

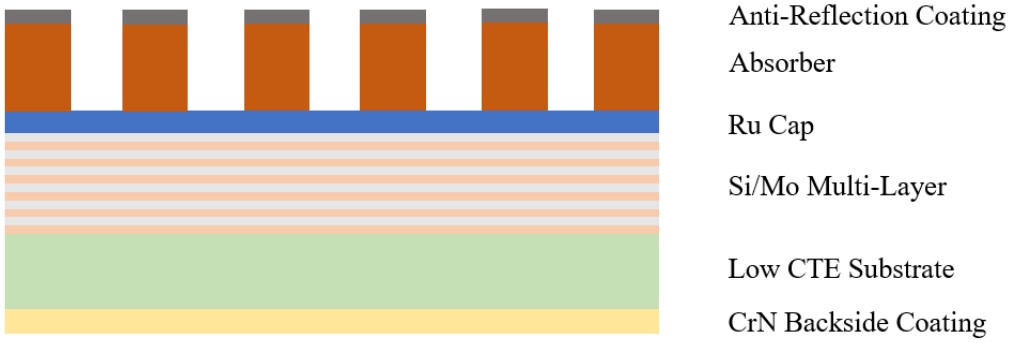

Figure 1.3 Cross-sectional view of a EUV lithography mask

From bottom to top, the mask is made up of a chromium nitride (CrN) backside coating for electrostatic chunking; a substrate that made of low thermal expansion material to minimize fidelity loss from temperature fluctuation during EUV exposure; 40 pairs of Si/Mo multilayer tuned to maximize reflection at around 13.5 nm; a ruthenium (Ru) capping layer to protect multilayer underneath from oxidation; an absorbing layer that patterned to absorb EUV light; and an anti-reflection coating on top for inspection. High contrast and sharpness are essential for high-fidelity image transferring. These properties require precise control of Si/Mo multilayer and absorbing layer during mask manufacturing. It is therefore of critical importance to develop a high precision absorbing layer patterning technique.

The contrast on the final patterns is controlled by the difference in reflectivity between exposing Si/Mo multilayer and the absorbing layer. It is therefore intuitive to look for materials with the greatest absorbing capability. 'Absorbing capability' is an optical property that could be quantified by the term 'extinction coefficient' (k) at a given wavelength, which is the imaginary part of the complex reflective index ($\bar{n} = n + ik$). Additionally, since refraction happens when light transmits between media with different refractive indexes (n), it is preferable to use a material

with n close to unity, to match that of vacuum. These optical properties are summarized in Figure 1.4 below.

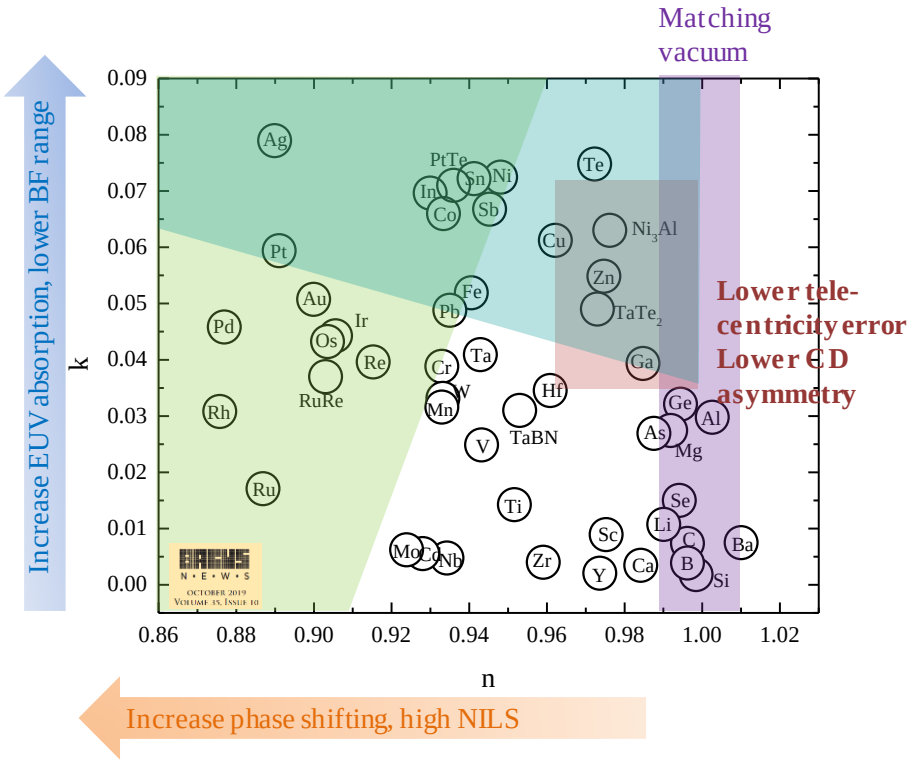

Figure 1.4 Extinction coefficient vs. Refractive index of light at wavelength of 13.5 nm. (Luong 2018)

It is clear from Figure 1.4 that the three elements with the highest extinction coefficient are silver (Ag), nickel (Ni), and tellurium (Te). Among these, Ag has the highest k but comes with the lowest n, Te is highly toxic thus is hard to manufacture and process, leaving Ni the most promising candidate as materials for next-generation EUV masks. Due to its high refractive index (n) and high extinction coefficient (k) compared to previously used Cr- and Ta-based masks, both experimental measurements and computational simulations suggest Ni to be a promising choice

for the next-generation EUV mask absorber material. More recent research also shows that Ni_3Al is another good candidate for its low crystallinity and high resistance to oxidation.

Table 1.3 Physical properties considered for EUV lithography masks and reported etching chemistries and outcomes.

	Cr	Ta	TaN	TaBN	Ni	Ni_3Al
n	0.933	0.944	0.926	0.953	0.948	0.976
k	0.038	0.040	0.043	0.031	0.073	0.063
Thickness	70 nm	60 nm	60 nm	50-80 nm	30 nm	TBD
Etching	Ion milling	Cl based	Cl based	Cl based	This work	This work
CD variation	40-60 nm	-	-	10 nm	-	-
Reference	(Mangat 2000, Letzkus 2004)	(Yan 2000)	(Yan 2000, Yan 2001)	(Shoki 2002)	-	-

Major advantages of using Ni as the absorber candidate over conventional Ta or Cr include the alleviation of the mask shadowing effect, as shown in Figure 1.5, and depth of focus, as shown in Figure 1.6.

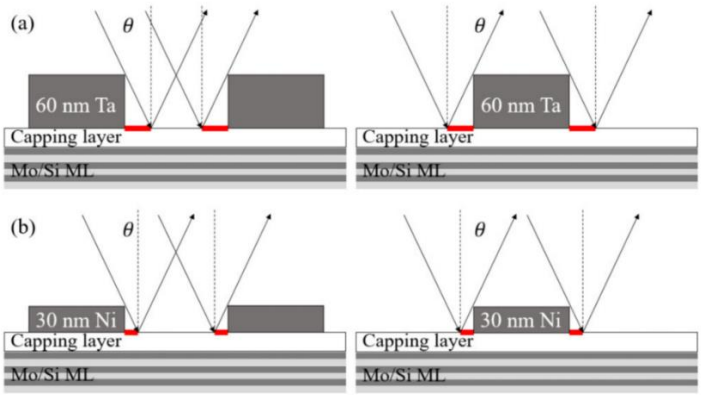

Figure 1.5 Schematic diagrams of EUV masks based on a patterned thin film metal absorber on complex multilayers. A (a) 60 nm Ta absorber and a (b) 30 nm Ni absorber are compared to show the difference in the mask shadowing effect due to the thickness difference.

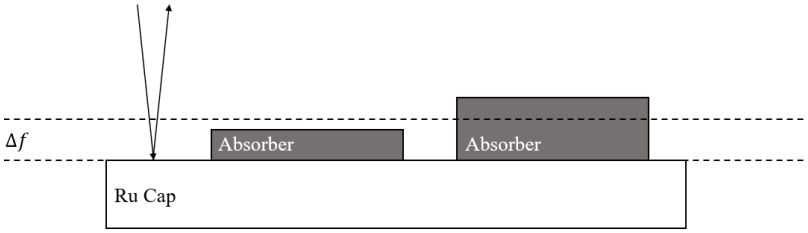

Figure 1.6 Depth of focus comparison between a thin absorber and a thick absorber.

With the EUV light source directed to the surface at an angle of θ off normal, the shadow created by the height of the absorber resulted in a change in the critical dimension (CD):

$$CD_{actual} = CD_{design} \pm 2dM \tan\theta \tag{1.2}$$

where d is the absorbing layer thickness, M is the EUV scanner reduction factor, and $\theta = 6°$ for the current generation EUV lithography system. The plus-minus sign corresponds to the CD change for the patterned lines and spaces, respectively. Assuming that all other optical properties remain comparable, reducing the absorbing layer thickness generally improves the fidelity of the mask absorber pattern. However, a thinner absorbing layer would require a metal that has an index of refraction (n) close to 1 and a large extinction coefficient (k). It has been measured experimentally (Luong 2018) and simulated computationally (Philipsen 2018) that Ni is such a candidate material where a much thinner Ni (∼30 nm) is as effective as the state-of-the-art absorber layers such as Cr- and Ta-based materials, commonly ranging from 50 to 70 nm (Scholze 2017), as shown in Figure 1.5 and Figure 1.6. The amount of deviation would be halved with the replacement of Ta by Ni (highlighted in red). The improvement is especially noticeable for extreme dimension features, where the deviation amount could be non-negligible to the actual feature sizes.

To continue the extreme shrinking of transistors, more emphasis is focused on mask patterning as well, which is also getting increasingly more difficult as more etch-resistant materials are incorporated, such as Ni. The aforementioned inertness of Ni suggests that it cannot be easily and selectively patterned, a prerequisite for its application in EUV. There has been some reported work on etching Ni, as summarized in Table 1.4, with many originating from the field of metallurgy. While the solution phase processes seem effective in etching Ni, the high etch rates and low selectivity to other materials render these processes incompatible with the requirement of patterning EUV absorbers. The predominant and successful gas-phase etching process relies heavily on either noble ion bombardment or halogenation. The former results in low selectivity and sidewall redeposition (Laegreid 1961), while the latter is prone to potential corrosion of other materials present in the system (Donnelly 2013). To address these issues and realize Ni patterning capable of delivering patterns for sub−10 nm features, a chemically effective technique with extreme precision and high selectivity, without halogen or argon, need to be developed.

Table 1.4 Reported chemistries for etching Ni in solution and gas phases.

Phase	Etchant	Temperature (℃)	Etch rate (nm/min)	Reference
Solution	30 HNO_3 : 10 H_2SO_4 : 50 Hac : 10 H_2O	85	10000	(Walker 1990)
	80% H_3PO_4 + 5% HNO_3 + 5% HAc + 10% H_2O	50	29	(Williams 2003)
	30% $FeCl_3$ + 4% HCl + 66% H_2O	20	21	(Williams 2003)
	3 HCl : 1 HNO_3 : 2 H_2O	30	100	(Williams 2003)
	50 H2SO4 :1 H2O2	120	380	(Williams 2003)
Gas	Ar_+ 500 V ion milling	-	66	(Williams 2003)
	50% CO + 50% NH_3 plasma	-	30-90	(Matsui 2002)
	20% Cl_2 + 80% Ar plasma	-	40	(Cho 2007)

1.1.2 Patterning Copper (Cu) for Back-End-of-Line (BEOL) Interconnect

The patterning of Cu could be dated back to the 15th century when artists in the medieval era uses acids in liquidous form to etch images from a copper plate. Such decorative purpose shares the essence with Cu etch for IC fabrication – covered regions need to be protected, while exposed regions need to be removed. Fast-forward to the late 1990s, Cu became the metal of choice for replacing the then-standard material, aluminum (Al), in interconnects. The transition happened as the industry continuously pushed for more responsive devices with smaller footprints, and the RC delay of the Al wire became the bottleneck. The advantages of Cu over the then-standard Al are summarized in Table 1.5. Cu is superior in key parameters such as lower electrical resistivity and higher thermal conductivity. In recent years, 13−15 levels of metal layers are typically required to

support technology nodes below 10 nm (Edelstein 2017) and thus the idea of developing a selective, low-temperature, gas phase etch process for Cu is revisited.

Table 1.5 Comparison of Al and Cu. (Quirk 2001)

	Aluminum	Copper
Electrical resistivity	2.65 $\mu\Omega$-cm	1.68 $\mu\Omega$-cm
Thermal conductivity	238 W/m-K	394 W/m-K
E_a for lattice diffusion	1.4 eV	2.2 eV
E_a for grain boundary diffusion	0.6 eV	0.9 eV

The incorporation of Cu introduces a completely different patterning process comparing to the Al-based interconnect system. The damascene process consisted of a Cu seed layer deposition over a patterned insulator layer. Such seed layer subsequently defines the growth region of an electroplated Cu; the electroplating process would fill up the trench without void. A chemical mechanical planarization (CMP) process, which mechanically abrases the surface alongside with the chemical-based slurry, was then used to remove the excess surface layer of Cu from electroplating. A step-by-step breakdown of the state-of-the-art damascene process used for manufacturing the Cu interconnect is shown in Figure 1.7.

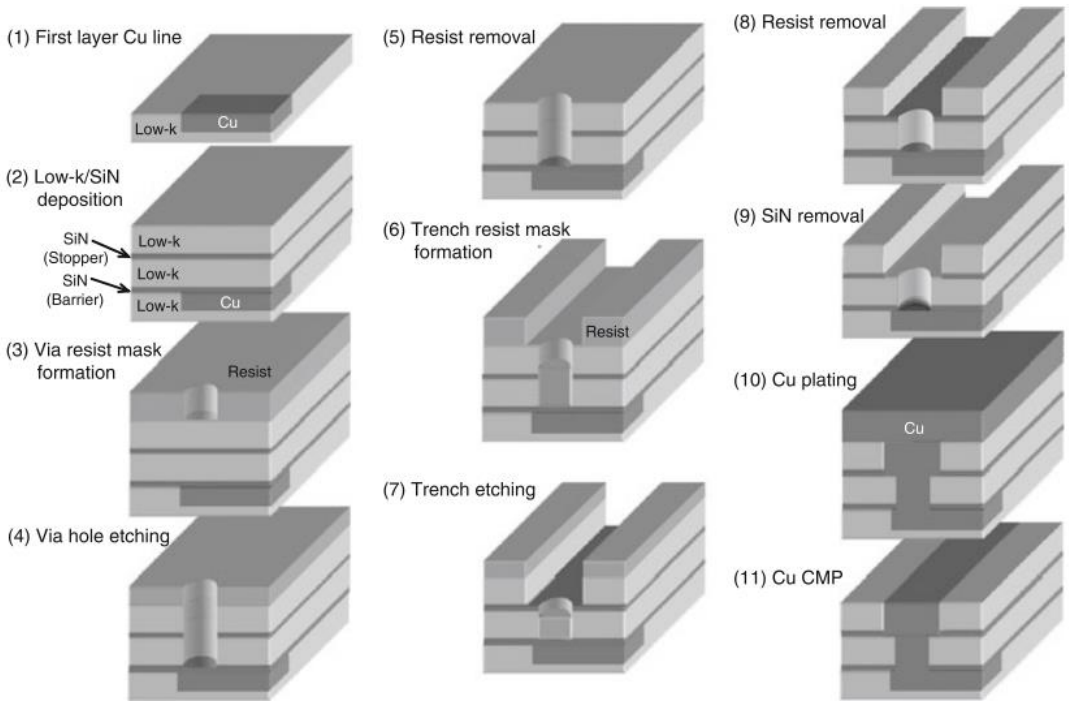

Figure 1.7 Illustration of the Cu damascene process. (Nojiri 2015)

The damascene process circumvents the dry etching of Cu, an issue perceived unresolvable in the early 2000s, and instead uses the patterned dielectrics to form trenches in which Cu would grow. Alternatively speaking, dielectric etch is easier than Cu etch that the addition of subsequent electroplating and CMP steps are considered reasonable trade-off. Over the past 25 years, the damascene process has been evolving alongside with the device shirking on the front-of-the-line (FEOL). Its complexity grew exponentially, as the number of transistors increased following Moore's Law. The most advanced BEOL interconnect could have up to a dozen of Cu layers, forming intricate, nanometer-scale highways, as shown in Figure 1.8.

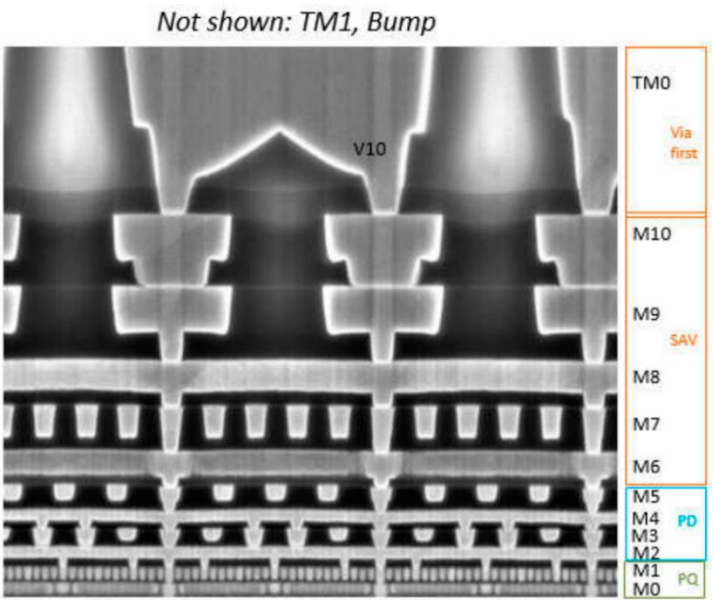

Figure 1.8 Cross-sectional image Cu BEOL interconnects. (Yeoh 2018)

As successful as it is, the damascene process is not without flaws. More importantly, the engineering challenges that could be solved or alleviated by process optimization, become insurmountable as the scaling of the devices become more extreme. Liner corrosion (Figure 1.9 left) is a typical emerging challenge. The end of cobalt (Co) liners is susceptible to corrosion when encountering slurries, an issue partially resolved by more advanced slurry chemistry but nevertheless persistent. Dishing (Figure 1.9 middle) is another common side effect from CMP, the extent of which is influenced by multiple factors such as linewidth, rotation speed, etc. Since Cu resistivity increases significantly with decreasing dimension at nanometer level, dishing could greatly affect the performance of the circuit and should be avoided. And finally, being a mechanical process, contamination such as particle formation (Figure 1.9 right) would be inevitable, which would lead to fatal circuit failure for advanced node chips.

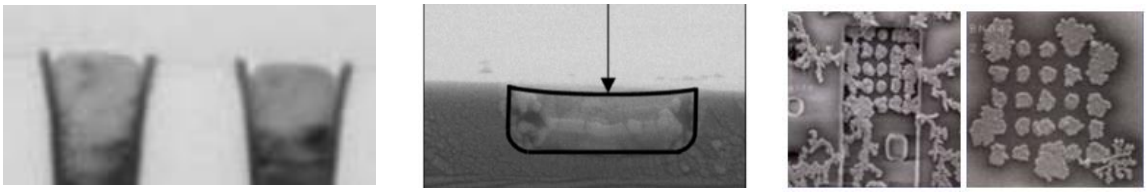

Figure 1.9 (Left) Liner Corrosion with missing Co, (Middle) Cu dishing with highlighted Cu contour, and (Right) Contamination on a post-CMP surface. (Chang 2005, Nogami 2013, Krishnan 2016)

These existing issues have already highlighted the imminent issues needed to be addressed in the BEOL patterning process to further extend the device scaling. There are, however, newer application scenarios that call for even more radical changes to the integration process, in which the conventional damascene process could be no longer applicable. Supervia, as shown in Figure 1.10, is an attractive new BEOL integration solution. As its name suggests, supervia is a via that goes beyond connecting M_x to M_{x+1} layer. In its simplest form, a supervia is capable of connecting M_x to M_{x+2} layer. The bypassing of M_{x+1} layer offers lower resistance and hence faster response time. It also provides better routing options to the overall design of the circuit.

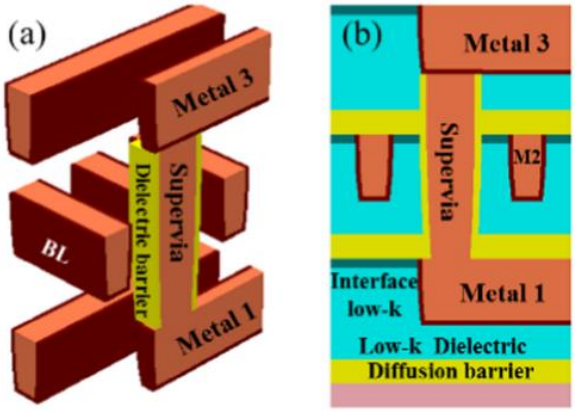

Figure 1.10 (a) Supervia routing from M_1 to M_3, (b) Full side view of metal low-k with supervia. (Gupta 2018)

It is not difficult to see why the traditional damascene process would be incompatible with applications like supervia – the previous layer-by-layer electroplating followed by across-the-wafer CMP could not produce location-specific interconnects that extend more than one layer. And supervias would be more prone to mechanical deformation due to their higher aspect ratio.

As CMP runs into numerous issues, the industry starts revisit the dry etch process of Cu, a task previously considered not possible. A handful of reported etching chemistry has been reported, as summarized in Table 1.6. The relatively high etch rate of the reported chemistries render them not applicable for using as BEOL patterning techniques. As such, new etching chemistry needs to be developed.

Table 1.6 Reactive ion etch chemistries reported for Cu.

Chemistry	Etch rate (nm/min)	Temperature (℃)	Reference
H_2	13	10	(Wu 2011)
12.5% CO + 87.5% NH_3	20	20	(Abe 2003)
CH_4	17	20	(Choi 2013)
50% CH_4 + 50% H_2	20	10	(Choi 2015)

1.2 Solution Etch of Metals

The need for etching metals started alongside with the development of metallurgy and, maybe to the surprise of today's semiconductor industry, medieval art. The former requires ore refining to increase the concentration of elements of interest, while the latter aims for the removal of specific regions to generate atheistically pleasing patterns. Whatever the purpose might be, similar traits are shared: to eliminate metals at certain locations, done in chemical solution baths. While the solution phase removal of metal is not the focus of this work, it is still valuable to reivew

its mechanism and to understand why it is not directly applicable to the atomic layer etch. It is well understood that, when metals are brought into contact with acids, ionized hydrogen would capture electrons from metals with lower electronegativity and result in metal ionized in solution. Such trend is tabulated as reduction potentials, the lower the reduction potential, the more susceptible that metal is to acids. Utilizing this reduction-oxidation mechanism, reactive metals are conveniently etched by various acids, while some of the more inert metals could not be treated as easily. A plethora of experimental data has been accumulated over the years on the effective etching of metals, and a number of them are used for etching metals in the context of IC fabrication (Walker 1990).

The glaring disadvantage of using solution etch in forming micro- or nanostructures is its omni-directionality, or isotropy. Since etchant molecules move with equal speed in all directions in the solution phase, they would attack the target molecule or atoms at the same rate in all directions. This would leave considerable amounts of undercut underneath the hard mask and result in a loss of pattern transfer fidelity. The undercut was tolerable when it was relatively negligible (nanometers) compared to the feature size (microns) and could be controlled via reasonable timing. However, with the requirement for ever-shrinking features (little room for undercut tolerance) and the incorporation of newer materials (requires new etchants with selectivity concerns), solution etch is less ideal due to its poor controllability.

Another major drawback of solution etch is the unsatisfactory results of defining high aspect ratio trenches and holes. Given the uncollimated flux and the viscosity of the liquid, surfaces near the entrance of the feature would be treated with higher flux and concentration compared to the regions deeper into the features, resulting in a non-uniform etching profile. Similarly, the

drying of the etchant is also non-trivial for features with high aspect ratios, as the capillary force would cause higher probability of recondensation, this would generally lead to unintended prolonged etch time. In short, different sections of the feature could no longer be treated using the same model when it comes to etching high aspect ratio features. Solution etch is not capable of etching those features with a uniform lateral etch rate.

1.3 Physical Sputtering of Metals

The conductivity and etch-resistance of metals share the same physical origin – their electron configurations. Unlike ionic bonds or covalent bonds, where electron pairs are localized within the vicinity of neighboring atoms, metallic bonds is characteristic with its delocalized electrons. While this delocalized, more evenly distributed electron configuration contributes to the macroscopic electrical conductivity, it also makes individual metal-metal bonds difficult to target, a prerequisite for nanometer-level etching processes. Therefore, physical sputtering, a process insensitive to the chemical bond cleavage, was investigated and remains widely adopted today (Kudriavtsev 2005, Seah 2010).

Physical sputtering uses ionized noble gas to physically bombard the surface. In a common setup, an argon gas is ionized inside a plasma chamber, accelerated towards the wafer as it travels through the plasma sheath, usually with an external applied bias. Incident ions collide with the surface species at a normal incident angle, during which the kinetic energy of the charged species would be transferred. Desorption of the surface species would occur if the incident energy exceeded the material-specific sputtering threshold. The sputtering yield, a quantitative measurement of sputtering effectiveness, is dictated by the relation:

$$Y = A\left(\sqrt{E_{ion}} - \sqrt{E_{threshold}}\right) \tag{1.3}$$

where Y is the sputtering yield, E_{ion} is the ion energy, $E_{threshold}$ is the sputtering threshold energy, and A is a projectile-target combination dependent constant (Chang 1997). As the bombardment process is purely physical, sputtering has been used extensively on chemically inert materials. It is also a directional process since the incident ions collide with the target species at the normal angle. The anisotropic etching behavior is however compromised by the angle-dependent yield characteristic of many of the target materials. Since the most effective sputtering typically takes place at ~45°, as shown in Figure 1.11, efficiency in sputtering contradicts the requirement of having vertical impinging momentum transfer, a requirement for highly direction etching. A fine balance between sputtering yield and final feature profile needs to be kept, which is extremely difficult for nanometer-level features.

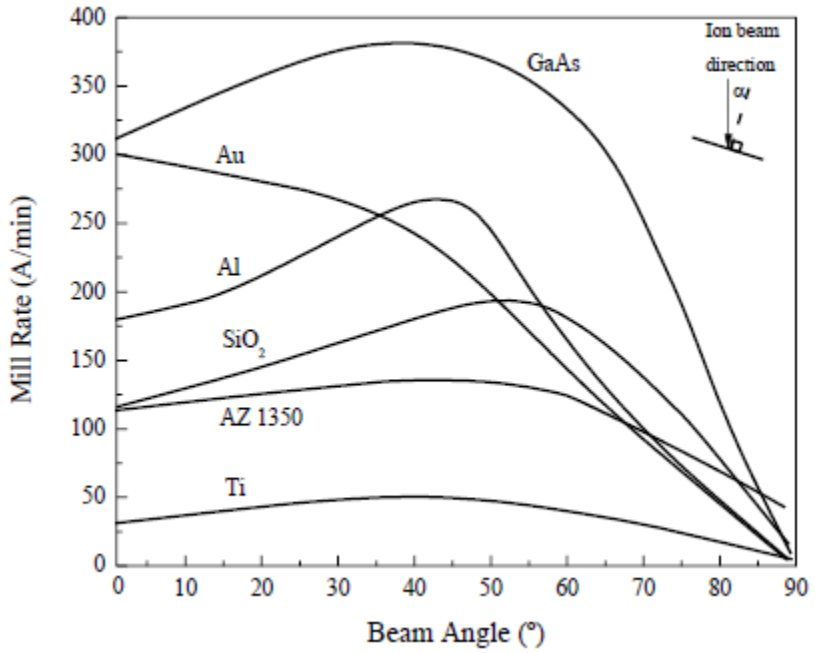

Figure 1.11 Argon ion sputtering rate of different materials as function of incident angle. (Smith 1973)

Another drawback of the physical sputtering technique is that such physical bombardment does not discriminate the target materials from its surrounding environment, which often resulted in poor selectivity of target material over hard masks, or worse, neighboring materials. It also suffers from sidewall redeposition of the etch products (Gonzalez 2014).

The overall surface reaction would be summarized by the reaction below:

$$\left[M - M - M_{(s)}\right] \xrightarrow{Ar^+} \left[M - M_{(s)}\right] + \left[M_{(g)}\right] \tag{1.4}$$

where M stands for one monolayer of metal atom and the square brackets group atoms that share the interconnecting chemical bonds. The tendency of sidewall redeposition could be explained by investigating the reaction. The transition from the condensed phase to the gas phase is facilitated by the kinetic energy of Ar ions alone, which means the etch product would return to its more energetically stable condensed state once the energy source is removed. The redeposition process from the gas phase back to the solid phase could be approximated by a poorly controlled physical vapor deposition (PVD) process, where the molecular impingement flux and surface concentration of the deposit are extremely non-uniform. To address this issue, a slight variation of the sputtering setup – ion beam etching (IBE) – is introduced, which utilizes highly directional and energetic Ar ions (instead of weakly ionized Ar ions from a plasma source). This approach is more ideal for etching high aspect ratio features as the energy (thus the directionality) of the incident Ar ion is not sheath dependent but preconfigured by the beam setup, up to keV range, versus tens of eV in a common plasma setup (Karahashi 2014). Creative techniques such as wafer tilting and rotation were also developed alongside the IBE processes, allowing ions to reach the bottom of the features,

alleviating the sidewall redeposition issue considerably. Wafer tilting angle is optimized so that sidewall etching fully compensates for redeposition, which is an empirical process that also factors in the calculation of etching and redeposition rates. An IBE system setup is represented in Figure 1.12.

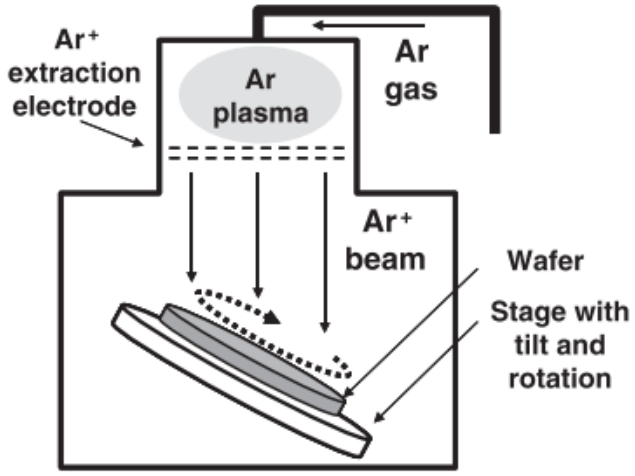

Figure 1.12 Ion beam etching setup with wafer tilting and rotation. (Sugiura 2009)

A comparison between features patterned by IBE before and after the incorporation of wafer tilting and rotation is shown in Figure 1.13.

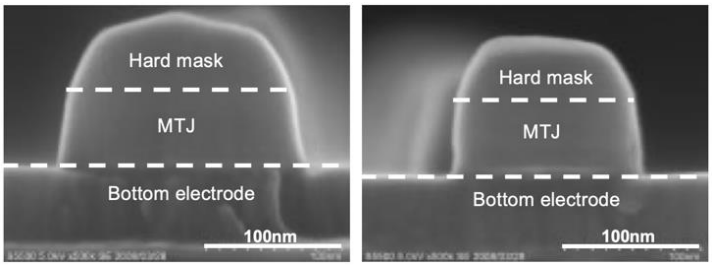

Figure 1.13 Patterning of magnetic tunnel junction without wafter tilting (left) and with wafer tilting (right). (Sugiura 2009)

One can easily think of the trade-offs that come with the wafer tilting approach. For instance, tilting greatly limits the feature geometry, making cylindrical feature the only viable configuration. Additionally, inter-feature spacing needs to be big enough for the ion beam to access the bottom of the sidewall without interfering with the neighboring stack, sacrificing the packaging density. And last but not least, the feature height is limited even with the help of wafer tilting. This approach is only applicable to specific stack configurations for specific applications.

Overall, physical sputtering is a reliable approach but far from ideal from the selectivity standpoint. In terms of the scope of this work, little published literature is available on the pure physical sputtering process of Ni or Cu, regardless of the setup. The lack of adequate tabulated data is not surprising since vapor phase etching of metal is investigated mostly in the context of IC fabrication, and the low selectivity nature of physical sputtering/ion beam etching renders them not an ideal approach for further optimization to begin with.

1.4 Reactive Ion Etching of Metals

Reactive ion etching (RIE) introduces a chemical component to the removal process and emphasizes the interplay between momentum transfer and chemical bond cleavage. The most iconic study of RIE, which has inspired and influenced the field for several decades and continues to provide insights into novel topics such as metal etching, is the work by Coburn and Winters that shows the combined chemical and physical effect on the etching of polysilicon (Coburn 1979). Figure 1.14 shows the data establishing the notion of ion-and-neutral synergy; the etch rate of silicon was measurable but small by either XeF_2 gas at a flux of 6×10^{15} molecules/cm^{2}s or a 450

eV Ar ion beam at a flux of 1.6×10^{14} ions/cm^{2}s. The etch rate then reached a ten-fold increase when Ar ions and XeF_2 gas were introduced to the system simultaneously.

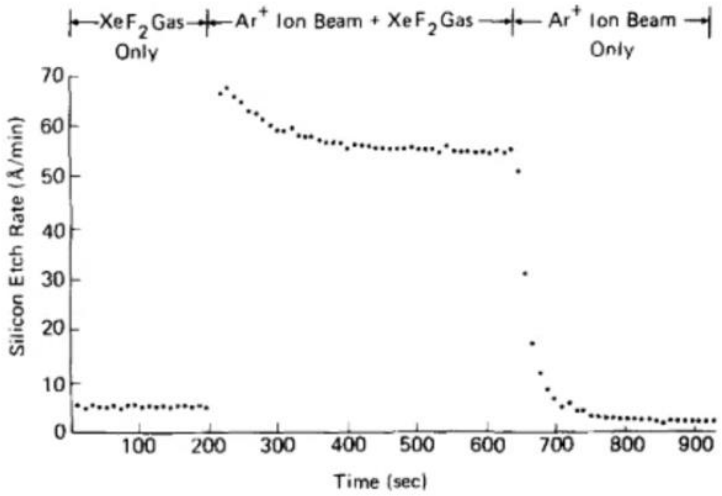

Figure 1.14 The synergistic effect between ions (Ar^+) and reactive neutrals (XeF_2) on etching silicon. (Coburn 1979)

The enhancement originated from a combination of various effects, including preferential dissociative chemisorption of XeF_2 on defect sites created by ion bombardment, ion-induced fragmentation of XeF_2 from momentum transfer, and collision-promoted cleaning of the gas-adsorbed surface. This original work led to many other studies where a spontaneous reaction with reactive neutrals led to the formation of volatile products, while an inert ion with energy higher than sputtering threshold energy can create a reactive site and facilitate the removal of the reaction products through momentum transfer. The general reactions, using the same notation introduced in the previous section, could be summarized as follows:

$$\left[M - M - M_{(s)}\right] + X/X^+ \rightarrow \left[M - M - MX_{(s)}\right] \tag{1.5}$$

$$\left[M-M-MX_{(s)}\right] \xrightarrow{Ar^+} \left[M-M_{(s)}\right] + \left[MX_{(g)}\right] \quad (1.6)$$

where X stands for the reactive chemical, usually halogen rich. The distinction between ionized species (X^+) and reactive neutrals (X) is made since the chemical effect of reactive neutrals is not negligible for common plasma setups, in which the degree of ionization is low (< 1%). It is noted that while the reactions are listed separately to delineate their respective role - chemical adsorption and physical desorption - the exposure to chemically reactive radicals and charged ions happen simultaneously on a macroscopic scale, as have been emphasized in Figure 1.14.

It is not surprising that, with the successful demonstration of RIE of Si, halogenation-Ar bombardment-based chemistries were quickly transferred to other target materials, including metals (Levinson 1997, Karahashi 2014, Paranjpe 2018). Vapor pressures of various metal fluorides and metal chlorides are systematically studied and summarized in Table 1.7. Temperatures are recorded when the corresponding metal halides reach a vapor pressure of 10 Torr, it can be observed that a temperature of hundreds of degrees Celsius is usually needed. The low vapor pressures at lower temperatures, a regime in which processing should take place, make metal halides rather difficult to stably form and subsequently get removed. The patterning of Ni for EUV mask absorber, for instance, needs to be carried out at a temperature under 200℃, as temperatures higher than that would cause irreversible intermixing of the Si/Mo multilayer, jeopardizing the reflecting capability. The patterning of Cu for BEOL interconnect also has a rather constrained thermal budget.

Table 1.7 Temperature at which the various metal halide achieve a vapor pressure of 10 Torr. (Nojiri 2015)

Element	Metal Halide	Temperature (℃)	Element	Metal Halide	Temperature (℃)
Ag	AgCl	1,074	Mg	$MgCl_2$	930
Al	AlF_3	1,324	Na	NaF	1,240
	$AlCl_3$	123.8	Ni	$NiCl_2$	759
Cd	CdF_2	1,559	Pb	PbF_2	904
	$CdCl_2$	656	Sb	$SbCl_3$	85.2
Cu	$CuCl_2$	702	Sn	$SnCl_2$	391
Fe	$FeCl_2$	700		$SnCl_4$	10.0
	$FeCl_3$	235.5	Zn	ZnF_2	1,369
Hg	$HgCl_2$	180.2		$ZnCl_2$	508
K	KF	1,039			
	KCl	968			

1.5 Atomic Layer Etching of Metals

With the development of the microelectronic industry, the focus of the etching field has been gradually shifted from “achieving higher etching rate” to “achieving greater etching profile”. As demonstrated earlier, the removal of the target film would be realized with enough external energy, either in the form of momentum transfer or chemical potential, or the combination of both. The finetuning of that energy, however, is a goal much more difficult to achieve. Using sculpture as an example, slamming hammer and chisel might serve the purpose for carving out rough features from a piece of marble, but much more delicate touches need to be applied (with the help of smaller hammers and chisels, of course) as the feature sizes become finer. To extend the analogy even further, that piece of marble is surrounded by tofu, and the integrity of the final structure relies on

minimizing tofu loss during the sculpturing. A marble-targeted, tofu-insensitive process needs to be developed.

That is exactly what the semiconductor industry has been trying to achieve. The idea of thin film processing with monolayer thickness precision has been avidly discussed for decades, as the realization of which would enable the ultimate control of device performance. The ability to deposit materials in a layer-by-layer fashion has been actively tested, developed, and commercialized, and the reaction scheme of atomic layer deposition (ALD) has been well-summarized: A modifying agent would be introduced to the surface, reacting at the available surface sites. The reaction would terminate itself once all surface sites are fully occupied. A deposition precursor would then be introduced to the system, react with the previously introduced modifier. The reaction would also self-terminate once all modifiers on the surface are consumed. (George 2009) The two reactions, commonly referred to as half-cycles, take place in an alternating manner, resulting in an extremely fine thin film growth. The overall reaction is graphically represented in Figure 1.15.

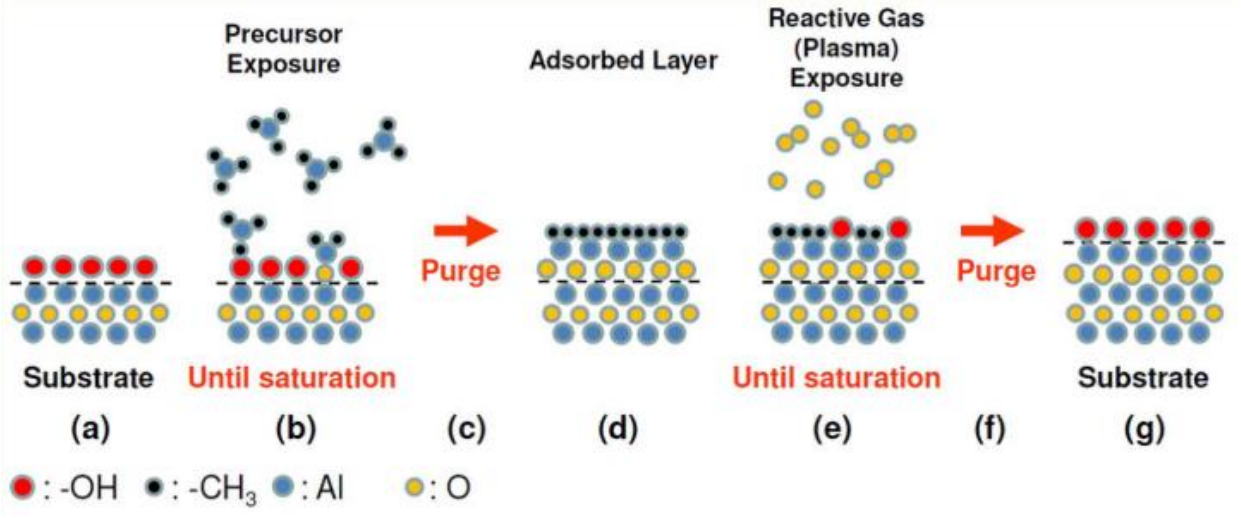

Figure 1.15 Schematic of one cycle of a typical ALD process. (Oehrlein 2015)

In the example shown in Figure 1.15, the surface modification half-cycle ((b)-(d)) is based on a self-limited adsorption process of a reactive precursor, followed by removal. The removal half cycle ((e)-(f)) involves exposure to an oxidizing gas, e.g., water, O_2 plasma, etc., followed by pump-out and transform the precursor layer into roughly a monolayer of the material. Multiple cycles of (a) to (f) would be repeated as needed to achieve the desired deposition amount (Oehrlein 2015).

This saturation behavior of the half-cycles makes the ALD process much more controllable compared to other deposition techniques such as physical vapor deposition (PVD) or chemical vapor deposition (CVD). ALD has been demonstrated to be successful on a vast variety of materials such as semiconductors and dielectrics, Table 1.8 shows a summary of reported metal ALD.

Table 1.8 Reported atomic layer deposition of selected metals.

Metal	Precursor	Reactant	Growth rate	Temperature	Reference
Ru	$Ru(EtCp)_2$	O_3	1.1 Å/cyc	250℃	(Kim 2012)
Rh	$Rh(acac)_3$	O_2	0.8 Å/cyc	200℃	(Aaltonen 2005)
Ir	(MeCp)Ir(CHD)	O_2	0.3 Å/cyc	275℃	(Hämäläinen 2010)
Pd	$Pd(thd)_2$	O_3	0.2 Å/cyc	160℃	(Hämäläinen 2013)
Pt	$MeCpPtMe_3$	O_2	0.5 Å/cyc	400℃	(Mackus 2012)
Ni	$Ni(dad)_2$	tert-butylamine	0.6 Å/cyc	200℃	(Kerrigan 2018)
Cu	$Cu(thd)_2$	H_2 plasma	0.1 Å/cyc	180℃	(Jezewski 2005)

With the successful experience of the bottom-up patterning technique, the industry started to investigate its top-down counterpart. The concept of atomic layer etching (ALE) was naturally

introduced as the reverse of ALD and utilized largely the same idea. But instead of a deposition reaction that leaves a reaction product stable enough in condensed phased on the surface, ALE requires a removal half-cycle generating etch product with high enough volatility to desorb from the surface and subsequently pumped away from the system. The overall reaction is illustrated in Figure 1.16.

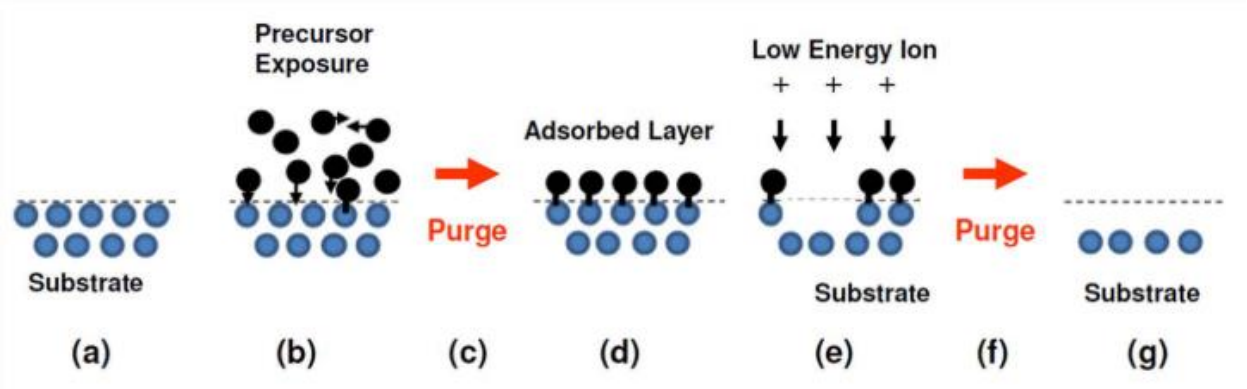

Figure 1.16 Schematic of one cycle of a typical ALE process. (Oehrlein 2015)

In the example shown in Figure 1.16, the surface modification half-cycle ((b)-(d)) may include self-limited adsorption, short deposition, etc., followed by removal. Low energy Ar ion bombardment is often used for selective removal half-cycle ((e),(f)). Multiple cycles of (a) to (f) would be repeated as needed to achieve the desired removal amount (Oehrlein 2015).

The concept of ALE is not a novel idea – related research could be traced back for more than 30 years. Like other constantly evolving technologies, ALE has been referred to by many previous nomenclatures such as molecular layer etching, digital etching, layer-by-layer etching, and others (Kanarik 2015). It is not surprising that the first attempts of ALE are on the patterning of Si and other semiconductor materials. ALE of silicon was first demonstrated using a chlorination-Ar bombardment cyclic process, as in Figure 1.17.

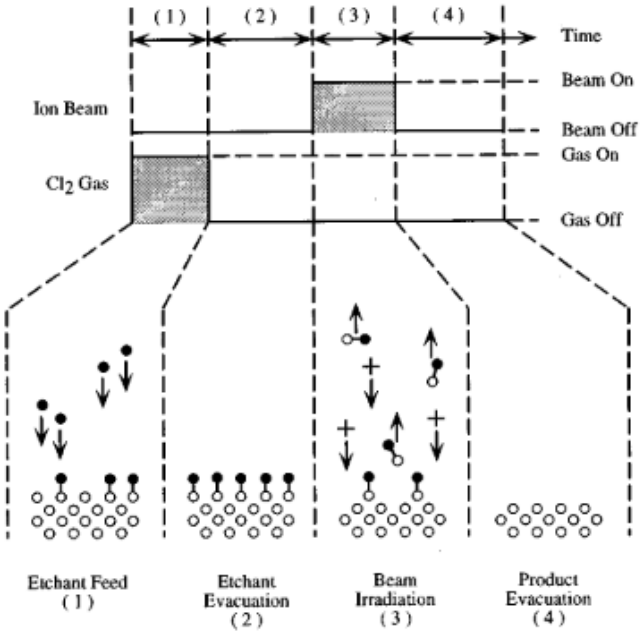

Figure 1.17 Schematic of first reported atomic layer etching of silicon. (Athavale 1995)

Pristine silicon surface was first exposed to chlorine, reaching surface site saturation while preventing further mixing into the subsurface layers of silicon. The covalent bond electron in the Si lattice would be attracted to the surface Cl atoms due to their higher electron negativity, weakening the underlying Si-Si bonds. The chlorine gas was purged, positively charged noble ions with a delicately tuned ion energy are then introduced. The incident charged ions have energy high enough to break the weakened Si-Si bond, but still below the sputtering threshold of pristine Si (an energy regime later termed "ALE window"). The reaction naturally stops after all surface Si-Cl are volatilized, leaving the underlying Si for the next cycle of chlorination. Since plasma is used in both the modification and removal half-cycles, this approach is conveniently named "plasma-ALE". This overall reaction could be represented by the following:

$$[M - M - M_{(s)}] + X/X^{+} \rightarrow [M - M - MX_{(s)}] \tag{1.7}$$

$$[M-M-MX_{(s)}] \xrightarrow{Ar^+} [M-M_{(s)}] + [MX_{(g)}] \quad (1.8)$$

While the symbolic representation of the reaction is the same as the RIE, plasma ALE bears major differences in two aspects. First, instead of the simultaneous exposure used in RIE, plasma ALE adopts a cyclic scheme since self-termination would only be possible with temporally separately half-cycles, resulting in an extremely controllable process. Second, the concept of "ALE window" is emphasized, as the removal Ar ions need to be energetic enough for modified region removal, but not too aggressive to damage the underlying pristine layers. This approach was subsequently extended to a wider range of materials, as listed in Table 1.9.

Table 1.9 Reported plasma atomic layer etching of selected metals and dielectrics.

Materials		Modification	Removal	Etch rate	Reference
Semiconductors	Si	Cl_2	Ar	0.7 Å/cyc	(Matsuura 1993)
	Ge	Cl_2	Ar	1.5 Å/cyc	(Sugiyama 1997)
	GaAs	Cl_2	Ar	0.9 Å/cyc	(Meguro 1990)
	InP	Cl_2	Ne	1.5 Å/cyc	(Park 2006)
	GaN	Cl_2	Ar	3.7 Å/cyc	(Kauppinen 2017)
	InGaAs	Cl_2	Ar	1.0 Å/cyc	(Park 2017)
	AlGaN	Cl_2	Ar	6.5 Å/cyc	(Fukumizu 2019)
Dielectrics	Si_3N_4	H_2	Ar	1.9 Å/cyc	(Matsuura 1999)
	SiO_2	C_4F_8	Ar	4.0 Å/cyc	(Metzler 2016)
	TiO_2	BCl_3	Ar	1.3 Å/cyc	(Yeom 2009)
	ZrO_2	BCl_3	Ar	1.1 Å/cyc	(Lim 2009)
	HfO_2	BCl_3	Ar	1.2 Å/cyc	(Park 2008)

The implementation of the ALE process is difficult since the tight ALE window requires extremely fine control of both modification and removal ion energy, which is even more challenging if the surface binding energy difference of pristine target material and its halide is insignificant. For example, the difference in surface binding energy between Si and $SiCl_2$ is about 2.4 eV, which results in a narrow ALE window of 20 eV. Additionally, considering the energy spread in most ion sources, ions with higher energies could inevitably introduce uncontrollable sputtering of the non-modified layer. The extension of the usual halogenation-bombardment plasma ALE scheme from semiconductors to metals could be difficult since metal halide is in general less volatile than $SiCl_x$ or $GeCl_x$. Etching selectivity over hard masks would also be of concern, as using other metals as hard masks would result in cross-contamination in the stack, while Si-based hard masks would be corroded at a much higher rate.

ALE could also be manifested in a different format - one that is a much closer resemblance to ALD. Instead of using charged ions in plasma as modification and removal reactants, "thermal ALE" relies entirely on thermally activated reactions in both half-cycles. Thermal ALE has a much wider ALE window as the reaction is dictated by thermodynamically favorable reactions without the presence of energetic ions. Reactions would stop at the boundary of the modified region as further reaction with the unmodified region is thermodynamically unfavorable. The overall reaction of thermal ALE could be summarized as the following:

$$\left[M - M - M_{(s)}\right] + X \rightarrow \left[M - M - MX_{(s)}\right] \tag{1.9}$$

$$\left[M - M - MX_{(s)}\right] + CL_{(g)} \rightarrow \left[M - M_{(s)}\right] + \left[LMX_{(g)}\right] + C_{(g)} \tag{1.10}$$

where C stands for the central atom in the organic complex and L stands for the ligand involved in the ligand exchange half-cycle. Compared to the reaction in the plasma ALE scenario, one sees the modification half-cycle utilize reactive molecules, not directional ions, and removal half-cycle accomplished by a ligand exchange process with organic complex, instead of physical bombardment. This showed great potential in certain applications where the binding energy difference between the plasma-modified region and pristine layer is indistinguishable. On the other hand, since both the modification and removal half-cycles use thermal reactions, thermal ALE is intrinsically isotropic and thus not compatible with applications requiring vertical feature sidewalls or high aspect ratios, which are usually required for patterning metals. A summary of materials reported to be etched using thermal ALE is listed in Table 1.10.

Table 1.10 Reported thermal atomic layer etching of selected metals and dielectrics.

Materials		Modification	Removal	Etch rate	Temperature	Reference
Metals	Co	Cl_2	hfac	2.0 Å/cyc	140℃	(Konh 2019)
	Cu	O_2/O_3	hfac	2.6 Å/cyc	275℃	(Mohimi 2018)
	W	O_3 & BCl_3	HF	2.6 Å/cyc	207℃	(Johnson 2017)
	Fe	Cl_2	acac	50 Å/cyc	135℃	(Lin 2018)
Dielectrics	TiN	O_3	HF	0.2 Å/cyc	250℃	(Lee 2017)
	Al_2O_3	$Sn(acac)_2$	HF	0.3 Å/cyc	200℃	(Lee 2015)
	ZnO	O_2	acac	1.3 Å/cyc	250℃	(Mameli 2018)

Reported literature of both plasma and thermal ALE overwhelmingly used halogen-based chemistries as the modifying agents, which is an intuitive choice as halogens have high

electronegativity and could easily bond to the surface atoms. The use of halogen, however, imposes long-term corrosion concerns on the processing chambers. From both equipment preservation and environmental protection perspectives, it is ideal to develop an alternative, halogen-free modifying chemistry capable of establishing the reaction selectivity, while alleviating issues such as corrosion and hard mask erosion.

1.6 Plasma-Thermal ALE of Metals

From the previous comparison and analysis, both plasma ALE and thermal ALE have their respective trade-offs. Plasma ALE grants both selectivity and anisotropy but requires separate control of individual steps, both are highly energy sensitive with sometimes narrow ALE windows. Thermal ALE leverages fine-tuned overall thermodynamics to enable new reaction pathways, but comes with the cost of elevating reaction temperature, which might not be acceptable for reaction schemes with limited thermal budgets. It also sacrifices the control over anisotropy, given the random-motion nature of neutral particle movements.

Based on the aforementioned discussions, a generalizable, hybrid plasma-thermal approach for ALE is proposed with the goal of combining the advantages from both the plasma ALE and thermal ALE while alleviating their respective drawbacks, and at the same time broadening the selection of modification and removal chemistries. The comparison between the three approaches can be summarized in Table 1.11.

Table 1.11 Comparison between plasma ALE, thermal ALE and proposed plasma-thermal ALE processes.

		Plasma ALE	Thermal ALE	Plasma-thermal ALE
Half-cycles		Plasma modification Ion sputtering	Chemical modification Chemical etching	Plasma modification Chemical etching
Modification	Chemical Contras Formation	Chemisorption of halogen atoms via plasma 	Conversion via thermal reactions 	Conversion via plasma 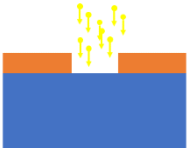
	Control Parameters	Plasma chemistry	Reactant pressure/temperature	Ion chemistry and energy
	Origin of Selectivity	Difference in surface binding energy 	Difference in reaction favorability 	Difference in reaction favorability 
Removal	Etch Product Formation	Physical, anisotropic 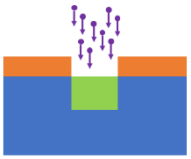	Chemical, isotropic 	Chemical, isotropic 
	Control Parameters	Argon ion energy 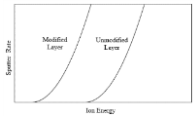	Pressure, temperature 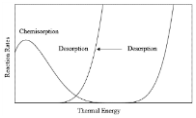	Pressure, temperature 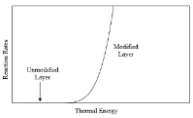
	Origin of Anisotropy	Directionality of Ar^+ 	Isotropic 	Chemical contrast 
Comments	ALE Window	Narrow, ion energy sensitive	Wide, determined by thermodynamics	Wide, determined by thermodynamics
	Control of Selectivity & Anisotropy	Both, in separate steps	Selectivity control only	Both, in single step

As shown in Table 1.11, plasma-thermal ALE has its modification half-cycle accomplished by plasma treatment, while the removal half-cycle is realized by thermal reactions. The respective advantages of both plasma ALE and thermal ALE are captured simultaneously. The origin of selectivity and anisotropy in the plasma-thermal ALE process is identical: difference in reaction favorability in the removal step. This has the advantage of only requiring control of ion energy during the modification step, once the chemical contrast is established, subsequent removal would only be allowed thermodynamically on the tailored region, anisotropy is intrinsically maintained. Directionality is not required in the removal step since previous chemical contrast would inherently guarantee proper etch stopping on the sides. By comparison, ALE conditions in these plasma-thermal-based etching chemistries are much more forgiving compared to plasma ALE setups since temperature and pressure are relatively easy to control than ion energies. The self-limiting characteristic of the proposed process comes from the selectivity between the target material and its surroundings, which is dictated by the difference in thermodynamic favorability that could be determined by means introduced previously. The difference in thermodynamic favorability of different materials when exposed to the same chemistry could be leveraged to serve as reaction gateways to enable selective removal of target materials. Plasma-thermal ALE could be summarized as the following:

$$\left[M - M - M_{(s)}\right] + Y/Y^{+} \rightarrow \left[M - M - MY_{(s)}\right] \tag{1.11}$$

$$\left[M - M - MX_{(s)}\right] + CL_{(g)} \rightarrow \left[M - M_{(s)}\right] + \left[LMY_{(g)}\right] + C_{(g)} \tag{1.12}$$

where the Y stands for a more general modifying agent, not limiting to halogen. The hybrid nature is also reflected by the reaction equations, where the modification half-cycle resembles that in the plasma ALE process and the removal half-cycle resembles that in the thermal ALE process.

1.7 Selectivity, Specificity and Anisotropy

The demonstration of ALE confirms the importance of chemical contrast, as it is essential to enable the layer-by-layer removal scheme. Plasma ALE and thermal ALE tackle the realization of chemical contrast via two mechanisms, energetic ions, and thermal reactions, respectively. To further leverage the chemical contrast, and the etching selectivity it enables, one needs to closely analyze its origin. The well-established, selective etching process of SiO_2 over Si could be used to borrow insights from. And from this example, one can see that halogenation is one of many potential means for surface modification.

It is well known that very large chemical selectivity can be achieved between Si and SiO_2: the most effective chemistry in selective etching of SiO_2 over Si is by hydrofluoric acids (HF). Diluted HF (6:1 = H_2O:HF by volume) can etch thermally grown SiO_2 at a rate of 1200 Å/min, whereas the highest etch rate of Si in HF solutions is reported to be ~0.2 Å/min, yielding a selectivity of ~6000. The overall reaction for HF etching SiO_2 could be represented by reaction (Campbell 2001):

$$SiO_2 + 4HF \rightarrow SiF_4 + 2H_2O \tag{1.13}$$

At the molecular level, which is relevant to ALE, it is the effect of oxidation state and the electron configurations of the surface atom that dictate the chemically selective reactions. In the case of Si/SiO_2 system being etched by HF, as shown in Figure 1.18, high selectivity is realized by the difference in electron configurations between the polarized Si–O bond and covalent Si–Si bond.

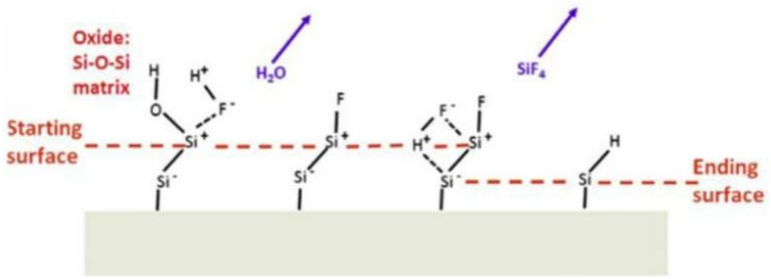

Figure 1.18 Mechanism leading to the formation of H-terminated Si surface by HF etching: The last step of oxygen removal involves HF attack of the Si–O bond, terminating the surface Si atom with F. Further attack of the polarized $Si^{\delta-}$–$Si^{\delta+}$ leads to H-termination. (Thissen 2012)

HF molecule is polar, due to the large difference in electronegativity between H and F. A similar but less pronounced polarity exists when Si is bonded to O (but not in Si–Si bonds). As HF approaches a Si–O bond, the relatively positive H would be attracted by the relatively negative O, forming H_2O and leaving the surface. After the complete removal of SiO_2 via HF wet etch, dangling bonds on the silicon surface would be bonded to fluorine atoms, given the higher Si–F bond energy (6.0 eV) compared to that of Si–H (3.5 eV). The ionic nature of Si–F bond would polarize the silicon back bond, making the surface silicon more positive and the atom underneath more negative. This asymmetric electron distribution allows the insertion of another HF molecule into the Si–Si bond, which in turn leads to the fluorination of the surface silicon and the hydrogenation of the silicon underneath. This process would repeat until the initial surface silicon is bonded by four fluorine atoms and leave the surface as SiF_4, exposing the second layer with hydrogen termination (Ubara 1984, Trucks 1990). The transition from an F-terminated surface to an H-terminated surface is accomplished via the removal of one monolayer of fluorinated silicon atoms—essentially an atomic layer etching process. This study, although not focused on patterning sub-nanometer features, is the basis of an important general model of atomic layer etching: surface

atom removal could be initiated by the polarization of surface bonding, which localizes electrons and creates a chemical contrast to the sub-surface layer. The change in electron configuration is macroscopically observed as the increase in surface oxidation state (commonly from zero to a higher value) and the subsequent change in composition (from metallic to compound). Comparing the SiO_2 removal by HF with $SiCl_x$ removal by Ar^+ introduced in the previous section, one could see this removal mechanism being applied even though the prior is a solution-phase reaction while the latter is done in the gas phase. This understanding is more critical for etching metal, where the electrons are delocalized and more evenly distributed.

Since surface modification (compositional control) is the critical first step, the use of plasmas should be considered as it has long been shown to be effective in modifying the surface composition of various materials. Preferential sputtering is a commonly observed phenomenon during ion bombardment, where energy and momentum transfer, which are highly mass-dependent, cause the incongruent removal of surface atoms. On the topic of whether mass or chemical bonding is more important to bombardment induced compositional change in alloys and oxides, however, it has been shown that chemical bonds play a more important role (Kudriavtsev 2005), which suggests that a chemical driving force during plasma exposure (with energetic ions) can be used to tailor and control the surface composition and chemical contrast (Kanarik 2018).

The polarization of surface bonding is essential for initiating the atomic layer process, but it alone is not sufficient. The effect of polarization acts differently on different crystallographic surfaces and has a different impact on the surface energy, as the pre-polarized surfaces occupied a different number of coordination numbers. Additionally, the energy of the removal half-reaction is also heavily subject to the electron configurations of different polarized surfaces, even the

general direction of the polarization is the same. For instance, the oxidation of Cu surface would, based on the conditions, results in the formation of Cu_2O, CuO, and $Cu(OH)_2$ to various degrees, respectively. While all three Cu-compounds share a similar electron polarization effect, they would react to subsequent removal chemistries with different favorability. This surface orientation-dependent reaction energies with compound dependent reaction favorability, necessitates the understanding of the thin film surface from a different perspective. A new term "specificity" is coined to reflect the focus on surface coordination and electron distribution, which is not emphasized in the conventional concept of selectivity.

1.8 Metal-Organic Compound Interactions

Complicated the metal-organic compound interaction process might be, etching is not the only field that focuses on metals' electron configurations and compositions, catalytic chemistry also devotes a considerable amount of focus, although for very different reasons. Metals, especially transition metals, are widely considered good catalysts for various reactions. Transition metals excel in this application due to their two-shell valence electron structure, in which electrons responsible for chemical reactions reside in not one, but two electron orbitals (Griffith 1964). This particular electron configuration allows easier losing or gaining of electrons from other molecules, ultimately resulting in interchanging between different oxidation states. In catalysis, it is always ideal to maintain a clean, external bond-free metal surface, in order to maximize the flexibility of electron bonding to different atoms. Deactivation of catalytic performance might occur as the consequence of one or more of the following causes: unwanted physisorption or chemisorption of foreign atoms on the catalyst surface; physical coverage of catalyst surfaces via change in

morphology and/or agglomeration. In the broadest sense, the deactivation process usually includes multiple reactions and is a combined effect of both physical and chemical loss of available surface sites. The term ‘catalyst poisoning’ is used to aptly describe the essence of the scenario. The concept of poisoning could be handily borrowed and repurposed in the development of etching processes, where the formation of surface metal-nonmental bonds is ideal for establishing chemical contrast. Unlike the environment in which catalysts are often located, the number of unwanted species is minimized in high vacuum systems used in fabricating integrated circuits, where nanometer level etching is carried out. The number of unintentional bond formation and unwanted reactions are thus avoided. Surface bonds could be formed controllably instead of inadvertently. In other words, metal surfaces could be purposefully ‘poisoned’ to localize valence electrons.

This ‘intentional poisoning’ approach can be particularly important for etching chemically inert metals such as Pd and Pt, which are chemically inert and etch-resistant but extensively used and studied as catalysts in a vast number of reactions. While catalysts are commonly treated as spectators of reactions, they do participate in intermediate reactions and the oxidation state of noble metals is not constant throughout the catalytic cycle. They typically lower the reaction energy barriers via altering oxidation states and return to the original state in the final step. An example extensively studied in the field is the Heck reaction, as shown in Figure 1.19.

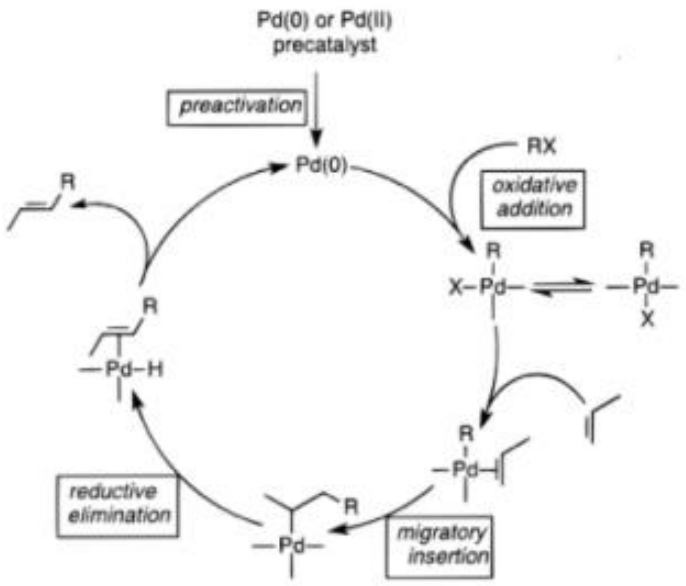

Figure 1.19 A simplified catalytic cycle for the Heck reaction, in which the oxidation state of Pd increases during oxidation addition and decreases during reductive elimination. (Beletskaya 2000)

The Heck reaction could be summarized as the formation of a substituted alkene from unsaturated halide (or triflate) with an alkene in the presence of a palladium catalyst. One of the basic types of reactivity in palladium-driven catalytic cycles comes from the ability of Pd(0) species to undergo oxidative addition to various R–X bonds and the addition of thus formed R–Pd–X intermediates to unsaturated bonds. The R–Pd–X intermediates have more flexible electron configurations and could be attached to external ligands, undergoing the migratory insertion step. Finally, a new bond between carbons is formed and Pd is freed from the complex, available for the next cycle of catalysis. This is an extremely simplified discussion of this reaction, but it nonetheless captures the importance of the oxidation state of Pd. While Pd is commonly regarded as inert and unreactive, the change of its oxidation state in the Heck reaction cycle is at the core of realizing the subsequent reaction.

The Heck reaction is one of many catalytic cycles to show the regeneration of catalysts, which means the full recovery of initial catalysts. But unlike many other catalytic cycles such as the Monsanto process or the Wacker process, where metalorganic complexes are used as catalysts, metallic Pd is used in the Heck reaction, and thus could provide potential insight into etching of metals. If the intermediate R–Pd–X could be extracted and react with other targeted chemistry, the irrecoverable removal of Pd (not ideal for catalysis but beneficial in ALE) could be realized. Abundant literature exists on the formation of Pd intermediates, but subsequent intermediate removal still lacks in-depth study. The importance of oxidation state could also be seen in the synthesis of organometallic precursors for chemical vapor deposition (CVD) of noble metals such as Pd and Pt, where the metalorganic compounds need to be volatile, such as metal β-diketonates complexes (Shushanyan 2019). Leveraging this knowledge, metal etching could be realized if the process leading to the formation of volatile metal β-ketohydrazonates can be achieved on surfaces via the control of the oxidation states. A systematic way of evaluating the feasibility of these reactions would provide insight into developing chemical etching processes that address both selectivity and directionality. Now that the importance of the oxidation state is addressed, the next question is how to manipulate the oxidation states of metals in a controlled manner. For ultra-thin (<3 nm) oxide on metal surfaces, Cabrera and Mott developed a theory characterizing the oxidation kinetics, starting with oxygen physisorption onto a surface (Cabrera 1949). For film thickness at which quantum tunneling effect is non-negligible, electrons could pass freely from the metal to the oxide surface to further ionize the physiosorbed oxygen atoms. The accumulation of electrons at the surface would establish a constant field inside the oxide layer, eventually setting up a quasi-equilibrium between the metal and the adsorbed oxygen. Oxide formation would terminate once the equivalent amount of charge is moved in the opposite direction via metal ion diffusion.

Therefore, if a chemical driving force during plasma exposure (with energetic ions) can be used to tailor and control the surface oxidation states, the resulting chemical contrast may be leveraged to realize ALE.

In short, ALD-originated modification-removal half-reactions reveal the possibility of achieving material subtraction utilizing similar cyclic approach. Such approach, partially observed and considered unideal in fields such as catalysis, could be intentionally pursued on chemically inert metals for their etching. Etching selectivity is enabled from reaction favorability difference between modified region and pristine region. Energetic ions also provide directionality required for patterning high aspect ratio features. On a microscopic scale, the interaction between modified metal surface and organic compound would happen preferentially on surface sites with certain electron configurations, thus etching specificity could be reached.

Chapter 2 Experimental Setup

This chapter describes the hardware setup and simulation background for performing surface modification and selective etching of hard-to-etch metals. This chapter also introduces various tools used for solution and thin film analysis, as well as sample characterizations and plasma diagnostics.

2.1 Sample Processing

2.1.1 UHV Transfer Tube and Load Lock

Handling, processing, and characterization of samples should be performed with the absence of contamination from the atmosphere. To achieve this, an ultra-high vacuum (UHV) system with a minimum pressure of 10^{-9} Torr is adopted. The system is made up of four major components, as shown in Figure 2.1: an inductively coupled plasma (ICP) reactor for performing plasma treatments; a transfer tube; an X-Ray photoelectron spectrometer; and a load lock for transferring samples for X-Ray photoelectron spectroscopy (XPS).

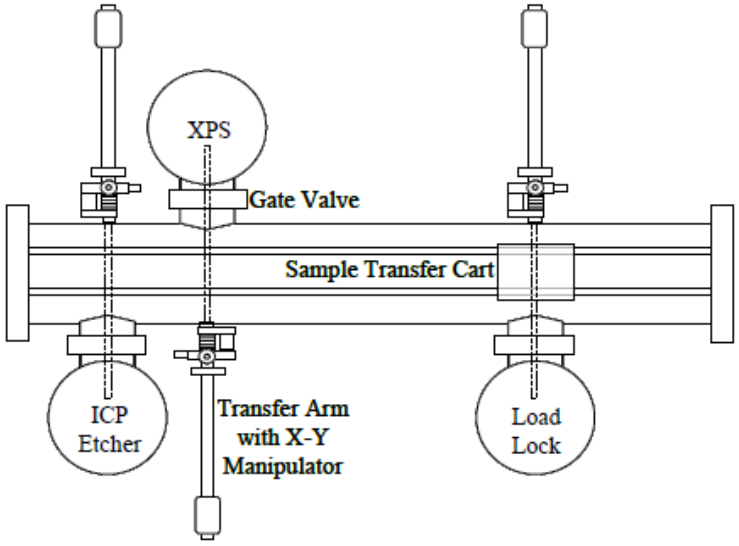

Figure 2.1 UHV system setup for in-situ sample transfer and XPS.

Three pumps are used to maintain low pressure: an Edwards E2M-18 mechanical pump, which is capable of lowering the pressure of the system from atmospheric to 10^{-3} Torr; a Leybold 360 turbomolecular pump, which lowers the pressure further down to 10^{-6} Torr; and a CTI CT-8 cryogenic pump, which can reach the lowest pressure of 10^{-9} Torr. A cold cathode gauge is used for pressure monitoring. Samples could be transferred from either the ICP chamber side or from the load lock side, which is pumped by another Leybold 360 turbomolecular pump. Linear transfer arms and transfer cart are used for transporting samples for XPS or loading/unloading.

2.1.2 Inductively Coupled Plasma (ICP) Reactor

The custom-built ICP reactor utilizes a planar structure, with flat helix wound from near the axis to near the outer radius of the discharge chamber. Inductive coil is driven by radio frequency (RF) power supply of 13.56 MHz. The body of the reactor is made of stainless steel and

has an upper and a lower compartment. Plasma is generated in the upper compartment, confined within a quartz jell bar, which acts as an insulating layer between plasma and stainless-steel chamber body. An electrode is present at the bottom of the upper compartment, which is connected to a power supply capable of applying 500 V of bias voltage. Setup of the ICP reactor is shown in Figure 2.2.

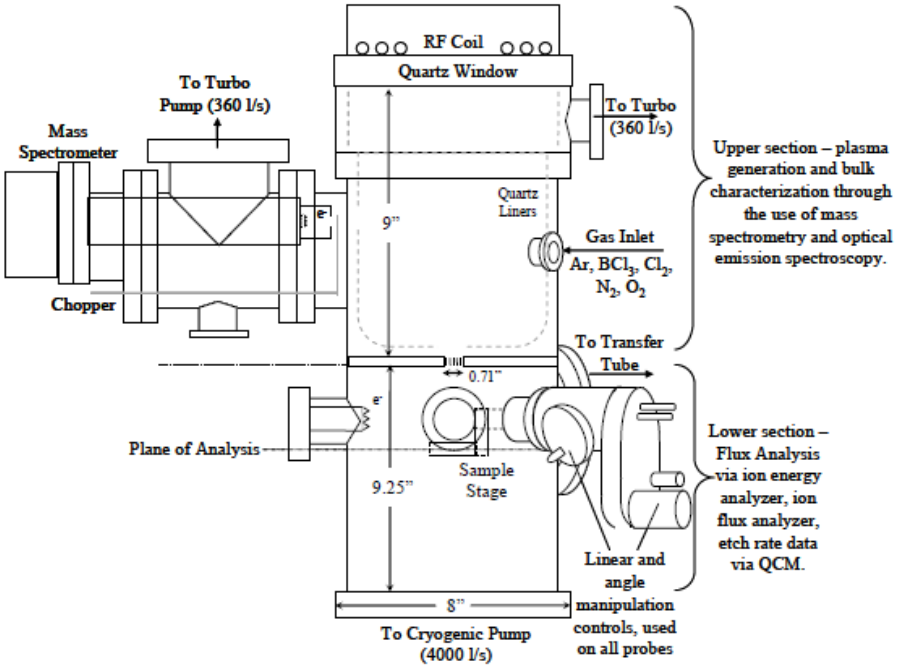

Figure 2.2 ICP reactor setup for in-situ sample processing.

The upper compartment is also used for plasma diagnostics like quadrupole mass spectrometer (QMS) and optical emission spectrometer (OES). An UTI 100C QMS could be connected for analysis of gas phase species by measuring the mass-over-charge ratio. An Ocean Optics S2000 OES system could be attached at the top of the quartz plate for species identification by reading characteristic emission spectra.

High vacuum in the ICP chamber is maintained through a Leybold D25 mechanical pump, a Leybold Turbovac 361C turbomolecular pump and a CTI CT-8 cryogenic pump. Various kinds of processing gases are introduced into the ICP chamber. Ar, N_2, O_2, Cl_2, and BCl_3 are fed from compressed gas cylinders. H_2, SF_6, and CH_4 are stored in smaller lecture bottles. Each gas flow is monitored by a corresponding mass flow controller. Experimental parameters used in the ICP system are detailed in Table 2.1.

Table 2.1 Experimental parameters used in the ICP chamber

Chemistry	Flow Rate (sccm)	Pressure (mTorr)	Power (W)	Bias (W)	Time (s)
O_2	30	30	500	0	120

2.1.3 Plasma-Therm 770 Reactor

Most of the experiments in this work were performed in a Plasma-Therm 770 reactor, located in the UCLA cleanroom. The system has an inductively coupled plasma (ICP) coil (13.56 MHz, 800 W) and a capacitively coupled substrate RF supply (13.56 MHz, 500 W), allowing relatively independent control of plasma density and ion energy. Helium back-side cooling is available to keep the sample cool during the process. The system is fully computer controlled and process detailed could be programmed by the user. The system incorporates a dual-chamber design. The system has a load lock, allowing sample loading and unloading. Load lock would be pumped to turbo pump pressure (~ 2 mTorr) before exposing to the processing chamber, and the sample, usually a coupon on a 4-inch carrier wafer, is transferred into the processing chamber with the help of a transfer arm. In the processing chamber, the carrier wafer ceramic is clamped on the outer ~5mm of the 100mm wafer to hold the sample on the RF chuck. A picture of the system is shown in Figure 2.3.

Figure 2.3 Plasma-Therm 770 Reactor for RIE and plasma modification reaction of ALE.

The system is capable of generating Ar, N_2, H_2, O_2, Cl_2 and BCl_3 plasmas. Gas flow rate, processing time, processing pressure, plasma power and plasma applied bias could be tuned by the user. Before the actual process, a 30 min of oxygen plasma process is typically performed on a cleaning wafer to remove any potential residue in the chamber from previous processes. Experimental parameters for RIE and ALE processes used in the Plasma-Therm 770 reactor are detailed in Table 2.2 and Table 2.3.

Table 2.2 Cyclic Chlorination-hydrogenation parameters used in the Plasma-Therm 770 reactor.

Chemistry	Flow Rate (sccm)	Pressure (mTorr)	Power (W)	Bias (W)	Time (s)
Cl_2	60	15	400	20	30
Ar		purge			90
H_2	20	60	200	60	15
			400		90

Table 2.3 Oxidation parameters used in the Plasma-Therm 770 reactor.

Chemistry	Flow Rate (sccm)	Pressure (mTorr)	Power (W)	Bias (W)	Time (s)
O_2	60	10	500	0	120

2.1.4 Vapor Chamber and Cold Trap

A custom-built vapor chamber is used for conducting experiments in the vapor phase. Due to the relatively high pressure of the experiment in this chamber, as well as concerns on contamination, the vapor chamber is separate from the other chambers described in this section and is not integrated onto the transfer tube system. This system is illustrated in Figure 2.4 and is largely made up of a 1.33” CF five-way cross. Samples are mounted to a steel rod on a rack and pinion drive that provides the linear motion needed to load and unload the sample and position it beneath the doser. Samples are cut into a size of 5 mm by 5 mm in order to fit the inlet of the chamber. Organic vapor is stored in solution phase in a quartz ampoule and is delivered with N_2 as the carrier gas. N_2 is also used as the venting gas after experiments. The organic solution flow is controlled by a Horiba liquid MFC LF-F20M-A and fed to a Horiba vaporizer MI-1141-PN, usually set to 80℃, while the carrier gas flow is controlled by an MKS Instruments MFC SEC-

E40 and also fed to the Horiba vaporizer. The mix of N_2 and organic vapor coming out of the vaporizer is fed through a 1.33" CF feedthrough that delivers the organic vapor directly above the sample mounted in the vapor chamber, which locates about 1 mm below the vapor delivery spot during exposure. It is noted that vaporizer is only operational with the presence of carrier gas, thus the pressure recorded in experiments is the sum of N_2 carrier gas and organic acid vapor. A Baratron gauge provides pressure measurement, and a mechanical rotary vane pump is used to keep the chamber at vacuum when not in operation, with a base pressure of 60 mTorr. During operation, the valve to the pump is closed, and the mixture of N_2 and organic vapor is usually allowed to reach pressures up to ~550 Torr. Both the vapor feed line and chamber are kept at 80℃ using metal heating wire, powered by two autotransformers. The system is also capable of delivering gas phase hydrogen dioxide (H_2O_2) via the attachment of a commercially available vaporizer vessel (RASIRC Brute Peroxide).

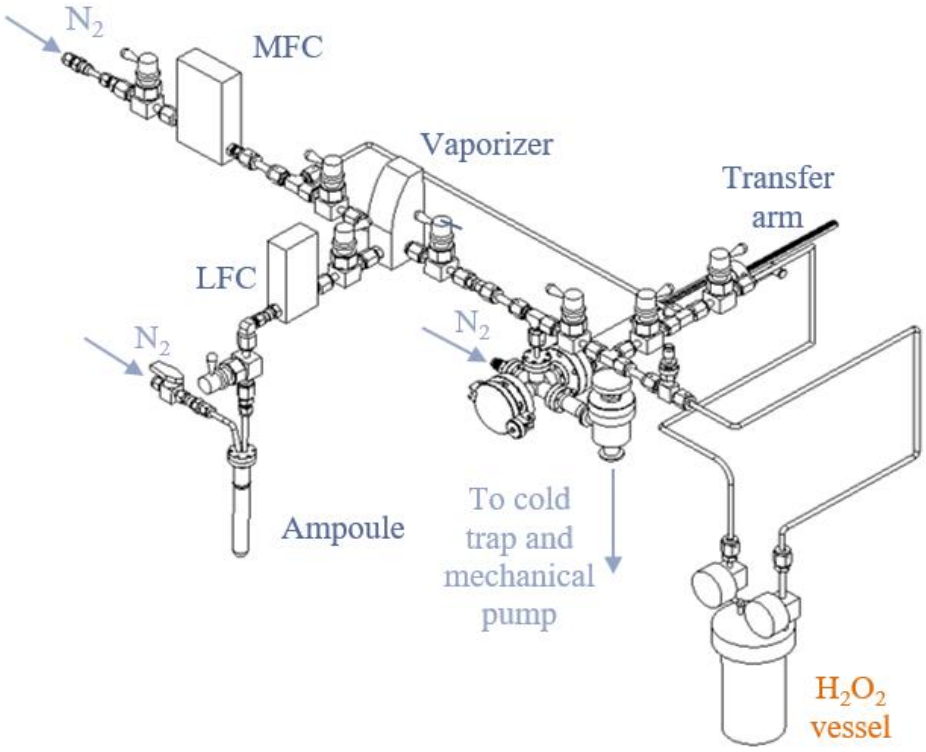

Figure 2.4 Vapor chamber setup for the removal reaction of ALE.

Experimental parameters used in the vapor system are detailed in Table 2.4

Table 2.4 Experimental parameters used in the vapor chamber.

Chemistry	Pressure (Torr)	Temperature ℃	Time (min)
Formic acid	150/350/550	80	60

Vapor chamber exhaust is connected to a MaxTrap -50C vacuum cold trap via a KF-25 connection, and the cold trap operates at -50℃ and has a stainless-steel cold well. Etch products would condense on the internal surface of the cold trap for later collection. Since formic acid, the etchant used in this work, has a melting temperature of 8.3℃, the setup has low enough of a temperature to fully condense the etch product.

The proper functioning of the could trap requires 800 mL of heat transfer fluid such as ethylene glycol. 30 minutes of ready time is required from turning on the system to reach its operation temperature. And reversely, about 30 minutes is required from turning off the system to reach room temperature. The cold trap also serves as a protection of the mechanical pump since the introduction of processing gas would severally damage the rotor of the mechanical pump and result in decrease in its lifespan.

2.2 Sample & Plasma Characterizations

2.2.1 X-Ray Photoelectron Spectroscopy

X-ray photoelectron spectroscopy (XPS) is a surface sensitive technique that is used to determine the chemical composition of the thin film. The detection limit of the XPS varies depending on the model and emission current, but generally fall in 7~10 nm range. Core-shell electrons of the atoms emit under X-ray exposure, carrying element specific information. Electron binding energies could be obtained from measuring their kinetic energies:

$$E_b = h\nu - E_k - \phi \tag{2.1}$$

where E_b is the characteristic binging energy of the electron, $h\nu$ is the energy of the incident X-ray photon, E_k is the kinetic energy of the emitted core-shell electron, and ϕ is the work function of the spectrometer. Elements presented could be determined once characteristic binding energies of electrons are obtained. Additionally, XPS could be used to distinguish the oxidation state of elements, by comparing the shift in binding energies with standard values. Shifts in binding energies is the result of the change in the chemical environment around any particular atom, including such factors as its charge, oxidation state, and local bonding structure. The photoelectron

energy analyzer counts all the incoming electrons within a range of binding energies to construct an XPS spectrum. These spectra can be collected over a very wide range of binding energies (1200 eV ~ 0 eV) to construct survey spectra, or they can be over a very narrow window of binding energies (40 ~ 50 eV range) to construct detailed spectra. Due to the scattering of electrons escaping from a sample, XPS is a surface-sensitive technique that samples from the first 7-10 nm of a surface. Using a Gaussian-Lorentzian fit, the contribution of each peak to the overall collected spectra shape can be determined, and the results can be used to determine the chemical composition of the sample by calculating the total areas under different peaks for each individual element. For Ni analysis, some of the most commonly used peaks and their binding energies are listed in Table 2.5, with corresponding colors highlighted in an example XPS spectra of Ni, shown in Figure 2.5.

Table 2.5 Binding energies for common chemical states of Ni.

Peak	Binding Energy (eV)		FWHM (eV)
	$2p_{3/2}$	$2p_{1/2}$	
Ni (red)	852.6	869.9	2.3
NiO (purple)	853.7	871.0	2.4
NiOH (blue)	855.6	872.9	2.4
NiO satellite (green)	860.7	878.0	2.6

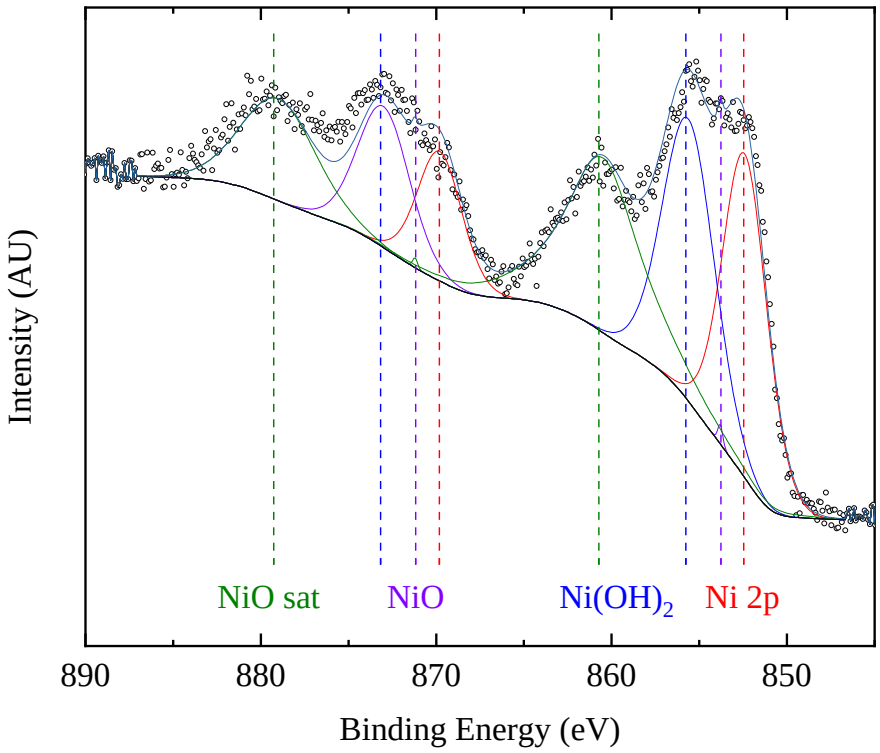

Figure 2.5 XPS spectrum of untreated Ni blanket thin film. Sample is a 40 nm PVD deposited Ni thin film on Si substrate.

2.2.2 Scanning Electron Microscopy

Scanning Electron Microscopy (SEM) is widely used for nanometer-scale imaging. Both top-down and cross-sectional measurements of etched blanked and patterned samples are conducted. Electrons are guided towards the sample using electromagnetic lenses at the energy of 200 eV to 30000 eV. Sample surface generates secondary electrons upon incident exposure, which are subsequently collected, amplified and finally displayed on a monitor. Different chemical compositions result in different secondary electron generation intensity, which translates to the grey scale on the final image. Etching efficacy could be determined by comparing the sample surface before and after etching. Etch rate could also be derived by measuring layer thicknesses

after a designed number of cycles. Additionally, sidewall profiles are essential for patterned samples in order to study etching anisotropy, which is also obtained by SEM imagining.

The microscope primarily used in this work is an FEI Nova 600 DualBeam SEM. The chamber is backed by a PVP variable volume piston pump and 240 l/s turbomolecular pump with pressures below 10^{-4} Torr while the electron beam column is maintained under high vacuum through three ion getter pumps. Nova 600 has a resolution down to 2 nm at 15 kV electron accelerating voltage. Realistically, due equipment aging and contamination from other users, resolution under 5 nm is not very reliable. It is noted that for extremely thin film, surface roughness and equipment error could potentially affect SEM measurements, therefore other complementary thickness measurement techniques such as ellipsometry and atomic force microscopy are needed. Example SEM images of a patterned Ni sample are shown in Figure 2.6. Typically, samples after multiple cycles of identical process are measured to obtain the average per-cycle effect of the applied process.

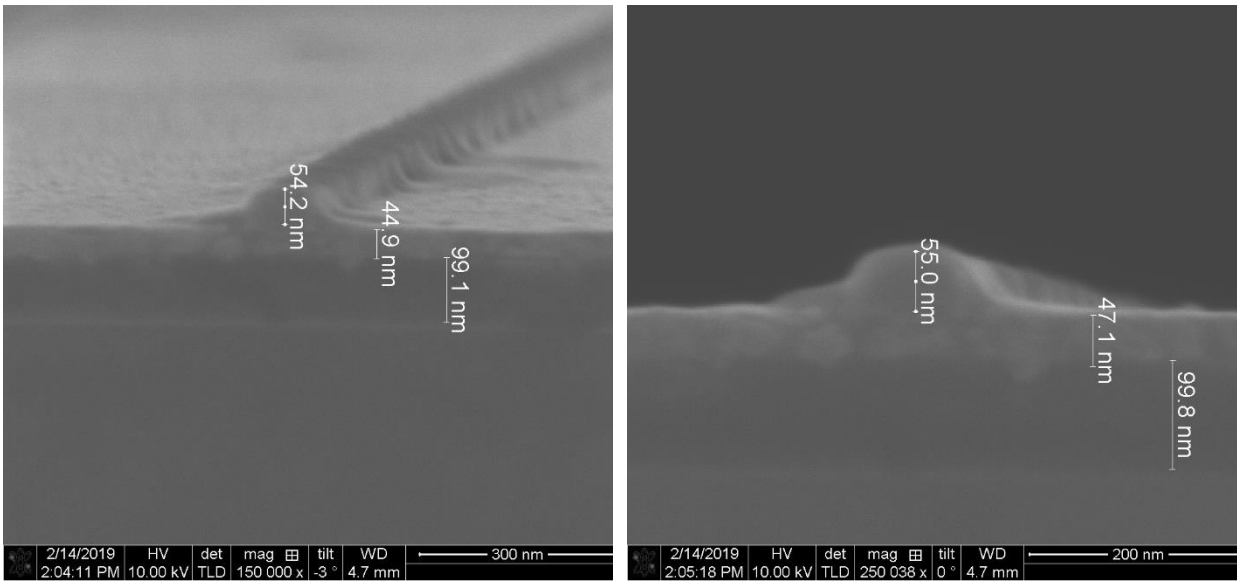

Figure 2.6 SEM images of as received patterned Ni thin film (thickness = 50 nm) with SiO_2 hard mask (thickness = 50 nm) on SiO_2 substrate (left) zoom-out bird's eye view (right) zoom-in cross sectional view.

2.2.3 Transmission Electron Microscopy

Transmission electron microscopy (TEM) is an imaging technique that shares similar working mechanism as SEM but provides higher resolution. Many properties not accessible by SEM, such as crystalline structure and grain orientation, could be characterized by TEM. Unlike SEM, where image is constructed by collecting secondary electrons, TEM collect electron that pass through the ultra-thin sample, revealing its internal structure. A typical TEM system is made up of four core components: 1) a monochromatic electron source, 2) a set of condenser lenses for illumination focus, 3) an objective lens used to form the first image of the specimen, and 4) a series of magnifying lenses to crease the final image. Samples for TEM analysis must be thin enough (~100 nm) to provide sufficient electron transmission and is usually processed by focused ion beam (FIB). In this work, gallium (Ga) ions at 40 keV energy are used to create the TEM samples. Layer structures in TEM images are also distinguished based on the interaction between the electrons and sample atoms. Two modes, bright field (BF) and dark field (DF) are available, in BF

mode only the transmitted (not diffracted) electrons are collected, making heavier elements to appear darker as they scatter a greater portion of the electron beam. The reverse is true in DF mode, as the electron beam is slightly tilted from the central axis and the diffracted beam is measured, making heavier elements appeared to be brighter on the final images. The system used in this work, Tian S/TEM, is shown in Figure 2.7, and a feature from patterned Ni sample after RIE treatment is imaged and shown in Figure 2.8.

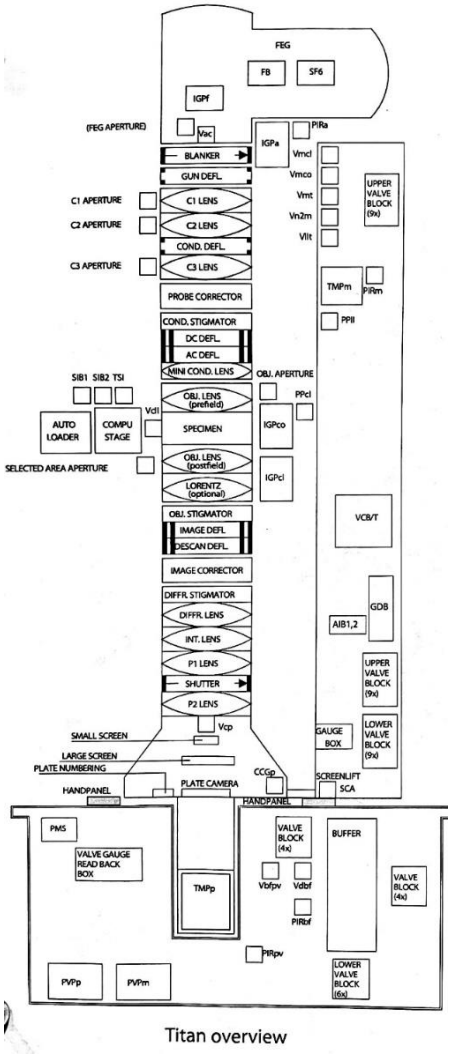

Figure 2.7 Titan S/TEM system layout.

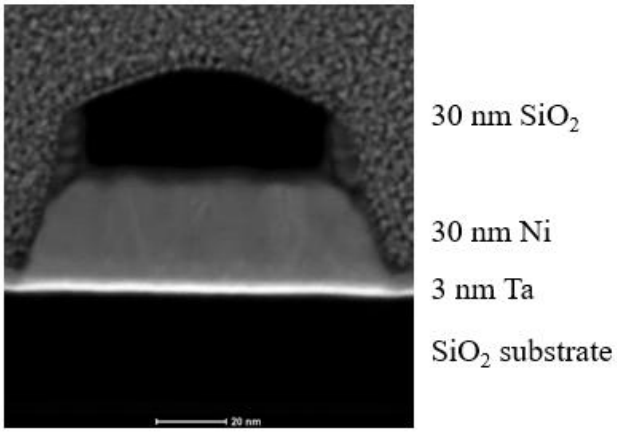

Figure 2.8 TEM image of SiO_2 hard mask (thickness = 50 nm, line width = 65 nm, line pitch = 200 nm) on Ni thin film (thickness = 30 nm), sample treated with 6 cycle of RIE process detailed in Table 2.2.

From Figure 2.8, the feature profile of sample post-processing is directly shown. It can be measured from the image that 30 nm of Ni was removed over the 6 RIE cycles, which gives an etch rate of 4.7 nm/cycle. At the same time, the initial 50 nm SiO_2 hard mask was etched partially and leaving 30 nm of remaining hard mask. The 20 nm of SiO_2 removal translate to an etch rate of 3.3 nm/cycle. Comparing the individual etch rate of Ni with that of SiO_2, a selectivity of 1.4 is established. The resulted sidewall angle is measured to be 70° for Ni and 80° for SiO_2 hard mask.

2.2.4 Electron Dispersive Spectroscopy

While XPS provides surface sensitive chemical information, signal collected is an average over the area detected (usually some square millimeters) and thus unable to distinguish the origin of the signal laterally on dense patterns. Additionally, it lacks the capability of generating vertical spatial data of elemental distribution, information essential for studying the etching result on multi-element stacks. Electron dispersive spectroscopy (EDS) is a widely adopted chemical

characterization technique that addresses this very issue. Coupled with either SEM or TEM, EDS could generate elemental maps that overlap with the microscope images, providing intuitive spatial distribution of elements. A typical EDS system includes an X-ray detector, a liquid nitrogen dewar for cooling, and a collecting software controlled via computer. As high energy electrons hit the sample during SEM or TEM measurements, part of the energy would be transferred to the electrons in the sample atoms, knocking them off and leaving holes behind. These holes would be in turn filled by electrons from higher energy shells, releasing X-ray characteristic to those energy transitions.

These characteristic X-rays are used to identify the existence of specific elements. The spatial resolution, however, comes with the cost of deeper probing depth (micrometers, comparing to nanometers in XPS), makes it less of a surface sensitive technique. It is therefore common to use XPS for capturing the average signal over a region and utilize EDS for location-specific information. A TEM-based EDS elemental mapping of Figure 2.8 is shown in Figure 2.9.

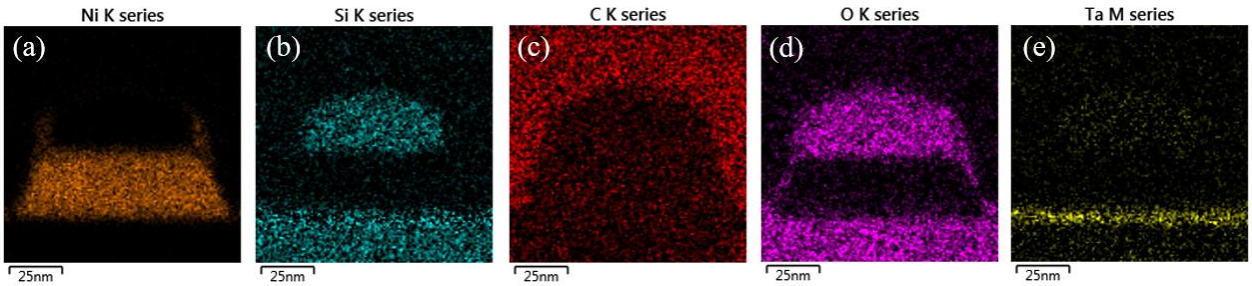

Figure 2.9 EDS elemental mapping of Figure 2.8 with (a) Ni K series, (b) Si K series, (c) C K series, (d) O K series and (e) Ta M series.

From Figure 2.9 the chemical information of the structure is clearly revealed. Ni in the exposed region is completely removed, oxidation of the exposed sidewall is observed with slight

re-deposition of Ni on the side of the SiO_2. The RIE chemistry has good selectivity over Ta, as shown by the intact Ta layer.

2.2.5 Electrospray Ionization Mass Spectroscopy

Identification, as well as quantification, of etch products is essential to validating the etching efficacy developed in this work as well as fully understanding the reaction mechanism and determining which chemistries are most effective in material removal. Electrospray Ionization Mass Spectroscopy (ESI-MS) is capable of determining solution phase etch products by breaking down molecules using electrospray. After liquid phase etching, etch solution sample is transferred into an injector, which pushed solution into the ESI-MS equipment. High voltage field is applied to the injected liquid, results in a Taylor cone which emits a jet of liquid droplets, from which excess solvent evaporates, forming a charged aerosol. As the evaporation process continues, the droplets become increasingly unstable due to charge-charge repulsion. Eventually, as the amount of charge in the droplet exceeds the Rayleigh limit, the maximum charge one droplet can take, the droplet aggressively decomposes into smaller droplets with greater stability (Fenn 2002). The ionization and decomposition process repeats until only ions remain, which subsequently travel into a mass spectrometer for analysis. ESI-MS is useful for determining the solution phase etch products of metalorganic etch products such as those seen in solution phase etch of metallic thin films. ESI-MS relies on the ability to ionize the complexes in solution and subsequently detect these ions using, in many cases, a quadrupole mass spectrometer to achieve high resolution in filtering ions of different mass-to-charge ratios. Example ESI-MS spectra of diluted formic acid with and without etching of Ni are shown in Figure 2.10, with the naturally existing isotopes listed in Table 2.6. It could be observed from the comparison that, the addition of Ni in formic acid

resulted in an increase of signal over the mass-over-charge ratio ranging from 143 to 153, showing additional molecules presented in the solution.

Table 2.6 Isotopes involved in the characterization of Ni etch products

Element	Isotope	Atomic Weight (amu)	Abundance
Hydrogen	^{1}H	1.00	99.98%
	^{2}H	2.01	0.02%
Carbon	^{12}C	12.00	98.9%
	^{13}C	13.00	1.1%
Oxygen	^{16}O	15.99	99.76%
	^{17}O	17.00	0.04%
	^{18}O	18.00	0.20%
Nickel	^{58}Ni	57.94	68.08%
	^{60}Ni	59.93	26.22%
	^{61}Ni	60.93	1.14%
	^{62}Ni	61.93	3.64%
	^{64}Ni	63.93	0.93%

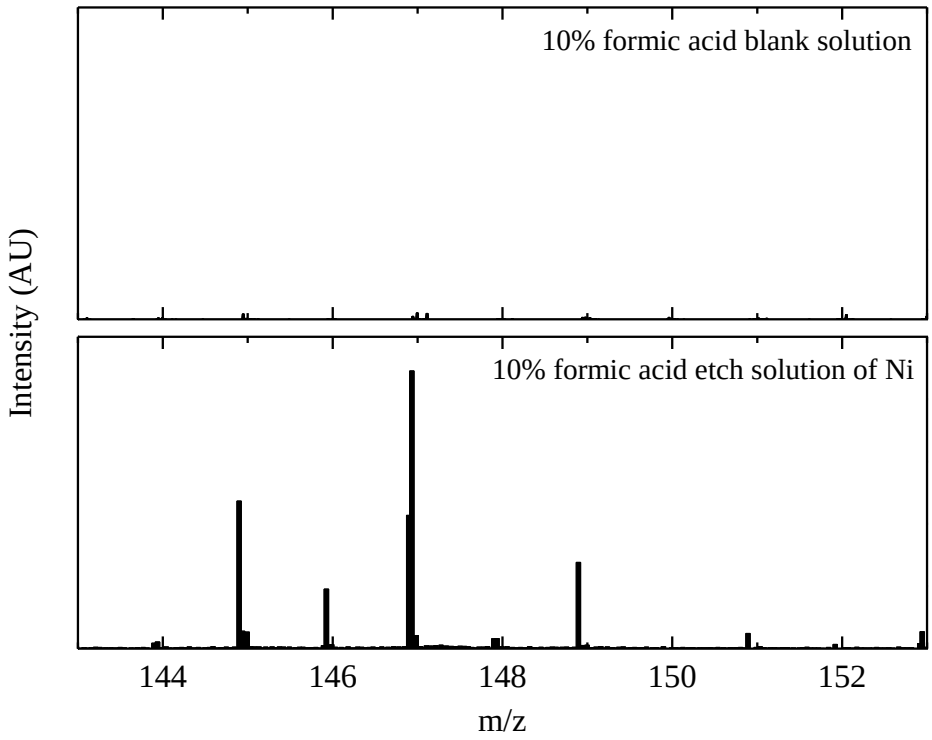

Figure 2.10 ESI-MS spectra for (top) 10% formic acid in water (bottom) 10% etch solution of Ni in formic acid.

2.2.6 Inductively Coupled Plasma Mass Spectroscopy

For ionic species, ESI-MS could be less effective since the solvation of the molecules would separate the ions and cations, leading to failure of recording the molecule m/z values. An alternative approach is needed for such case to individually capture the atomic information of the analyte. Inductively coupled plasma mass spectroscopy (ICP-MS) is used in this work for such analysis. ICP-MS is a mass spectrometry technique that is capable of dissociating and ionizing molecules into their constituent atomic species. A carrier gas, usually Argon, is needed for the introduction of the liquid sample via the formation of an aerosol. Ar^+ from the inductively coupled plasma is used to ionize the neutral species. The ionized species are then fed in the form of an ionized beam from the ICP torch, through a lens with a shadow stop which functions to block

photon emission from the plasma. The species pass through a small orifice known as a skimmer cone, ultimately through a secondary sampler cone. These passes result in pressure reduction of the sample stream to 10^{-5} Torr (Montaser 1998). Dilution of the sample solution is required to avoid the clogging of the delivery system. Finally, the stream of ions is focused by an electrostatic lens into a quadrupole mass spectrometer, in which the m/z value of different species are recorded.

The ICP-MS used in this study was a PerkinElmer NexION 2000. Argon was used as the carrier gas with a 20 L/min flow rate. The calibration curve was established using a standard solution while the dwell time was 50 ms with thirty sweeps and three replicates with background correction. A sample spectrum of a formic acid control is shown in. The analysis of ICP-MS result is similar to that of ESI-MS, m/z values of target spices are inspected in both techniques. A captured spectrum of copper formate tetrahydrate saturated solution is shown in Figure 2.11. Cu signal is shown at m/z values of 63 and 65, with an intensity ratio of close to 2.1:1, which matches the naturally occurring isotope ratio.

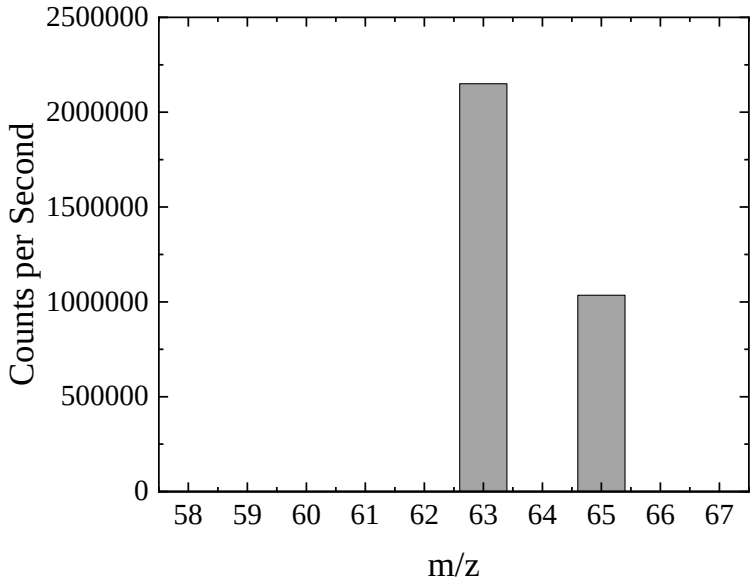

Figure 2.11 ICP-MS spectrum of copper formate tetrahydrate saturated solution.

2.2.7 Optical Emission Spectroscopy

In order to monitor the presence of different species and interactions between them in an in-situ and real-time manner, a custom-built optical emission spectroscopy (OES) system provided is used. As various charged and neutral species relaxed from excitation states, characterization photon emission associated with quantum energy states of different electron energy levels would be observed. These measured energies could be used to identify species within the plasma by determining the wavelengths of light. OES is particularly useful since it is a non-intrusive technique, as the probe in not physically in contact with the plasma. It could be used to monitor etching endpoints, quantify relative concentration of species, and even obtain plasma parameters such as electron temperatures and densities. An example OES spectrum of oxygen plasma is shown Figure 2.12, with oxygen peaks highlighted.

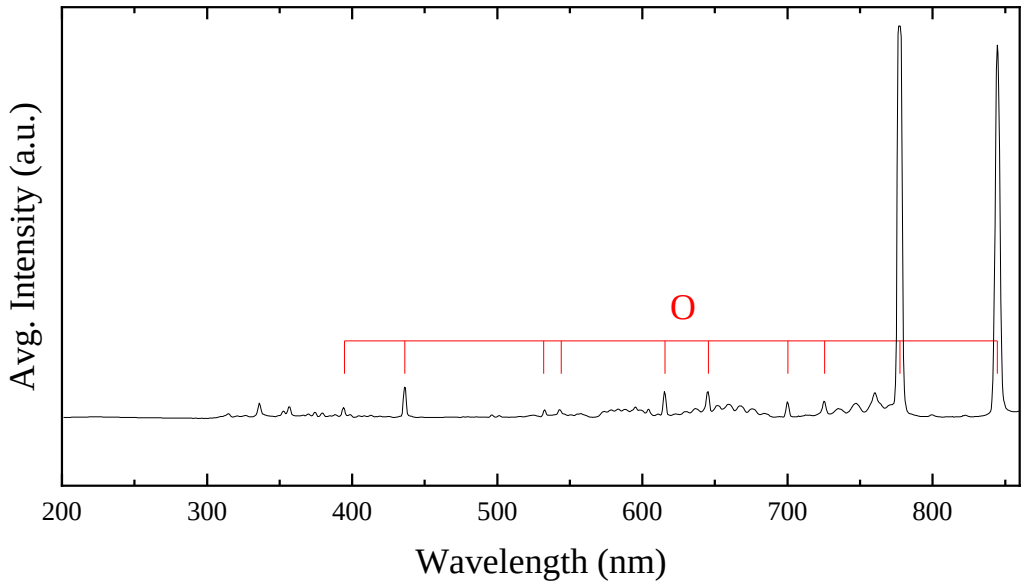

Figure 2.12 Sample OES spectrum of an oxygen plasma, 500 W ICP power, 0 W applied bias, 35 mTorr pressure.

2.2.8 Atomic Force Microscopy

Atomic Force Microscopy (AFM) is used to capture the surface morphology, which could be the roughness for blanket samples, or feature profile for patterned samples. AFM typically consists of three parts: a finely etched probe with a typical surface radius of a couple of nanometers, a laser beam that focused on the probe cantilever, and a photodiode detector (Rugar 1990). During the measurement, the probe scans across the surface in a line-by-line fashion. As the probe tip encounters changes in surface altitude, the cantilever would be bended, deflecting the laser beam from its original position. This interaction between the surface roughness and beam intensity would be recorded by the photodiode. With the proper choice of probe, measurement mode and engagement frequency, change in surface altitude can be constructed with nanometer resolution. Two measurement modes, contact mode and tapping mode, can be used. As their names suggest, the tip is constantly in mechanical contact with the surface in contact mode, and the deflection is recorded to construct surface morphology; for tapping mode, the probe is oscillated at a probe-specific default frequency while tapping along the sample surface. Any non-constant height signal would result in a change of the resonating frequency of the probe, which is used to back-calculate the change in altitude. Tapping mode is used in this work as it provides better spatial resolution due to the incorporation of a lock-in amplifier. It is also superior to contact mode since it reduces the time the probe touches the sample, which leads to decrease in probe sharpness. The choice of probe material is rather straightforward in this work, as sample hardness is of little concern. The probe geometry, however, is of crucial importance, as specific probe models enable the probing of hard-to-access regions. The probe used for surface roughness measurement is Bruker ScanAsyst (Si_3N_4, tip radius 2 nm), and the probe used for feature profile characterization is Bruker VTESPA-70 (Si_3N_4, tip radius 5 nm). Their respective images are shown in Figure 2.13.

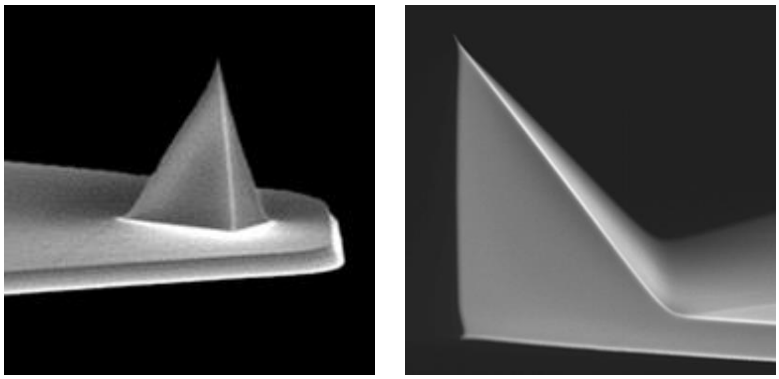

Figure 2.13 SEM image of (left) ScanAsyst tip and (right) VTESPA-70 tip.

AFM was used extensively in this work for quantifying the change in the feature profile after each processing step. Being a non-destructive technique, it is especially useful on samples that need to be processed multiple times, as destructive techniques such as SEM require cleaving the sample, thus reducing the available area for subsequent experiments and characterizations. An example of utilizing AFM to analyze feature profile evolution is given in Figure 2.14, along with the line scans. In performing the AFM measurement, due to the slanted tip used, the sidewall angle analysis focuses on the side of the feature where the tip points toward. While repeating measurement on the exact locations of the pattern was difficult, efforts were made to keep the measurement position as consistent as possible.

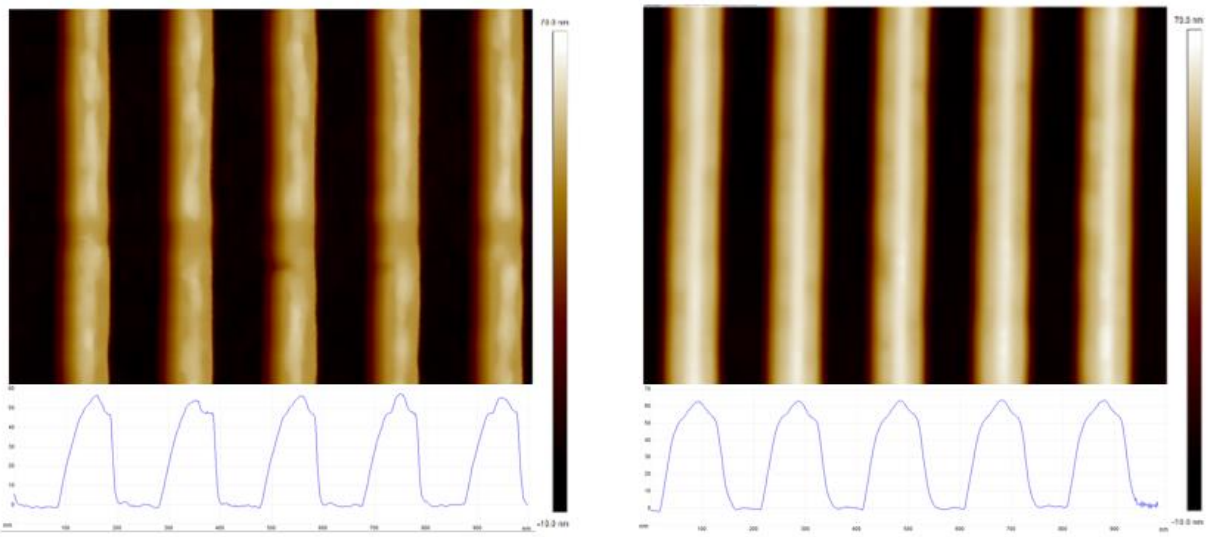

Figure 2.14 (Left) As-received SiO_2 isolated lines on Ni thin film, (Right) Patterned structure after 6 cycles of chlorine/hydrogen alternating plasma process. Each AFM scan has height line scan at the bottom.

In Figure 2.14, the left figure is a 1μm by 1μm scan of an as-received 55 nm SiO_2 deposited on Ni thin film using VTESPA-70 probe. The right figure is the same sample after 6 cycles of RIE chemistry detailed in Table 2.2. Two scans have the same height scale shown on the right. A side-by-side comparison shows that a total height gain is observed, as shown by the brighter color on the post-processed samples. Height signal confirms that the overall feature height increased from 55 nm to 62 nm. It is also noted that the feature linewidth is increased after processing, from 120 nm to 145 nm. The two observations gave intuitive indication regarding how features change after various cycles of processes. It is important to point out, however, that the height change from the AFM image should not be directly interpreted as the thickness reduction of the target materials, since processes could also affect the height of the hard masks, a distinction that AFM could not capture. Generally speaking, AFM provides an overall height difference, which is a combined

effect from multiple sources of thickness changes. Information acquired from AFM need to be analyzed in conjunction with other techniques such as XPS and SEM to give a more comprehensive understanding of the samples.

2.2.9 Nuclear Magnetic Resonance

Nuclear magnetic resonance (NMR) is a widely used technique for determining molecular structure of unknown substances. Spectral libraries are usually referred when chemical shifts of unknown species are acquired, or their basic structure could be deduced from the working principles of NMR. On top of the information about the composition of atomic groups, which could be obtained by analyzing the chemical shift, several other information could be retrieved via NMR. For instance, information about adjacent atoms could be obtained by analyzing the spin-spin coupling constant, and further information on molecular dynamics could be achieved via studying the relaxation time of the signals. Since many nuclei have spin and all nuclei are electrically non-neutral, energy transfer is enabled between different energy levels upon the introduction of external magnetic fields. Such energy transfer could be translated to a radio frequency when the spin returns to its base level. The frequency, and in turn the energy, is recorded as a fingerprint of that chemical, which is further used to analyze the chemical environment of the nucleus.

In this work, cross-referencing with the tabulated library was used as the approach to identify the composition. Heavy water is used as the standard. Related anticipated peaks are listed in Table 2.7, and the spectrum of formic acid control with D_2O is shown in Figure 2.15.

Table 2.7 ^{1}H NMR anticipated peak reference.

Chemical	Shift (ppm)
Heavy water (D_2O)	4.79
Formic acid (HCOOH)	8.22

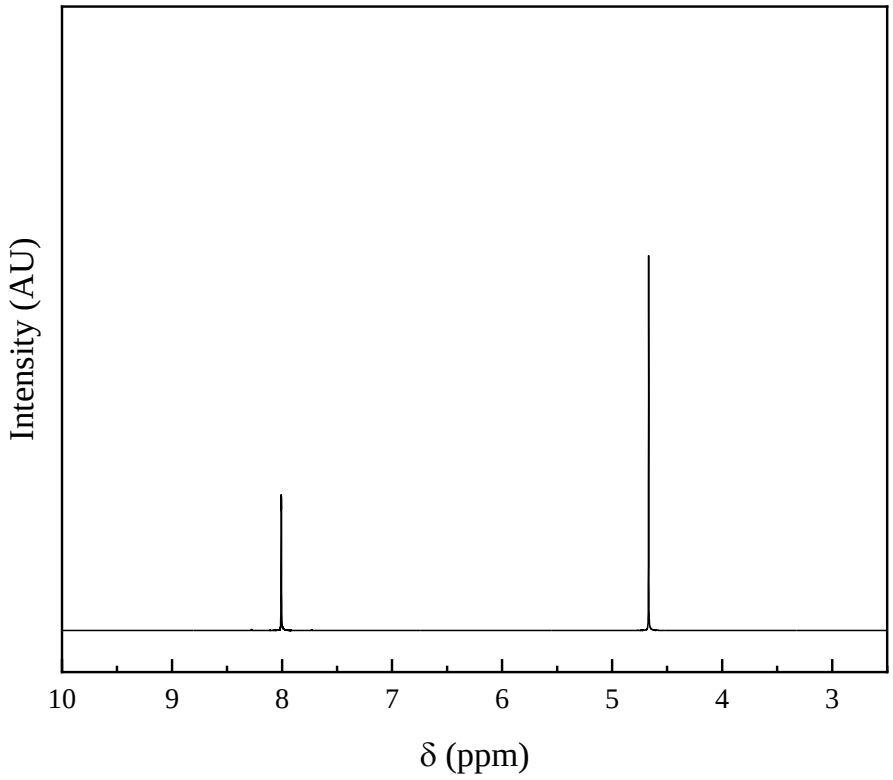

Figure 2.15 ^{1}H NMR spectrum of formic acid with D_2O.

2.2.10 Electron Paramagnetic Resonance

Transition metal ions become paramagnetic when they have unpaired electrons, given the partially filled nature of electron orbits of transition metals, paramagnetic complexes are ubiquitous. Such transitional metal ions are available to be combined with thousands of organic or inorganic ligands, resulting in a virtually infinite combination of soluble compounds. It is also possible to bind radical ligands to diamagnetic metal ions (Köhler 2007). Electron paramagnetic

resonance (EPR) spectroscopy is a powerful tool specially designed for the study of the environments and structures of species that contain paramagnetic transitional metal ions. It is the electronic analog of NMR spectroscopy that probes the nuclear spin of molecules. Details about the surrounding, as well as the structural information of the metal-organic complexes could be deduced from analyzing the EPR spectra (Garribba 2006). Electron density distribution could be inferred from electron delocalization, which in turns provides information regarding the reactivity of these compounds, the character of metal-ligand bonds in d-metal coordination compounds with chelate ligands, the magnetic properties in the presence of unpaired electrons, etc. (Larin 2007).

In this work, a Bruker EMXplus EPR Spectrometer is used, which has a microwave frequency range from 9 to 9.8 GHz (CW X-Band). Similar to the characterization using NMR, cross-referencing with the reference spectrum was used as the approach to identify the composition. A reference Cu-containing sample spectrum is shown in Figure 2.16, where $g_{\perp}$ and $g_{//}$ are factors accounting for electrons' spin and orbital angular momenta perpendicular and vertical to the magnetic field orientation, respectively. For samples with low concentration, such feature would not be observable.

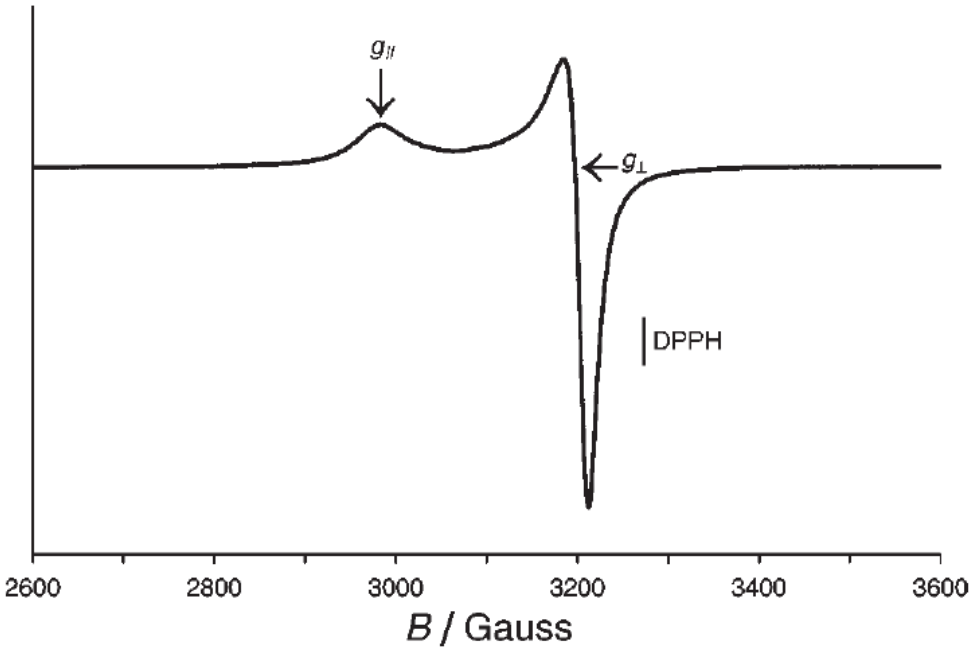

Figure 2.16 EPR spectrum of $[Cu(en)_2(ClO_4)_2]$. (Garribba 2006)

2.3 Density Functional Theory Simulation Setup

2.3.1 Simulation Setup for Ni Etch Reactions

To provide molecular scale understanding and assess the reaction products during formic acid etching of oxidized nickel, density functional theory (DFT) calculations were performed. The Perdew-Burke-Ernzerhof (PBE) exchange correlation functional was used using the VASP code (Blöchl 1994, Kresse 1996, Kresse 1996, Perdew 1996, Kresse 1999). One-electron functions are developed on a basis set of plane-waves, with an energy cutoff at 400 eV. The energies and forces are converged to 1×10^{-6} eV and 2×10^{-2} eV/Å, respectively. The Gibbs free energies of the reaction are evaluated at conditions specified in etching experiments: 80 °C, 350 Torr (Larsen 2017). Three nickel surfaces, (100), (111), and (211), were selected since they are representative of facet and edge sites present on polycrystalline surfaces. To create an oxidized nickel surface,

atomic oxygen was chemisorbed on nickel. At the coverages of interests, the most stable phase is surface adsorption (overlayer). The metastable structures likely to be present after oxygen adsorption are probed by placing oxygen in the sublayer interstitial sites (sublayer structures). The adsorption sites are compared on each surface and the most stable one, respectively on-surface and subsurface, are selected. In a real oxidation process, some overlayer sites are likely to be populated first due to the kinetic barriers of accessing the sublayer sites; therefore, a mixed structure presenting overlayer and sublayer sites is also included.

2.3.2 Simulation Setup for Cu Etch Reactions

All of the simulations were performed within the projector augmented-wave (PAW) (Blöchl 1994) periodic-planewave DFT formalism as implemented in the Vienna Ab-initio Simulation Package (VASP) version 5.4.4 (Kresse 1996). The Perdew−Burke−Ernzerhof (PBE) exchange-correlation functional was used in the evaluation of the Kohn−Sham electronic energies (Perdew 1996). PAW potentials were used for all elements, with frozen core orbitals of 1s for C and O, and (1s2s2p3s3p) for Cu. The simplified rotationally invariant effective Hubbard U correction (Dudarev 1998) (+U) was included for Cu 3d orbitals (U = 3.6 eV, derived from unrestricted Hartree−Fock theory on electrostatically embedded Cu_2O clusters (Yu 2014)). van der Waals interactions were simulated via the D3 method with Becke−Johnson damping (D3BJ) (Grimme 2010, Grimme 2011). A 660 eV planewave basis kinetic-energy cutoff was imposed. A Gaussian electronic smearing (0.01 eV) was applied. The electron spin of Cu^{2+} was initialized with one unpaired electron, as expected for a valence d^9 transition metal. The Cu^{2+} ion(s) in all species, bulk and molecular complexes, converged to an absolute projected net electronic spin of

approximately 0.6−0.7 e, thus confirming the existence of Cu^{2+}. Cu^{1+}-containing species were simulated spin-unpolarized, since Cu^{1+}has a closed-shell d^{10} electronic valence.

An absolute atomic force threshold of 0.002 eV/Å was imposed during lattice vector and atomic-position optimizations. To reduce numerical noise in forces and stresses, the fine-grid fast Fourier transform (FFT) was set to 4 times the coarse FFT, and the PAW core compensation charge was evaluated at 8 times the default grid. The converged lattice vectors of the various antiferromagnetic (AFM) and ferromagnetic (FM) monoclinic CuO (Figure B.1), orthorhombic $Cu(OH)_2$ (Figure B.2), and their respective Brillouin zone (k-point) sampling, are summarized in Tables B.1 and B.2. The pristine cubic Cu_2O has no unpaired electrons; therefore, no optimization of the magnetic structure was performed. The Cu^{1+} oxide's optimized lattice parameters and accompanying k-point sampling are in Table B.3. The phonon frequencies of the three solids were calculated by generating multiple finite atomic displacements (±0.01 Å from equilibrium) using phonopy (version 2.4.1) (Togo 2015) and calculating atomic forces using VASP. The subsequent postprocessing to obtain the phonon densities of states (phDOS) and vibrational free energy contributions (Table B.4) were performed also using phonopy. The solids' phDOS (Figure B.3) confirm the stability of the optimized crystal structures found.

A periodic box size of 22 × 22 × 18 $Å^3$ was used to isolate the gas-phase HCOOH, $(HCOOH)_2$, H_2O, CO_2 molecules and Cu^{2+} and Cu^{1+} complexes (vide infra), with a dipole correction applied in all directions, which include corrections for both the energy and potential (Neugebauer 1992, Makov 1995). A Γ-point-only k-point sampling was employed. An absolute atomic force threshold of 0.01 eV/Å was imposed for atomic structure optimization. The vibrational frequencies were evaluated within the harmonic approximation, with the Hessians

constructed via the finite atomic displacement method (±0.02 Å from equilibrium). The calculation of the free energy contributions from the translational, rotational, and vibrational degrees of freedom are described in the Tables B.4 and B.5. Benchmarking of the same DFT parameters used here for both gaseous HCOOH and $(HCOOH)_2$ are available in ref (Chen 2019).

The free energy of the gaseous O_2 molecule at temperature T($G(O_2(g), T)$) was calculated from the DFT energy of an O atom (Malcolm 1998):

$$G(O_2(g), T) = 2\left(E_O^{DFT} + G_{trans}(O(g), T) - \Delta G_f^{exp}(O(g), T)\right) \quad (2.2)$$

The O_2 molecule weas not explicitly modeled in DFT because PBE is known to over-stabilize the molecule; it overestimates the molecule's atomization energy by as much as 1 eV/O_2 (Perdew 1996).

Chapter 3 Nanometer Scale Patterning of Ni

In this chapter, a chlorine-hydrogen-based plasma RIE process is investigated to effectively remove Ni, utilizing the high volatility of $NiCl_2$ with the presence of hydrogen radicals. A linear etch rate of 3.8 ± 0.5 nm/cycle is observed, a selectivity of 1.4 is measured with respect to SiO_2 hard mask, and a 70° sidewall angle is recorded. Additionally, a plasma-thermal ALE process is developed where an oxygen plasma is used to convert the metallic Ni layer into NiO, followed by formic acid vapor reacting with NiO to form nickel formate [$Ni(COOH)_2$], thereby removing nickel. With the processing conditions used, an etch rate of ~2 nm/cycle is recorded. The directionality of the oxygen ions is used to create a directional chemical conversion of Ni into NiO, resulting in an anisotropic etch profile. Using the SiO_2 patterned Ni thin film, a high etching selectivity to the mask (virtually no etching of SiO_2) and a high etching anisotropy (a sidewall angle up to 87°) are achieved. To improve the overall throughput of the patterning process, RIE and ALE are combined in a hybrid process. The hybrid RIE-ALE approach achieved the same level of anisotropy with ~75% reduction of processing time. Density functional theory-based reaction simulation is incorporated to understand the reaction mechanism at an atomic scale. It is revealed that Ni thin film with oxygen sublayer is energetically favorable to react with formic acid molecules, while the same reaction is unfavorable on Ni bulk, Ni thin film, or Ni thin film with oxygen overlayer.

3.1 Thermodynamic Assessment of Nickel Compounds

Thermodynamics serves as a powerful tool for analyzing chemical reactions within a system. By mathematically minimizing total Gibbs free energy of materials and potential etchants from the standpoint of equilibrium, patterning chemistries can be identified without physically implementing a process for trial-and-error studies, saving a substantial amount of time and cost. Through the process of Gibbs minimization, a composition of constituent molecules present within the system can be calculated at fixed pressure and temperature. These absolute amounts are then plotted as functions of temperature. Such calculations rely heavily on thermochemical information like standard enthalpies, entropies and Gibbs free energies of formation. A commercially available software - HSC Chemistry - is used for calculation of the equilibrium composition of a specified system. Figure 3.1 shows the equilibrium composition of Ni-Cl system wherein 1 kmol of Ni is modeled to equilibrate in an atmosphere of 20 kmol Cl_2 at atmospheric pressure. It is noted that atmospheric pressure is used due to limitations of thermodynamic data in other pressure ranges. Also, result from Gibbs free energy minimization represents the final outcome of the prescribed system in equilibrium, which is not necessarily satisfied with the presence of plasma.

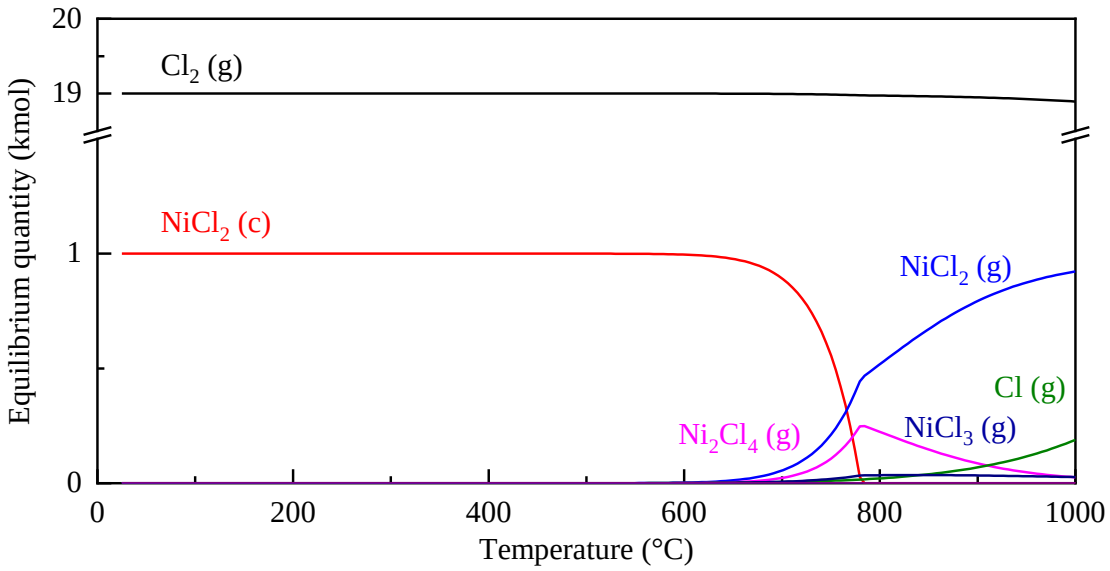

Figure 3.1 Product distribution of Ni-Cl system at equilibrium at atmospheric pressure at temperature from 50 to 1000 ℃.

From the results of Gibbs energy minimization, it can be observed that the production of condensed phase $NiCl_2$ is formed at around room temperature up to about 800℃, and gas phase $NiCl_2$ requires relatively high ambient temperature. The Gibbs energy minimization implies that while gas phase $NiCl_2$ is achievable, the operating condition might be at too high of a temperature for semiconductor processing purposes. As mentioned previously, thermodynamic data usually only exists in a narrow pressure range near that of atmospheric, which is insightful but not very practical for low-pressure processing. One approach that takes account of partial pressures of different reaction species is the construction of volatility diagram. The feasibility of achieving any noticeable amount of etching can be determined by investigating the position of equilibrium lines for the condensed-vapor phase that specific product. For the system of interest, Ni-Cl_2 system, reactions considered are listed in Table 3.1. The final volatility diagram is shown in Figure 3.2.

Table 3.1 Reactions in for Ni-Cl_2 system (calculations done for 50℃, data from HSC)

Number	Reaction	$\Delta G_{rxn}\ (kJ/mol)$
1	$Ni(s)+Cl_2(g) \rightarrow NiCl_2(s)$	-255.2
2	$Ni(s) \rightarrow Ni(g)$	380.8
3	$NiCl_2(s) \rightarrow Ni(g)+Cl_2(g)$	635.9
4	$Ni(s)+Cl_2(g) \rightarrow NiCl_2(g)$	-87.4
5	$NiCl_2(s) \rightarrow NiCl_2(g)$	167.8
6	$Ni(s)+1.5Cl_2(g) \rightarrow NiCl_3(g)$	-112.5
7	$2NiCl_2(s)+Cl_2(g) \rightarrow 2NiCl_3(g)$	285.4
8	$2Ni(s)+2Cl_2(g) \rightarrow Ni_2Cl_4(g)$	-314.5
9	$2NiCl_2(s) \rightarrow Ni_2Cl_4(g)$	195.9

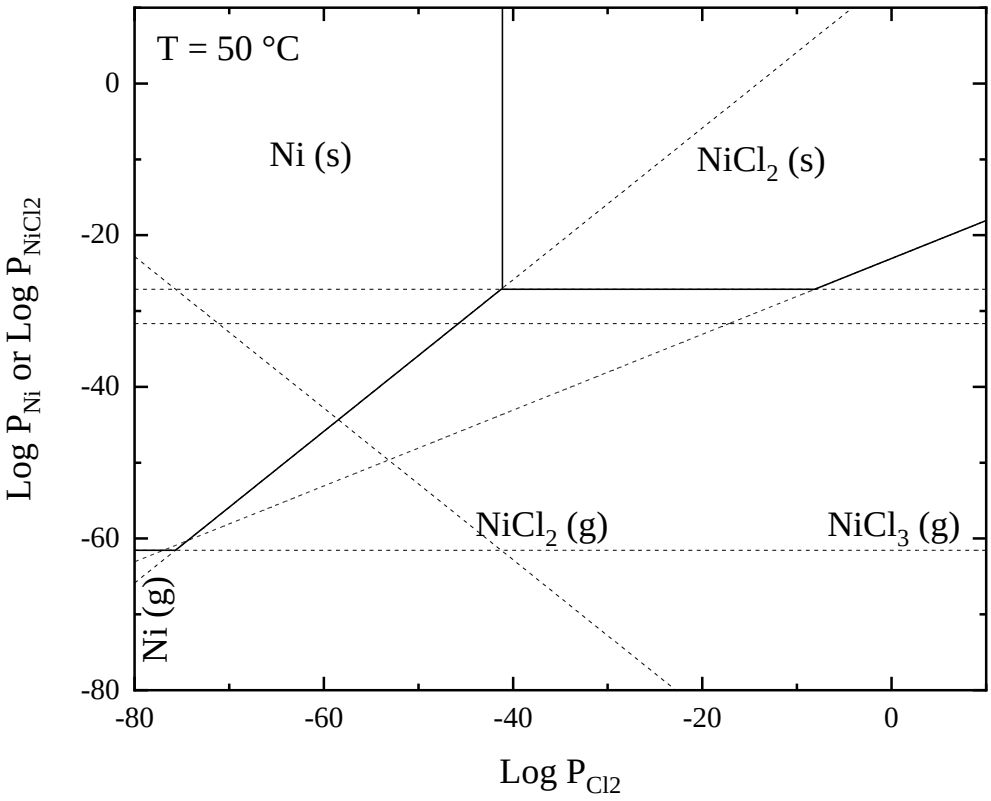

Figure 3.2 Volatility diagram for Ni-Cl_2 system.

It can be seen that the partial pressure of gas phase $NiCl_x$ never exceeds 10^{-8} atm, which is the required pressure to be considered etchable (Kim 2014). Hydrogen is then introduced into the system to assist the removal of the non-volatile $NiCl_x$. By exposing the condensed phase species to plasma at a fixed partial pressure of hydrogen, there is an indication that the metal can be volatilized and removed. Analysis of the inclusion of auxiliary hydrogen in this process is characterized by fixing the partial pressure of hydrogen introduced into the system and subsequently analyzing reactions for the formation of volatile NiH(g). From a graphical standpoint used in the volatility diagrams, this hydrogen isobar is characterized by negatively sloped colored dotted lines present in the analysis of Ni-Cl_2 system. The reaction between $NiCl_2$(s) and atomic H(g) generated in the inductively coupled hydrogen plasma results in formation of NiH(g) and

HCl(g), which has a Gibbs free energy of reaction of -193.9 kJ/mol at 50℃, indicating that the reaction is spontaneous and implies a reaction pathway suitable for the removal of nonvolatile $NiCl_2$(s) under H_2 discharge. The volatility diagram with the addition of hydrogen plasma is shown in Figure 3.3.

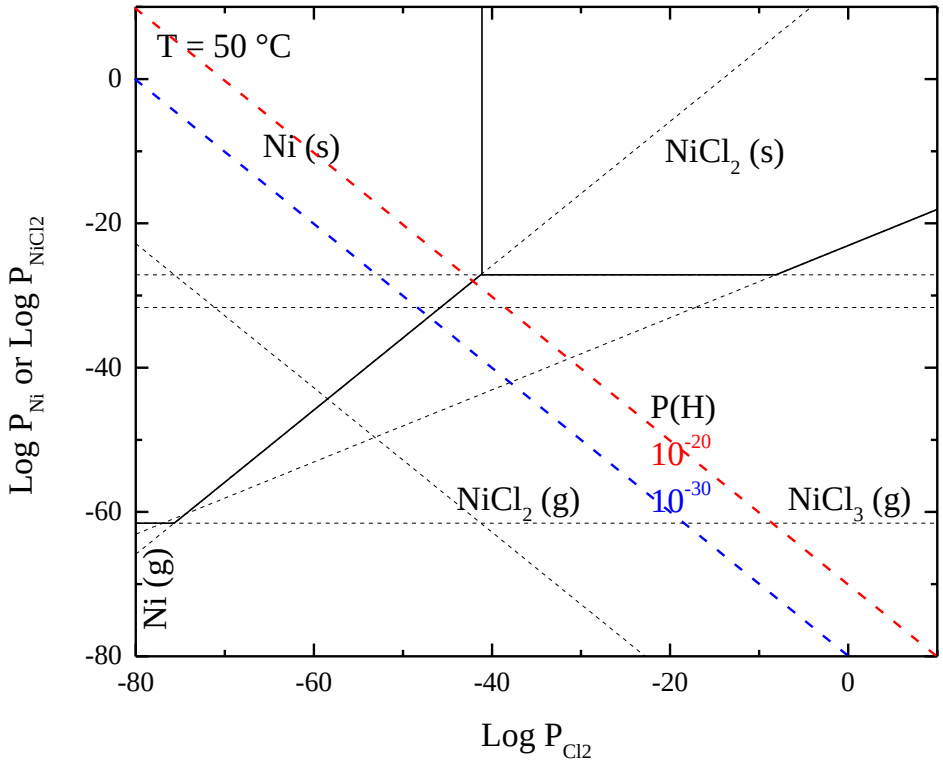

Figure 3.3 Volatility diagram for Ni-Cl_2 system with addition of hydrogen atoms.

It is worth comparing this reaction, which indicates the thermodynamically favorable formation of volatile nickel hydrides, to the direct reaction of nickel with atomic hydrogen (i.e. Ni(s) + H(g) → NiH(g)), which has Gibbs free energy of reaction of 147.3 kJ/mol, indicating that such direct transition is not spontaneous.

Reaction thermodynamics between Ni/NiO and acetic acid/formic acid in both liquid and gas phase are considered and listed in Table 3.2. It is noted that while acetic acid and formic acid, with the available value, are capable of etching Ni and NiO in both liquid and gas phase, the removal of NiO has a much lower reaction energy and thus would be more spontaneous. With proper tuning of formic acid pressure and exposure temperature, the difference in reaction energy between Ni and NiO could be leveraged, so that reaction is only spontaneous on the oxide, but not on the metal. The difference in reaction favorability is the key to enable selective removal, a prerequisite for ALE.

Table 3.2 Gibbs free energy of reaction between metallic nickel and nickel oxide and different organic etchants. Data obtained from HSC, calculation done in 25 °C, 1 atm.

	Ni Reactions	ΔG (kJ/mol)	NiO Reactions	ΔG (kJ/mol)
Acetic acid	$Ni(s)+2CH_3COOH(l)\rightarrow Ni(CH_3COO)_2(aq)+H_2(g)$	-4.3	$NiO(s)+2CH_3COOH(l)\rightarrow Ni(CH_3COO)_2(aq)+H_2O(g)$	-29.8
	$Ni(s)+2CH_3COOH(g)\rightarrow Ni(CH_3COO)_2(g)+H_2(g)$	NA	$NiO(s)+2CH_3COOH(g)\rightarrow Ni(CH_3COO)_2(g)+H_2O(g)$	NA
Formic acid	$Ni(s)+2HCOOH(l)\rightarrow Ni(HCOO)_2(aq)+H_2(g)$	-41.4	$NiO(s)+2HCOOH(l)\rightarrow Ni(HCOO)_2(aq)+H_2O(g)$	-66.9
	$Ni(s)+2HCOOH(g)\rightarrow Ni(HCOO)_2(g)+H_2(g)$	-62.7	$NiO(s)+2HCOOH(g)\rightarrow Ni(HCOO)_2(g)+H_2O(g)$	-79.7

3.2 Cyclic Chlorine-Hydrogen Reactive Ion Etching of Nickel

The first step of examining the previously proposed chlorination-removal reaction scheme is to study the surface composition after different treatments. As shown in Figure 3.4, XPS measurement were taken on Ni sample surface before any plasma exposure, after 30 seconds of chlorine plasma (400 W RF power, sample bias was 100 W, 10 mTorr pressure) exposure and 30

seconds of chlorine plasma exposure followed by 30 seconds of hydrogen plasma exposure (800 W RF power, sample bias was 100 W, 30 mTorr pressure) (Kim 2014).

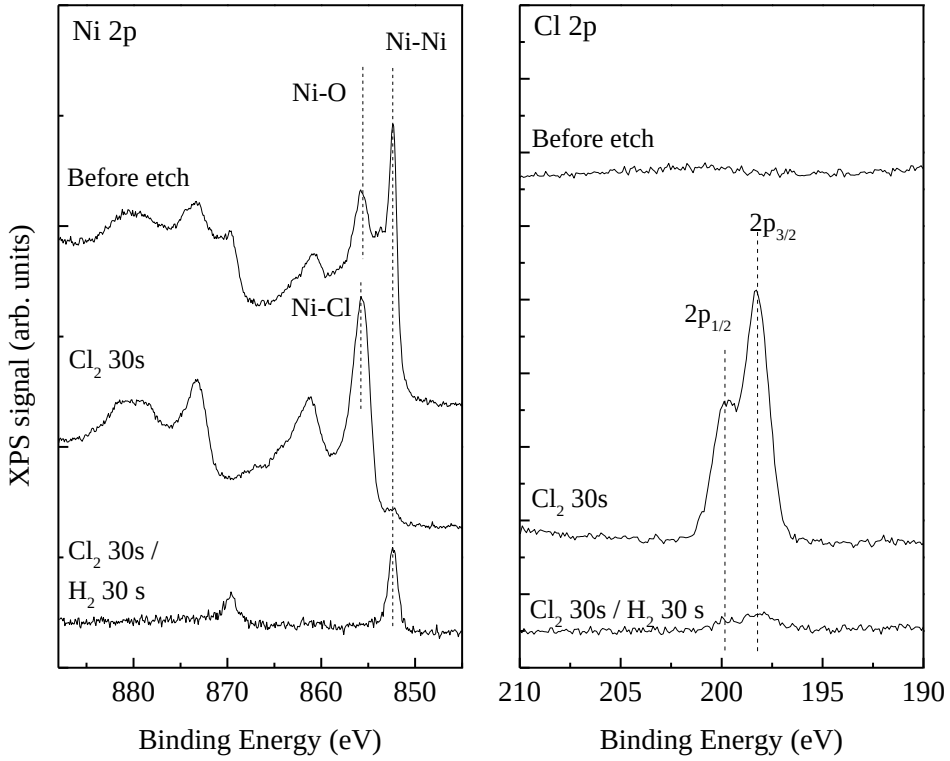

Figure 3.4 XPS spectra for Ni sample before etch, after 30 seconds of chlorine plasma exposure and 30 seconds of chlorine plasma exposure followed by 30 seconds of hydrogen plasma exposure. (Kim 2014)

To further verify the outcome of thermodynamic equilibrium calculation for Ni in process chemistries such as Cl_2 and H_2 in the previous section, experiments were conducted utilizing the inductively coupled plasma chamber. Using the proposed cyclic process with chlorine and hydrogen plasmas, an etch rate of 3.8 ± 0.5 nm/cycle is extrapolated from Figure 3.5, where the etched Ni thickness is shown as a function of the cycle number. Comparing with the etch rate of sub-nanometer per cycle of typical ALE chemistries, this reported RIE chemistry is considerably

higher. Additionally, the notion of thickness per cycle does not factor in the time used in one cycle, rendering the ALE chemistries usually even less efficient than what could be achieved by RIE chemistries.

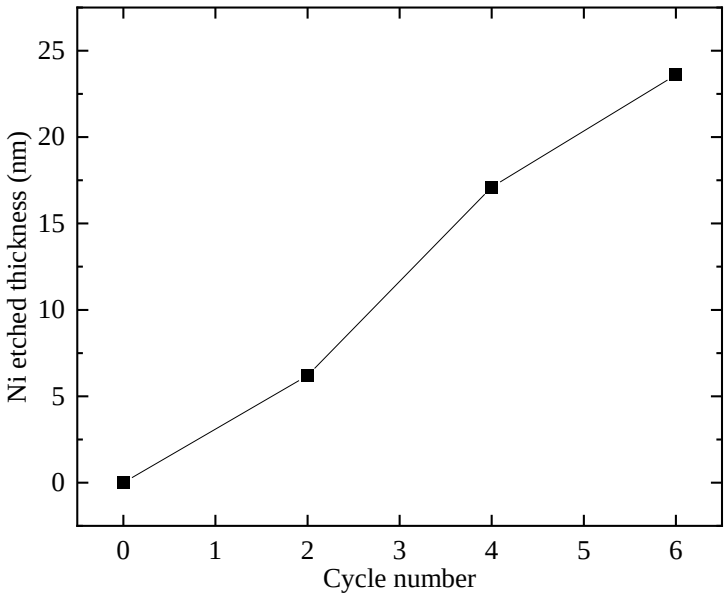

Figure 3.5 Ni etched thickness as a function of RIE cycle number. Conditions detailed in Table 2.2.

OES was performed to quantify the reactants (ionic and atomic chlorine and hydrogen) as well as to detect the reaction products. The data shown in Figure 3.6 included the OES scan during the hydrogen plasma, immediately following a chlorine plasma step. A baseline for comparison is an identical process where there was no preceding chlorine plasma. A major difference between these two spectra was at around 340 and 415 nm. NIST database of atomic spectra listed peaks at 341.57 nm and 413.39 nm are characteristics of singly charged Ni and Cl atoms, respectively. Though OES was not able to directly detect the presence of $NiCl_x$, the data nonetheless confirmed the removal of nickel and chlorine from the surface. These results are consistent with previous

work done on other transition metals (Kim 2014), where an enhanced removal of metal-chloride from the surface was observed with the addition of hydrogen atoms.

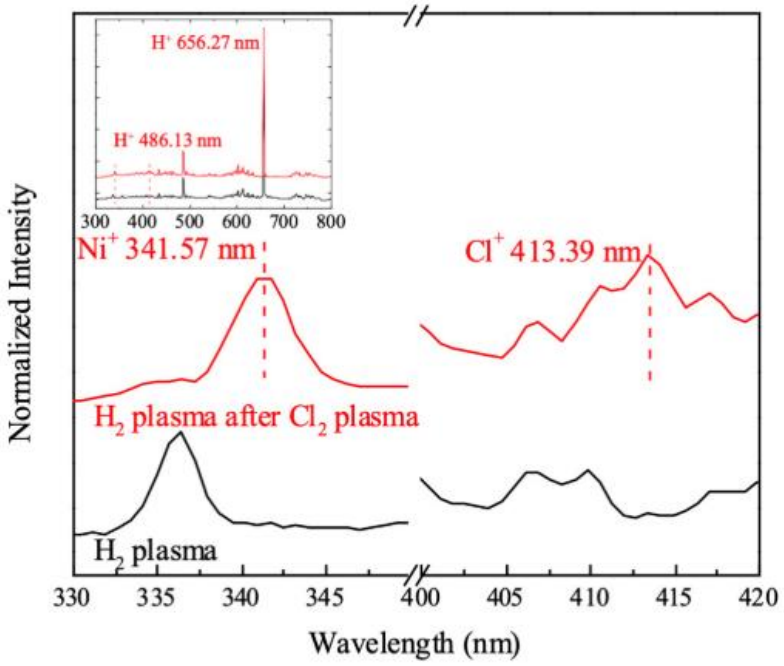

Figure 3.6 Normalized OES spectrum during hydrogen plasma exposure half cycles for hydrogen-only and hydrogen following chlorine plasma, zoom-in spectra for 320–360 nm and 400–440 nm. The full-spectrum scans are shown in the inset.

Surface composition analysis by XPS also confirmed the formation and removal $NiCl_x$, as shown in Figure 3.7, where patterned Ni samples [SiO_2 hard mask (thickness = 50 nm, line width = 65 nm, line pitch = 200 nm) on Ni thin film (thickness = 30 nm) on Ta adhesion layer (thickness = 3 nm) on SiO_2 substrate] were etched by (a) only a chlorine plasma, (b) one cycle of chlorine followed by hydrogen plasma, and (c) six cycles of chlorine followed by hydrogen plasma. The Ni 2p, Cl 2p, and Ta 4f spectra are deconvoluted to show the chemical bonding configurations on the etched surface. After the hydrogen half-cycle, signal intensity of the metallic Ni peak at 852.7 eV increased from 3% to 15% and signal intensity of the Ni-Cl peak at 854.4 eV decreased from

5% to 0%, again confirming the etching effectiveness of hydrogen chemistry. Repeating the treatment for six cycles resulted in a decrease in signal intensity of both Ni and Cl peaks. A maximum remaining Ni layer thickness of 7 nm could be deduced from the final spectrum as previously undetectable Ta signal is measured.

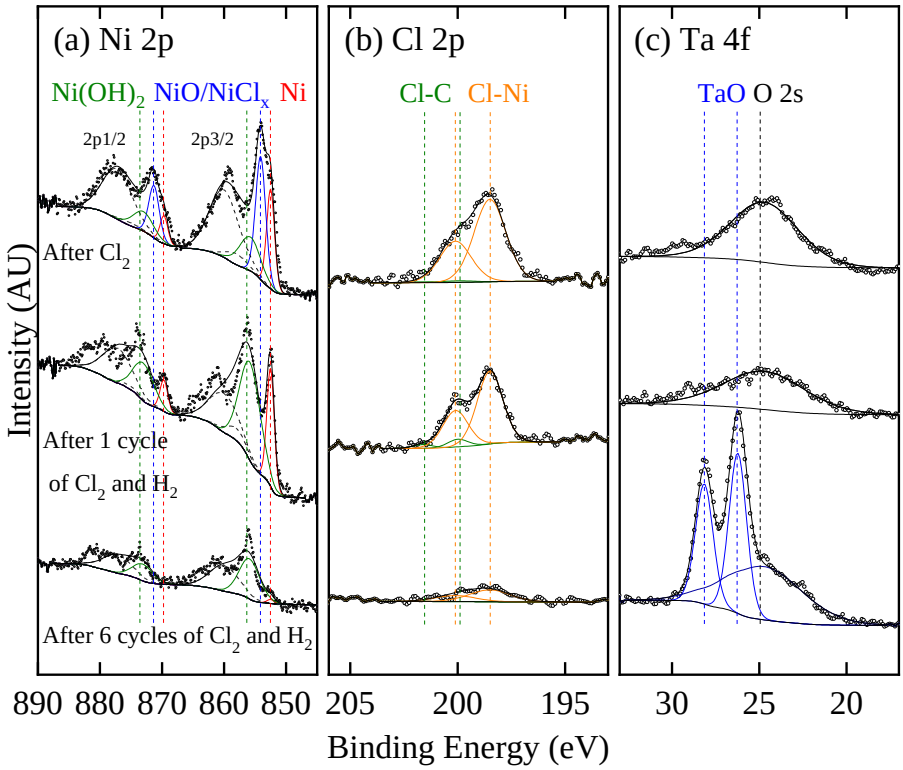

Figure 3.7 XPS analysis of surface composition of Ni patterned samples, showing (a) Ni 2p, (b) Cl 2p, and (c) Ta 4f spectra. Within each panel, the spectra corresponded to the surface states after different plasma treatment: (top) Cl_2 plasma, 400 W RF power, 20 W substrate bias, and 30 s; (middle) one cycle of Cl_2 plasma (400 W RF power, 20 W substrate bias, and 30 s) followed by an H_2 plasma (400 W RF power, 60 W substrate bias, 90 s); and (bottom) six cycles of alternating Cl_2 and H_2 plasma treatment.

Figure 3.8 (s) shows the schematic diagram of the patterned Ni sample. The TEM image for a feature from a sample after six cycles of the aforementioned RIE treatment is shown in Figure 3.8 (b), while Figure 3.8 (c)–(g) showed the corresponding EDS elemental maps of Ni, Si, O, Cl,

and Ta to allow for the inspection of the spatial distribution of each element. 30 nm of exposing Ni is completely removed in the vertical direction in the exposed regions; at the same time, 20 nm of the SiO_2 hard mask is etched by the chlorine and hydrogen plasmas. An etch selectivity of 1.5 is thus calculated for Ni over SiO_2. Sidewall angles of 45° and 70° are measured at the top and bottom of the feature, respectively. The RIE step resulted in a trapezoid-like feature. The convex curvature near the top of the feature indicates redeposition of the reaction products during the cyclic etching by chlorine and hydrogen plasmas. The EDS scan of Ni confirmed this and also showed Ni deposition on the sidewall of the SiO_2 hard mask. The angle discontinuity at the SiO_2-Ni interface implies that $SiCl_x$ is more volatile compared to $NiCl_x$, which is consistent with the measured vapor pressure of 167.2 kPa for $SiCl_2$ at 25 °C (Cheng 1984). This RIE-etched profile, though not perfectly directional, serves as an ideal starting profile to assess the effect of the plasma-thermal ALE process. It is worth mentioning that six cycles of the aforementioned treatment took about 30 min, with about half of the time used for residual gas pumping and nitrogen purging, leaving considerable room for throughput improvements.

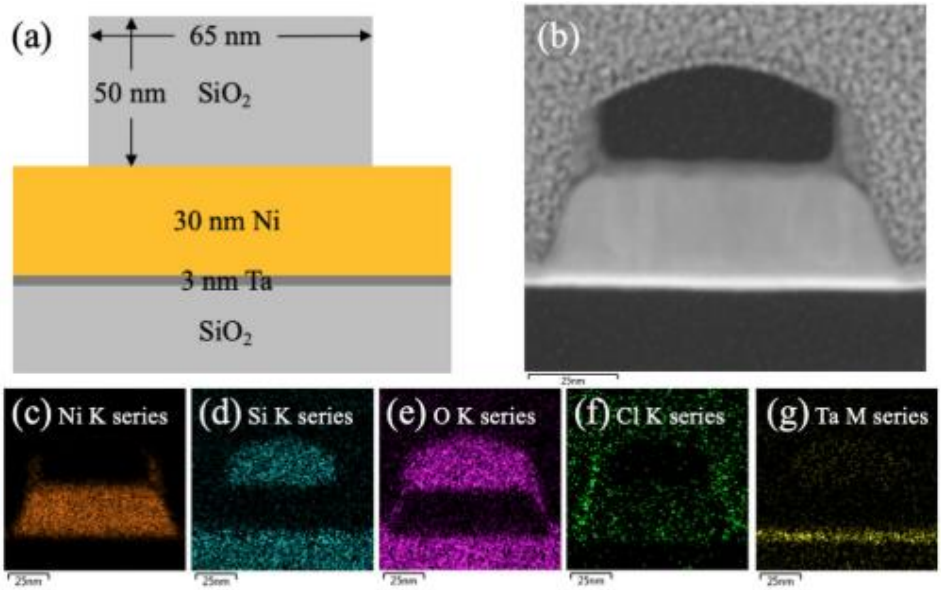

Figure 3.8 (a) Schematic of as-patterned Ni thin film structure; (b) TEM image of an etched Ni structure after six cycles of RIE processing; (c)–(g) EDS elemental mapping of Ni, Si, O, Cl, and Ta.

3.3 Organic Solution Phase Etching of Nickel

Etching of Ni was investigated using solution phase processing at elevated temperatures with stock solutions of acetylacetone (99%, Sigma-Aldrich), hexafluoroacetylacetone (97%, Sigma-Aldrich), acetic acid (97%, Sigma-Aldrich) and formic acid (95%, Sigma-Aldrich). For acetylacetone, acetic acid and formic acid, ten milliliters of each solution were pipetted into 10 dram glass vials and heated to 80°C in a water bath using a temperature-controlled hotplate to ensure uniform heating of the etch solution. For hexafluoroacetylacetone, a similar setup is used except that experiment is conducted in a water bath temperature of 60°C to prevent boiling. Square (1 cm x 1 cm) coupons of 46 nm Ni deposited on Si were each immersed in 10 ml of aforementioned solutions for etch times up to 30 minutes. After etching, samples were cleaved, and their cross-sections were measured to determine the change in thickness using SEM. This

etched thickness was then plotted as a function of etch time, as shown in Figure 3.9. The resulting etch rates of Ni in acetic acid (~3.5 nm/min) and formic acid (~1.5 nm/min) was significantly higher than those in acetylacetone and hexafluoroacetylacetone, in which negligible thickness removal was measured.

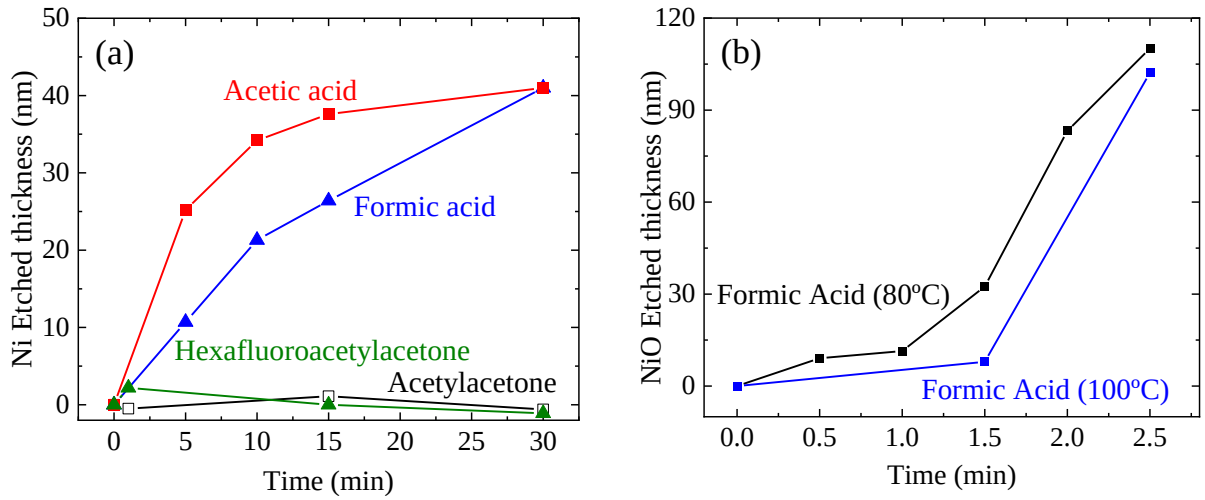

Figure 3.9 (a) Measured etched thickness for nickel as functions of solution etch time in different organic etchants and (b) Measured etched thickness for nickel oxide as functions of solution etch time in 80 °C and 100 °C formic acid.

To chemically verify the etched products from different organic acids, post-etch solutions of Ni in acetic acid and formic acid were examined using electro-spray ionization mass spectrometry (ESI-MS). Results indicate that Ni form different etch products with formic acid and acetic acid as predicted. For formic acid etch solution, it is calculated that m/z ratio is expected to have the distribution of 146.92 (relative intensity 69%), 148.92 (relative intensity 27%) and 150.92 (relative intensity 4%). For acetic acid etch solution, it is calculated that m/z ratio is expected to have the distribution of 174.95 (relative intensity 69%), 176.95 (relative intensity 27%) and 178.95 (relative intensity 4%). Comparing to the calculated pattern, experimental data showed similar distribution, with relative intensity ratios of different peaks close to calculated value. Deviations from theoretical value and additional peaks could be due to loss of single or multiple hydrogen

atom in the dissolution and ionization process. The proposed composition of experimental data is color-coded and shown above the experimental data.

ESI-MS spectra of the etch solutions with m/z value range of 10 around the peak of interest are shown in Figure 3.10. For each measured spectrum, calculated m/z values for proposed etch products: nickel acetate and nickel formate, were shown in light grey above the data. It is assumed that m/z values of interest correspond to singly ionized species, further fragmentation of etch products and doubly ionized species are not considered in the present study.

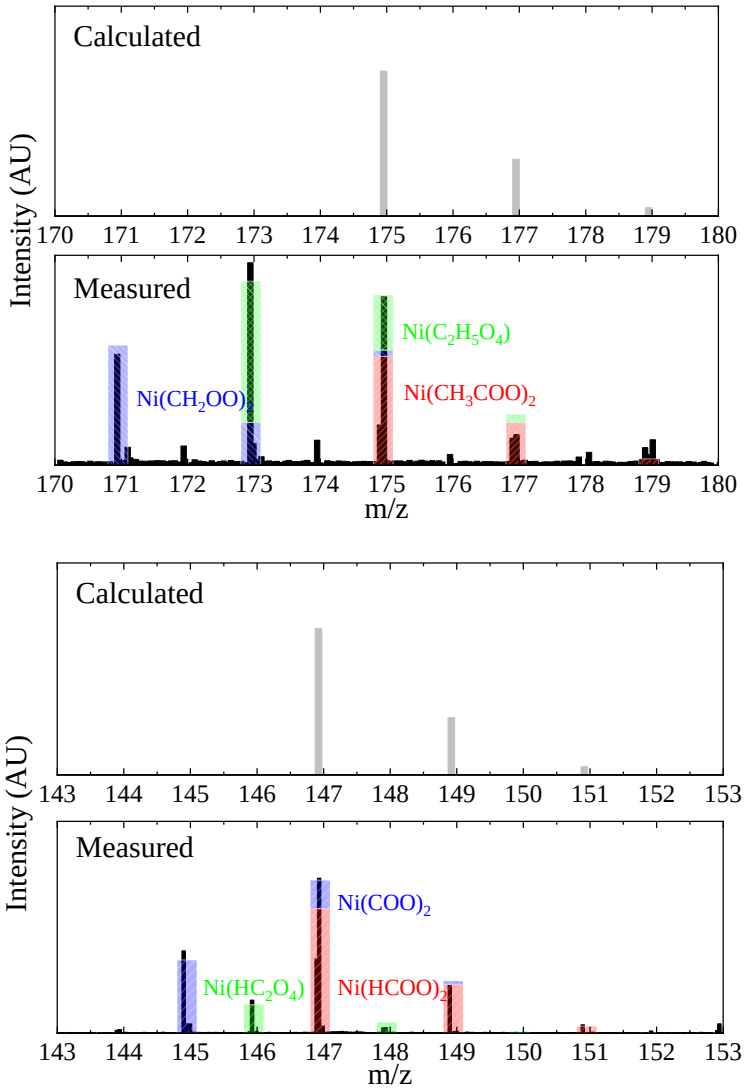

Figure 3.10 ESI-MS result for (top) etch solution of Ni in acetic acid for 1 hour at 80℃ and (bottom) etch solution of Ni in formic acid for 1 hour at 80℃.

Based on experimental data from both thickness reduction measurement and etched product analysis, the efficacy of acetic acid and formic acid in etching Ni has been proved. It is expected, however, that the translation of these chemistries into the gas phase results in a substantial decrease in etch rate, due to reductions in the concentration of the organic molecules, hindering the chemical etch process. Such reduction in the overall etch rate, on both metallic Ni and oxidized NiO, is nevertheless ideal for ALE that requires extreme selectivity. Once the overall pressure is below a certain threshold, the gas-phase removal would only be feasible on NiO, while Ni would not be affected by the acid exposure. Coupling this selectivity with proper control of the surface oxidation mechanism, a self-limiting, layer-by-layer removal scheme could be achieved.

3.4 Plasma-Thermal Atomic Layer Etching of Ni

3.4.1 Controlled Surface Oxidation

To assess controlled surface oxidation, a low energy plasma oxidation process (30 mTorr, 500W source power, no applied substrate bias or heating, 2 min) was used to convert the surface of 30–40 nm Ni thin films into oxides. As shown in Figure 3.11, the Ni sample was first sputter-cleaned by 4 keV Ar ions to remove the native oxide layer and establish a baseline for compositional analysis. It was then exposed to oxygen plasma ex-situ for 2 min. Due to ambient exposure, some adventitious carbon was observed, which caused signal attenuation of other elements. Without the applied substrate bias, the ion energy was about the plasma self-bias potential, ~10 eV, which was lower than the sputtering threshold of Ni which was reported to be ~16 eV (Matsunami 1984). It is thus expected that the main effect of these low energy ions was oxidation and no significant sputtering due to small populations of ions at the high energy tail of

the ion energy distribution function. The formation of NiO is confirmed from the ex-situ XPS analysis where the signal intensity of metallic Ni (852.6 eV) is considerably reduced and that of NiO (854.1 eV) is greatly increased. Increase in signal intensity is also noticed for $Ni(OH)_2$ (855.8 eV) and satellite features (858.1 and 859.9 eV). With the known photoelectron mean-free paths of Ni and NiO and the atomic sensitivity factors for Ni and O, the oxide layer thickness can be calculated using the following equation:

$$\frac{I_{ox}^{t}}{I_{Ni}^{t}} = \frac{I_{ox}^{\infty}}{I_{Ni}^{\infty}} \frac{1 - \exp\left(-\frac{t_{ox}}{\lambda_{ox}^{o} \sin\theta}\right)}{\exp\left(-\frac{t_{ox}}{\lambda_{ox}^{Nt} \sin\theta}\right)} \tag{3.1}$$

where I_{ox}^{t} and I_{Nt}^{t} are the integrated intensities of O 1s and Ni $2p_{3/2}$ peaks, t_{ox} is the oxide thickness, λ_{ox}^{o} and λ_{ox}^{Ni} are the photoelectron mean-free paths for O 1s and Ni 2p, and θ is the angle between the sample surface and the electron analyzer, 90° in this work. The ratio $I_{ox}^{\infty}/I_{Ni}^{\infty}$ has been experimentally measured to be 0.17 and confirmed with theoretical calculation. (Lambers 1996) The mean-free path of O1s and Ni2p photoelectrons in the oxide was determined to be 2.1 and 1.7 nm, respectively, using the relation of

$$\lambda = \frac{2170}{E^2} + 0.72(aE)^{0.66} \tag{3.2}$$

where E is the electron kinetic energy in eV and a is the molecule size in nanometer as derived from the relation $\rho N n a^3 = 10^{24} A_0$,where ρ is the material density, N is the Avogadro's number, n is the number of atoms per molecule, and A_0 is the molar mass. Therefore, the oxide thickness was determined to be ~6 nm.

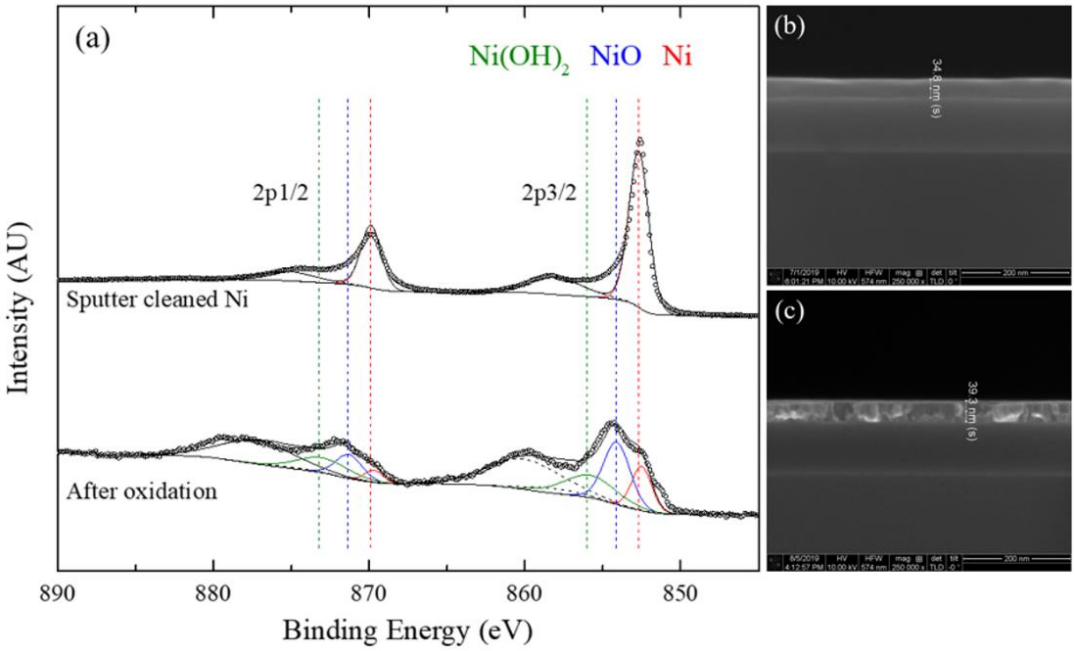

Figure 3.11 (a) Ex situ XPS detail scan of Ni 2p and SEM cross-sectional image for Ni blanket sample (b) before and (c) after 2 min of oxygen plasma exposure, 500 W power, and 0 W applied bias.

The calculated NiO thickness is corroborated by the SEM analysis, where a thickness increase of ~5 nm is measured on the oxidized Ni thin film comparing to the non-oxidized surface. It is noted that the formation of a native oxide layer of ~2 nm takes ~24 h in the ambient condition, which is considerably longer than the time required to transfer the post-oxidation samples for ex situ XPS measurements. Figure 3.12 (a) shows Ni 2p, C 1s, and O 1s spectra with various oxidation times under the same plasma conditions. The amount of Ni in its metallic, oxide, hydroxide states is shown in Figure 3.12 (b), where it is clear that more oxides are formed with longer oxidation time, but the relative concentration between hydroxides and oxides began to change at longer oxidation time (1–4 min). Figure 3.13 (a) shows Ni 2p, C 1s, and O 1s spectra with various substrate bias powers applied for 30 s for the same plasma oxidation conditions. The amount of Ni

in its metallic, oxide, hydroxide states is shown in Figure 3.13 (b), where a nearly monotonic increase in the amount of oxidized nickel was observed with increasing substrate bias (0–20 W). Since the formic acid chemistry in the gas phase is only reactive with oxidized nickel, the extent of oxidation translates to attainable etching rates, while realizing a very high selectivity. The targeted reaction in the directionally oxidized region would lead to directional removal, where the reaction viability is determined by the thermodynamics of the reaction, not the energy of the ions.

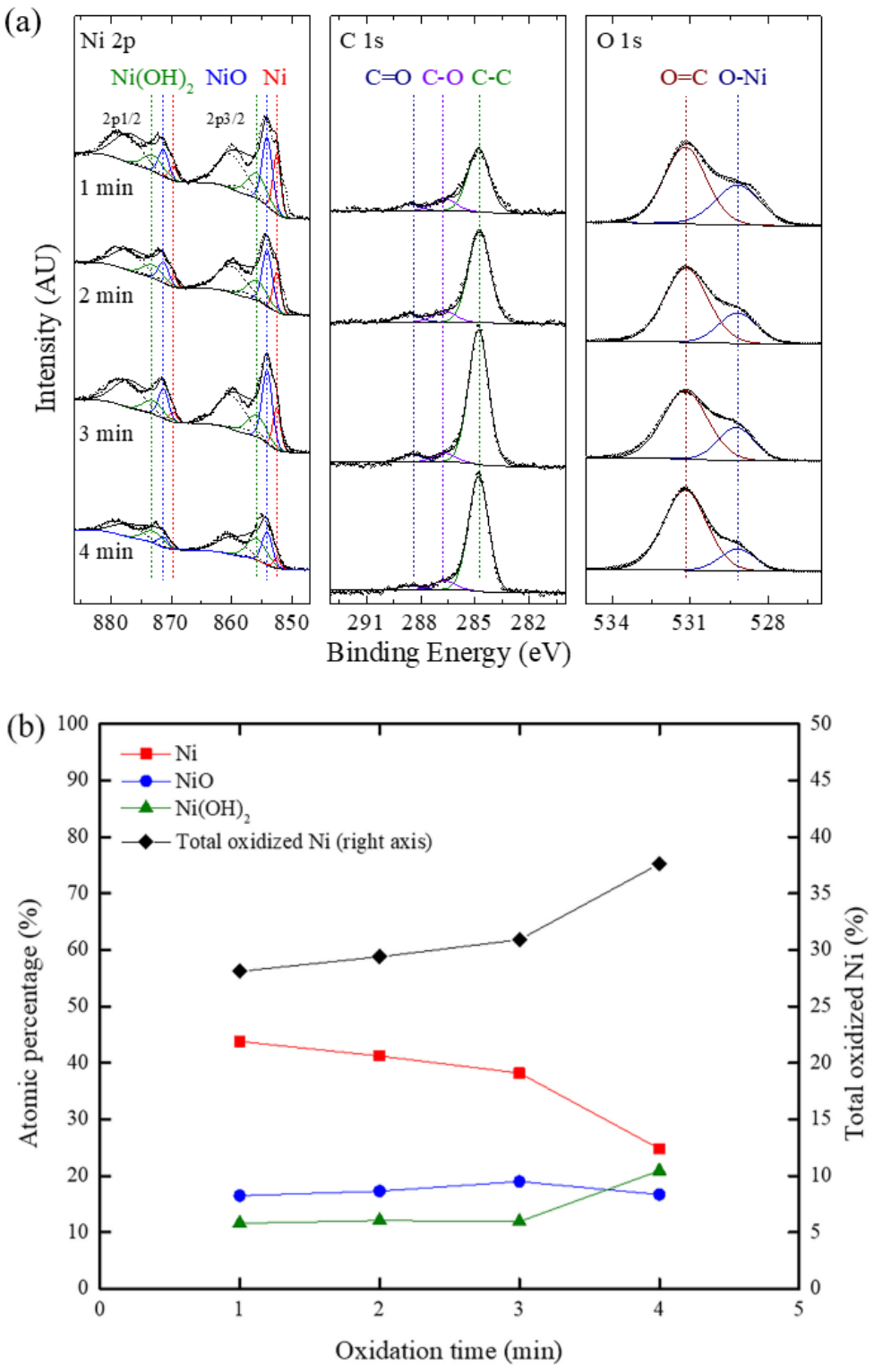

Figure 3.12 (a) XPS of Ni 2p, C 1s, and O 1s and (b) the relative atomic percentage of different nickel chemical states as a function of oxidation time.

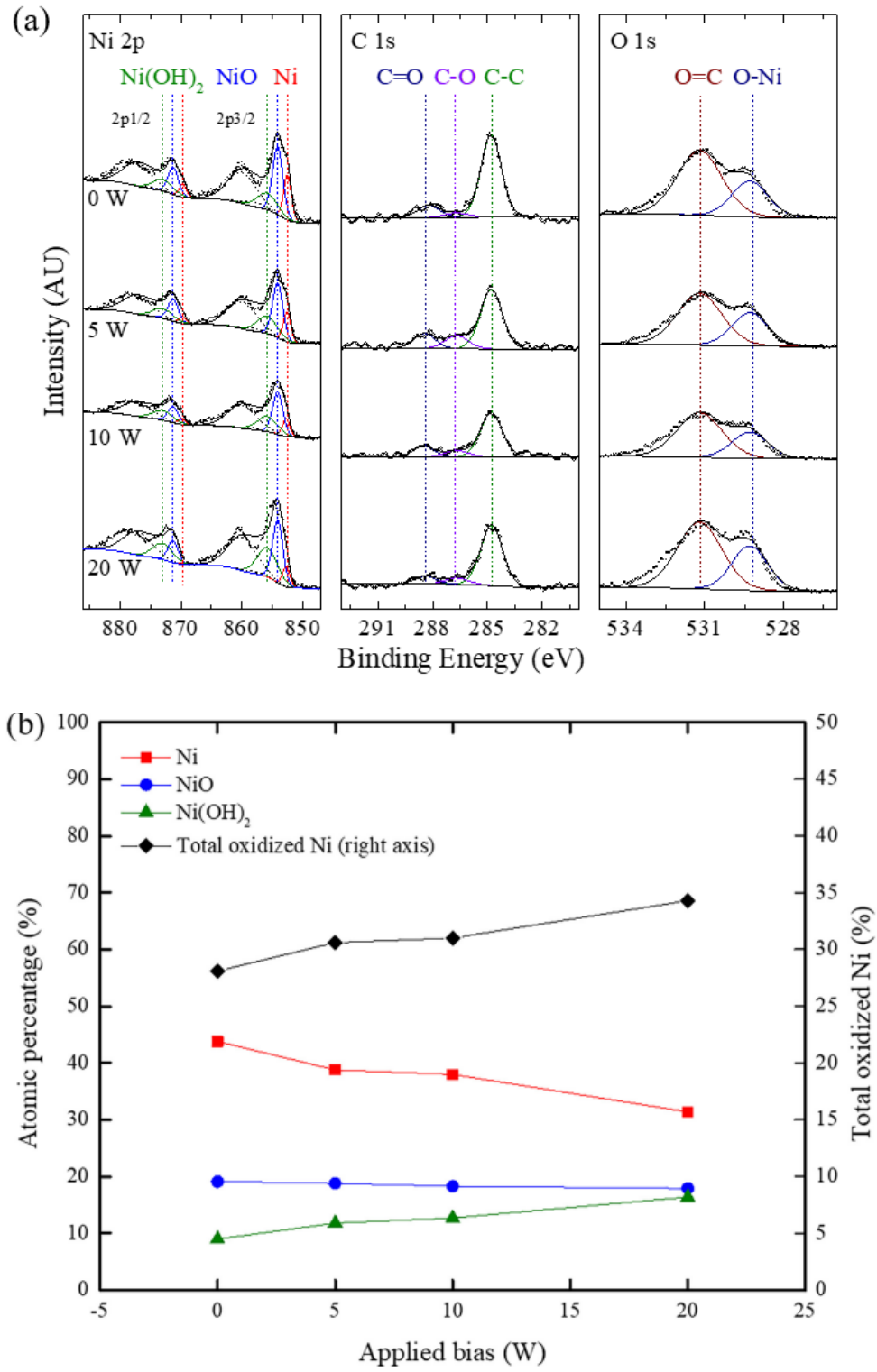

Figure 3.13 (a) XPS of Ni 2p, C 1s, and O 1s, and (b) the relative atomic percentage of different nickel chemical states as a function of substrate bias.

3.4.2 Selective Removal of Surface Oxides

In addition to the effect of oxidation conditions, the effects the chamber pressure during formic acid exposure was also examined in this work. Since a higher substrate bias leads to higher energy ions, which could physically sputter the hard mask, the effect of lower energy ions was also evaluated. The lowest attainable ion energy in this work is equivalent to the plasma self-bias when the applied bias was set to zero. Figure 3.14 shows compositional analysis of the etched nickel surface where the oxide was formed with an oxygen plasma with zero substrate bias, while the formic acid exposure was carried out at various formic acid pressures. The ex-situ XPS analysis included Ni 2p, C 1s, and O 1s spectra that are deconvoluted to show the chemical bonding configurations on the etched surface. Qualitatively, the spectra obtained after the cyclic etch process at 550 Torr were distinct from the other two spectra. The amount of surface oxide remained could be quantitatively represented by the signal intensity ratio of NiO over that of Ni, which is 0.80, 0.82, and 0.45 at formic acid exposure pressures of 150 Torr, 350 Torr, and 550 Torr, respectively. Based on the attenuation length of electrons in Ni and NiO, the oxide thicknesses remained on the surface were 5.3 nm, 5.2 nm, and 0 nm (due to absent Ni-O peak in O 1s) at 150 Torr, 350 Torr, and 550 Torr, respectively, based on references to clean metallic nickel and thick nickel oxide references. Since all the oxidation half-cycles were performed under the same conditions in this set of experiments, the calculated oxide thickness suggested incomplete removal of the oxidized nickel at lower pressure conditions but complete removal of oxidized nickel at the highest pressure used.

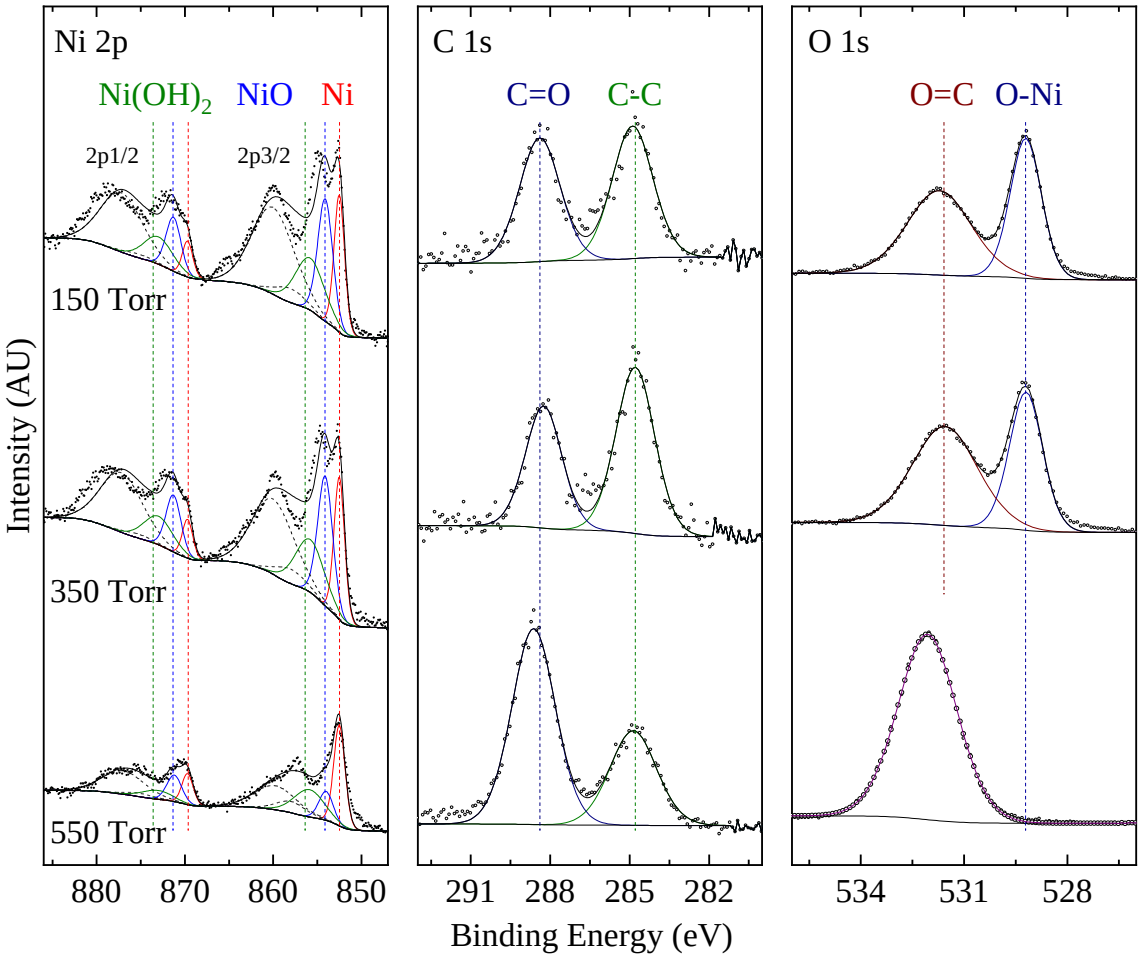

Figure 3.14 Surface composition measurements of the Ni blanket film after 1 min of 500 W RF power 0 W applied bias plasma oxidation followed by 1 h of 150 Torr, 350 Torr, and 550 Torr formic acid exposure.

3.4.3 Plasma-Thermal ALE of Ni Thin Films

Calculations based on available thermodynamic data indicate spontaneous reactions between gas-phase formic acid with both metallic nickel and nickel oxide. However, given the much-reduced reactant concentration in a vacuum environment, very little etching was observed in the gas phase with metallic nickel: a thickness reduction of about 1 nm, which is within the detection limit of the SEM measurement, may have occurred at a chamber pressure of 350 Torr

and a chamber temperature of 80 ℃ for 3 h [Figure 3.15 (a)]. Shown in the same figure, it is noted that the same chemistry has no effect on etching SiO_2. The work was then focused on the use of an oxygen plasma to promote surface oxidation with a substrate bias of 50W, creating an oxide layer, which was then exposed to formic acid vapor at 350 Torr and 80 °C. The data shown in Figure 3.15 (a) are the etched thickness of nickel, as measured by SEM, as a function of the cumulative formic acid exposure time in this cyclic process (since the nominal formic acid exposure time per cycle is 60 min, this corresponded to three cycles). A very linear etch rate was observed with this cyclic process, with an etch rate of 0.1 nm/min. The lower etch rate compared to that in the solution is attributable to the reduced reactant concentration. The oxidation step is not self-limiting; the self-limiting reaction step is where the organic vapor removes the oxides, as very high etching selectivity were recorded on NiO to Ni (∼100) and NiO to hard masks (essentially infinite) at 80 °C and 350 Torr. The effectiveness of this cyclic etching process is also confirmed by the XPS analysis of the etched Ni samples. As shown in Fig. 3(b), there are many features in the measured XPS spectra, namely, the Ni 2p core level emission in various chemical states (colored solid lines) as well as the satellite peaks (black dash lines). To differentiate these chemical states, a detailed XPS analysis was done with reference spectra taken on clean metallic Ni and fully oxidized Ni thin films in the same XPS system. By fitting the Ni $2p_{3/2}$ and $2p_{1/2}$ regions simultaneously with the fixed spin orbital split and ratio, these features were assigned to nickel in metallic, oxide, and hydroxide forms. The formation of $Ni(OH)_2$ has been widely observed with the presence of moisture in the air (Aggarwal 1961). Given the purity of formic acid used in the experiment and the base pressure of the reactor, nickel hydroxide formation was expected. The formation of higher oxidation state oxide (Ni^{3+}) was not considered, as “attempts to prepare Ni_2O_3 by heating the hydroxide, basic carbonate or nitrate of nickel in air or oxygen resulted in the

formation of NiO only (Lambers 1996).” It has been suggested in the literature that the differentiation between Ni^{2+} and Ni^{3+} could be realized by measuring electrical conductivity (Dubey 2018); however, this was not viable with such thin films. Finally, the possibility of incomplete removal of the reaction production and redeposition of the reaction products was also considered in analyzing the XPS data. The redeposition of etch product is possible; however, the EDS map from TEM analysis detailed later did not show Ni over the hard mask, which suggests that this is unlikely. The incomplete removal of the reaction products is also possible, but the XPS resolution did not allow such differentiation. Figure 3.15 (b) clearly shows that the signal intensities of both metallic Ni and NiO decreased significantly, confirming removal of nickel after cyclic treatments. Though the melting temperature of nickel formate is reported to be ~140 °C at STP condition (Karaffa 2013), as etching in a reduced pressure leads to a gaseous product, the reaction would be thermodynamically more favorable due to the entropy gain.

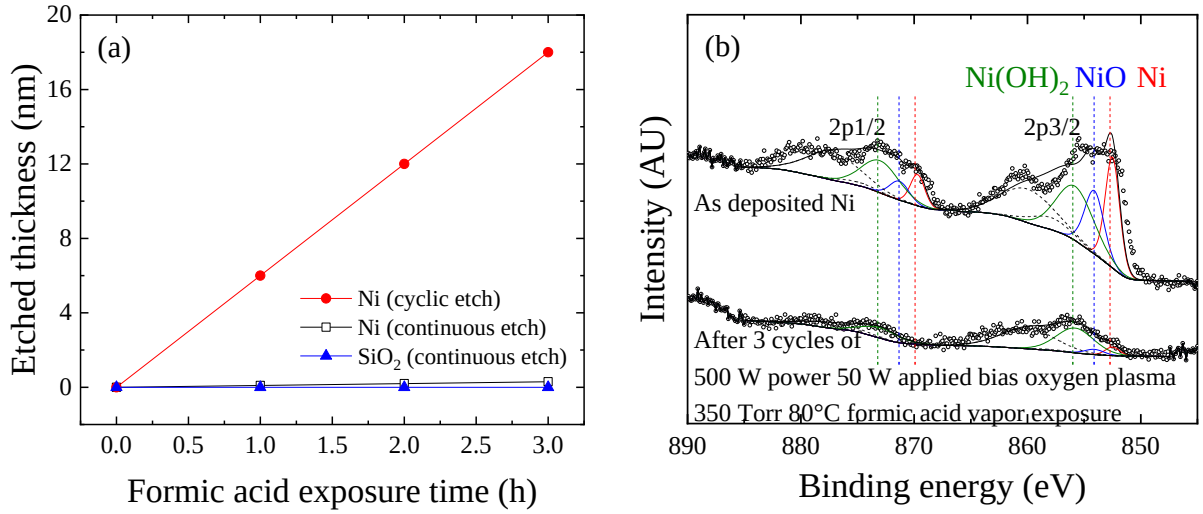

Figure 3.15 (a) Etched thicknesses for Ni and SiO2 as functions of gas-phase formic acid exposure time at 80 C and 350 Torr and (b) XPS detail scan of Ni 2p spectrum of blanket Ni thin film as deposited and after three cycles of oxygen plasma and formic acid vapor.

In reviewing available literature concerning Ni-complexes regarding their potential applications in soldering (Ivankovits 2000), catalysis (Ananikov 2010), and as CVD precursors (Ananikov 2010), the physical properties of nickel acetate have been detailed (Tappmeyer 1963), indicating a stable complex in condensed form. The solubility of nickel acetylacetate was studied, with anhydrous $Ni(acac)_2$ forming trimers to achieve an octahedral coordination around each nickel atom. When water is present, each $Ni(acac)_2$ prefers to form an octahedral complex with two water molecules (Tappmeyer 1963). Volatility of $Ni(hfac)_2$ was cited to be higher than that of $Ni(acac)_2$ due to the weaker intermolecular hydrogen bonding and van der Waals force (Ivankovits 2000). Regardless of the type of ligands bonded to Ni atom, multiple literature reports emphasized the role of oxidizing agents, either as designed reactants (Ivankovits 2000) or as sources of adventitious reactions (Weiss 2015). The formation of nickel oxide, either from oxidizing nickel in metallic state or from decomposition of nickel-complex implies that the potential reaction path could be explored with controlled surface oxidation. This is consistent with the observed high selectivity between etching NiO and Ni in formic acid, making the creation of a chemical contrast in nickel by oxidation a viable approach to achieve ALE.

3.4.4 Plasma-Thermal ALE of Ni Patterned Thin Films

To assess the profile control of the developed ALE process, patterned samples were used. Processing pressures ranging from 150 to 550 Torr were evaluated, while the chamber temperature was maintained at 80 ℃. From AFM analysis, it is noted that the initial sidewall angles varied between 60° and 80°, which is another parameter to consider in analyzing the results. Finally, since the calibration experiments confirmed that formic acid vapor does not etch SiO_2 hard mask (as shown in Figure 3.15), the AFM measured height change is fully attributed to the etching of NiO

(which is also corroborated by HRTEM analysis). Figure 3.16 shows the AFM contour plots for patterned samples etched by the plasma-thermal cyclic process at three different pressures and after various cycles (only results after two and six cycles are shown for clarity). At a low pressure (150 Torr), some changes in the sidewall profile may have been resulted but there is no significant reduction in the Ni film thickness in the open area. As the pressure increased to 350 Torr, a measurable etch rate of 3 nm/cycle was recorded, with some erosion on the corner of the hard mask. As the pressure increased further to 550 Torr, a much more substantial etching was observed, with an overall higher etch rate of 6 nm/cycle, consistent with the compositional analysis by XPS on etched blanked samples. More importantly, the average sidewall angle after six cycle of treatment was measured to be 87°, making it possible to categorize the etching as anisotropic.

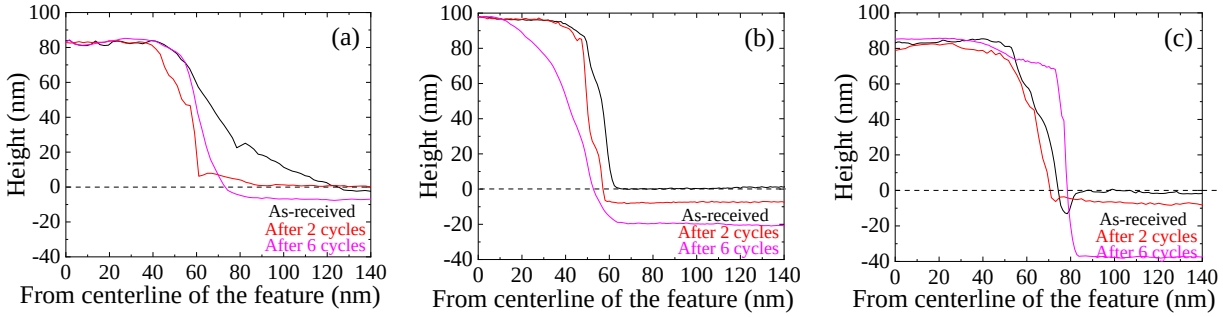

Figure 3.16 AFM measurement of sidewall profile of as-received sample and samples after numbers of treatment with 2 min of 500 W RF power 0 W applied bias plasma oxidation followed by 1 h of (a) 150 Torr, (b) 350 Torr, and (c) 550 Torr formic acid exposure.

Figure 3.17 summarizes the results by evaluating the remaining Ni layer thickness and sidewall angle as a function of the number of cycles of the plasma-thermal process. The shaded pink region at the top represents the targeted sidewall angle (87°–90°). It is observed that processing at the lower formic acid pressure did not reach the etching end point, leaving a less anisotropic sidewall profile. The etch rate as well as the sidewall angle increased as the formic acid pressure increased. The repetition of cycles at higher pressures allows more thorough removal

of the oxidized region, which is anisotropic due to the directionality of the oxygen ions when traversing through the plasma sheath, thereby reaching the etching end point after six cycles.

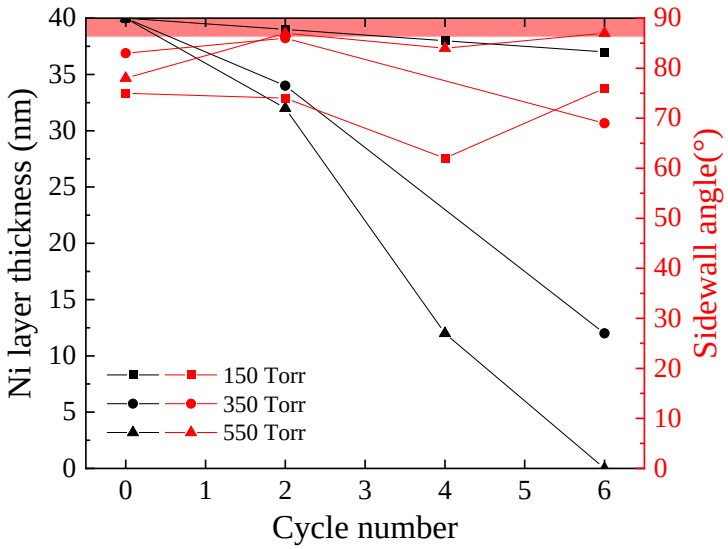

Figure 3.17 Ni layer thickness (left axis, measured by SEM) and sidewall angle (right axis, measured by AFM) as functions of number of cycles for different exposure pressures.

To confirm whether etching is anisotropic with higher precision, as well as to inspect the elemental distribution of the final feature, HRTEM and EDS were performed on a sample treated by 6 cycles of ALE with an oxidation step at zero bias and a pressure of 550 Torr during formic acid exposure, as shown in Figure 3.18. HRTEM analysis confirmed the vertical Ni sidewall (87°), as determined by AFM measurements. The EDS showed no Ni over the hard mask, suggesting that redeposition of the etch products is unlikely. The EDS also showed that the exposed sidewalls are slightly oxidized, which is expected due to ambient exposure before the HRTEM analysis. Comparing the oxygen and nickel EDS mapping, the oxidized sidewall thickness is on the order of 10 nm, which is about the same as the normally observed native oxide layer thickness due to

ambient exposure (~5 nm). It is concluded that this ALE process is capable of etching patterned Ni thin film with high selectivity and anisotropy.

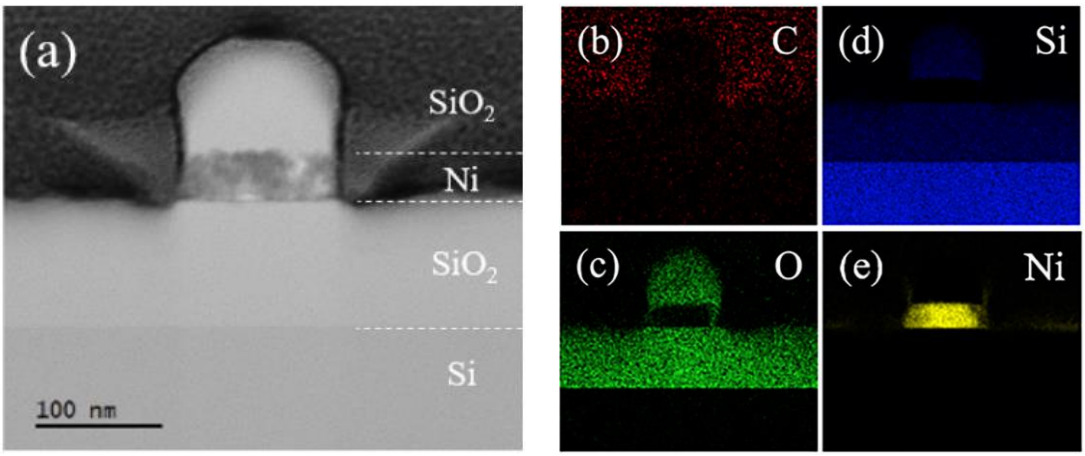

Figure 3.18 (a) TEM image of sample treated with six cycles of ALE with 550 Torr formic acid exposure pressure. (b)–(e) EDS elemental mapping of C, O, Si, and Ni.

This plasma-thermal approach is novel in that a plasma-driven oxidation step introduces an anisotropic conversion of the surface layer. The isotropic component of the process comes from the removal step utilizing an isotropic organic vapor—in this step, the organic vapor (intrinsically isotropic) leaves behind an anisotropic profile, because the organic vapor only reacts with the nickel oxide but not the nickel. In other words, the anisotropy introduced by the oxidation is only revealed in the subsequent isotropic chemical vapor exposure. A number of published works suggested the realization of various degrees of anisotropy using the alternative plasma exposure and thermochemical reactions, but no microscopic image of the patterned final features was shown (Park 2006, Miyoshi 2017, Mameli 2018, Johnson 2019), especially not with detailed cross-sectional images of etched metal with nanoscale patterns.

3.5 Density Functional Theory Based Reaction Modeling

In order for the simulation to be finished within reasonable amount of time using acceptable computational power, trade-offs need to be made between simulation precision and speed. It is of interest that the simulation environment would mirror the experimental condition as much as possible, however such modeling would take enormous amount of time as layers of atoms not participating the reactions are involved. Therefore, the modeled initial oxidation of the Ni surface and Ni layer thickness are both much thinner than the experimental NiO layer on Ni. They should, nevertheless, provide general insights into the thermodynamics and pathway for the etching process. Figure 3.19 shows the structures for the three surfaces.

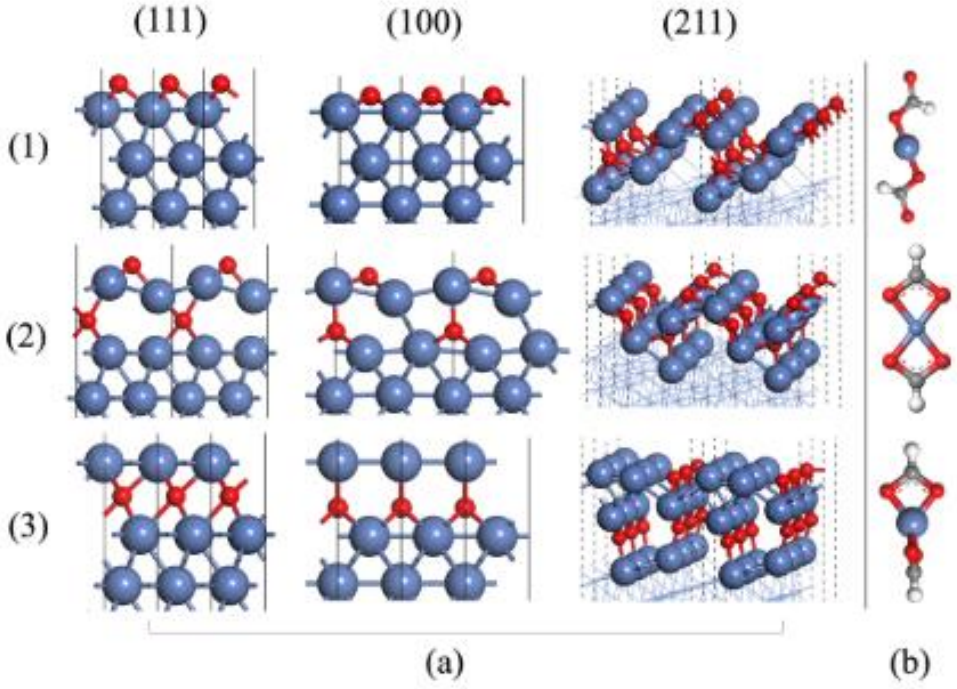

Figure 3.19 (a) Illustration of the relaxed structures of (111), (100), and (211) surfaces with (1) overlayer, (2) mixed, and (3) sublayer oxygen adsorption, (b) From top to bottom: monodentate, bidentate planar, bidentate tetrahedral geometry for the Ni diformate complexes.

To study the coverage effects, three scenarios are considered, representing the following chemical reactions:

Table 3.3 Reactions considered in DFT calculation.

Oxygen atom incorporation	Reaction
Pristine Ni	$Ni + 2HCOOH \rightarrow Ni(HCOO)_2 + H_2$
Low O coverage	$NiO_\theta + 2\theta HCOOH \rightarrow Ni(HCOO)_2 + \theta H_2O$
1 monolayer O adsorption	$NiO + 2HCOOH \rightarrow Ni(HCOO)_2 + H_2O$

The monolayer (ML) coverage is redefined with respect to the number of nickel atoms exposed to modifiers (O). For p(2 × 1) cells used in the (111) mixed structure, for instance, two nickel atoms are exposed; hence, 1 ML corresponds to two oxygen atoms, one in the overlayer and the other in the sublayer.

Since no experimental characterization of the gas phase nickel diformate complex [$Ni(HCOO)_2$] is available, various structures were considered with DFT, and the most stable one is used in the energy calculation. The formate structure candidates are shown in Figure 3.19. The monodentate structure corresponds to the configuration in solid state nickel formate dihydrate (Edwards 1992), but it is not stable in the gas phase. The bidentate planar structure is the most stable one. Note that this is a 16-electron square planar structure, common for d^8 metal complexes.

The reaction energy for the simpler 1 ML case is given by the following equation:

$$\Delta G_{et} = \left[G_{l+,NiO} - G_{l,Ni} + \left(n^{\circ}_{Ni} G_{[Ni(HCOO)_2]} + n^{\circ}_{Ni} G_{H_2O} - 2n^{\circ}_{Ni} G_{HCOOH}\right)\right] \cdot \frac{1}{n^{\circ}_{M}} \qquad (3.3)$$

Figure 3.20 shows the reaction energy of various activated surfaces considered (per Ni atom removed). Most notably, for the 1 ML case, oxygen activated nickel surfaces can be favorably

etched via formate chemistry, consistent with the experimental work. Etching of the pristine nickel surface to produce Ni diformate and gas phase hydrogen is calculated to be endergonic by 1.7 eV and is hence highly unlikely. This is consistent with our experiments where the unmodified clean nickel was not etched. The purple bars in Figure 3.20 show that the etching reaction for Ni surfaces modified by a low coverage of oxygen adatoms is also thermodynamically unfavorable by more than 1.5 eV. Hence, only surfaces modified by a high coverage of O atoms, with occupation of subsurface sites and the formation of a surface NiO layer, result in a favorable etching reaction with formic acid, in agreement with experiments. Note that the favorable etching reaction for these oxidized surfaces is not resulting from a greater stability of the products (Ni diformate and water), since the energies are already normalized with respect to the number of metal atoms, but from a reduced binding of the Ni atoms in the "reactant" surface.

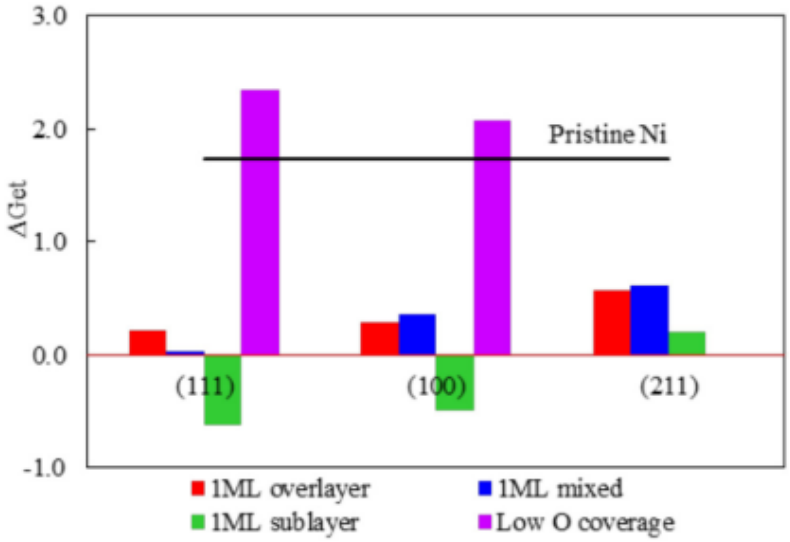

Figure 3.20 Etching reaction energies (ΔG_{et} in eV) of oxidized nickel (111), (100), and (211) surfaces using a layer-by-layer removal model, normalized to one Ni atom removal.

The site dependence trend is quite complex. For (111), increasing access to sublayer sites increasingly destabilizes the surface, while (100) and (211) surfaces are not significantly destabilized by occupying a fraction of the sublayer sites in a mixed adsorption structure. (100) and (211) results indicate that occupying the sublayer sites using low energy oxygen ions can make the etching reaction favorable. A closer look at Figure 3.20 reveals that etch becomes more favorable when Ni atoms in the top layer have a longer bonding distance with the layers underneath due to occupation by oxygen atoms in the sublayer. In particular, all the sublayer structures show a large vertical relaxation of the top layer, moving away from the bulk, while the mixed and overlayer structures still have one or more Ni atoms at short bonding distance from the underlying metal. It suggests that the geometry distortion caused by the oxygen modifier provides a favorable driving force. Overall, (211) has a higher reaction energy compared with (100) and (111). This is due to the fact that while the (211) surface itself has a higher surface energy, occupying the undercoordinated sites on the edge initially stabilized the surface, to a higher extent than that of (100) and (111), where the terrace atoms have a higher coordination number. These results suggest that site specificity can play a role in atomic layer etching of surface species.

3.6 Realizing Combined RIE + ALE of Ni

It has been shown in the previous sections that, individually, with the proper tuning and carful pressure adjustment, both RIE and plasma-thermal ALE are capable of removing Ni at a nanometer-per-cycle rate. However, RIE leaves tapered sidewalls, while plasma-thermal ALE is a prolonged process, rendering neither a sufficiently good process by themselves. Specifically, in an integrated process for mass production, low throughput steps could bottleneck the entire process

and should be circumvented if possible. The trade-off between throughput and precision would depend on the specific application scenarios as the target amount of material removal is largely dictated by the preceding deposition step. It is therefore natural to seek for the hybrid process of combining the two approaches, where a fast, non-self-limiting RIE is used to quickly remove the bulk of the materials, leaving the profile close (within 1–3 nm) to etch endpoint with considerable amount of tapered sidewall. The plasma-thermal ALE process is then subsequently introduced to directionally remove the exposed sidewalls. The overall process is schematically represented in Figure 3.21. Specifically, a chlorine plasma is used to facilitate the formation of chlorinated nickel, while a hydrogen plasma was used subsequently to remove the chlorinated nickel. With different levels of redeposition of the RIE etch product, the post-RIE sidewall profile would show concave down (little or no redeposition, route c-e) or concave up (significant redeposition, route c’ to e’). These imperfect sidewall profile would be then tailored by a plasma-thermal ALE process to achieve the desirable angle.

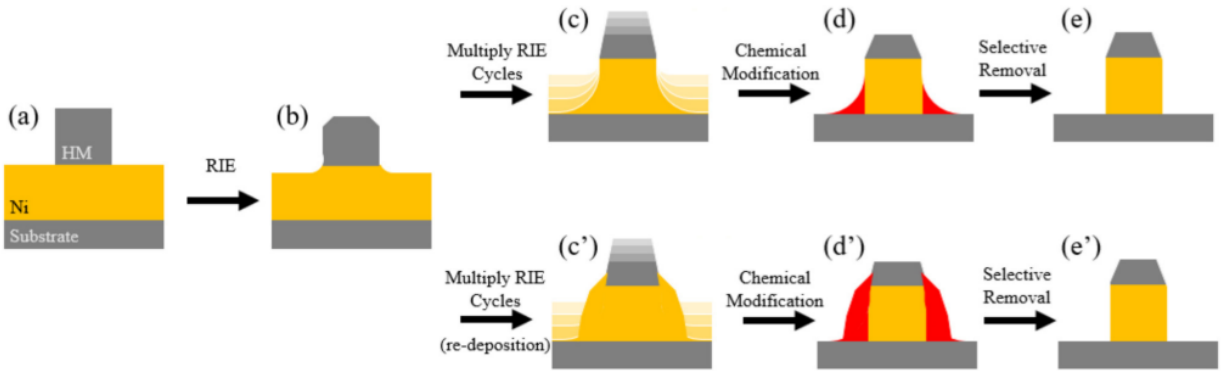

Figure 3.21 Proposed hybrid RIE-ALE process, first with the RIE process: (a) initial patterned structure and (b) structure after one RIE treatment. Depending on if the reaction products from the RIE process redeposit, a sidewall profile after multiple RIE cycles results in either (c) a convex curvature or (c') a concave curvature. These structures can be then used to test the effectiveness of the ALE process, where (d/d') represent chemical modification via plasma oxidation to define vertical modified region using directional ions and (e/e') illustrate selective removal of the oxides leaving the final structure with an anisotropic sidewall profile.

The overall effect on the final feature profile by combining high-throughput RIE with high-precision ALE is shown. RIE-etched samples were then etched by ALE processes that are based on 1-min plasma oxidation and 30-min formic acid vapor exposure at 550 Torr. To capture the trend of profile evolution, TEM image of features after six cycles of RIE, six cycles of RIE and one cycle of ALE, and six cycles of RIE and two cycles of ALE were taken and shown in Figure 3.22 (a)–(c). Comparing images of samples before and after one cycle of ALE treatment, it is observed that the remaining Ni from RIE in the exposed regions were mostly removed, leaving footing at the edge of the feature. Another ALE cycle effectively removed the footing, resulting in a vertical sidewall of 90° at the bottom of the feature as shown in Figure 3.22 (c).

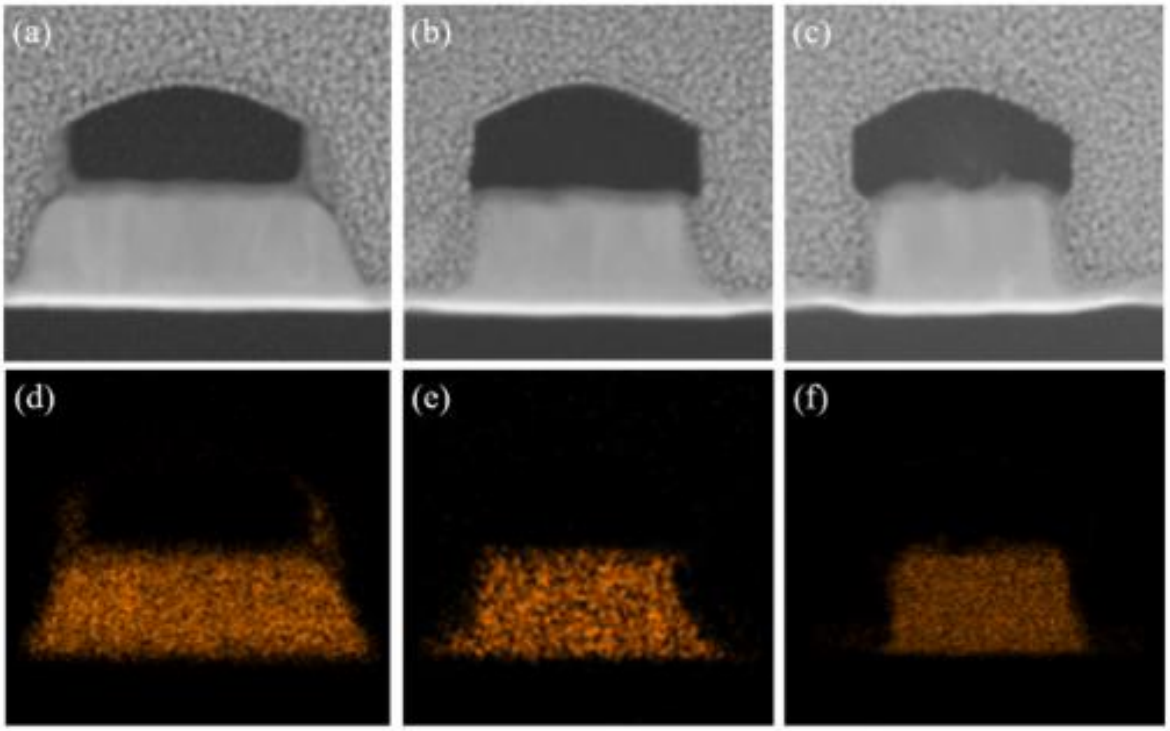

Figure 3.22 HRTEM of patterned Ni features after (a) six cycles of RIE, (b) six cycles of RIE and one cycle of ALE and (c) six cycles of RIE and two cycles of ALE. (d)–(f) The corresponding elemental mapping of Ni for (a)–(c).

Uniformity is also a crucial factor of the process, the combined RIE + ALE process showed good uniformity across multiple samples over 20 micrometer range. Zoom-out view of individual features shown in Figure 3.22 is shown in Figure 3.23. Feature-to-feature variation is small, and changes across different processing steps are uniform.

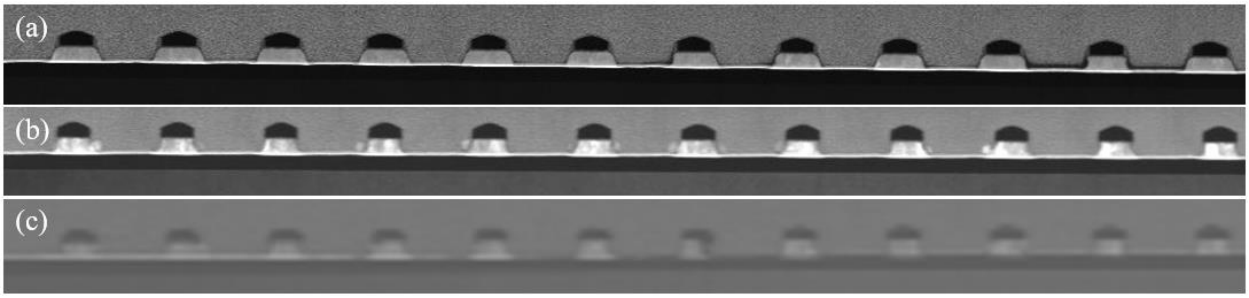

Figure 3.23 Zoom-out view of patterned Ni features after (a) six cycles of RIE, (b) six cycles of RIE and one cycle of ALE and (c) six cycles of RIE and two cycles of ALE.

The trend of feature width and sidewall angle after each processing step is plotted in Figure 3.24 with targeted values highlighted by the grey shading (≈65 nm initial hard mask width, ≥87° sidewall angle for anisotropy). The decrease in the sidewall angle at the bottom of the feature after one cycle of ALE is due to the thickness of the convex shaped sidewall reaching maximum at those regions, as the oxygen plasma did not convert the entire thickness to oxide, leaving metallic layer underneath, which was then not removed. The final sidewall angle returned to vertical as expected once the footing was oxidized and removed. It is noted that the expansion of the Ta adhesion layer during oxidation half-cycles covered some of the Ni footing, making part of the regions inaccessible for formic acid. It is expected that more complete removal could be achieved without the adhesion layer or with an adhesion layer less prone to expansion during oxidation.

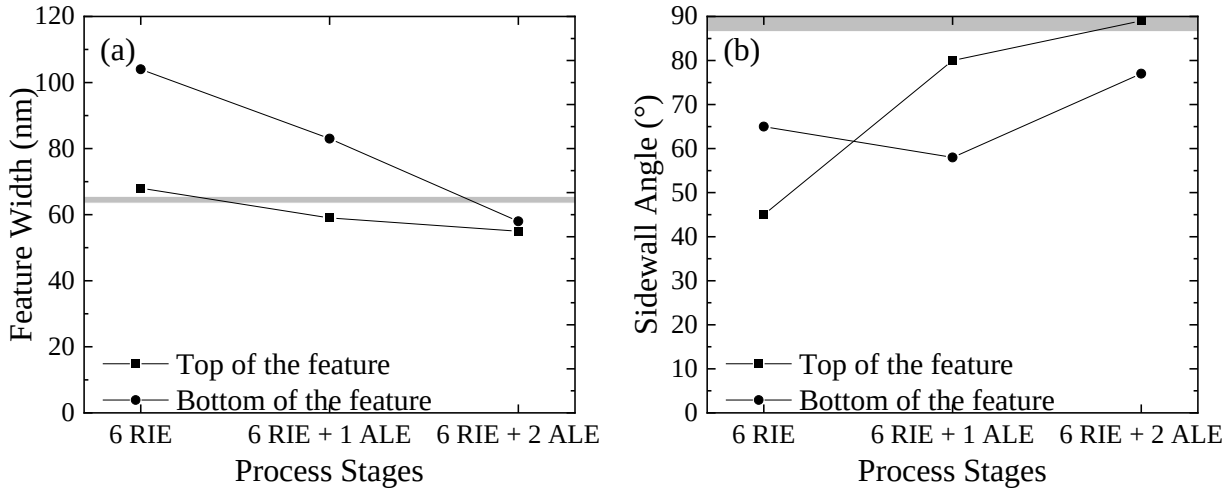

Figure 3.24 (a) Feature width and (b) feature sidewall angle after different processing steps.

Feature outlines for three TEM images were digitized and superimposed in Figure 3.25. It is noted that a vertical etch rate of 20 nm/cycle is measured, which is considerably higher than the 6 nm/cycle upper bound recorded in the previous section. This increase could be attributed to the effect of RIE process preceding the ALE process: the characteristic concave shape after the RIE process indicates redeposition of reaction products due to the low volatility of the nickel halides. This concave sidewall shape is due to reaction product redeposition. The redeposited layer is expected to have a different density and composition compared to the pristine layer and thus could be more prone to reaction with the ALE chemistry, leading to an increased removal rate.

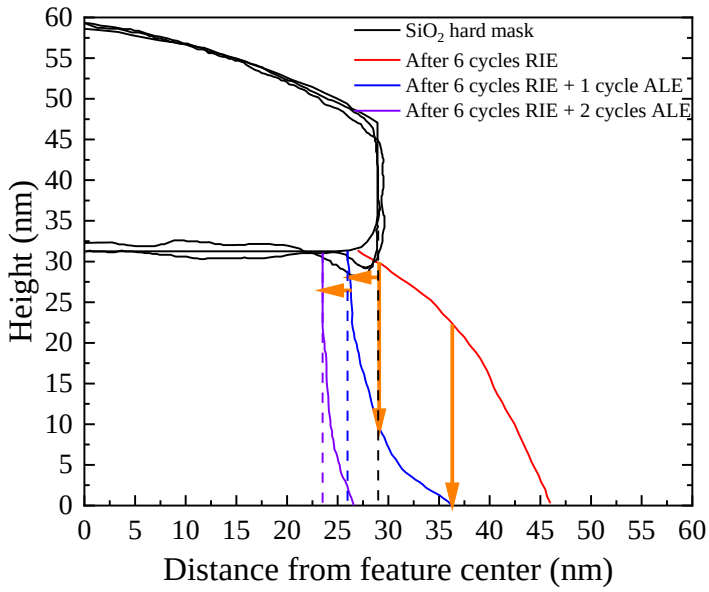

Figure 3.25 Digitized etch features after different processing stages, with arrows indicating the amount of nickel removed in both vertical and horizontal directions.

In addition, the digitized features also show a consistent lateral etch rate of 2.5 nm/cycle. This undercut could be due to the presence of oxygen atoms in the plasma, which is isotropic and would oxidize the sidewall laterally. Overall, the chemistry is proven to be highly directional as the vertical etch rate is about eight times the lateral etch rate. Further improvement in anisotropy could be achieved via the implementation of the ion source with low neutral to ion ratio, or with a directional ion source. In this work, the ALE portion of the process took 1.5 h to complete, combined with 0.5 h of the RIE process; the overall processing time is about 2 h. Compared to the final feature profile achieved in the plasma-thermal ALE section, this hybrid RIE-ALE approach resulted in a partially removed hard mask and about 5 nm of undercut, but the overall processing time is less than 25% of that of the ALE-only process. This drastic improvement provides a new perspective for patterning materials with thickness higher or on the order of tens of nanometers, opening up new etching pathways for high throughput and high-precision etching.

3.7 Controlled Etching of Ni_3Al

As shown in Table 1.3, Ni_3Al is recently proposed to be an alternative candidate of the EUV mask absorbing material. The controlled etching of Ni_3Al is more complex since surface stoichiometry needs to be considered during the processing. In light of previous result on the etching of Ni, this section focuses on exploring the etching of Ni_3Al, with process optimization and monitoring of surface compositions. Experiments were carried out on three different thin films; the structure information is listed in Table 3.4.

Table 3.4 Samples used for studying Ni_3Al etch.

	Material	Thickness
Blanket Thin Film	Ni_3Al	25 nm
Blanket Thin Film	Ru	33 nm
Patterned Thin Film	Si_3N_4	190 nm
	Ni_3Al	22 nm
	Ru	35 nm

Process conditions are listed in Table 3.5. Comparing to conditions listed in Table 2.2, the chlorine exposure time is increased by a factor of two.

Table 3.5 Cyclic Chlorination-hydrogenation parameters used on Ni_3Al etch.

Chemistry	Flow Rate (sccm)	Pressure (mTorr)	Power (W)	Bias (W)	Time (s)
Cl_2	60	15	400	20	60
Ar		purge			90
H_2	20	60	200	60	15
			400		90

Figure 3.26 shows the quantification of Ni to Al ratio at different XPS take-off angle, which could be treated as recording averaged signal from different probing depths. The lower the take-off angle, the shallower depth XPS is probing from. With a perfectly deposited Ni_3Al thin film with a uniform Ni_3Al removal, Ni to Al ratio should be a constant value at around 3. Deviation from the ideal value could be attributed to preferential removal of one element over the other during etch, inconsistent deposition conditions, or relative sensitivity of different elements on the XPS. The potential imperfection of the measurement, however, does not affect the relative comparison between the thin film before and after treatment. It is observed that the cyclic chlorination-hydrogenation process resulted in an enrichment of Ni over Al, implying preferential removal of Al. Within the same thin film, Al tends to aggregate at the surface.

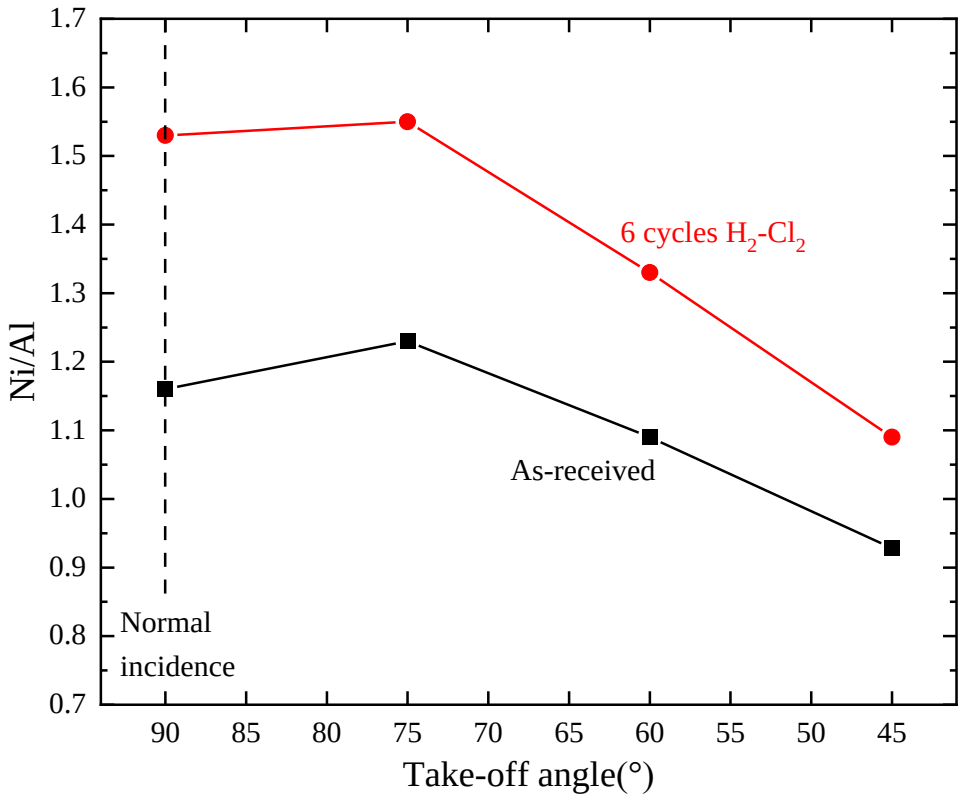

Figure 3.26 Ni/Al ratio of both as-rec and cyclic RIE treated Ni_3Al thin film at different XPS take-off angles.

Etching chemistries' selectivity over Ru is also of interest given the EUV mask structure shown in Figure 1.5, hence Ru thin film is included in the same processing treatment for selectivity measurement. From SEM thickness measurements shown in Figure 3.27, etch rate of 1.4 nm/cycle and 3.5 nm/cycle is determined for Ni_3Al and Ru, respectively. The overall selectivity of Ni_3Al with respect to Ru is calculated to be 0.4. A less-than-unity selectivity means Ru would be etched at a higher rate than Ni_3Al, imposing controllability issue when approaching the etch end point.

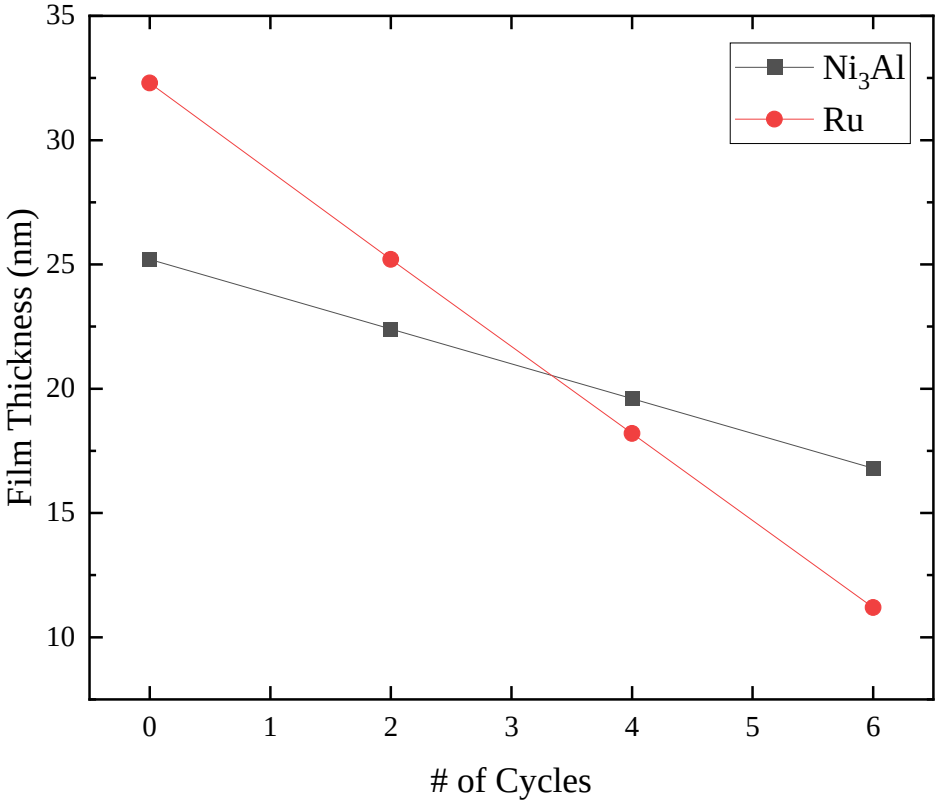

Figure 3.27 Film thickness of Ni_3Al and Ru after different cycles of cyclic RIE treatments.

The cyclic chlorination-hydrogenation RIE of the patterned Ni_3Al thin film resulted in considerable amount of Ni_3Al removal in the exposed region. Al_xO_y was observed using EDS at the sidewall of the feature, preventing regions underneath been etched. The localized increase of Al matches previous study of preferential Al removal by the RIE chemistry. Buffered oxide etch (BOE, 6:1 volume ratio of 40% NH_4F in water to 49% HF in water) was used to remove the redeposited Al_xO_y region while avoiding excessive hard mask lost, Ni and Al were not affected by the BOE dip. Directional oxygen ions were used again to introduce anisotropy for the subsequent formic acid vapor exposure, oxidized Ni_3Al was then removed by formic acid vapor. TEM images and EDS mapping of Ni and Al of patterned Ni_3Al thin film after RIE process, after RIE and BOE

processes, and after RIE, BOE and ALE processes are shown in Figure 3.28. The validity of such plasma-thermal ALE process is again confirmed.

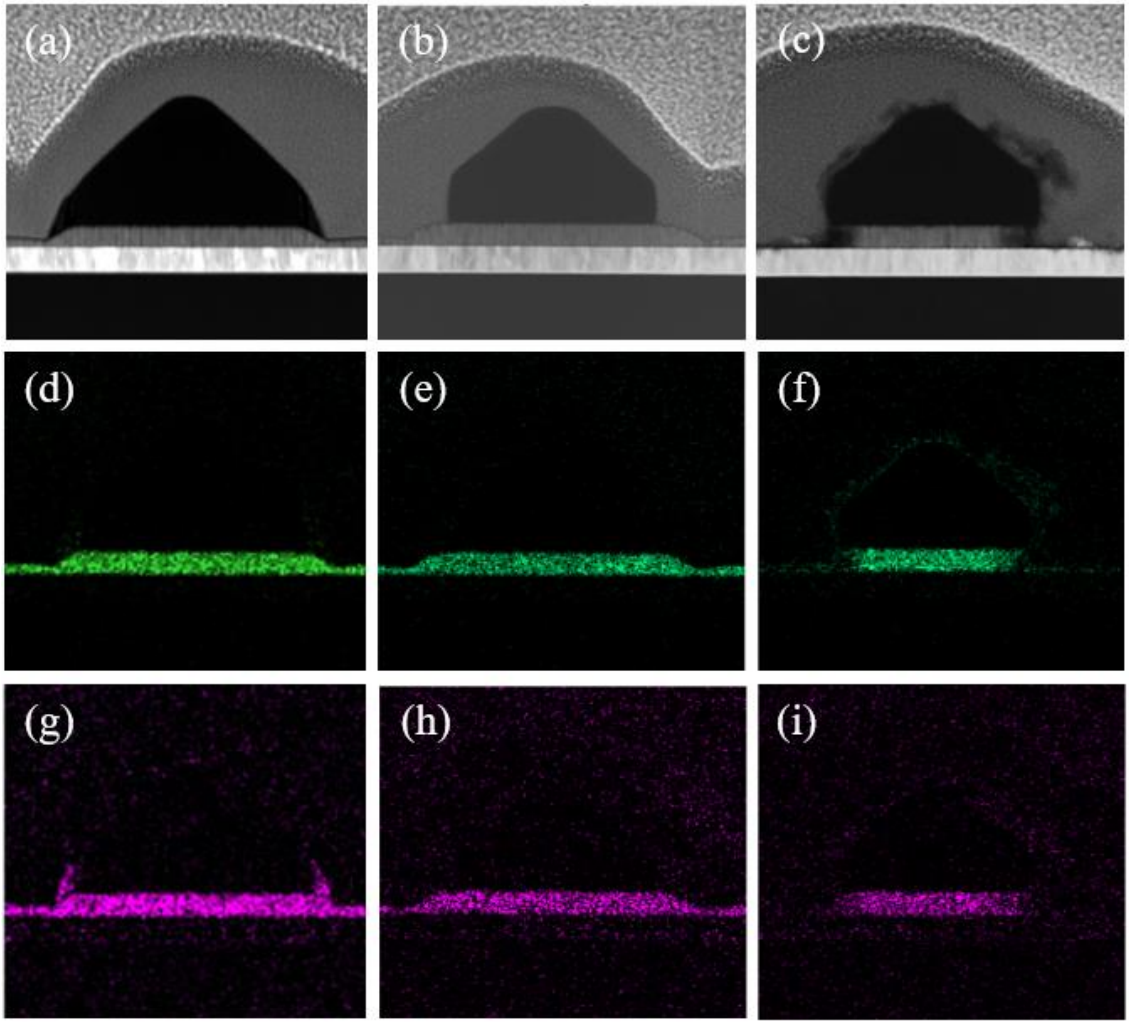

Figure 3.28 HRTEM of patterned Ni_3Al features after (a) 24 cycles of RIE, (b) 24 cycles of RIE and 5 seconds of BOE dip and (c) 24 cycles of RIE, 5 seconds of BOE dip and 4 cycles of ALE. (d)–(f) The corresponding elemental mapping of Ni for (a)–(c). (g)-(i) The corresponding elemental mapping of Al for (a)–(c).

Chapter 4 Nanometer Scale Patterning of Cu

In this chapter, a cyclic process for selective and anisotropic atomic layer etching of copper is analyzed: an oxygen plasma modulates the depth and directionality of the oxidized layer, while formic acid vapor selectively removes the copper oxide over the metallic copper. Via density functional theory, with finite temperature and pressure free energy corrections, the feasibility of the formation of gas-phase Cu^{2+} and Cu^{1+} complexes with formate, water, formic acid, and combinations thereof as ligands, was analyzed. These complexes result from the neutralization reaction between copper oxide (CuO and Cu_2O) and formic acid, with and without water. The formation free energies of formato, formic acid, aquahydroxo, and aquaformato complexes of Cu^{2+} and Cu^{1+} was identified. Under relevant experimental pressures, the water-free dimeric tetra(μ-formato)dicopper^{2+} "paddlewheel" complex ($Cu_2(HCOO)_4$) was found to be the most favorable etching product, with its formation reaching equilibrium conditions from CuO. The most likely precursor for the dimer is the diformatodi(formic acid)copper^{2+} monomer, which favorably dimerizes under the same water-lean condition at which the dimer persists. Stabilization of gas-phase Cu oxide derivatives thus can be achieved through complexation, enabling gas-phase etching of Cu. This work provides complementary experimental and theoretical studies that illuminate the nature of highly controlled etching with formic acid of nanoscopic CuO layers covering Cu nanoarchitectures, which is relevant for the fabrication of next-generation integrated circuits.

4.1 Developing Plasma-Thermal ALE Chemistry of Cu

To determine the etch selectivity of Cu compared to CuO_x via reaction with formic acid, solution-phase etching was first performed. Figure 4.1 shows the film thickness change as a function of time for Cu and CuO_x (CuO_x sample thickness is 110 nm due to expansion from thermal oxidation); it is evident that the etch rate is significantly higher for the oxide as compared to the metal. Figure 4.1 shows the evolution of residual CuO_x as a function of etching time. Due to the inhomogeneity of the solution phase etch at very short times, an accurate etch rate was difficult to determine from the slope of the curve. However, a conservative etch rate can be estimated at the longest etch time (10 s) to be ~520 nm/min. In comparison to the etch rate of Cu (1.7 nm/min), the selectivity would be >300 (calculated from the ratio of the etch rates). Although the selectivity is large for etching CuO_x over Cu in HCOOH solution, the use of a solution process is not desired due to the isotropic nature of the etching process that can undercut the features under a mask. It is also difficult to completely remove the remaining chemical, due to the surface tension effect, from the nanoscale-patterned surface features.

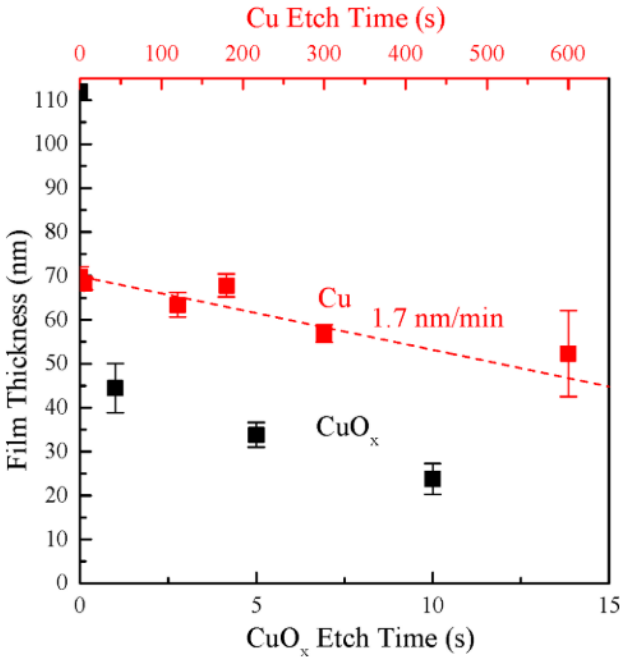

Figure 4.1 Remaining film thickness as a function of etching time for copper and copper oxide in formic acid solution at 80 °C.

Having established the selectivity of etching copper oxide versus copper metal to be >300 in the HCOOH solution, the corresponding selectivity in HCOOH vapor was determined. Figure 4.2 shows high-resolution XPS spectra over the Cu 2p region for the (a) as-deposited Cu as well as (b) a sample treated with 250 Torr HCOOH (with N_2 as carrier gas) for 20 min at 80 °C. XPS was performed ex situ, but air exposure was minimized between HCOOH exposure and characterization. As can be seen in the XPS spectra, the reduction of Cu $2p_{3/2}$ peaks associated with $Cu(OH)_2$ (934.5 eV) and CuO (933.5 eV) as well as Cu $2p_{3/2}$ satellite (sat.) features (944.5 eV) was consistent with the removal of CuO. Cu_2O and Cu could not be resolved at the resolution of the spectrometer (difference ~0.1 eV), where Cu_2O has been observed to form first upon native oxide formation (Chu 1999).

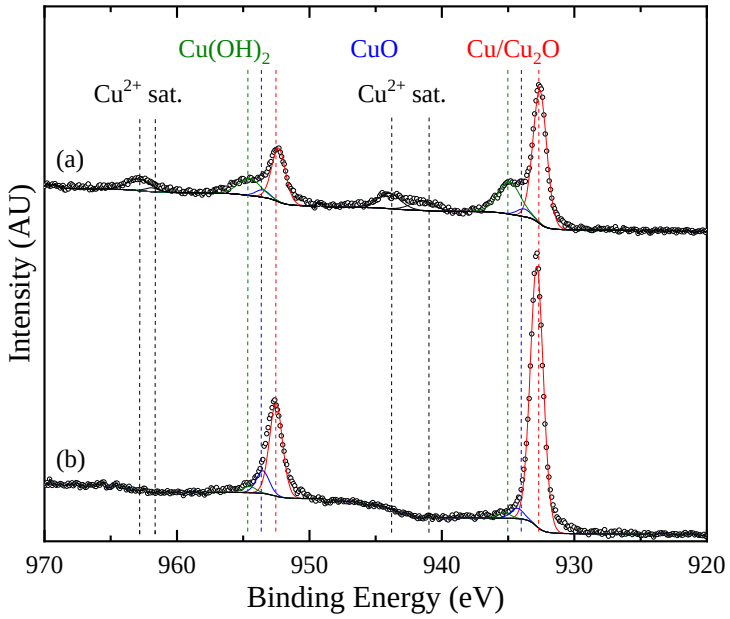

Figure 4.2 XPS Cu 2p spectra from a 25 nm Cu film in the (a) as-deposited state and (b) post-HCOOH-vapor-exposure (20 min, 250 Torr, 80 °C).

To better distinguish different Cu species, the Cu LMM Auger line also was examined; the transition from Cu to Cu^{2+} was clearly observed in Figure 4.3, where the surface changed from Cu-dominant on the as-received condition (orange line), to CuO dominant after oxidation (pink line), to $Cu(OH)_2$ dominant after oxidation and etch (green line). The identification of different Cu oxidation states was further confirmed by plotting the kinetic energy of the Auger peaks verse the binding energy of the core level peaks (so-called Wagner plot), as shown in Figure 4.4. Wagner noted that the combined use of both photoelectron and X-ray excited Auger lines increases the utility of XPS, for identifying chemical states (Moretti 1998). The positions of the most intense Auger line and the most intense binding energy value, recorded on a two-dimensional plot of compounds of each element, form the basis for a new approach to chemical state identification (Moretti 1998). In this work, relative shift from the reported values is used as a qualitative tool for examining the chemical state determination. Stars stand for values recorded in this work and are

compared against reported values in grey in the background. The colors of the stars match the Auger peak assignment in Figure 4.3. It is observed that Cu and $Cu(OH)_2$ deviate less than 0.3 eV from the reported literature values, a decent match considering the systematic and random error associated with the measurement process. Cu_2O and CuO, on the other hand, see slightly higher amounts of deviation, as high as close to 1 eV. This deviation is expected given the difficulty of Cu-oxide deconvolution. Overall, the chemical states match reasonably well with the documented values and are considered valid.

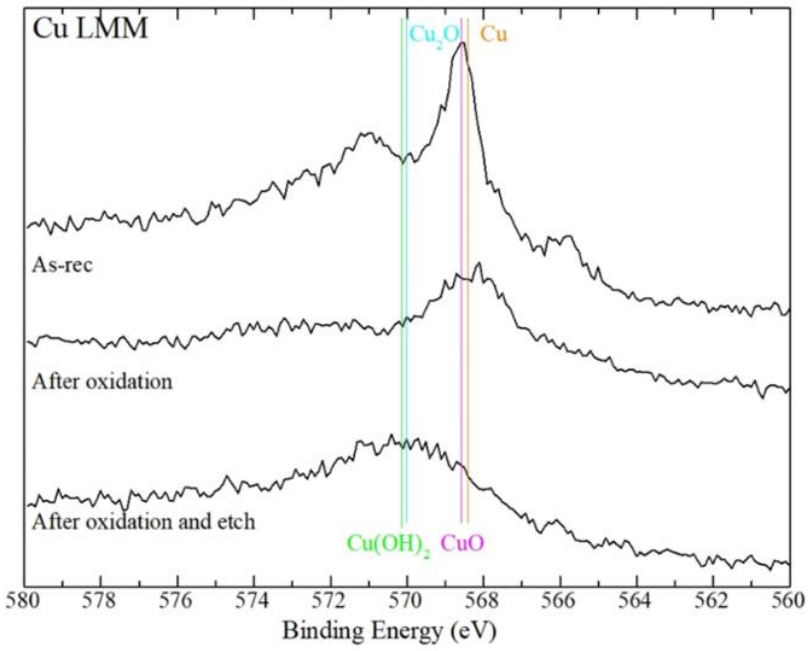

Figure 4.3 Cu LMM Auger line XPS detail scan for Cu blanket thin film as received, after 2 min plasma oxidation, and after 2 min plasma oxidation and 5 min 250 Torr formic acid vapor exposure at 80°C.

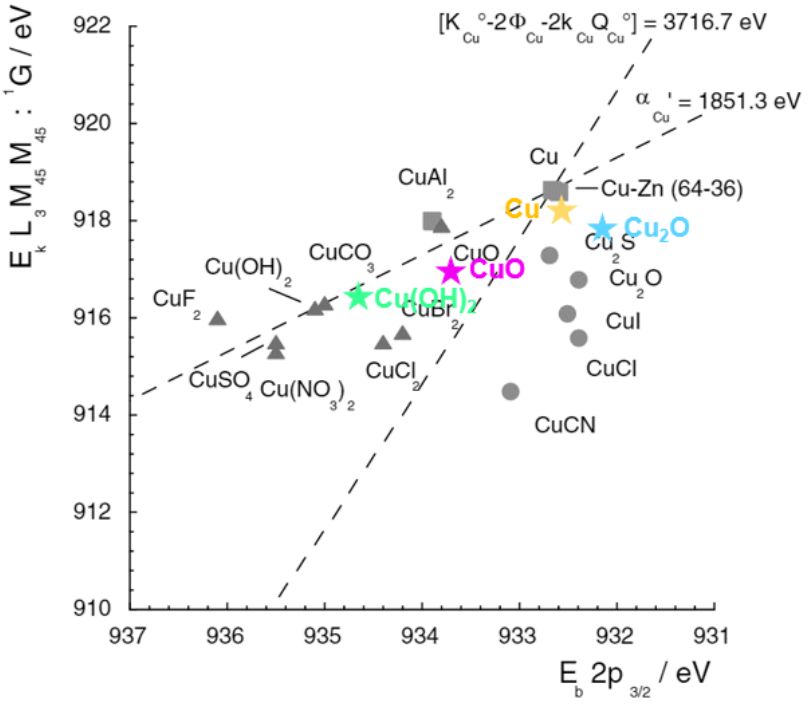

Figure 4.4 Wagner plot for Cu, the data from this work are shown with stars. The rest of the data are from (Moretti 1998).

To leverage the etch selectivity of Cu via CuO_x with HCOOH vapor, an ALE approach was developed, consisting of plasma oxidation followed by self-limiting removal of the oxide layer by HCOOH vapor. Therefore, controlled etch and subsequent Cu removal can be finely controlled by the oxidation step in which O_2 plasma as an oxidant modulates the etch anisotropy though substrate biasing. The process approaches self-limiting behavior for both half-steps when the oxidation conditions produce a diffusion-limited oxide layer. A cyclic etch process consisting of an O_2 plasma oxidation step (500 W rf power, 0 W bias, 2 min) and a formic acid vapor step (250 Torr HCOOH (with N_2) at 80 °C, 5 min) was performed for several cycles on a 25 nm Cu film. An etch rate of 2.4 nm/cycle was observed at the conditions tested [Figure 4.5 (a)]. Figure 4.5 (b)

shows the high-resolution XPS spectra of the Cu 2p region for the as-deposited film and after 4 and 8 cycles of ALE, where the Cu was nearly completely removed.

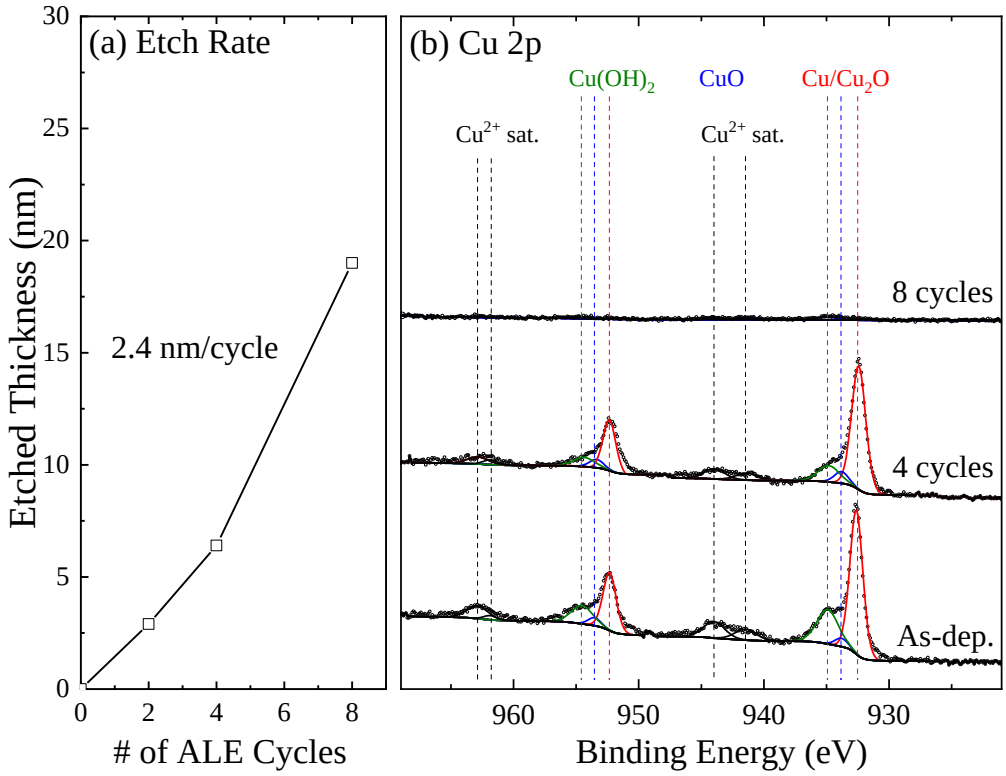

Figure 4.5 (a) Thickness change of 25 nm Cu by cycles of O_2 plasma and formic acid vapor, as determined via cross-section SEM with 2 min oxidation (500 W, 0 W bias, 35 mTorr) and 5 min HCOOH vapor exposure (250 Torr (formic acid with N2), 80 °C). (b) Corresponding high resolution XPS spectra of the Cu 2p spectra, confirming the removal of copper.

The process described above was then applied to patterned Cu samples to assess profile control. The patterned sample was first treated with a 2 min oxidation for cleaning mask opening residue at 800 W rf and 70 W applied bias. During this pretreatment process, around 55 nm of the hard mask was removed, but the Cu layer was not etched. Figure 4.6 shows the comparison between the as-patterned Cu thin film before and after 5 cycles consisting of an oxidation step (500 W rf power and 0 W applied bias for 2 min) and a HCOOH (with N_2) exposure (250 Torr, 80 °C

for 5 min). The cross-sectional SEM images [Figure 4.6 (a)(b)] show that Cu in the exposed region was completely removed, with limited change in the hard mask thickness during the cyclic process utilizing oxygen plasma at lower power and bias. Top-down SEM images [Figure 4.6 (c)(d)] were taken from regions in close proximity before and after the process to compare the profile; the brighter regions in the pretreatment sample image correspond to the exposed Cu while the darker regions are those blocked by the SiCN hard mask. EDS line scans [Figure 4.6 (e)(f)], along highlighted arrows in Figure 4.6 (c)(d), chemically confirmed the removal of Cu from the sample surface. The Cu signal intensity, denoted by the black curve, decreased drastically from the masked to the exposed region on the treated sample, as compared to the uniform intensity observed for the as-deposited sample. Partial removal of the SiCN hard mask was noted from the SEM images before and after etching, which is not a concern for verifying the validity of the etching chemistry since the line width remains constant and the underlying Cu was protected from oxidation and etching.

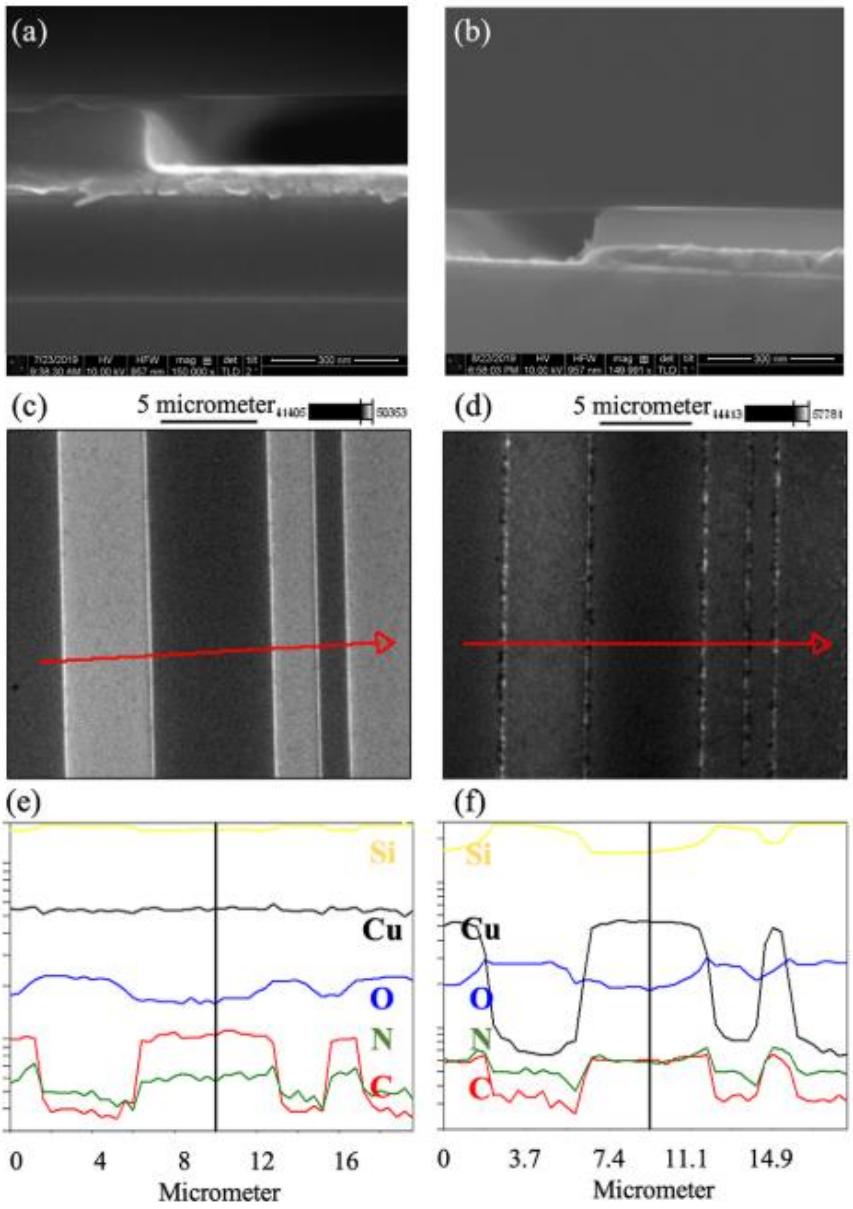

Figure 4.6 Characterization of the cyclic etch process (described in the main text) on patterned Cu. SEM cross-sectional image of (a) as-deposited patterned Cu and (b) processed patterned Cu. Top-down SEM of (c) as-deposited patterned Cu and (d) processed patterned Cu, with EDS line scan routes indicated by the arrows. EDS line scans along the arrows of the (e) as-deposited patterned Cu and (f) processed patterned Cu.

While the effectiveness is confirmed by both XPS and SEM, the experimental characterizations of the samples before and after processing, and the comparison between them, reflect only the macroscopic average of the surface reactions. DFT-based simulation was once again used to give insight on the microscopic reaction mechanisms.

4.2 Density Functional Based Reaction Simulation

The relatively large volume of the chamber compared to the miniscule amounts of etched material made direct characterization of the etching products difficult. HCOOH vapor clearly directly interacts with the oxide layer, CuO, and $Cu(OH)_2$; however, the reaction product and its fate in the chamber is unknown. As in the solution-phase etching, the CuO (and $Cu(OH)_2$) is expected to react with HCOOH via an acid−base (neutralization) reaction, followed by complexation with either water and hydroxide, unreacted HCOOH and its conjugate base formate ($HCOO^-$), or some combination. Thermodynamics indicate that HCOOH also may act as a reducing agent, enabling the formation of Cu_2O from CuO. The Cu LMM Auger line XPS spectra in Figure 4.3 show no Cu_2O after plasma O_2 oxidation, but it suggests its emergence after etching (it is also possible that the vacuum break prior to the XPS measurement post etching may have introduced the Cu^{1+} species along with the hydration of residual CuO to $Cu(OH)_2$). Below, the complexation and etching of Cu^{2+} from CuO and $Cu(OH)_2$ were presented. This is followed by an exploration of the possible participation of Cu^{1+} species, from Cu_2O, in the formation of volatile Cu species. Lastly, the thermodynamics of the formation of gaseous neutral Cu^{2+} and Cu^{1+} molecular complexes under likely experimental conditions were assessed.

4.2.1 Etching through Neutralization and Complexation of $Cu^{2+}OH_x$

To explore the gas-phase complexes of Cu^{2+} with water/hydroxide, formic acid, and $HCOO^-$, various Cu^{2+} complexes were investigated by means of DFT approximations. Figure 4.7 summarizes the optimized structures of the various complexes that may form, which include both Cu^{2+} monomer and dimer complexes.

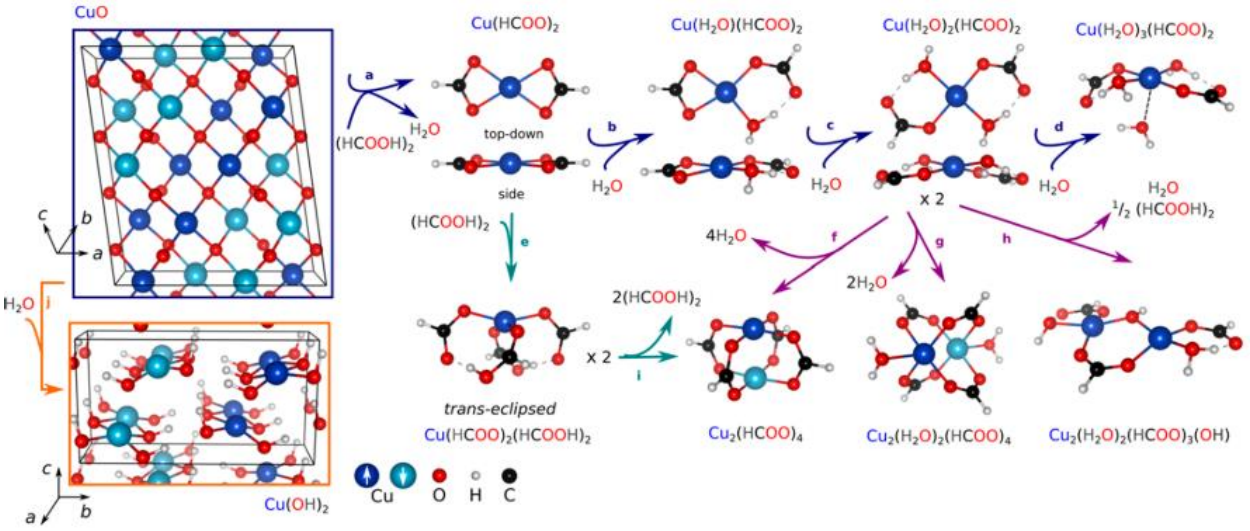

Figure 4.7 DFT-predicted candidate gas-phase products from etching crystalline CuO and $Cu(OH)_2$ in the presence of formic acid and water vapor. Reactions are indexed from a to i. The product molecules are formato (product of reaction a) and aquaformato (b−d), and diformatodi(formic acid) (e) complexes of Cu^{2+}. Dinuclear formato (f) and aquaformato (g and h) complexes are products of the dimerization of $Cu(H_2O)_2(HCOO)_2$ releasing water (f and g) or both water and formic acid (h). An alternative path for dimerization is through the diformatodi(formic acid) complex (i). Hydration of CuO to $Cu(OH)_2$ (j). Two different colors of Cu denote distinct electron spins and illustrate the AFM ordering in both CuO and $Cu(OH)_2$.

Note that only neutral complexes were studied, because unlike in aqueous phase generation of gaseous charged species off of the $CuO/Cu(OH)_2$ surface is not stabilized by a polarizable medium, e.g., bulk water, and therefore will be extremely unfavorable. Starting from the monoclinic AFM CuO, Figure 4.7 shows in sequence the formation of complexes, growing from

two coordinating ligands to five (blue paths, a−d), and from monomer to dimer (violet paths, f−h). Also in the figure is the reaction connecting CuO and $Cu(OH)_2$ (orange path, j). The AFM structures of CuO and $Cu(OH)_2$ are shown through two different, blue-colored Cu ions, one for excess electron spin-up and another for excess electron spin-down. For CuO, FM interactions persist along the [010] and [101] directions, with alternating AFM and FM interactions along the $[10\bar{1}]$, as demonstrated in the literature (Yang 1988, Jin 2012). For $Cu(OH)_2$, FM interactions exist along [001] and [100], with alternating AFM and FM interactions along [010].

Although the complexation reactions are presented in sequence, they need not proceed in this manner. In this study, only the thermodynamics was assessed for the formation of these complexes, with $CuO/Cu(OH)_2$, water vapor, and formic acid as reactants (as a dimer $(HCOOH)_2$, which is the majority form of HCOOH in the gas phase (Chadwick 1988), Figure B.5). Although kinetics may play a role in the feasibility of forming these chemical species, thermodynamics of course is needed to set the stage in determining possible chemical pathways. Table 4.1 lists the standard reaction free energies at three different temperatures, namely, room, experimental (T = 353 K (80 °C)), and "extreme" (T = 403 K; 29° above the boiling point of HCOOH), along with the chemical equations representing the reactions in Figure 4.7. Three temperatures were given to illuminate the dependence of the spontaneity of these reactions with temperature. From these standard reaction free energies, the nonstandard reaction free energies under a (likely) range of experimental reactant and product partial pressures (vide infra) can be extrapolated.

Table 4.1 Standard Reaction Free Energies (eV/Cu at Standard 750 Torr Pressure) for the Formation of Cu^{2+} and Cu^{1+} formato, formic acid, and aquaformato complexes and bulk phase reactions involving $Cu(OH)_2$, CuO and Cu_2O as depicted in Figure 4.7 and Figure 4.8.

Reaction index	Reaction equation	298 K	353 K	403 K
a	$CuO + (HCOOH)_2 \rightarrow Cu(HCOO)_2 + H_2O$	0.95	0.85	0.77
b	$Cu(HCOO)_2 + H_2O \rightarrow Cu(H_2O)(HCOO)_2$	-0.27	-0.19	-0.12
c	$Cu(H_2O)(HCOO)_2 + H_2O \rightarrow Cu(H_2O)_2(HCOO)_2$	-0.20	-0.11	-0.03
d	$Cu(H_2O)_2(HCOO)_2 + H_2O \rightarrow Cu(H_2O)_3(HCOO)_2$	0.13	0.19	0.25
e	$Cu(HCOO)_2 + (HCOOH)_2 \rightarrow Cu(HCOOH)_2(HCOO)_2$	-0.33	-0.26	-0.20
f	$Cu(H_2O)_2(HCOO)_2 \rightarrow ½\ Cu_2(HCOO)_4 + 2H_2O$	0.00	-0.11	-0.21
g	$Cu(H_2O)_2(HCOO)_2 \rightarrow ½\ Cu_2(H_2O)_2(HCOO)_4 + H_2O$	-0.06	-0.10	-0.14
h	$Cu(H_2O)_2(HCOO)_2 \rightarrow ½\ Cu_2(H_2O)_2(HCOO)_3(OH) + ½H_2O + ¼(HCOOH)_2$	-0.04	-0.06	-0.08
i	$Cu(HCOOH)_2(HCOO)_2 \rightarrow ½\ Cu_2(HCOO)_4 + (HCOOH)_2$	-0.14	-0.15	-0.16
j	$CuO + H_2O \rightarrow Cu(OH)_2$	0.08[b]	0.17	0.25
M_1 = a+b+c	$CuO + (HCOOH)_2 + H_2O \rightarrow Cu(H_2O)_2(HCOO)_2$	0.48	0.55	0.62
M_2 = a+e	$CuO + 2(HCOOH)_2 \rightarrow Cu(HCOOH)_2(HCOO)_2 + H_2O$	0.62	0.60	0.57
D_1 = M1+f	$CuO + (HCOOH)_2 \rightarrow ½Cu_2(HCOO)_4 + H_2O$	0.48	0.44	0.41
D_2 = M1+g	$CuO + (HCOOH)_2 \rightarrow ½Cu_2(H_2O)_2(HCOO)_4$	0.41	0.45	0.48
D_3 = M1+h	$CuO + ¾(HCOOH)_2 + ½H_2O \rightarrow ½Cu_2(H_2O)_2(HCOO)_3(OH)$	0.44	0.49	0.54
	$CuO + ¼(HCOOH)_2 \rightarrow ½Cu_2O + ½CO_2 + ½H_2O$	-0.71[c]	-0.75	-0.78
	$½Cu_2O + ¼O_2 \rightarrow CuO$	-0.75[c]	-0.75[d]	-0.76[d]
a’	$½Cu_2O + ½(HCOOH)_2 + ½H_2O \rightarrow Cu(H_2O)(HCOO)$	1.34	1.32	1.29
b’	$Cu(H_2O)(HCOO) + H_2O \rightarrow Cu(H_2O)_2(HCOO)$	-0.50	-0.41	-0.33
c’	$½Cu_2O + (HCOOH)_2 \rightarrow Cu(HCOO)(HCOOH) + ½H_2O$	0.84	0.79	0.75
d’	$Cu(H_2O)(HCOO) \rightarrow ½Cu_2(HCOO)_2 + H_2O$	-0.84	-0.85	-0.86
e’	$½Cu_2(HCOO)_2 + H_2O \rightarrow ½Cu_2(H_2O)_2(HCOO)_2$	0.10	0.16	0.22
f’	$Cu(HCOO)(HCOOH) \rightarrow ½Cu_2(HCOO)_2 + ½(HCOOH)_2$	-0.33	-0.33	-0.33
g’	$½Cu_2(HCOO)_2 + ½(HCOOH)_2 \rightarrow ½Cu(HCOO)_2(HCOOH)_2$	0.03	0.06	0.09
M_1’ = a’+b’	$½Cu_2O + ½(HCOOH)_2 + {}^3/_2H_2O \rightarrow Cu(H_2O)_2(HCOO)$	0.84	0.90	0.96
M_2’ = c’	$½Cu_2O + (HCOOH)_2 \rightarrow Cu(HCOO)(HCOOH) + ½H_2O$	0.84	0.79	0.75
D_1’ = a’+d’	$½Cu_2O + ½(HCOOH)_2 \rightarrow ½Cu_2(HCOO)_2 + ½H_2O$	0.51	0.46	0.43
D_2’ = D_1’+e’	$½Cu_2O + ½(HCOOH)_2 + ½H_2O \rightarrow ½Cu_2(H_2O)_2(HCOO)_2$	0.61	0.63	0.65
	$½Cu_2O + (HCOOH)_2 \rightarrow ½Cu(HCOO)_2(HCOOH)_2 + ½H_2O$	0.54	0.53	0.52

Reaction a in Figure 4.7 describes the formation of the $Cu(\kappa^2\text{-}HCOO)_2$ from $(HCOOH)_2$ reacting with a unit of CuO, releasing water. $HCOO^-$ is a bidentate ligand, κ^2, which means it has two noncontiguous coordinating atoms: the two O atoms. The two protons from $(HCOOH)_2$ form a water molecule with an O in the CuO lattice (acid−base or neutralization reaction), while the resulting two $HCOO^-$ ions coordinate with a Cu^{2+} ion (complexation). This reaction is highly unfavorable with a standard free energy of reaction of $\Delta G° \sim 1eV$. $Cu(\kappa^2\text{-}HCOO)_2$ exhibits a square planar structure, as in the bulk CuO. However, the molecule may be in a nonideal, constrained configuration. Cu^{2+} is a d^9 transition metal cation (one unpaired electron) that forms tetrahedral, square planar, or some intermediate coordination, the preference of which depends on the ligand and even the counterion (Miessler 2008).

Cu^{2+} can only accommodate two formate ions to maintain a neutral complex, thus, to build larger neutral mononuclear complexes, only a neutral ligand, such as H_2O, can be added. Reactions b and c progressively relieve the strain in the complex by adding H_2O as ligand, converting an $HCOO^-$ from being a bidentate (κ^2) to a monodentate (κ^1) ligand for every H_2O added: $Cu(H_2O)(\kappa^1\text{-}HCOO)(\kappa^2\text{-}HCOO)$ or simply $Cu(H_2O)(HCOO)_2$, and $Cu(H_2O)_2(\kappa^1\text{-}HCOO)_2$ or simply $Cu(H2O)_2(HCOO)_2$. Furthermore, the uncoordinated O atom of the $\kappa^1\text{-}HCOO^-$ ligand forms a hydrogen bond with the coordinated H_2O. The addition of two H_2O molecules is favorable under standard conditions, despite it being entropically unfavorable (note that the reaction becomes less spontaneous as the temperature increases). This attests to the structural (and perhaps to some degree electrostatic) nature of the significant stabilizing effect of H_2O. Indeed, in reaction d, where a third H_2O is added simply as an axial ligand, the process becomes unfavorable. This is because the third H_2O, in contrast to the first two H_2O, does not reduce the strain in the coordination of the

equatorial ligands and because Cu^{2+} favorably accommodates only up to four ligands (the antibonding d_z^2-derived orbital of a square-planar-coordinated Cu^{2+} is fully occupied).

Higher-energy alternative structures for $Cu(HCOO)_2$, $Cu(H_2O)(HCOO)_2$,and $Cu(H_2O)_2(HCOO)_2$ complexes are shown in Figure B.6. In the alternative $Cu(HCOO)_2$, the two $HCOO^-$ ions are bound via a κ^1 motif, leaving Cu^{2+} with only two bonds. The higher-energy $Cu(H_2O)(HCOO)_2$ and $Cu(H_2O)_2(HCOO)_2$ in Figure B.6, however, maintain the κ^2 bonding motif for $HCOO^-$ ions, with H_2O as axial ligand(s) of Cu^{2+}. These structures thus retain the strained square planar geometry exhibited by $Cu(\kappa^2\text{-}HCOO)_2$, while also expanding the coordination number of Cu^{2+} beyond four, which is unfavorable.

In the absence of water, formic acid can take the place of water as a neutral ligand, with the carbonyl oxygen as the coordinating atom. Reaction e (first blue-green path) shows the formation of trans-$Cu(\kappa^1\text{-}HCOO)_2(HCOOH)_2$ in an eclipsed configuration, or simply $Cu(HCOO)_2(HCOOH)_2$, from $Cu(HCOO)_2$. The trans prefix refers to the relative position of the two HCOOH, where they are opposite to each other, where the same is true for the two $HCOO^-$. In the complex, $HCOO^-$ is hydrogen bonded to a neighbor HCOOH. Since the HCOOH−OOCH hydrogen-bonded pairs are on the same side of the (distorted) CuO_4 plane, this configuration is referred as eclipsed. Two of its higher-energy isomers, the trans-staggered conformer (the HCOOH−OOCH hydrogen-bonded pairs are on the opposite sides of the CuO_4 plane) and a cis isomer, are presented in Figure B.6. Under standard conditions, the addition of two neutral HCOOH onto $Cu(HCOO)_2$, much like the addition of two water molecules, is favorable (Table 4.1, reaction e). The standard free energy of this addition reaction is −0.33 eV at 298 K, just 0.14

eV less negative than that of the addition of two waters, which is −0.47 eV at 298 K (Table 4.1, reactions b and c).

The possibility of forming gaseous aquahydroxo complexes from $Cu(OH)_2$ (Figure B.7) was examined, to rule out the need for $HCOO^-$ to directly participate in the complexation of Cu^{2+}. Indeed, the formation of the aquahydroxo complexes is much more difficult, with standard free energies of formation relative to $Cu(OH)_2$ and $H_2O(g)$ > 1.6 eV/complex at 298 K, which highlights the critical role of $HCOO^-$ in the removal of Cu^{2+}. This finding is consistent with the very low solubility of $Cu(OH)_2$ in pure water ($Ksp = 2.2 \times 10^{-20}$) (Miessler 2008).

Dimerization of the complex can satisfy the coordination sphere of Cu^{2+}, while using less molecules as ligands and also relieving bonding strain. This would enable the reduction of the entropic penalty of producing the complex by using less gaseous reactants per Cu^{2+} ion etched. The bidenticity of the $HCOO^-$ ion make dimerization possible by acting as a bridging ligand (μ). The purple paths (f–h) in Figure 4.7 describe formation of the candidate dimers from the most stable (under standard pressure and temperature) monomer: $Cu(H_2O)_2(\kappa^1\text{-}HCOO)_2$. Reaction f is the formation of the paddlewheel complex $Cu_2(\mu\text{-}HCOO)_4$ or tetra(μ-formato)dicopper^{2+}, which sheds all four H_2O molecules from the two $Cu(H_2O)_2(\kappa^1\text{-}HCOO)_2$ molecules. The four $HCOO^-$ bridge the two Cu^{2+} ions with the two $Cu(O)_4$ planes on top of each other, forming a paddlewheel-like structure, hence the name. Reaction g is a similar reaction but expels one less H_2O molecule per Cu^{2+}, forming a fully hydrated paddlewheel complex: $Cu_2(H_2O)_2(\mu\text{-}HCOO)_4$, with two H_2O as axial ligands. The formations of these complexes are mildly favorable (−0.11 and −0.10 eV/Cu) relative to $Cu(H_2O)_2(\kappa^1\text{-}HCOO)_2$ at 353 K, which become more favorable at higher temperatures, e.g., −0.21 and −0.14 eV/ Cu at 403 K, because these reactions result in a net positive formation

of gaseous molecules (Table 4.1, reactions f and g). An alternative monomer that may serve as a precursor to $Cu_2(\mu\text{-}HCOO)_4$ in the absence of water is $Cu(HCOO)_2(HCOOH)_2$. Dimerization is achieved by shedding two $(HCOOH)_2$ molecules per $Cu_2(\mu\text{-}HCOO)_4$ (Figure 4.7, reaction i, second blue-green path). Similar to the aqua analogue, this dimerization reaction is exoergic (−0.15 eV/Cu at 353 K). Paddlewheel transition-metal complexes are well documented in the literature (Patmore 2010), with Cu^{2+}-based complexes containing large organic carboxylates achieving prominence because of its central chemical motif in many metal organic frameworks (MOFs) (Chui 1999, Rungtaweevoranit 2017). Earlier documentation of Cu^{2+} paddlewheel complexes involved small organic carboxylates, such as crystalline hydrated tetraacetatodicopper^{2+}, $Cu_2(H_2O)_2(\mu\text{-}CH3COO)_4$ (Van Niekerk 1953), and anhydrous tetrapropionatodicopper^{2+}, $Cu_2(\mu\text{-}C_2H_5COO)_4$, dissolved in chloroform (Graddon 1959). Recently, infrared multiphoton dissociation has been shown to decompose anionic Cu^{2+} formate clusters of the formula $Cu_n(HCOO)_{2n+1}^-$ ($2 < n \leq 8$, generated via electrospray ionization or ESI), proceeding via favorable sequential loss (evaporation) of neutral dimeric $Cu_2(HCOO)_4$ until n = 3, at which point $Cu(HCOO)_2$ is released (Pascher 2019). The aforementioned observation was supported by the authors' DFT-B3LYP/def2TZVP simulations (Pascher 2019).

For reaction h,$Cu_2(H2O)_2(HCOO)_3(OH)$ or $Cu_2(H2O)_2\text{-}(\mu\text{-}HCOO)(\kappa^1\text{-}HCOO)_2(\mu\text{-}OH)$ forms where both an $HCOO^-$ and an OH^- act as bridging ligands. It consists of two complexes side-by-side, instead of being on top of each other as in the paddlewheel complexes. This reaction has similar thermodynamics as f and g but exhibits weaker dependence on temperature than f and g, because it results in fewer gaseous products compared to the other two reactions.

4.2.2 Etching after Pre-Reduction of CuO into Cu_2O

So far, HCOOH chemistry has been considered as an acid and complexing agent. In this section the possibility of HCOOH acting as a reductant was explored. Reduction of CuO to Cu_2O with HCOOH as a reducing agent is thermodynamically feasible. In this reaction, HCOOH oxidizes into CO_2, while two Cu^{2+} ions reduce to Cu^{1+} as the two H atoms from the decomposition of HCOOH remove an O atom from the lattice to form H_2O. The empirical standard reaction free energy at 298 K for this rection is −0.81 eV/CuO, while the predicted value is −0.71 eV/CuO, an approximately 0.1 eV error. At the experimental etching temperature (353 K) and $(HCOOH)_2$ pressure (approximately within 125−250 Torr, see below for the rationale of the estimates), the reaction is predicted to remain spontaneous (Figure 4.8 (a), blue lines). The CO_2 and H_2O partial pressures were set to be at 0.08 Torr, or 1/10 of the vacuum base pressure.

\

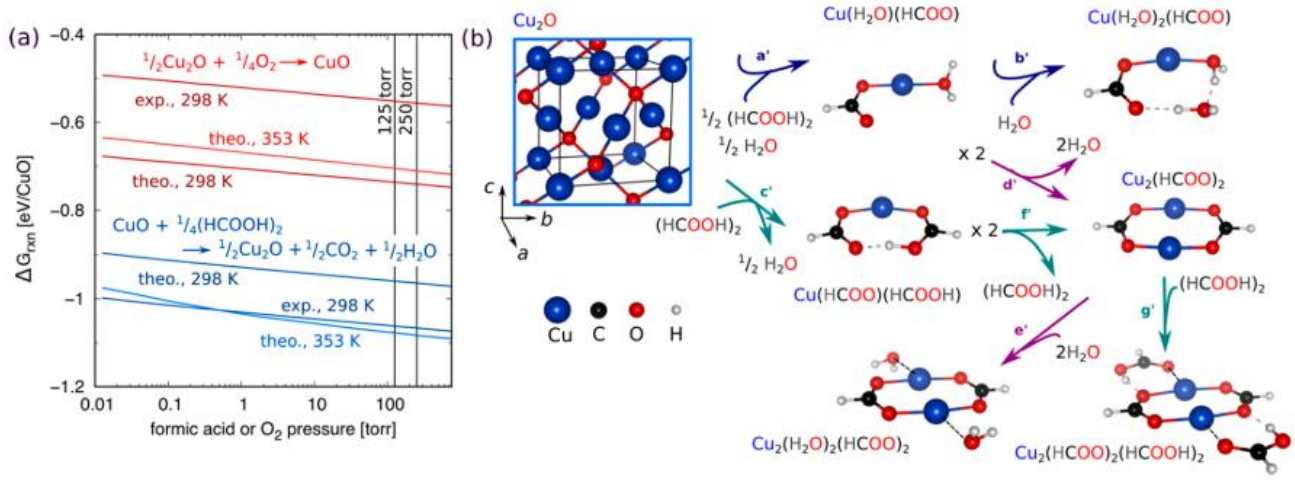

Figure 4.8 (a) Free energy of CuO reduction to Cu_2O, with $(HCOOH)_2$ as the reductant, and Cu_2O oxidation to CuO, with O_2 as the oxidant, as functions of the partial pressures of the reductant and oxidant molecules. Upper and lower bound total pressures of all HCOOH species ($(HCOOH)_n$): 250 and 125 Torr are marked, representing 100 and 50% $(HCOOH)_n$ in the $(HCOOH)_n+N_2$ gas stream at the total exposure pressure of 250 Torr, respectively. CO_2 and H_2O partial pressures are set to 0.08 Torr (1/10 of the vacuum base pressure). (b) DFT-predicted candidate gas-phase products from etching crystalline Cu_2O in the presence of formic acid and water vapor. Reactions are indexed from a' to g'. The product molecules are aquaformato (a' and b') and formato (formic acid) (c') complexes of Cu^{1+}. Dinuclear diformato (d') and diaquadiformato (e') complexes are products, for example, of the dimerization of $Cu(H_2O)(HCOO)$. An alternative path for dimerization, relevant at low H_2O and high HCOOH conditions, is through Cu(HCOO)(HCOOH) (f'), which may be followed by coordination of two more HCOOH molecules forming $Cu_2(HCOO)_2(HCOOH)_2$ (g').

In Figure 4.8 (a), the experimental and theoretical data at 298 K are also plotted to provide an estimate to the error of the prediction at 353 K. A competing reaction that will oxidize Cu_2O back to CuO is via reaction with molecular oxygen. The standard oxidation free energy at 298 K has been also measured to be very negative: −0.56 eV/CuO. PBE+U+D3BJ overestimates the exoergicity of this reaction to −0.75 eV/CuO, an approximately −0.2 eV error. At very low O2 partial pressure, e.g., 0.01 Torr, and at 353 K, this reaction remains very thermodynamically

favorable even when accounting for the possible error in the prediction of the oxidation free energy (Figure 4.8 (a), red lines). Cu_2O thus will dominate only when the chamber is completely depleted ofO2. The relative rates of the reductive and oxidative reactions will dictate the relative amounts of Cu^{2+} and Cu^{1+} exposed for etching. From previous thermogravimetry coupled with quadrupole mass spectroscopy experiments, reduction of CuO nanoparticles to Cu_2O with formic acid was found to occur between 220−250 °C (498−523 K), which is then followed by reduction to metallic Cu at T > 350 °C (623 K) (Fujino 2017). Temperature-programmed desorption (TPD) studies also found that the CO_2 desorption peak on Cu_2O film pre-exposed to HCOOH vapor at 300 K appears at around 545 K (Poulston 1998). TPD experiments on copper surfaces, from metallic Cu to CuO, showed positive correlation between the HCOOH decomposition TPD peak temperature and degree of oxidation of the surface (Poulston 1998). Lower temperature reduction of CuO and Cu_2O with HCOOH only occurs in the presence of a catalyst, e.g., Pt, which can facilitate the formation of H radicals from HCOOH at a lower temperature (Fujino 2017, Chou 2018). Reduction of CuO (and Cu_2O) with HCOOH thus is kinetically suppressed.

A possible combination of Cu^{2+} and Cu^{1+} is suggested in the Cu LMM Auger line XPS spectra post-etching. Below, the extent of participation of Cu^{1+} in the etching process was computationally analyzed and it is shown that Cu^{1+} is harder to remove than Cu^{2+}. At the O_2 plasma step, both the residual Cu^{1+} and re-exposed Cu were oxidized to Cu^{2+}, which facilitate the removal of Cu.

A similar analysis on the possible etching products of Cu_2O with the formate ion and neutral molecules was performed, namely, water and formic acid as shown in Figure 4.8 (b). Cu^{1+} is a closed-shell d^{10} transition-metal ion and forms a linear coordination with two lattice O in the

cubic Cu_2O crystal (Kirfel 1990). Much like in the solid, Cu^{1+} complexes were also found to prefer two-fold coordination, e.g., aquaformato Cu^{1+} complex, $Cu(H_2O)(\kappa^1\text{-}HCOO)$ or simply $Cu(H_2O)(HCOO)$ (Figure 4.8 (b), reaction a'). The linear coordination in $Cu(H_2O)(HCOO)$ is found to be favored over a bent structure, although only by 0.08 eV at 298 K (Figure B.8 and Table B.5). $Cu(H_2O)(HCOO)$ was found to be unable to accommodate a second H_2O molecule as a third ligand and simply binds the second H_2O molecule via hydrogen bonding with the coordinated H_2O and $HCOO^-$ (reaction b'). The intramolecular hydrogen bonding in $Cu(H_2O)_2(HCOO)$ renders the second H_2O to be bound favorably (Table 4.1, reaction b'). Another monomer, the formato (formic acid) Cu^{1+} complex, $Cu(\kappa^1\text{-}HCOO)(\kappa^1\text{-}HCOOH)$ or $Cu(HCOO)(HCOOH)$, exhibits interligand hydrogen bonding (reaction c'), which slightly bends the molecule. When this interligand hydrogen bonding breaks, as in a staggered ligand conformation, which recovers a perfectly linear configuration (Figure B.8 and Table B.5), its energy increases by 0.60 eV at 298 K. Finally, the dimerization of Cu^{1+} was explored. Much like in Cu^{2+}, the dimeric Cu^{1+} formato complex, $Cu_2(\mu HCOO)_2$, may form by dehydration of the monomeric aquaformato complexes ($Cu(H_2O)(HCOO)$ or $Cu(H_2O)_2(HCOO)$). Reaction d' in Figure 4.8 (b) shows the dimerization from $Cu(H_2O)(HCOO)$ (−0.85 eV/Cu at 353 K, Table 4.1). A dimer can also form from $Cu(H_2O)(HCOO)$ without losing water to form instead $Cu_2(H_2O)_2(\mu\text{-}HCOO)_2$, corresponding to the sum of reactions d' and e' in Figure 4.8 (b) (−0.68 eV/Cu at 353 K, Table 4.1). Under water-lean conditions, the formation of $Cu_2(\mu\text{-}HCOO)_2$ may be better facilitated by the dimerization of $Cu(HCOO)(HCOOH)$ represented by reaction f' in Figure 4.8 (b), (−0.33 eV/Cu at 353 K, Table 4.1). At HCOOH-rich conditions, additional HCOOH may coordinate with $Cu_2(\mu\text{-}HCOO)_2$ (reaction g', Figure 4.8 (b)) to form $Cu_2(\mu\text{-}HCOO)_2(\kappa^1\text{-}HCOOH)_2$ or simply $Cu_2(HCOO)_2(HCOOH)_2$. Unlike in Cu^{2+}, $Cu_2(HCOO)_2(HCOOH)_2$ is incapable of forming a

paddlewheel structure. This is largely due to the preference of Cu^{1+} to remain in a two-fold coordinated environment. In both $Cu_2(H_2O)_2(HCOO)_2$ and $Cu_2(HCOO)_2(HCOOH)_2$, the third ligand around a Cu ion is bound much weakly and the formation of a fourth dative bond, e.g., in $Cu_2(\mu\text{-}HCOO)_2(\mu\text{-}HCOOH)_2$, is outright unfavorable.

4.2.3 Predicted Thermodynamics under Experimental Conditions

Although the reactions are shown in a particular sequence in Figure 4.7 for Cu^{2+} and Figure 4.8 for Cu^{1+}, the formation of these complexes need not proceed in the same manner presented. Therefore, Table 4.1 also presents the standard reaction free energies to form the most stable monomers $Cu(H_2O)_2(HCOO)_2$ and $Cu(HCOO)_2(HCOOH)_2$ (reactions M_m, m = 1 and 2) and dimers $Cu_2(HCOO)_4$,$Cu_2(H_2O)_2(HCOO)_4$, and $Cu_2(H_2O)_2(HCOO)_3(OH)$ (reactions D_m, m = 1, 2, and 3). Table 4.1 also presents the standard reaction free energies to form the most stable monomers $Cu(H_2O)_2(HCOO)$ and Cu(HCOO)(HCOOH) (reactions M_m', m = 1 and 2) and dimers $Cu(HCOO)_2$,$Cu_2(H_2O)_2(HCOO)_2$, and $Cu_2(HCOO)_2(HCOOH)_2$ (reactions D_m', m = 1, 2, and 3). Henceforth, the free energies of these reactions are referred to as "formation" free energies (in contrast to the regular definition of a formation free energy, which uses the pure standard forms of the constituent elements as references). These standard formation Gibb's free energies then were extrapolated to experimental pressures of the gaseous reactants and products.

To calculate the partial pressure of $(HCOOH)_2$ given the total pressure of all the formic acid species, the calculated dimerization free energy for HCOOH(g) was used. The total chamber pressure is the result of unreacted HCOOH and the carrier gas N_2 (both deemed to be the majority gases), the product Cu complex, and H_2O (initially present or as a product of the neutralization

reaction). 8.0×10^{-2} Torr or 1/10 of the vacuum base pressure (0.8 Torr) was used as the upper bound for the complex (vacuum condition is achieved pre-etching). As for the H_2O vapor pressure, two extreme cases were defined: (1) 356 Torr and (2) 1/100 of the vacuum chamber base pressure, 8.0×10^{-3} Torr. Case (1) occurs when the vacuum condition is broken and never recovered (vacuum is broken between O_2 plasma exposure and HCOOH etching, and the saturation pressure of water at the experimental temperature of 353 K (80 °C) is 356 Torr) (Standards 2018). Case (2) is relevant during etching (performed at 250 Torr) where the vacuum condition is recovered prior (base pressure of 0.8 Torr) and the chamber is subsequently filled with $HCOOH/N_2$ at 250 Torr, displacing more H_2O out of the reaction vessel ("dry" condition). The latter is the more relevant case in the current experiment, whereas the former is shown for comparison as a hypothetical case. It is predicted that due to the difference in water content in the complexes described above, the monomer and dimers may prevail at the higher water vapor pressure conditions. For Cu^{2+}, under water condition (1), $Cu(H_2O)_2(HCOO)_2$ is the most preferred monomer while $Cu_2(\mu\text{-}HCOO)_4$ is favored among the three dimers, and overall. Under water condition (2) or the "dry" condition, the dehydrated $Cu_2(\mu\text{-}HCOO)_4$ dominates, and the monomeric $Cu(HCOO)_2(HCOOH)_2$ is favored over $Cu(H_2O)_2(HCOO)_2$, where the latter is significantly destabilized. For Cu^{1+}, $Cu_2(\mu\text{-}HCOO)_2$ prevails in both water conditions and is more difficult to form than $Cu_2(\mu\text{-}HCOO)_4$ from their respective oxides of the same Cu oxidation state.

Figure 4.9 (a) shows the reaction free energies for reactions M_1, M_2 and D_1–D_3 (Table 4.1) as a function of the total pressure of all the formic acid species ($(HCOOH)_n$), which can be directly measured or estimated from the experiment. Given a total etchant pressure of 250 Torr, an upper bound of 250 Torr and a lower bound 125 Torr were defined for the partial pressure of $(HCOOH)_n$. These pressures are marked in the plots in Figure 4.9.

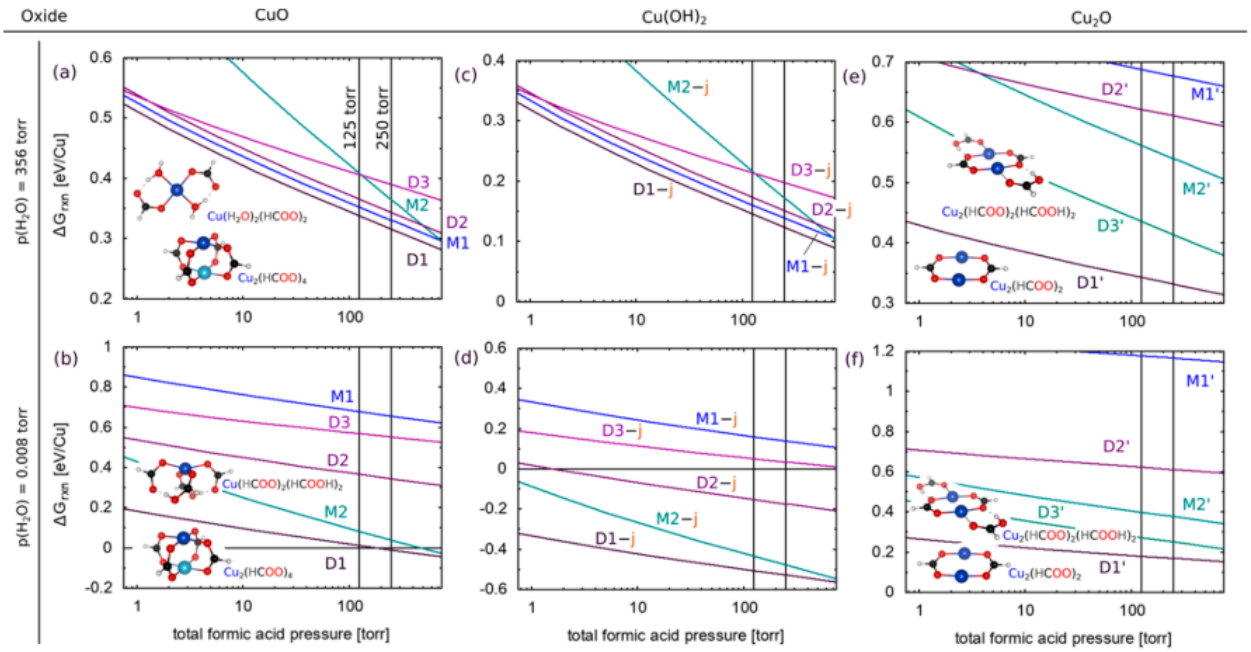

Figure 4.9 (a), (b) and (c), (d) Reaction free energy (eV/Cu) to form the most stable Cu^{2+} monomers: $Cu(H2O)_2(HCOO)_2$ and $Cu(HCOO)_2(HCOOH)_2$ (reactions M_1 and M_2), and dimers $Cu_2(HCOO)_4$,$Cu_2(H_2O)_2(HCOO)_4$, and $Cu_2(H_2O)_2(HCOO)_3(OH)$ (reactions D_m, m =1−3), from CuO and $Cu(OH)_2$, respectively, as a function of the total pressure of formic acid species (logarithmic scale) at 353 K (80°C), at two different ambient water vapor pressures (356 and 8.0 × 10^{-3} Torr). For (c), (d), j is the free energy to form $Cu(OH)_2$ from CuO (Table 4.1). (e), (f) A similar plot for the Cu^{1+} complexes. The most stable molecules are, monomers $Cu(H_2O)(HCOO)$ and $Cu(HCOO)(HCOOH)$ (reactions M_1' and M_2') and dimers $Cu_2(HCOO)_2$, $Cu_2(H_2O)_2(HCOO)_2$, and $Cu(HCOO)_2(HCOOH)_2$ (reactions D_m', m =1−3). In all plots, a low Cu complex pressure of 8.0 × 10^{-2} Torr was assumed (1/10 of the vacuum base pressure). Insets show the two lowest-energy structures for each water vapor pressure condition. Upper and lower bound total pressures of all HCOOH species ($(HCOOH)_n$): 250 and 125 Torr are marked, representing 100 and 50% $(HCOOH)_n$ in the $(HCOOH)_n$+N_2 gas stream at the total exposure pressure of 250 Torr, respectively. The plots were constructed from the standard reaction free energies in Table 4.1. See also Table 4.1 for the definition of the reaction indices.

It becomes apparent from the plots that the monomer $Cu(H_2O)_2(HCOO)_2$ and dimers are most likely to form competitively during etching in the presence of ambient water vapor, albeit with $Cu_2(\mu\text{-}HCOO)_4$ slightly more favored with a slightly positive formation free energy of

0.32−0.34 eV/Cu at relevant $(HCOOH)_n$ pressures. However, under the "dry" condition, only the water-free dimer $Cu_2(\mu\text{-}HCOO)_4$ prevails, with nearly zero formation free energy that is between −0.01 and +0.01 eV/Cu. Thus, recovery of the vacuum prior to etching is imperative to drive the etching to spontaneity because it deprives the chamber of one of the neutralization products: water vapor. The formation of $Cu(H_2O)_2(HCOO)_2$ under this condition is highly unfavorable; however, the thermodynamics of $Cu(HCOO)_2(HCOOH)_2$ formation is enhanced. $Cu(HCOO)_2(HCOOH)_2$ then may act as a more favorable intermediate for the formation of $Cu_2(\mu\text{-}HCOO)_4$.The dimerization, which releases $(HCOOH)_2$, is between −0.07 and −0.05 eV/Cu from 125 to 250 Torr total formic acid at 353 K (these energies are independent of the partial pressure of H_2O). $Cu_2(\mu\text{-}HCOO)_4$ can also form from the reaction of $Cu(HCOO)_2(HCOOH)_2$ with a unit of CuO(s):

$$Cu(HCOO)_2(HCOOH) + CuO(s) \rightarrow Cu_2(HCOO)_4 + H_2O(g) \qquad (4.1)$$

In such a reaction, the two protons from the two HCOOH ligands react with a lattice O to form H_2O, and the resulting four free carboxyl O anions anchor onto and extract a Cu^{2+} ion. This pathway is also spontaneous at 0.008 Torr H_2O, with a reaction free energy of −0.06 eV/dimer or −0.03 eV/Cu at 353 K (independent of the partial pressure of $(HCOOH)_2$) and is thus competitive with the dimerization reaction described above. Note that this step is unfavorable at 356 Torr H2O (+0.27 eV at 353 K). Because the experiment demonstrated the existence of $Cu(OH)_2$, the same plots using $Cu(OH)_2$ instead of CuO as reactant were obtained. This is easily achieved by subtracting the water-vapor-pressure-dependent free energy to form $Cu(OH)_2$ from CuO and H_2O(g) (reaction j in Figure 4.7 and Table 4.1) from the free energies in Figure 4.9 (a), (b). The resulting plots appear in Figure 4.9 (c), (d). Because j has a positive free energy (especially at very low H_2O partial pressures), the formation energies are more negative than in the case of CuO.

Despite the energy shift, the relative stability of the complexes is maintained. However, it is known experimentally that under low humidity conditions for oxidation, little or no $Cu(OH)_2$ forms. The relevant reactions are therefore those that involve CuO as the reactant.

As for Cu^{1+} complexation, Figure 4.9 (e), (f) depict the formation free energy versus total formic acid pressure of the notable monomer and dimer Cu^{1+} complexes: M_1', M_2' and D_1'− D_3' (Table 4.1). In both water-rich and -deprived conditions, the dimer $Cu_2(\mu\text{-}HCOO)_2$ (D_1') is the most favorable to form. Another dimer, $Cu_2(\mu\text{-}HCOO)_2(HCOOH)_2$ (D_3'), is the second most favorable species. The free energy of formation of $Cu_2(\mu\text{-}HCOO)_2$ from Cu_2O ranges from 0.33 to 0.34 eV/Cu at 356 Torr H_2O and 353 K, which slightly improves to 0.17−0.18 eV/Cu at 0.008 Torr H_2O. Addition of two HCOOH to form D_3' slightly increases the free energy of this dimer by ∼0.1 eV/Cu. Cu(HCOO)(HCOOH) (M_2') on the other hand is ∼0.2 eV/Cu higher in energy than D_1'. Cu(HCOO)(HCOOH), therefore, cannot facilitate the formation of the most stable dimer.

Etching of Cu^{1+} through complexation is thermodynamically less favorable than Cu^{2+} by ∼0.2 eV/Cu, and unlike in Cu^{2+}, a Cu^{1+} monomer that is energetically adjacent to the most stable Cu^{1+} dimer does not exist. Therefore, Cu^{2+} is expected to be the species that may be etched by HCOOH, which highlights the importance of the oxidation half-cycle with plasma O_2, to oxidize the newly exposed Cu after etching and any Cu^{1+} that may form.

The etching of oxidized Cu mediated by HCOOH vapor may be regarded as rather "inefficient" considering it proceeds only a few nm per cycle with a 5 min exposure to HCOOH per cycle, but desirable because it enables a nanometer-resolved etch rate. This "inefficiency" is reflected in the predicted nearly zero etching free energy of Cu^{2+} through complexation under

experimental conditions (Figure 4.9 (b)). Atomic resolution thus is achieved by the complexation reactions that are at or near equilibrium.

4.3 Experimental Verification of Reaction Mechanism and Etch Product

It has been theoretically shown in the previous section that the formation of a paddlewheel-like structured dimer of copper formate is the most energetically favorable etch product configuration under the temperature and pressure of experiments conducted: between 150 to 250 Torr of formic acid vapor and nitrogen carrier gas and 80℃ temperature. The prediction of the etch product – an idealized, well-specified process with no kinetic input – does not guarantee the actual existence of the etch product, which is generated in an experimental condition with inevitable ambient exposure, contamination, and equipment imperfections. And even if the predicted etch product does exist, the detection and characterization of such product could be difficult, in lieu of the low vapor pressure of metal organics (Hagen 2019). Additionally, since the ALE process is designed to happen near equilibrium, the amount of reaction product generated would be minuscule during one cycle of processing. The confirmation of the etch products is thus still an unsolved scientific issue of interest, as it provides information essential to understand the reaction mechanism and could guide the future exploration of potential patterning chemistries.

Maximizing the concentration and volume of the reaction product is attempted to compensate for its low vapor pressure and low yield. Copper foam, instead of Cu thin film deposited on Si substrate, was used to utilize its high surface area and more reaction sites. The copper foam was cut into roughly 1 cm by 1 cm squares, thermally oxidized in ambient at 200℃ for two hours, and then placed in the vapor chamber for conditions detailed in Table 2.4 for 5

minutes. The prolonged thermal oxidation was intended to convert as much of the Cu to CuO as possible. The exposure of formic acid vapor, on the other hand, avoids temperature and pressure higher than those used in the previous section, since a near-equilibrium reaction is still desired. Etching of four thermally oxidized samples was performed to accumulate enough etch product for subsequent analyses. Images of the Cu foam were taken after each processing step, as shown in Figure 4.10.

Figure 4.10 Cu foam (right) as received, (middle) after 2 hr 200 ℃ thermal oxidation, and (right) after 2 hr 200 C oxidation and 5 min 80℃ formic acid vapor exposure.

It is clear that, from this rather aggressive treatment, the oxidation-reduction process happened at the very surface level of the Cu foam with the facilitation of oxygen at elevated temperature and formic acid. The bright, shiny bronze color of the Cu surface was converted to the dark, matte CuO after extended oxidation in air, then partially recovered after the formic acid vapor exposure. The microscopic change of the change was imaged by SEM, as shown in Figure 4.11.

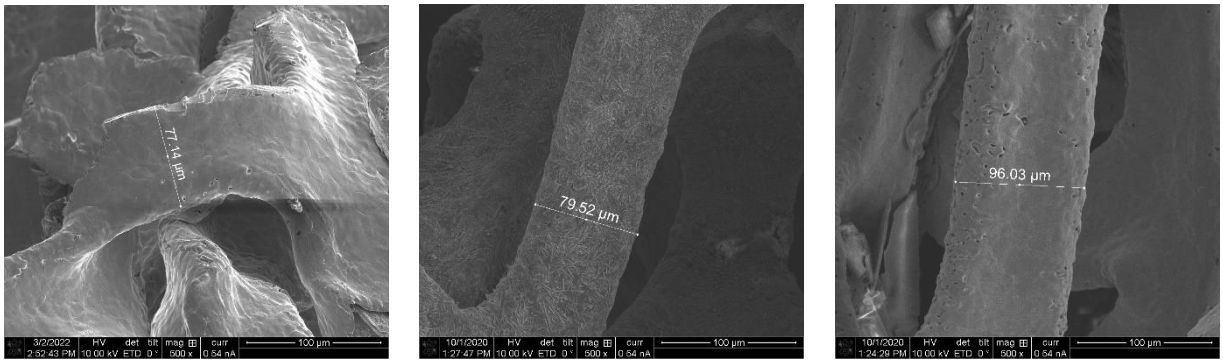

Figure 4.11 SEM of Cu foam (right) as received, (middle) after 2 hr 200℃ thermal oxidation, and (right) after 2 hr 200 C oxidation and 5 min 80℃ formic acid vapor exposure.

A direct comparison of the width of the structure was attempted but rendered unsuccessful, since the width is close to 100 μm, 5 orders of magnitude higher than the change per cycle in the ALE process. The comparison of the SEM images still valuable since it can be seen that the grain structure on the oxidized sample (Figure 4.11 middle) is largely removed after formic acid vapor exposure (Figure 4.11 right), a change on a much smaller scale. Downstream of the vapor chamber is the cold trap, which condense and store the gas phase etch product during pumping at the end of each experiment. To collect sufficient amount of etch product for subsequent analysis, multiple cycles of vapor exposure was performed on oxidized Cu foam. The cold trap was opened after being turned off for 30 minutes, allowing temperature to increase to close to ambient. Etch product was then transfer out from the cold trap via sterilized glass pipettes. To confirm this process is indeed connected to the reaction process anticipated, three foams shown in Figure 4.10, together with the condensed etch solution dried on a wafer, was analyzed by XPS. The XPS detail scan of Cu 2p, C 1s, and O 1s is shown in Figure 4.12.

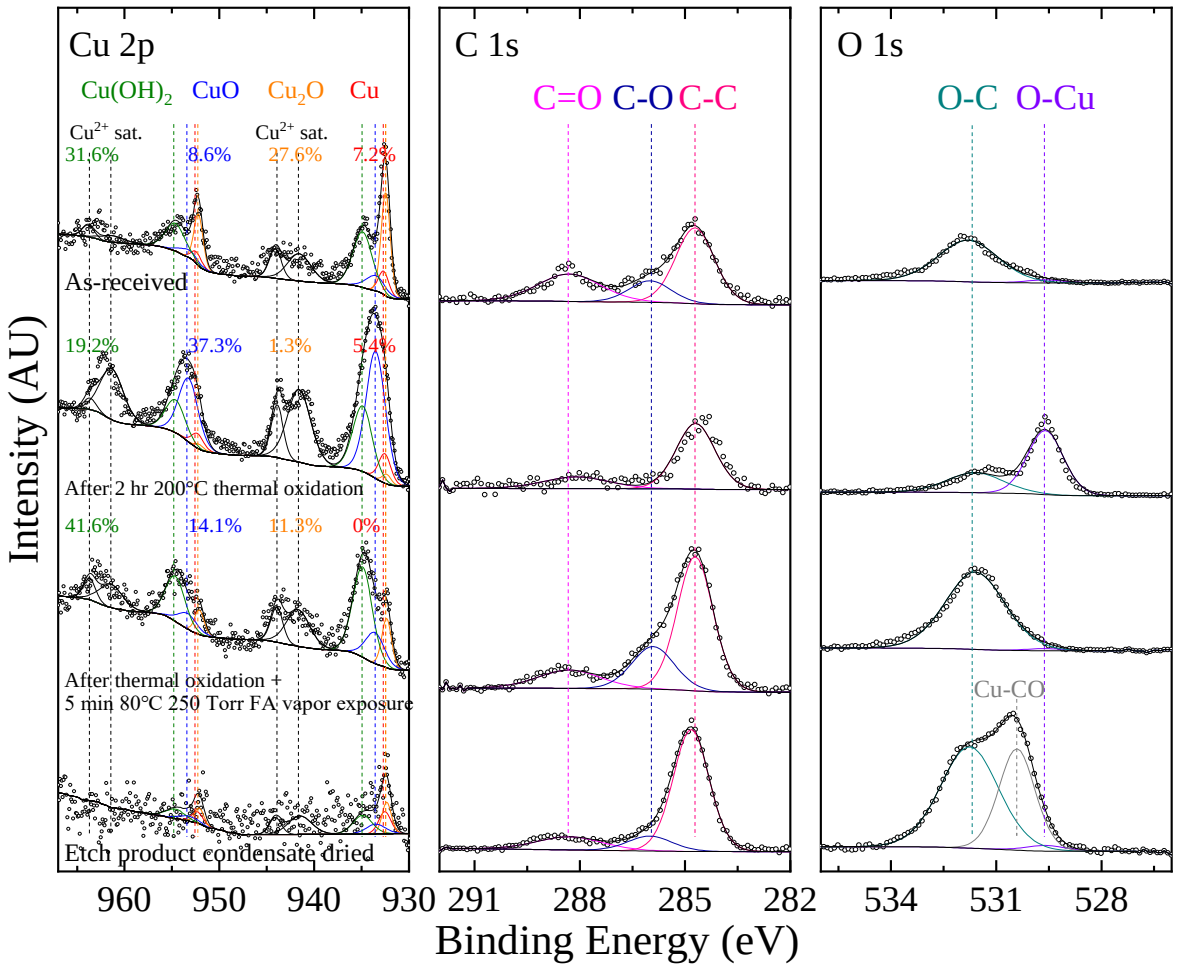

Figure 4.12 XPS detail scan of Cu foam, showing (left) Cu 2p, (middle) C 1s and (right) O 1s for Cu foam as-received, after 2 hr 200℃ thermal oxidation, after thermal oxidation then 5 min 80℃ 250 Torr formic acid vapor exposure, and etch product drop-casted and dried on Si wafer.

Deconvolution of the Cu 2p scan was performed by quantifying the Cu metallic (red), Cu_2O (orange), CuO (blue), $Cu(OH)_2$ (green), and Cu^{2+} satellite (black) peaks. Their relative percentages are labeled by the colored numbers accordingly except for the satellite peaks. A close inspection of the change in surface composition gives a trend of Cu chemical stages. The percentage of surface metallic Cu was low on the as-received sample (7.2%), which is expected since the sample was stored in the ambient condition. Thermal oxidation converted the remaining surface Cu to

CuO, as shown by the depletion of metallic Cu signal and increase in CuO signal. Also confirmed by the change in XPS signal is the reemergence of metallic Cu signal after formic acid vapor exposure, together with the increase in $Cu(OH)_2$ signal, as part of the surface oxide was converted to hydroxide with the inevitable presence of water molecules, which matches the simulation results. The increase in O-C and C-C bond also shows a trace of residual formic acid (or Cu-containing organics) not being effectively pumped away. The dried etch product condensate also showed, albeit weak, Cu metallic and Cu-CO signals. The changes in surface Cu chemical state from XPS, together with surface smoothness change from SEM and color change from naked-eye observation, painted a picture of oxidation of surface metallic Cu and subsequent removal of surface oxide, leaving the underlying Cu with residual hydrocarbon-rich etch products. It is however still of interest to inspect the constituents of the etch condensate for any chemical footprints of the predicted $Cu_2(\mu\text{-}HCOO)_4$.

In the attempt of resolving the chemical structure of the etch product, a set of four samples (including three control samples and one actual sample) is prepared for NMR, EPR, and ICP-MS. All four samples are 20 mL in volume, stored in glass vials prior to characterizations. The breakdown of sample conditions is shown in Table 4.2.

Table 4.2 Conditions of liquid samples for etch product characterizations.

Sample name	Sample condition
Formic acid	Formic acid stock solution (Sigma-Aldrich, 95%)
$Cu(HCOO)_2$ saturated solution	Copper formate tetrahydrate powder (Fisher Scientific, 98%) saturated water solution
Wet etch solution	Etch solution of copper foam in formic acid (1 hr, 80℃)
Vapor etch condensate	Condensed etch product of copper foam processed by vapor

Room temperature ^{1}H NMR spectra of the samples listed is shown in Figure 4.13. All four samples show the solvent residual peak at ~4.79 ppm as expected. The formic acid peak (~8.22 ppm) is only visible from spectra of formic acid, wet etch solution, and vapor etch condensate. Multiple factors could contribute to the inconclusive NMR result. First and foremost, the quadrupolar (spin 3/2), paramagnetic ($1s^2 2s^2 2p^6 3s^2 3p^6 3d^9$) Cu^{2+} ions have short relaxation times, which in terms lead to wider, less distinguishable NMR peaks. The hydrogen-deuterium exchange between formic acid and deuterium oxide (heavy water) also partially contributes to the broadening of signals. This exchange is difficult to eliminate as heavy water is used as the solvent and reference, other commonly used organic solvents ($CDCl_3$, DMSO, etc.) are not compatible as copper formate has little solubility in them. It is observed that the NMR spectrum for $Cu(HCOO)_2$ solution is missing the formic acid peak, which is due to the formate ligand being in close proximity to Cu^{2+} ions, the signal of which is therefore broadened and not distinguishable. An overall very low Cu^{2+} concentration (vapor etch condensate) would have little broadening to the formic acid peak (close to the spectrum of formic acid), while a very high Cu^{2+} concentration would have so significant broadening to the formic acid peak that it is no longer detected ($Cu(HCOO)_2$ solution). Intermediate Cu^{2+} concentration would have formic acid peak broadening within the range of detection (wet etch solution) with observable broadening. Since the sample spectrum is close to that of the formic acid control, it is inclusive to confirm the existence of the copper formate.

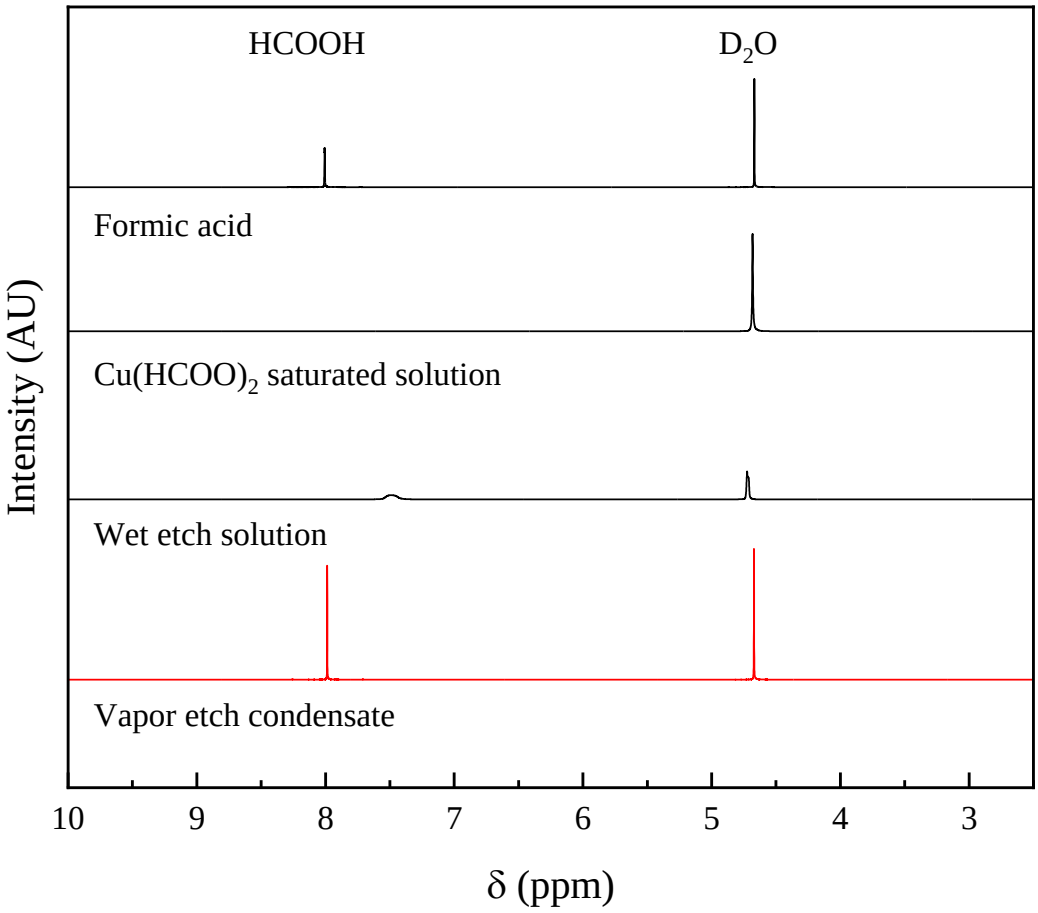

Figure 4.13 Room temperature ^{1}H NMR spectra of samples listed in Table 4.2.

Room temperature EPR first derivative spectra of the samples listed are shown in Figure 4.14, note that the signal intensity of $Cu(HCOO)_2$ solution is reduced to one-hundredth of its original value to fit in the same plot. A paramagnetic shift of around 3250 G is expected for Cu^{2+}-containing molecules. Formic acid shows the spectrum of a Cu^{2+}-free condition, while the (compressed) spectrum of $Cu(HCOO)_2$ solution shows that of a Cu^{2+}-rich condition. The sinuous first derivative spectrum is characteristic of electron magnetic moment resonating with the magnetic moment of the target nucleus (Cu), such resonance is significantly decreased in the spectrum of wet etch solution, liquid with much lower Cu^{2+} concentration. And finally, the

resonance almost disappeared in the spectrum of the vapor etch condensate, with only a trace amount of resonance. It is difficult to determine the existence of Cu^{2+} ions from the amplitude of resonance in the sample spectrum. Perhaps more importantly, for $Cu(HCOO)_2$ solution, where the resonance signal is the most intense, $g_{||}$ peaks that correspond to the neighboring atoms as shown in are still missing, implying an ionic nature of the Cu-containing etch product. This ionic-dominant characteristic is backed by the observation from the NMR spectrum, where the broadening of the formic acid peak is attributed to the close-range hydrogen-deuterium interaction, which means hydrogen in the proposed copper formate molecule is more intended to be in close vicinity of deuterium cations, instead of Cu^{2+}.

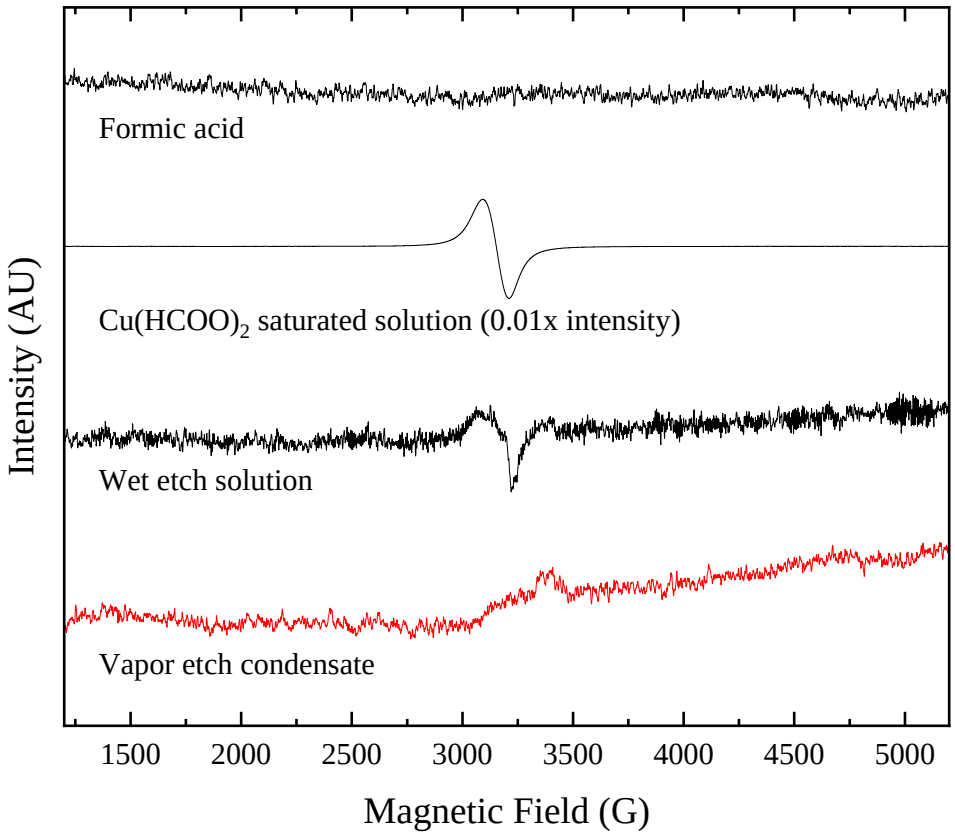

Figure 4.14 Room temperature EPR first derivative spectra of samples listed in Table 4.2.

ICP-MS of the samples listed are shown in Figure 4.15, the dilution factor adjusted measured Cu concentration is listed in Table 4.3. ICP-MS was set to individual mode, namely, instead of scanning the full range of m/z and analyzing all possible constituents, a forced range of m/z values are scanned (in this experiment 58 to 67) without pre-assigning elemental input. From formic acid spectrum, a blank background was established for subsequent measurements and comparisons. Signal intensities from the 10 consecutive scanned m/z values fluctuate within the same order of magnitude, assuring both the etchant and the container are free of significant amounts of contamination. For $Cu(HCOO)_2$ solution, wet etch solution, and vapor etch condensate scans, the ICP-MS scans successfully confirmed the presence of Cu, as shown by the close to naturally occurring 2.1:1 ratio of Cu^{63}:Cu^{65} signals. Background impurity signals from the sample are still detectable in the sample scan, as can be told from their relative intensities, but are much lower than the signals from Cu isotopes. From the dilution factor adjusted concentration measurements, it is noted that the Cu concentration is one order of magnitude higher than that in formic acid, four and two orders of magnitude lower than that in the $Cu(HCOO)_2$ solution and wet etch solution, respectively. This is once again expected based on the sample preparation, and the measured concentration difference is in line with the previous observation from both NMR and EPR. Given the concentration in the sample is not much higher than that in the formic acid control, and the largely ionic behavior upon dissolution, it is not surprising to see structural analysis such as NMR and EPR yield limited results.

Table 4.3 Cu concentrations determined by ICP-MS, accounted for respective dilution factors.

	Dilution factor	Concentration (μg/mL)	Concentration std (μg/mL)
Formic acid	83	0.24	0.00
$Cu(HCOO)_2$ saturated solution	62250	25575.84	1070.70
Wet etch solution	990	137.97	4.71
Vapor etch condensate	99	2.34	0.19

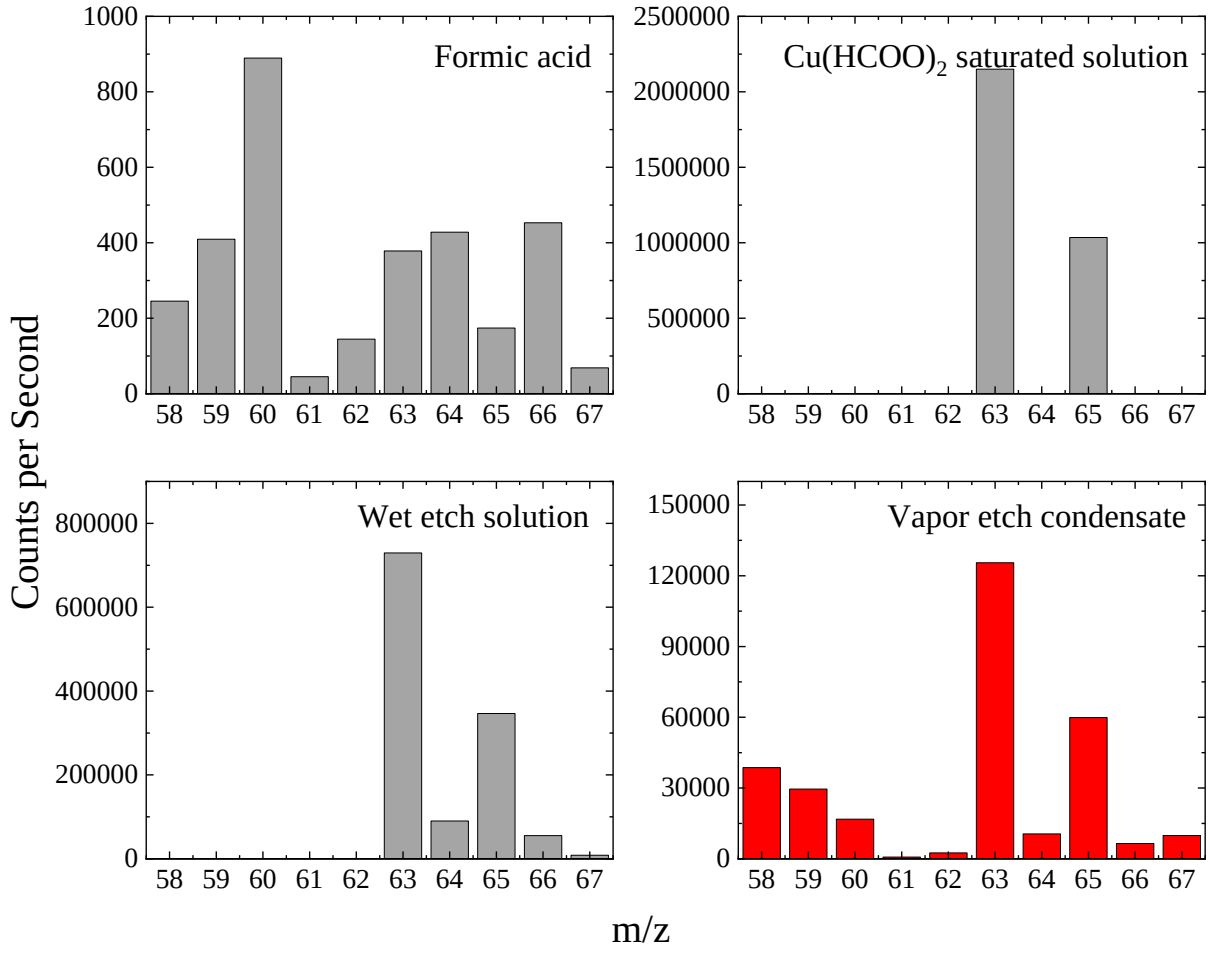

Figure 4.15 ICP-MS counts per second after dilution for sample listed in Table 4.2. Dilution factors listed in Table 4.3. 2.1:1 ratio of 63:65 m/z from the vapor etch condensate confirms the existence of Cu.

Chapter 5 Summary

This work developed a generalizable atomic layer etching technique for etch-resistant metals. The introduction of new materials into the IC manufacturing process calls for suitable patterning techniques to be developed. Metals, metal alloys, and metal oxides are among the most note-worthy functional materials with limited reported etching processes. However, the etching of these newly introduced materials needs to be assessed through new lenses, as the chemical environment is more complicated, their layer structure is more sophisticated, and the reactions involved are more intertwined. The controlled etching of these materials requires different approaches from the etching of Si, and precision is emphasized over yield. Atomic layer etching, a concept for patterning high aspect ratio features and small critical dimensions, is of increasing interest for the patterning of etch-resistant materials such as metals.

Dry etch of Ni was considered difficult due to the chemical inertness of the element. Current development on the gas phase Ni etch mostly focuses on the RIE processes involving halogen-based chemistry, which leverage the relatively high vapor pressure of the metal halides but have the drawback of introducing corrosive gases into the processing chamber. A similar process is tested in this work, but instead of using a continuous, halogen-only plasma, a cyclic, hydrogen-involved chemistry is used. The etching validity was predicted via thermodynamic analysis, which shows hydrogen radicals enhancing the removal of surface Ni halides at reduced pressures. With the elevated energy of hydrogen ions in a plasma, such an auxiliary effect is noticeable. An average etch rate of 3~5 nm/cycle is recorded, the variation depends on sample preparation and plasma conditions, with a selectivity of 1.4 with respect to SiO_2 hard mask.

Thermodynamic calculations utilizing the existing database also showed an alternative, halogen-free reaction pathway leading to the gas phase Ni etch product. The lower reaction free energies on the oxides compared to the metals implies selectivity is achievable if reactant concentration could be controlled in the window that only enables reactions on the former, not the latter. Subsequent etch using vapor phase formic acid at elevated temperatures and reduced pressures showed measurable etch rates for plasma oxidized Ni thin films and negligible etch rate on pristine metallic thin films. A cyclical process, involving converting the surface of Ni to NiO using O_2 plasma and removing that NiO using formic acid vapor was developed to etch Ni in a cyclical manner, which resulted in etch rates in the range of 2~6 nm/cycle based on different formic acid exposure pressures, and high selectivity with respect to Ni (over 100) is recorded. For etching patterned structures, the selectivity over SiO_2 hard mask is close to infinite (no SiO_2 etch measured).

The contributing factors toward an overall controllable, self-limiting removal process are studied. Both the time and applied bias of the oxidation process played crucial roles in the formation of the NiO surface layer. The increase of either parameter led to an increase in surface oxide percentage, however, neither showed a self-limiting behavior necessary for an ALE process. The controllability is secured via a highly selective removal half-cycle, which removed the entirety of the surface oxide with no measurable metal etch. Surface composition after formic acid exposure at different pressures was tested and a high-pressure condition was determined to be necessary for complete surface oxide removal. This favorable removal technique is backed by DFT-based reaction simulations, where none of the Ni bulk model, thin film model, and thin film model with oxygen overlayer showed spontaneous reaction with formic acid. Such reaction is only spontaneous between formic acid molecules and Ni thin film model with oxygen underlayer.

Pairing the self-limiting removal scheme with the directional formation of the oxide using the oxygen ion, a vertical sidewall was achieved on Ni thin film with SiO_2 hard mask.

Leveraging the high removal rate of the RIE process and the fine controllability of the ALE process, a directional, highly selective Ni removal is demonstrated with significantly improved processing efficiency. Same 87 ° final feature sidewall was achieved with ~75% reduced processing time.

The development of Cu dry etch process is another major focus in the metal patterning field, as it is crucial to the extension of Cu-based interconnect materials. The enormous challenges the damascene process faced call for a simpler removal technique. It has been previously established that removal of CuO could be selectively achieved over Cu via introducing formic acid molecules to the surface at reduced pressure. This work furthered the studies on reaction mechanisms as well as the reaction products.

Similar to the implementation of the Ni plasma-thermal ALE, Cu plasma-thermal ALE also uses oxidation as means to modify the surface layer and to establish chemical contrast, formic acid is again used as the removal chemistry at elevated temperature (80℃) and reduced pressure (250 Torr). An overall 2.4 nm/cycle of etch rate was recorded and etching directionality was confirmed by EDS line scans. Through DFT simulations, $Cu_2(HCOO)_4$ paddlewheel structure was determined to be the most energetically favorable etch product configuration, and the reaction has close to zero overall free energy at the conditions applied. The etch product was condensed, accumulated, and collected using a cold trap. Cu signal was confirmed by ICP-MS.

In both the ALE processes for Ni and Cu, plasma oxidation was utilized as the main source for surface modification, though which a thin modified layer on top of the metallic surface was

created. The thickness of the oxide layer thickness depends strongly on both the plasma oxidation time and applied bias. With the mean of quasi-controllable oxide thin film formation via tuning plasma oxidation time and bias, an organic vapor etch process was subsequently developed. The reaction is spontaneous on the oxide layer while not favorable on the underlying metal, creating chemical contrast essential for selective removal. Formic acid vapor was observed to etch both NiO and CuO at measurable rates while not etching metal. This chemical contrast-induced selectivity between the surface oxide and the underlying metal suggests a cyclical process of separate plasma oxidation followed by chemical vapor etch. Etching chemistries studied in this work, as well as their results, are summarized in Table 5.1.

Table 5.1 Summary of etching chemistries studied in this work.

	Ni		Cu
Etching technique	RIE	ALE	ALE
Chemistry	Cl_2/H_2 cyclic	O_2/Formic acid cyclic	O_2/Formic acid cyclic
Etch rate	~ 3.5 nm/cyc	~ 2 nm/cyc	~ 2.4 nm/cyc
Selectivity	1.4 to SiO_2	∞ to SiO_2, >100 to Ni	1.1 to SiCN, >100 to Cu
Sidewall angle	70°	87°	-
Self-limiting	No	Yes	Yes
Etch product characterization	OES	-	ICP-MS

This work demonstrated the role of low-energy ions in realizing both etching selectivity and anisotropy. The concept of etching specificity was proposed, and it is theoretically shown that, within the same oxidation states, certain metal-oxygen bonding configurations are more favorable to react with subsequent organic acid vapor, however the experimental verification of which is not yet achievable with the current setup. Similarly, the analysis of the metal-organic etch products

faced considerable challenges due to their chemical properties and low concentrations. Moving forward, this ALE technique could be applied to a wider range of materials such as Pd and Pt. Additionally, other modification chemistries such as nitridation could also be potentially viable for establishing chemical contrast. The inertness of noble metals and high dissociation energy of nitrogen could render such combinations not as easily achievable as oxidation of Ni and Cu showed in this work, thus the importance of DFT-based reaction simulation needs to be emphasized.

Appendices

A. Supplemental Materials for DFT Based Reaction Simulation of Ni Etch

A.1 Computational details and thermodynamics of the layer-by-layer removal model

The PAW basis set employed by VASP code is cut off at 400 eV. Surface species are calculated with orbitals occupancies evaluated with second order Methfessel-Paxton electron smearing at $\sigma = 0.2$ eV. Molecular species are calculated with gaussian smearing at $\sigma = 0.01$ eV. Geometry optimizations were terminated when forces are smaller than 0.02 eV/Å. Electronic steps are converged to 10^{-6} eV. Vacuum layers of 16Å were used to pad the slabs to avoid unphysical slab interaction. Surface dipole corrections were used to obtain correct electrostatic energies. Spin polarization was included for all periodic systems and all molecules except H_2, where spin-polarization leads to incorrect ground state energy.

A.2 Layer-by-layer removal model

The layer-by-layer removal model is a way to evaluate the etch reaction energetics.

The energetics for the pristine Ni can be evaluated with the bulk formation energy of Ni. When modifiers (oxygen) are introduced, the coverage effect must be accounted for.

Consider the general ALE reaction of formic acid reacting with nickel oxide below:

$$*.NiO \; + \; 2\,HCOOH \; \rightarrow * \; + [Ni(HCOO)_2] \; + \; H_2O$$

To incorporate the effect of changing coverage, a more general reaction (unbalanced) is considered:

$$\{l+1, NiO_\theta\} + \{HCOOH\} \rightarrow \{l, Ni\} + \{l+1, Ni\} + \{[Ni(HCOO)_2]\} + \{H_2O\} \quad \text{Eqn. S1}$$

In Eqn. S1, $\{l+1, NiO_\theta\}$ represents unetched activated surface with $l+1$ layers of nickel, θ is the oxygen coverage. $\{l, Ni\}$ and $\{l+1, Ni\}$ is the bare surface with l and $l+1$ layers, respectively. This corresponds to the case where the coverage is less than that required to remove one layer, leaving some Ni atoms in the top layer on the surface after all the oxygen are reacted away.

In this simple model, the explicit modelling of this potentially complex post-etch reconstruction is avoided. Instead, the assumption is that the left-behind Ni atoms are mobile enough to form islands large enough for edge effects to be neglected. With this assumption, these islands can be modelled as the original surface with $l+1$ layers. The balanced reaction is given in Eqn. S2,

$$\alpha\{l+1, NiO_\theta\} + 2\{HCOOH\} \rightarrow \{l, Ni\} + (\alpha - 1)\{l+1, Ni\} + \{[Ni(HCOO)_2]\} + \{H_2O\} \quad \text{Eqn. S2}$$

where $\alpha = 1/\theta$ is the copies (fractional) of modified surface needed to have enough modifiers to remove one nickel atom. In this case the correct stoichiometry is Ni:O = 1:1. Figure A.1 illustrates the situation when oxygen coverage is ½ ML.

Figure A.1 the layer-by-layer removal model on oxygen activated Ni surface at ½ ML coverage. Two copies of the activated surface are needed to remove one layer on a single copy, leaving the other copy unetched.

With this model in place, the etch free energy is calculated as:

$$\Delta G_{et} = [(\alpha - 1)G_{l+1,Ni} + G_{l,Ni} + G_{[Ni(HCOO)_2]} + G_{H_2O}] - [\alpha G_{l+1,NiO_\theta} + 2G_{HCOOH}]$$

$$= \alpha(G_{l+1,Ni} - G_{l+1,NiO_\theta}) - (G_{l+1,Ni} - G_{l,Ni}) + (G_{[Ni(HCOO)_2]} + G_{H_2O} - 2G_{HCOOH}) \quad \text{Eqn. S3}$$

In Eqn. S3, only the first term is related to the activated surface, related to the adsorption energy and the coverage. The second term is the energy difference of adding one layer to the slab model, equivalent to the Ni bulk formation energy. The approximation is exact when the slab surface energy is converged with respect to the number of layers. The third term is a uniform shift only related to the modifier/ligand chemistry pair.

In the case of high-coverage limit (ML), substituting $\alpha = 1$ in Eqn. S3 recovers the simpler expression:

$$\Delta G_{et} = [G_{l,Ni} + G_{[Ni(HCOO)_2]} + G_{H_2O}] - [G_{l+1,NiO_\theta} + 2G_{HCOOH}]$$

The Gibbs free energy of the surface species are further approximated by the DFT-calculated electronic energy (hence ignoring lattice vibrations). Gibbs free energy of the gas phase species are evaluated at 80 °C and 350 Torr with DFT-calculated electronic energies and vibrational, rotational, and translational entropy contributions.

A.3 The optimized structure of nickel formate complex

Main structural parameters of the most stable [Ni(HCOO)$_2$] complex is given in labels in Figure A.0.2. In addition, two ligands are completely in plane with no distortion.

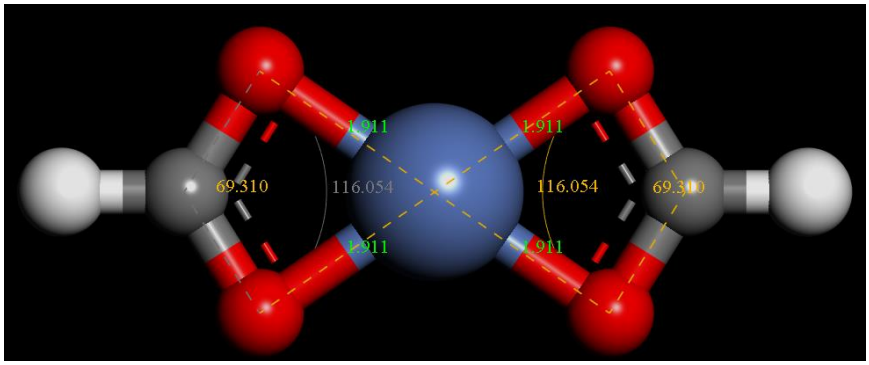

Figure A.0.2 The optimized structure of nickel formate complex in bidentate square planar configuration. The bond lengths and bond angles are marked in degrees and angstroms, respectively. The two ligands are completely in plane with no distortion.

Table A.1 Details of slab models

Surface	Supercell	#O atom in cell	Coverage/ ML	#Layers/#Relaxed	KPOINTS
Ni(100) – overlayer	p(1×1)	1	1	5L/3R	9×9×1
Ni(100) – mixed	p(2×1)	2	1	5L/3R	5×9×1
Ni(100) – sublayer	p(1×1)	1	1	5L/3R	9×9×1
Ni(100) – low coverage	p(3×3)	1	1/12	5L/3R	3×3×1
Ni(111) – overlayer	p(1×1)	1	1	5L/3R	9×9×1
Ni(111) – mixed	p(2×1)	2	1	5L/3R	5×9×1
Ni(111) – sublayer	p(1×1)	1	1	5L/3R	9×9×1
Ni(111) – low coverage	p(3×3)	1	1/9	5L/3R	3×3×1
Ni(211) – overlayer	p(1×1)	3	1	12L/8R	9×3×1
Ni(211) – mixed	p(1×1)	3	1	12L/8R	9×3×1
Ni(211) – sublayer	p(1×1)	3	1	12L/8R	9×3×1

B. Supplemental Materials for DFT Based Reaction Simulation of Cu Etch

B.1 Gas phase translational, rotational, and vibrational free energy corrections

The gas phase enthalpy and entropy from vibrational, rotational, and translational degrees of freedom were accounted for using statistical mechanics for ideal gas molecules, as described below.

Translational energy. The translational energy was calculated assuming the molecules are ideal (monoatomic) gas particles, where the enthalpy of translation at temperature *T* is thus

$$H_{trans}(T) - H_{trans}(0\ K) = \frac{5}{2}k_B T$$

while the entropy is given by the Sackur-Tetrode equation:

$$S_{trans} = k_B\left[\frac{3}{2}\ln\left(\frac{2\pi m}{h^2}\right) + \frac{5}{2}\ln(k_B T) - \ln(p) + \frac{5}{2}\right]$$

where $k_B T$ is the thermal energy (k_B is the Boltzmann constant), m is the molar mass of the molecule, p is pressure (in Pa), and h is the Planck constant.

Rotational energy. The rotational energy was calculated using the rigid rotor model, where the internal rotations within the molecules were ignored. The enthalpy for non-linear molecules is given by

$$H_{rot}(T) - H_{rot}(0\ K) = \frac{3}{2}k_B T$$

and for linear molecules, which only has two rotational degrees of freedom:

$$H_{rot}(T) - H_{rot}(0\ K) = k_B T$$

whereas the entropy for non-linear molecule is

$$S_{rot} = k_B\left[\frac{3}{2}\ln\left(\frac{k_B T}{h}\right) - \frac{1}{2}\ln\left(\frac{ABC}{\pi}\right) - \ln(\sigma_{rot}) + \frac{3}{2}\right]$$

where the product of three rotational constants, ABC, depends inversely on the product of the three moments of inertia I_A, I_B, and I_C (Bernath 2005):

$$ABC = {h^2}/{(8\pi^2)^3(I_A I_B I_C)}$$

$$I_A I_B I_C = I_{xx}I_{yy}I_{zz} + 2I_{xy}I_{xz}I_{yz} - I_{xx}{I_{yz}}^2 - I_{yy}{I_{xz}}^2 - I_{zz}{I_{xy}}^2$$

where

$$I_{xx} = \sum_i^N m_i(y_i^2 + z_i^2) \quad I_{yy} = \sum_i^N m_i(x_i^2 + z_i^2) \quad I_{zz} = \sum_i^N m_i(x_i^2 + y_i^2)$$

and

$$I_{xy} = -\sum_i^N m_i(x_i y_i) \quad I_{yz} = -\sum_i^N m_i(y_i z_i) \quad I_{xz} = -\sum_i^N m_i(x_i z_i)$$

where m_i and (x_i, y_i, z_i) are the atomic mass and the Cartesian coordinates, relative to the center of mass, of atom i. N is the number of atoms in the molecule. σ_{rot} is the rotational symmetry number based on the molecule's point group symmetry (Table). For linear molecules, the entropy is given by:

$$S_{rot} = k_B \left[\ln\left(\frac{k_B T}{h}\right) - \frac{1}{2}\ln(B^2) - \ln(\sigma_{rot}) + 1 \right]$$

where

$$B = {}^{h}/_{(8\pi^2 I_B)}$$

with I_A = 0 and $I_B = I_C$, corresponding to two degenerate rotational degrees of freedom.

Vibrational energies. The internal energy (E_{vib}), entropy (S_{vib}), and Helmholtz free energy (A_{vib}) of vibration of a (non-linear) molecule, assuming Harmonic oscillators, were calculated as follows:

$$E_{vib} = \sum_{j=1}^{3N-6} \left[\frac{h\nu_j}{2} + \frac{h\nu_j}{e^{\beta h\nu_j} - 1} \right]$$

$$TS_{vib} = \sum_{j=1}^{3N-6} \left[\frac{h\nu_j}{e^{\beta h\nu_j} - 1} - \frac{1}{\beta} ln\left(1 - e^{-\beta h\nu_j}\right) \right]$$

while

$$A_{vib} = \sum_{j=1}^{3N-6} \left[\frac{h\nu_j}{2} + \frac{1}{\beta} ln\left(1 - e^{-\beta h\nu_j}\right) \right]$$

where ν_j are the normal mode frequencies and β is the inverse of thermal energy $1/k_B T$ (k_B is the Boltzmann constant). For linear molecules, the summation upper bound is $3N - 5$.

The translational and rotational enthalpies and entropies (Table) were calculated from the optimized molecular structures and using an HTML/JavaScript-based calculator by T. W. Shattuck (Shattuck 2011). The vibrational enthalpies and entropies (Table) were evaluated using the calculated normal mode frequencies also of the optimized molecular structures (see Methods: Theory and simulations for details).

B.2 Partial pressures of formic acid monomer and dimer

Formic acid is predominantly in the form of a dimer in the gas phase (Hietala 2016), bound via hydrogen bonds (Fig. S5). The partial pressures of the dimer, $p[(\mathrm{HCOOH})_2]$, and the monomer, $p[\mathrm{HCOOH}]$, given a total pressure of all formic acid species $p[(\mathrm{HCOOH})_n]$ ($(\mathrm{HCOOH})_n$ represents both monomer and dimer), are related through the following equations

$$p[(\mathrm{HCOOH})_n] = p[(\mathrm{HCOOH})_2] + p[\mathrm{HCOOH}]$$

$$\frac{\Delta G_{dimer}}{k_B T} = \ln(p[\mathrm{HCOOH}]^2 / p[(\mathrm{HCOOH})_2])$$

$\Delta G_{dimer}$is the dimerization free energy of the HCOOH molecules. Thus, $p[(\mathrm{HCOOH})_2]$ is the solution to the quadratic equation

$$0 = p[(\mathrm{HCOOH})_n]^2 - \left(2p[(\mathrm{HCOOH})_n] + \exp\left(\frac{\Delta G_{dimer}}{k_B T}\right)\right) p[(\mathrm{HCOOH})_2] + p[(\mathrm{HCOOH})_2]^2$$

that yields positive values for both $p[(\mathrm{HCOOH})_2]$ and $p[\mathrm{HCOOH}]$. For example, at $p[(\mathrm{HCOOH})_n] = 250$ torr (0.333 bar) and $T = 80$℃ (353.15 K), $p[(\mathrm{HCOOH})_2]$ = 235 torr (0.313 bar) and $p[\mathrm{HCOOH}]$= 15 torr (0.020 bar), which were evaluated using the calculated ΔG_{dimer}= -0.101 eV/ HCOOH or -0.202 eV/$(\mathrm{HCOOH})_2$ at $T = 353.15$ K (from data in Table).

B.3 Pressure dependence of the reaction free energies

The dependence of the reaction free energies on the partial pressures of $(HCOOH)_2$, H_2O, CO_2, O_2, and a given complex is given by

$$\Delta G_{rxn} = \Delta G^\circ_{rxn} + k_B T \ln(p[M]^x)$$

where *x* is the reaction coefficient of any of the gas-phase reactant and product molecule *M* (> 0 for products, < 0 for reactants, Table). ΔG°_{rxn} is the standard reaction free energy (Figure 4.9) and the partial pressures are also expressed in bar. Note that here, pressures in bar are used for ease of evaluation, since the standard pressure is p° = 1 bar.

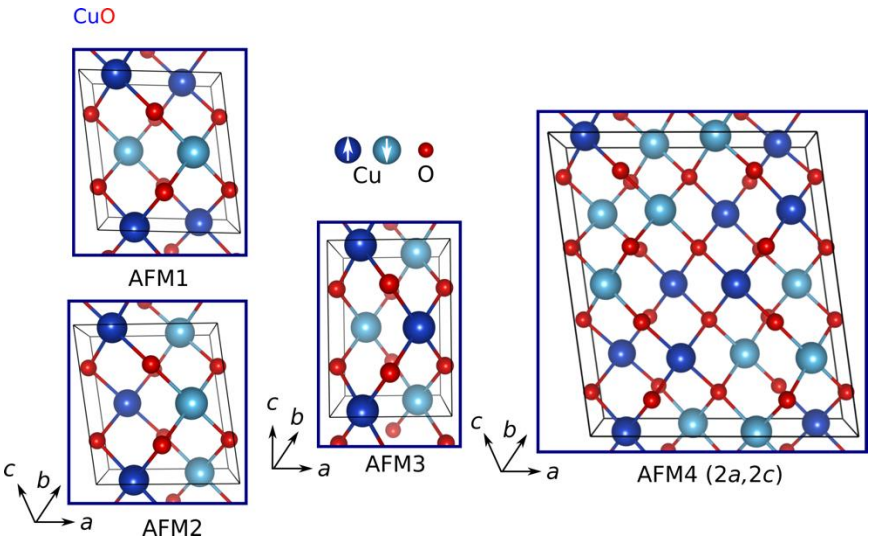

Figure B.1 Anti-ferromagnetic structures of bulk CuO. AFM1 to AFM3 are the three possible non-equivalent AFM structures for a four-formula-unit cell characterized by lattice vectors *a*, *b*, and *c*. Doubling along *a* and *c*, with a combination of AFM1 and AFM2 magnetic ordering, yields the experimental and theoretical ground-state magnetic structure AFM4. Optimized atomic structural parameters, and relative energies between the different AFM and ferromagnetic (FM) structures, are shown in Table . The FM phase is higher in energy relative to all AFM structures shown.

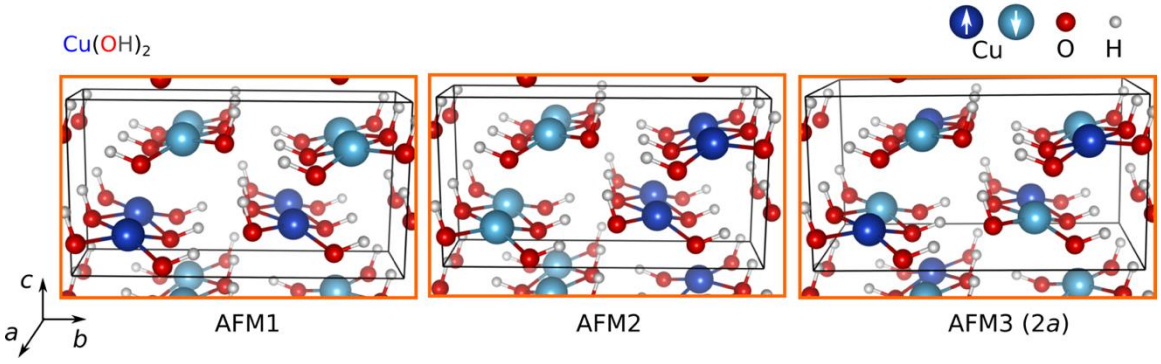

Figure B.2 Anti-ferromagnetic structures of bulk $Cu(OH)_2$. AFM1 and AFM2 are the two possible non-equivalent AFM structures for a four-formula-unit cell characterized by lattice vectors *a*, *b*, and *c*. Doubling of *a* enables AFM interaction between nearest-neighbor Cu^{2+} ions (AFM3). However, this results in a (nearly negligible) higher energy magnetic structure relative to AFM2. Optimized atomic structural parameters, and relative energies between the different AFM and FM magnetic structures, are shown in Table . The FM phase also is nearly degenerate with all the AFM structures shown.

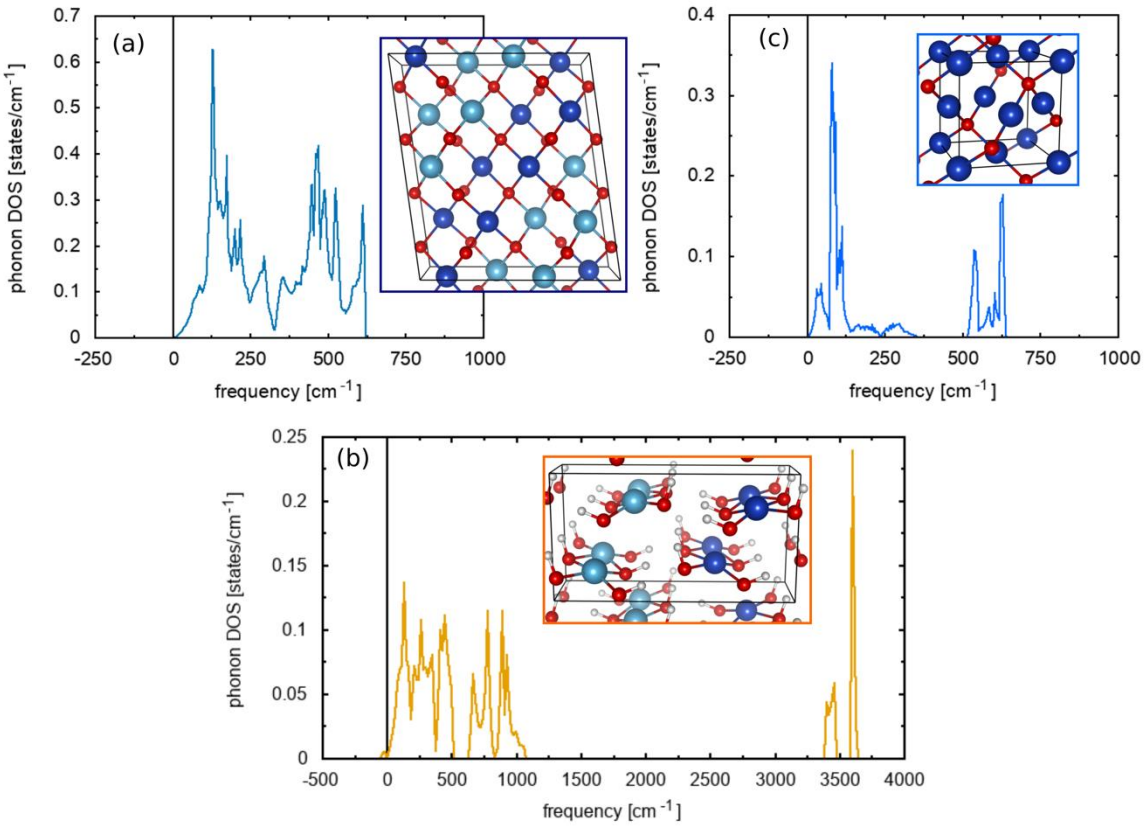

Figure B.3 Bulk phonon densities of states (phDOS). (a), CuO phDOS for the ground-state AFM4 magnetic structure (Fig. S1). (b), $Cu(OH)_2$ phDOS for the ground-state AFM2 magnetic structure (Figure). (c), Cu_2O phDOS (Fig. 8). Insets show the oxides' unit cells, which are a 16-formula-unit $2a \times b \times 2c$ cell for CuO, a four-formula-unit $a \times b \times c$ cell for $Cu(OH)_2$, and a two-formula-unit $a \times b \times c$ cell for Cu_2O (see Table , Table and Table , for the actual cell dimensions). The Hessian matrices were constructed from a 32-formula-unit $2a \times 2b \times 2c$ supercell for CuO, 16-formula-unit $2a \times b \times 2c$ supercell for $Cu(OH)_2$, and 16-formula-unit $2a \times 2b \times 2c$ supercell for Cu_2O. Nearly negligible imaginary frequencies are present in $Cu(OH)_2$ phDOS (plotted as negative values), which are < $52i$ cm^{-1} and thus are ascribed to numerical noise.

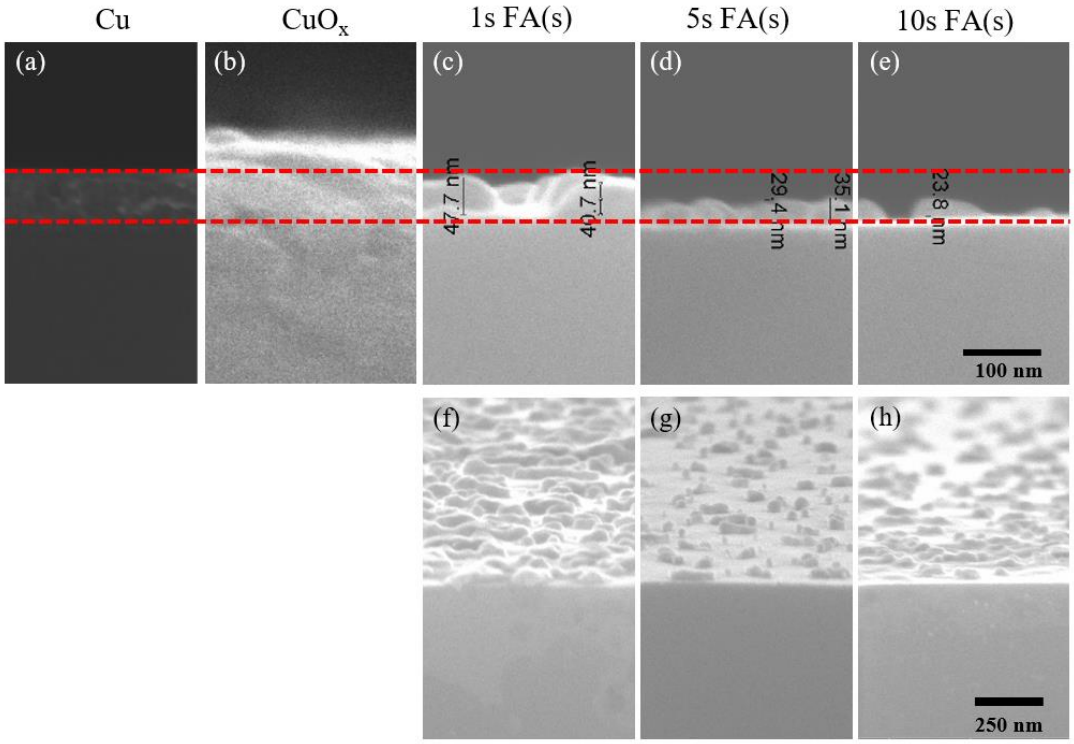

Figure B.4 SEM images of (a) as-deposited PVD Cu, (b) CuO_x formed after oxidation of Cu, (c/f,d/g,e/h) CuO_x after 1s, 5s, 10s etch in formic acid solution, respectively, at 80^{o}C. The surface morphology of CuO_x changed significantly after etching by formic acid solution. Even with just 1s of formic acid exposure, portions of the film were completely removed. From the SEM analysis, the etching rate was determined by considering the average thickness of the residuals as measured by the cross-sectional image (a-e) and the surface coverage by the plane view of the image (f-h).

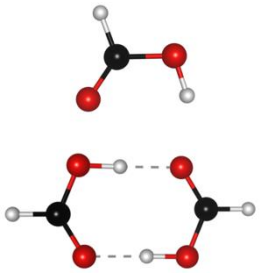

Figure B.5 The more stable trans rotamer (Pettersson 2003) of HCOOH in monomeric (top) and dimeric (bottom) forms. The molecule forms stable dimers by forming two hydrogen bonds, which constitute the majority of the form in the gas phase. (Elvers 1991) Note that in older literature, the *trans* isomer may be referred to as the *cis*, and *vice versa* (the older notation refers to the relative position of the carbonyl O and hydroxo H; in contrast, more current literature refers to the relative position of the two H atoms).

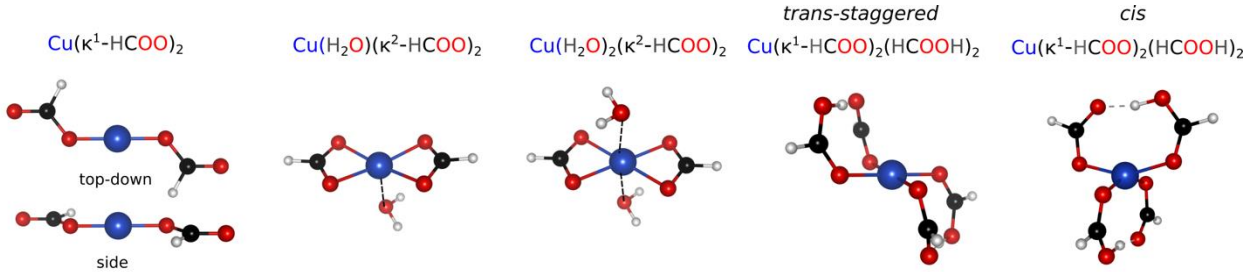

Figure B.6 Alternative higher-energy structures for some of the Cu(II) complexes shown in Fig. 6 in the main text. The free energies of these molecules relative to their more stable isomer, from left to right, are 1.26, 0.31, 0.67, 0.06, and 0.26 eV at 298 K (see Table for energies).

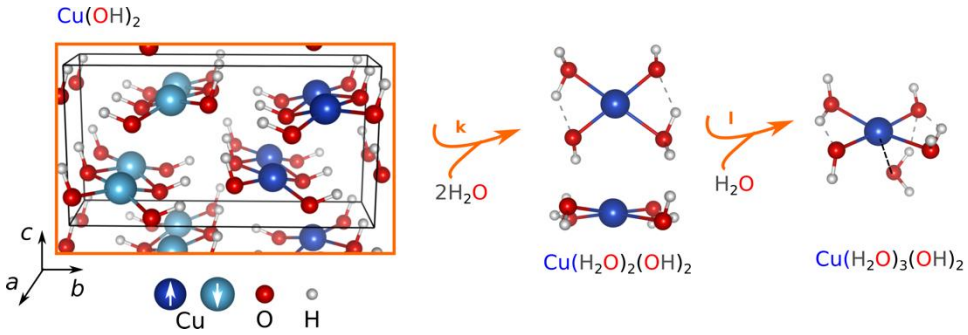

Figure B.7 Formation of gas-phase aquahydroxo complexes from $Cu(OH)_2$. Formation of these complexes are highly endoergic, with standard reaction free energies $\Delta G°_k$ = 1.65 eV and $\Delta G°_{k+l}$ = 1.72 eV at 298.15 K. The reaction free energies were calculated from the data in Table and Table .

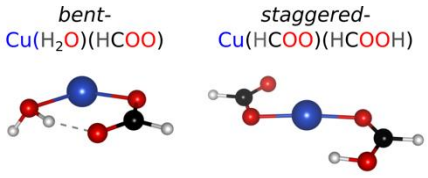

Figure B.8 Alternative higher-energy structures for some of the Cu^{1+} complexes shown in Figure 4.9 in the main text. The free energies of these molecules relative to their more stable isomer. from left to right, are 0.08 and 0.60 eV at 298 K (see Table for energies).

Table B.1 Predicted lattice parameters, k-point grids, and relative energies per formula unit (f.u.) for monoclinic CuO.

Structure	*a*,*b*,*c* (Å)	α,β,γ (°)	*k*-point sampling[a]	Energy (meV/f.u.)
AFM1	4.562, 3.542, 5.152	90.0, 98.1, 90.0	$4 \times 6 \times 4$	29
AFM2	4.589, 3.532, 5.143	90.0, 97.5, 90.0	$4 \times 6 \times 4$	21
AFM3[b]	3.604, 4.524, 5.186	90.1, 90.0, 90.0	$4 \times 6 \times 4$	23
AFM4[c]	**4.507, 3.617, 5.140 (9.014, 3.617, 10.280)[d]**	**90.0, 97.9, 90.0**	$\mathbf{2 \times 6 \times 2}$	**0**
FM	4.182, 3.984, 5.182	90.0, 90.2, 90.0	$4 \times 6 \times 4$	74
exp[e]	4.6833(2), 3.4208(1), 5.1294(2)	90.0, 99.567(1), 90.0	n/a	n/a

[a]For AFM1, *k*-point convergence is $E(4 \times 6 \times 4) - E(6 \times 8 \times 6) = -0.04$ meV/atom at 660 eV planewave (PW) basis kinetic-energy cut-off, and a PW basis kinetic-energy cut-off convergence of *E*(660 eV) – E(760 eV) = 0.89 meV/atom at $4 \times 6 \times 4$ *k*-point mesh.

[b]Because AFM4 is lower in energy than AFM3, relaxation of the AFM3 structure (FM plane orthogonal to *b*) attempts to relax towards an AFM4 ordering (FM plane orthogonal to *a*) by contracting *a*, expanding *b*, and reducing angle β. β appears to have been trapped at 90°.

[c]AFM4 is the lowest-energy magnetic structure (bolded).

[d]Actual cell size ($2a \times b \times 2c$) in parentheses, [e]Taken from (Brese 1990).

Table B.2 Predicted lattice parameters and relative energies per formula unit (f.u.) for orthorhombic $Cu(OH)_2$.

Structure	*a*,*b*,*c* (Å)	α,β,γ (°)	*k*-point sampling	Energy (meV/f.u.)
AFM1	2.933, 10.298, 5.493	90.0, 90.0, 90.0	$8 \times 2 \times 4$	4
AFM2[a]	**2.933, 10.292, 5.495**	**90.0, 90.0, 90.0**	$\mathbf{8 \times 2 \times 4}$	**0**
AFM2 w/o D3BJ[b]	2.949, 10.586, 5.676	90.0, 90.0, 90.0	$8 \times 2 \times 4$	15
AFM3	2.944, 10.310, 5.464 (5.888, 10.310, 5.464)[c]	90.0, 90.0, 90.0	$4 \times 2 \times 4$	3
FM	2.933, 10.295, 5.496	90.0, 90.0, 90.0	$8 \times 2 \times 4$	1
exp[d]	2.9471(5), 10.593(1), 5.2564(7)	90.0, 90.0, 90.0	n/a	n/a

[a]AFM2 is the lowest-energy magnetic structure (bolded)

[b]Structure was reoptimized without the D3BJ van der Waals correction. The energy is revaluated with D3BJ using the reoptimized structure to be able to compare its energy with the rest of the data. In the absence of D3BJ, the *b* vector, along which the material is held primarily *via* hydrogen bonds, is better reproduced. However, the *c* vector, along which the $Cu(OH)_4$ planes are held primarily by electrostatics, is worse. The lattice errors are consistent with the tendency of PBE+D3BJ to over-bind (producing shorter) hydrogen bonds, e.g., in water clusters (Grimme 2010, Grimme 2011), compared to underbound, longer bonds with PBE. [c]Actual cell size ($2a \times b \times c$) in parentheses, [d]Taken from (Oswald 1990).

Table B.3 Predicted lattice parameters for cubic Cu_2O.

Structure	*a*,*b*,*c* (Å)	α,β,γ (°)	*k*-point sampling
this work	4.243, 4.243, 4.243	90.0, 90.0, 90.0	6 × 6 × 6
exp[a]	4.2685(5), 4.2685(5), 4.2685(5)	90.0, 90.0, 90.0	n/a

[a]Taken from (Kirfel 1990). The discrepancy between the predicted and experimental lattice parameter is at -0.60 %.

Table B.4 Benchmarking thermodynamic data (all in eV/f.u.) for the gas-phase molecules, and solids at standard pressure (750 torr or 1 bar).[a]

Compound	H(298 K)-H(0 K)		$TS_{298\ K}$		G(298 K)-G(0 K)	
	calc.	exp.	calc.	exp.	calc.	exp.
CuO[b]	0.070	0.074	0.128	0.132	-0.058	-0.058
$Cu(OH)_2$[b]	0.121	--	0.221	0.335	-0.100	--
Cu_2O[b]	0.133	0.131	0.304	0.285	-0.171	-0.155
HCOOH(*g*)[c]	0.113	0.114 - 0.117	0.770	0.770 - 0.773	-0.657	-0.660 - -0.653[d]
H_2O(*g*)	0.103	0.103	0.584	0.584	-0.481	-0.481
CO_2(*g*)	0.094	0.097	0.657	0.661	-0.563	-0.564
O(*g*)	0.064	0.070	0.443	0.498	-0.379	-0.428

[a]Experimental data from: (Chase 1986) (CuO and $Cu(OH)_2$), (Fukushima 1971) (HCOOH), and (Chase 1986) (H_2O)

[b]The PBE+*U*+D3BJ energies of the solids are -9.322 eV/f.u. (CuO AFM4), -24.032 eV/f.u. ($Cu(OH)_2$ AFM2), and -12.311 eV/f.u. (Cu_2O)

[c]The calculated standard gas-phase dimerization free energy is -0.15 eV/HCOOH, which is more negative than the experimental value of -0.07 eV/HCOOH obtained from the standard free energies of formation of the monomer and dimer in (Green 1961). The discrepancy is, however, within the expected accuracy for a DFT approximation and consistent with the known tendency of PBE+D3BJ to over-bind hydrogen bonds, e.g., in water clusters (Grimme 2010, Grimme 2011).

[d]The lower and upper bounds of G were defined by the lower H and higher TS, and higher H and lower TS values, respectively

Table B.5 Symmetry and calculated thermodynamic quantities of the gas phase molecules at 298.15 K and 750 torr (10^5 pascal or 1 bar) pressure.

Molecule[a]	Point group symmetry(Shattuck 2011)	$E_{\mathrm{PBE}+U+\mathrm{D3BJ}}$(eV)	TS_{trans} (eV)[b]	TS_{rot} (eV)[b]	σ_{rot}	E_{vib} (eV)	TS_{vib} (eV)
HCOOH	C_s	-29.945	0.484	0.273	1	0.898	0.013
$(HCOOH)_2$	C_{2h}	-60.727	0.511	0.331	2	1.934	0.191
H_2O	C_{2v}	-14.238	0.448	0.136	2	0.568	0.000
CO_2	$D_{\infty h}$	-23.011	0.482	0.170	2	0.271	0.005
O atom	--	-1.907	0.443	--	--	--	--
$Cu(\kappa^2\text{-}HCOO)_2$	D_{2h}	-54.278	0.530	0.322	4	1.382	0.237
$Cu(\kappa^1\text{-}HCOO)_2$	C_{2h}	-52.827	0.530	0.337	2	1.313	0.345
$Cu(H_2O)(\kappa^1\text{-}HCOO)(\kappa^2\text{-}HCOO)$	C_1	-69.253	0.535	0.373	1	2.091	0.338
$Cu(H_2O)(\kappa^2\text{-}HCOO)_2$	C_1	-68.876	0.535	0.372	1	2.116	0.432
$Cu(H_2O)_2(\kappa^1\text{-}HCOO)_2$	C_2	-84.241	0.538	0.368	2	2.819	0.431
$Cu(H_2O)_2(\kappa^2\text{-}HCOO)_2$	C_i	-83.375	0.538	0.383	1	2.846	0.642
$Cu(H_2O)_3(HCOO)_2$	C_1	-98.804	0.542	0.393	1	3.576	0.622
$Cu_2(HCOO)_4$	D_{4h}	-110.244	0.557	0.354	8	2.939	0.596
$Cu_2(H_2O)_2(HCOO)_4$	C_{2h}	-139.710	0.561	0.403	2	4.421	0.985
$Cu_2(H_2O)_2(HCOO)_3(OH)$	C_s	-123.692	0.558	0.430	1	4.058	0.852
trans-eclipsed $Cu(HCOO)_2(HCOOH)_2$	C_2	-115.681	0.548	0.390	2	3.380	0.797
trans-staggered $Cu(HCOO)_2(HCOOH)_2$	C_1	-115.657	0.548	0.410	1	3.348	0.708
cis- $Cu(HCOO)_2(HCOOH)_2$	C_1	-115.554	0.548	0.408	1	3.431	0.702
$Cu(H_2O)_2(OH)_2$	C_2	-51.127	0.525	0.332	2	2.191	0.298
$Cu(H_2O)_3(OH)_2$	C_1	-65.735	0.530	0.364	1	2.933	0.478
$Cu(H_2O)(HCOO)$	C_1	-42.147	0.523	0.344	1	1.391	0.241
bent-$Cu(H_2O)(HCOO)$	C_1	-42.112	0.523	0.344	1	1.368	0.171
$Cu(H_2O)_2(HCOO)$	C_1	-57.438	0.528	0.364	1	2.108	0.297
Cu(HCOO)(HCOOH)	C_s	-58.601	0.530	0.366	1	1.654	0.235
staggered- Cu(HCOO)(HCOOH)	C_1	-57.972	0.530	0.365	1	1.703	0.313
$Cu_2(HCOO)_2$	D_{2h}	-57.283	0.544	0.347	4	1.478	0.302
$Cu_2(H_2O)_2(HCOO)_2$	C_i	-86.373	0.549	0.403	1	2.939	0.713
$Cu_2(HCOO)_2(HCOOH)_2$	C_1	-118.377	0.557	0.425	1	3.573	0.873

[a]In some cases a second isomer was investigated, where the bonding motifs of $HCOO^-$ ligands or the conformation of the ligands are explicitly stated to differentiate the different isomers (Figure B.5 and Figure B.7).

[b]The translational and rotational enthalpies are functions only of temperature, which are $\frac{5}{2}k_BT$ and $\frac{3}{2}k_BT$, respectively, for non-linear molecules, and $\frac{5}{2}k_BT$ and k_BT, respectively, for linear molecules (see Supplementary methods section I).

Table B.6 Relative PBE+*U*+D3BJ energies of the FM and AFM dimeric Cu complexes in meV/Cu. The lower energy magnetic structure is assigned a zero energy.

Molecule	FM	AFM
$Cu_2(HCOO)_4$	44	0
$Cu_2(H_2O)_2(HCOO)_4$	38	0
$Cu_2(H_2O)_2(HCOO)_3(OH)$	0	0.7

C. Plasma-Therm 770 Reactor Operation Guidelines

C.1 Safety Check list:

1. Previous entry in logbook shows no problem.

2. Check the exhaust gauge(magnehelic gauge) at top of sink on the left side of the machine. If it is blow 2.5 inch, please do not run the machine and report to nanostaff.

C.2 System Operation:

1. Place system in Standby Mode (if it isn't already) by clicking on Standby button. Move the mouse if the screen is blanked by the screen saver.

2. Verify from chamber view that chamber pressure is <.5 mT and chamber is being pumped (Turbo and Mech Pump are green in the drawing). Verify that the utilities: air, water, power are in the green zone also (bottom right of screen).

3. Check Log book for any problems previous user may have had. Alternately you can check any recent alarms by going to

Display-> Alarm History.

Do not proceed if there are unresolved problems.

4. Vent the loadlock:

Utilities->Loadlock->Vent

Set view to OVERVIEW so that both chambers' status can be monitored. The loadlock (leftmost chamber) will first turn red and then read ATMOSPHERE on the drawing when it is vented which takes 3 or 4 minutes.

NOTE : Make any thickness or depth measurements before loading if you need to measure selectivity eg photoresist or oxide thickness on Nanospec or Alphastep or Dektak8.

CAUTION: Your wafer should be cleaned and hard baked if it has photoresist. Wafers or pieces smaller than 4 inch must be glued to a 4 inch carrier wafer using very small drops of photoresist or other approved material. For very thick resists, (>10 microns) you must remove the edge bead otherwise the wafer will stick to the clamp at the end of the etch and will break.

CAUTION: Wear a face mask whenever loading and unloading a wafer.

5. Lift the hinged loadlock cover and load your wafer with flat facing in and side to be etched facing up. It must sit snug against the loading arm pocket.

6. Close and hold the cover and begin pump down by selecting:

Utilities->Loadlock->Pump

7. When the loadlock pressure is <.3 Torr, transfer the wafer to the process chamber by selecting:

Service->Maintenance->Wafer Handling

Press Load at the bottom left of the dialog screen. An animation shows wafer being transferred. When wafer transfer is complete (you can look thru the viewport with the desk lamp to the right of the machine), press EXIT button to exit screen.

8. Wait 3-4 minutes and then run a Leak-check:

Make sure ion gauge is off

Utilities->Ion Gauge Off

Service->Maintenance->Leak Test

Push Start in Dialog box

NOTE : System pumps chamber down to base pressure, closes gate valve and after a minute begins displaying instantaneous leak rate. Note the starting chamber pressure, and then the pressure after 1 minute (Top box). Leakback pressure must be < .3 mTorr per minute. Press End in Dialog box to end test. In chamber view, make sure the throttle valve is open and chamber pressure is <.3 mT.

9. The first step of every recipe is a pump-down step which is set at 8 E-6. If the chamber is dirty or hot (after several runs), the chamber may take a long time to complete the step. Also, if the ion gauge is contaminated it may need degassing. To degas the ion gauge, it must be off first (as in previous step). To Degas:

Service->Maintenance->Degas

Push the start button and allow a 2 minute degas (burn off). Then push Stop to end the degas.

10. Edit recipe:

Use most recent data from logsheet or test run for etch rate data. Divide desired thickness (μm) by etch rate to get time (min). CAUTION: Etch rate is a function of chamber history, % exposed III-V or Metal and many other factors. When in doubt make a test run with an identical sample. Do not change flow, pressure or power without consulting with Nanostaff.

Process->Chamber->Open

Select recipe from list and press OK

Check each step against the step in the log book for time, power, gas flows etc. If a change needs to be made report it to lab management.

Double click on Etch Step to set the etch time.

Input the etch time in the time box at the bottom left of the screen.

Make sure correct loop start step is highlighted in the Dialog Box (as this determines the loop starting point.

Click OK

Save Recipe? ->Yes

Exit

11. Load and run recipe

Process->Chamber->Load

Select recipe to load, Press “OK”

Verify desired recipe is shown in “Process” box at lower right screen

Put machine into Ready mode, press Ready button

Press Run to begin processing

12. Verify in Dialog box that correct recipe is running and parameters are correct. It is a good idea, if at all possible, to stay and make sure the process runs correctly. The first step is always a pump down step and is usually set to 8 E –6. If the system is taking longer than 10 minutes to complete this step AND the base pressure is <1 E–5, press END STEP at the bottom of the screen to advance to the next step. This may be necessary if many runs or a long run has just been completed (ie chamber is hot).

13. After etch is completed, click OK in Dialog box, if the Dialog box is present (Depends on how program was run.)

14. Put machine in Standby mode by pressing Standby button.

15. Transfer wafer to loadlock:

Service->Maintenance->Wafer Handling

Press Unload at bottom of screen

After wafer is in Loadlock press Exit

16. Vent Loadlock as before:

Go to OVERVIEW View then,

Utilities->Loadlock->Vent

17. After lock vents, remove wafer close lid and pump loadlock down again:

Utilities->Loadlock->Pump

18. Leave system in Standby mode and record all data in logbook.

C.3 Miscellaneous Problems

1. SYSTEM LOCKUP

Occasionally the system may lock up and not respond to any commands. Try exiting the Program Sysmon if possible or if that doesn’t work try exiting windows and restarting (type win after getting the DOS prompt). If this fails, open the lower panel and press the red reset button on the computer at the bottom. This should reboot all the software and a dialog box requesting user and password

will come up. Enter 3333 in both boxes. If a wafer is in the process chamber it should still know this. If not get help.

2. IDENTIFYING & ACKNOWLEDGING ALARMS

If something went wrong and you are not sure what happened (check info box at the bottom of screen first) go to:

Display->Alarm History

Date and time appear next to each alarm and can help you identify what went wrong. Press ALARM SILENCE at the bottom right of screen to silence an alarm or at the end of a run. If there is a problem, the HOLD button illuminates when the alarm is silenced. Push the HOLD button to put the system back in Standby or Ready. If the alarm condition is still present, however, the alarm will continue to go off. In this case the problem must be fixed first.

3. UNLOADING PROBLEMS

Wafer transfer problems generally occur because of either poor procedure of attaching a wafer to a carrier or thick PR at the wafer edge which gets sticky with heat causing the wafer to stick to the clamp and break in the process chamber. For thicker resist, use edge bead removal or keep your etches short. For gluing wafers use very small dabs of photoresist or approved material and bake thoroughly. If a wafer breaks or gets stuck in process chamber, you must get help. Do not attempt to fix the problem yourself.

4. CHAMBER CLEANING

As mentioned previously, an oxygen plasma clean (recipe O2Clean) should be run every time when etch substrate material been changed. Load the dummy clean wafer kept at the machine and load the recipe following standard procedures. After clean run please follow up one 5 min dummy run. Use the recipe you are going to etch for dummy run. And use the dummy wafer coated by photoresist. Make the entry in the log book that the O2Clean and dummy were run. There is no charge for this.

5. ADDITIONAL RECIPES

An approved recipe list is kept at the machine. You must get approval and help in writing your own recipe since small changes in a parameter can have a large detrimental effect on the process and machine. Once the recipe is approved it will be added to the recipe list. Anyone may run any of the posted recipes but may change only the etch time, nothing else.

6. SYSTEM ABORT

The abort button at the bottom of the screen aborts the entire recipe but may cause a system crash. If possible try using End Step several times first.

7. EMERGENCY SHUT OFF

The big red button at the front side of the machine will kill all the power and is to be used only in extreme emergency ie smoke or burning smell coming from the machine, etc. Do NOT attempt to turn on the machine if it is shut down in this manner.

8. GAS SUSPECTED IN CHAMBER

This alarm may occur from a system abort, a logic error or a real problem. If the turbopump is still on (green) and the throttle valve is closed (as seen in Chamber View) try pumping the system in the Standby mode by selecting:

Service->Maintenance->Pump->System

D. Vapor Chamber and Cold Trap Operating Guidelines

D.1 Chemical Used

Formic Acid (HCOOH), Nitrogen (N_2), Ethylene glycol ($C_2H_6O_2$), Hydrogen peroxide (H_2O_2).

D.2 Emergency Shutdown

1. Turn off heaters for vaporizer, gas delivery line, and chamber.

2. Close V1, FV1, FV2, and FV7.

3. Unplug vaporizer heater, LFC controller, and MFC controller.

4. Turn off cold trap power on the right side of the cold trap, as circled in Figure D.2.

D.3 Hydrogen Peroxide Detector

1. The monitor for the H2O2 detector is located on the southern wall of 1021, and reports H_2O_2 concentration in parts per million (see Figure D.5).

2. The H_2O_2 sensor is located behind the H_2O_2 vessel near the ground (see Figure D.6).

3. While the vapor chamber is in use, periodically check the monitor to make sure the concentration is below 1.0 ppm. Above 1.0 ppm, the yellow light will begin to flash, but no alarm will sound.

4. When the concentration is above 2.0 ppm, the red light will flash, and the alarm will sound. If this occurs, close the vessel valves (FV1 and FV2) and exit the room. Wait until the concentration to reduce to below 2.0 ppm (alarm stop).

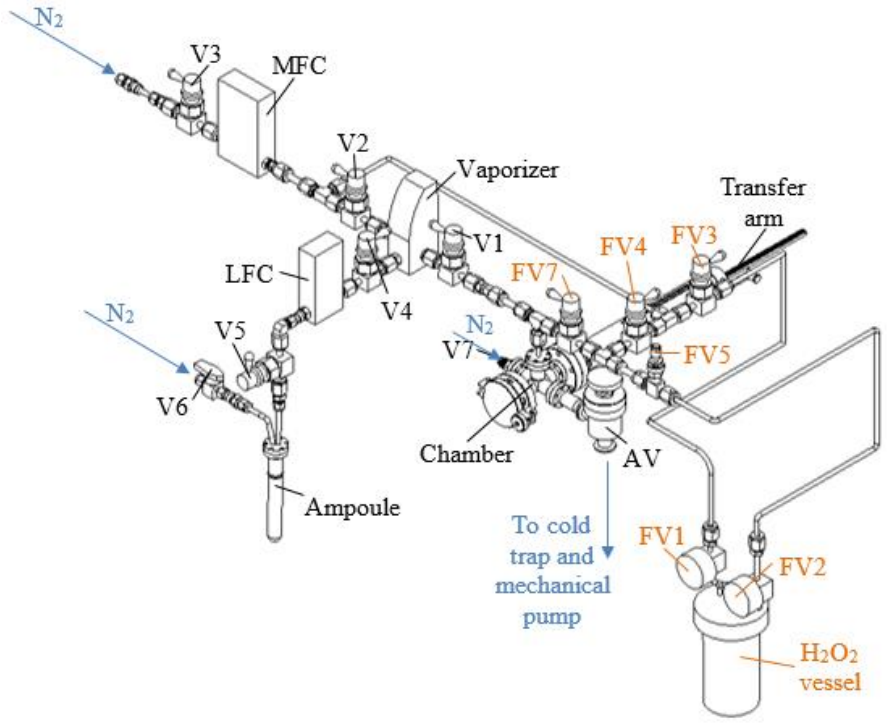

Figure D.1 Vapor chamber setup schematic.

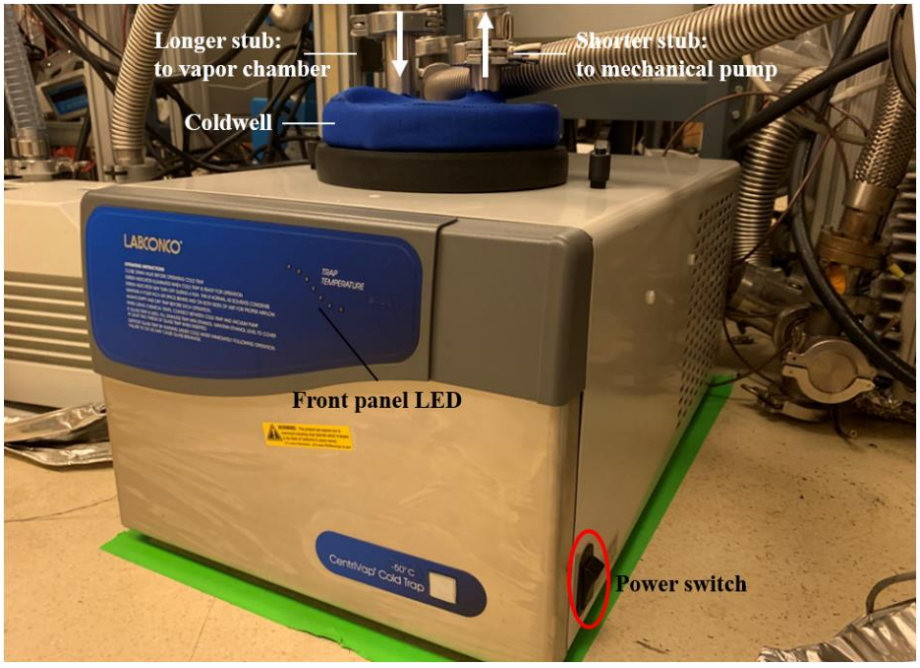

Figure D.2 Cold trap setup image.

Figure D.3 Coldwell after disassembling.

Figure D.4 Hydrogen peroxide vessel.

Figure D.5 Hydrogen peroxide monitor located on south wall of Eng V 1021.

Figure D.6 Hydrogen peroxide sensor (circled in red).

D.4 Operating Procedure

1. Initial Check: Make sure all the diaphragm valves (V1~V7, FV3-FV5,FV7) and H2O2 vessel valves FV1 and FV2 are closed, heaters are off, chamber is pumped down

   a. Heaters should be off, vaporizer heater and thermocouples should show room temperature.

   b. Angle valve to mechanical pump (AV) should be open, baratron gauge readout should show ~0.79 Torr.

2. Prepare for Operation:

   a. Open the V1 to V5 in the numerical order, the order of opening is designed so that any formic acid from leaky LFC and/or valves would be carried away by N_2.

   b. Turn on heaters. Allow approximately 30 minutes for the chamber to reach desired temperature, check with thermocouple.

      i. For 80ºC operation, set vaporizer heater to 80ºC, line and chamber variac to 28.

      ii. For 100ºC operation, set vaporizer heater to 100ºC, line variac to 29, chamber variac to 36.

   c. Turn on cold trap. Allow approximately 30 minutes for the cold trap to reach desired temperature (-50ºC). Front panel LED should all light up.

3. Hydrogen Peroxide Cycle Purge:

   a. Open V2, V3, FV3-FV5, and FV7.

   b. Press Cont. on the N2 MFC, wait for ~30 seconds.

   c. Press Close on the N2 MFC and close FV4.

4. Load Sample into Chamber:

   a. Close the injection valves to chamber (V1 and FV7).

   b. Close the valve to the mechanical pump (AV).

   c. Open vent line valve (V7) slowly until viewport door opens. Pressure gauge should read approx. 750 Torr.

   d. Loosen transfer arm lock and bring arm forward by turning the rack and pinion handle until the stage is out of the vapor chamber.

   e. Attach sample to stage using copper tape.

   f. Retract transfer arm into the chamber by turning the rack and pinion handle. Check that the sample will not collide with the vapor delivery line. Position of the linear motion feedthrough should be set at 40 for the sample stage to be beneath vapor delivery line. Tighten the transfer arm lock.

5. Pump Down Chamber:

a. Close viewport door and lock it.

b. Close vent line valve (V7) after sample loading to minimize moisture adsorption.

c. Open angle valve (AV) to mechanical pump slowly.

6. Deliver Vapor to System (Organic/acid):

a. Check that vent line valve (V7) is closed.

b. Close FV3 and FV7.

c. Pressurize the ampoule by briefly opening then closing V6 (~ 1 s).

d. Close valve (AV) to the mechanical pump.

e. Baratron gauge should show an increase in pressure (up ~10 Torr). Press Cont on the N_2 MFC and Open on the formic acid LFC simultaneously. If simultaneous pressing is difficult to achieve, open N_2 first to minimize acid exposure.

f. Allow the chamber to fill to the desired pressure (~350 Torr for Ni etching), then press Close on both MFC & LFC and close the valve to the chamber (V1) when the desired pressure is met. Allow the sample to mount in the chamber for the desired etch time. Condensation should occur on the viewport door.

g. Once process is finished, open the valve to the mechanical pump (AV) and press Open on the N2 MFC to push out remaining formic acid in the vapor delivery line (this should take ~1 minute). Press Off to stop N_2 MFC flow.

7. Deliver Vapor to System (Hydrogen Peroxide):

a. Make sure that vent line valve (V7), V1, and H_2O_2 bypass valve (FV4) are closed.

b. Open FV3 and FV7.

c. Press Cont. on the N2 MFC and close the angle valve (AV), then open FV5 to the desired flowrate (usually half turn).

d. Allow the chamber to fill to the desired pressure. Close FV5 and press Close on the N_2 MFC.

e. Once the process is finished, open the angle valve (AV) and close the vessel valves (FV1 and FV2).

8. Unload Sample from Vapor Chamber:

a. Close the injection valves to chamber (V1 and FV7).

b. Close the valve to the mechanical pump (AV).

c. Open vent line valve (V7) slowly until viewport door opens. Pressure gauge should read approx. 750 Torr.

d. Loosen transfer arm lock and bring arm forward by turning the rack and pinion handle until the stage is out of the vapor chamber.

e. Remove sample from stage. If another sample needs to be processed, attach it to the stage now using copper tape.

f. Retract transfer arm into the chamber by turning the rack and pinion handle. Check that the sample will not collide with the vapor delivery line. Position for stage to be beneath vapor delivery line is 30. Tighten the transfer arm lock.

9. Refill Ampoule:

a. For sample exposure at 350 Torr of mixture pressure (MFC & LFC fully opened), ampoule can sustain approximately 15 exposures before needing a refill.

b. If formic acid is suspected to still be in the LFC line, check that V1, V4, and AV are open and press Open on the MFC & LFC to pump out as much formic acid as possible.

c. Check that V5 and V6 are closed. Disconnect the N2 line leading to V6 downstream of V6. Disconnect the liquid formic acid line leading out of V5 upstream of V5.

d. Fill formic acid in the fume hood. Disconnect the CF connection between the 1.33" CF liquid feedthrough and the 1.33" to 2.75" CF zero-length adapter. Refill the ampoule, leaving about ½ inch below the steel-quartz joint for the doser tubing. Residual formic acid might present in the liquid delivery line due to the setup, use cleanroom wipes to wipe off the residual, safely dispose the wipes.

e. Once ampoule is full, reconnect the liquid feedthrough to the rest of the ampoule assembly.

f. Connect V5 and V6. New VCR gasket is needed for V5. A zip tie may be helpful in keeping the stainless-steel casing in place during the connection process.

10. Empty Cold Trap:

a. To prevent the condensed etch product from entering the mechanical pump, as well as to preserve the product for further analysis, it is recommended to empty the cold trap before the system is turned off.

b. Clear out an empty space in fume hood at north side of 1011, avoid conflict with other people's schedules.

c. Close angle valve (AV).

d. Turn off mechanical pump.

e. Turn off cold trap, allow approximately 1 hour for ethylene glycol to raise temperature. Check periodically if the coldwell could be lifted.

f. Wear glove and lab coat, make sure forearm is fully covered.

g. Disconnect the two KF25 clamps on the coldwell.

h. Lift the coldwell, use paper towel to wipe any ethylene glycol from the bottom of the Coldwell.

i. Move the coldwell to the fume hood, open the 6'' sanitary clamp.

j. Open the steel coldwell, fitting a jewelers flathead screwdriver underneath the cap will help with the removal but be careful not to damage the 6'' Viton gasket.

k. Pull the cap straight up, be careful not to smash the underneath structure to the inner wall of the coldwell.

l. If condensate does not need further analysis: use cleanroom wipe to absorb condensate, properly dispose the wipe after cleaning.

If condensate needs to be preserved for future analysis: use micropipette to move condensate to glass vials, clearly label experimental conditions on the vials. Clean up of the remaining condensate using cleanroom wipe and safely dispose the wipe.

m. Reseal the cap, tighten the 6'' sanitary clamp.

n. 800ml (~3.5 cm from the bottom of the well) of ethylene glycol is required in the cold trap for effective cooling. As taking out the coldwell also removes some ethylene glycol, refill ~50ml ethylene glycol into the cold trap before putting back the coldwell.

o. Put the coldwell back into the cold trap, check the perimeter for proper sealing, use paper towel to clean up excessive ethylene glycol.

p. Connect the two KF25 clamps, the taller stub connects to vapor chamber outlet, and the shorter stub connects to the mechanical pump inlet.

q. Turn on mechanical pump.

r. Open angle valve (AV).

11. Dismantling Hydrogen Peroxide Vaporizer:

a. Close the vessel valves FV1 and FV2.

b. Cycle purge the gas as written above, with FV3-FV5 open.

c. Make sure all of FV1-FV5 are closed.

d. Unplug grounding cable.

e. Disconnect vaporizer.

f. Place VCR caps on vaporizer in a safe and timely fashion.

g. Use original packaging materials to package the vessel.

Bibliography

(NIST), The National Institute of Standards and Technology Atomic Spectra Database. https://www.nist.gov/pml/atomic-spectra-database.

Aaltonen, Titta, Mikko Ritala and Markku Leskelä (2005). "ALD of rhodium thin films from Rh (acac) 3 and oxygen." Electrochemical and Solid-State Letters **8**(8): C99.

Abe, Takashi, Youn Gi Hong and Masayoshi Esashi (2003). "Highly selective reactive-ion etching using CO/NH 3/Xe gases for microstructuring of Au, Pt, Cu, and 20% Fe–Ni." Journal of Vacuum Science & Technology B: Microelectronics and Nanometer Structures Processing, Measurement, and Phenomena **21**(5): 2159-2162.

Aggarwal, PS and A Goswami (1961). "An oxide of tervalent nickel." The Journal of Physical Chemistry **65**(11): 2105-2105.

Ananikov, Valentine P, Konstantin A Gayduk, Zoya A Starikova and Irina P Beletskaya (2010). "Ni (acac) 2/Phosphine as an Excellent Precursor of Nickel (0) for Catalytic Systems." Organometallics **29**(21): 5098-5102.

Andrieu, S, Thomas Hauet, M Gottwald, A Rajanikanth, Lionel Calmels, AM Bataille, F Montaigne, S Mangin, E Otero and P Ohresser (2018). "Co/Ni multilayers for spintronics: High spin polarization and tunable magnetic anisotropy." Physical review materials **2**(6): 064410.

ASML (2019). EUV: Enabling Cost Efficiency, Tech Innovation and Future Industry Growth.

Athavale, Satish D and Demetre J Economou (1995). "Molecular dynamics simulation of atomic layer etching of silicon." Journal of Vacuum Science & Technology A: Vacuum, Surfaces, and Films **13**(3): 966-971.

Beletskaya, Irina P and Andrei V Cheprakov (2000). "The Heck reaction as a sharpening stone of palladium catalysis." Chemical Reviews **100**(8): 3009-3066.

Bernath, Peter F.; (2005). Spectra of Atoms and Molecules. New York, New York, Oxford University Press, Inc.

Blöchl, Peter E (1994). "Projector augmented-wave method." Physical review B **50**(24): 17953.

Brese, N. E., M. Okeeffe, B. L. Ramakrishna and R. B. Vondreele (1990). "LOW-TEMPERATURE STRUCTURES OF CUO AND AGO AND THEIR RELATIONSHIPS TO THOSE OF MGO AND PDO." Journal of Solid State Chemistry **89**(1): 184-190.

Cabrera, NFMN and Nevill Francis Mott (1949). "Theory of the oxidation of metals." Reports on progress in physics **12**(1): 163.

Campbell, Stephen A (2001). The science and engineering of microelectronic fabrication, Oxford university press.

Chadwick, Sharon S (1988). "Ullmann's encyclopedia of industrial chemistry." Reference Services Review.

Chang, Jane P, John C Arnold, Gavin CH Zau, Hyung-Shik Shin and Herbert H Sawin (1997). "Kinetic study of low energy argon ion-enhanced plasma etching of polysilicon with atomic/molecular chlorine." Journal of Vacuum Science & Technology A: Vacuum, Surfaces, and Films **15**(4): 1853-1863.

Chang, Runzi and Costas J Spanos (2005). "Dishing-radius model of copper CMP dishing effects." IEEE transactions on semiconductor manufacturing **18**(2): 297-303.

Chase, M.W., C.A. Davies, J.R. Downey, D.J. Frurip, R.A. McDonald and A.N. Syverud (1986). NIST JANAF Thermochemical Tables 1985. Gaithersburg, MD 20899, National Institute of Standards and Technology.

Chen, Zhu, John Mark P Martirez, Percy Zahl, Emily A Carter and Bruce E Koel (2019). "Self-assembling of formic acid on the partially oxidized p (2× 1) Cu (110) surface reconstruction at low coverages." The Journal of Chemical Physics **150**(4): 041720.

Cheng, Jeng Shia, Carl L Yaws, Larry L Dickens, Jack R Hopper, George Hsu and Ralph Lutwack (1984). "Physical and thermodynamic properties of dichlorosilane." Industrial & Engineering Chemistry Process Design and Development **23**(1): 48-52.

Cho, Han Na, Su Ryun Min, Hyung Jin Bae, Jung Hyun Lee and Chee Won Chung (2007). "High density plasma etching of nickel thin films using a Cl2/Ar plasma." Journal of Industrial and Engineering Chemistry **13**(6): 939-943.

Choi, Tae-Seop and Dennis W Hess (2015). "Chemical etching and patterning of copper, silver, and gold films at low temperatures." ECS Journal of Solid State Science and Technology **4**(1): N3084-N3093.

Choi, Tae-Seop, Galit Levitin and Dennis W Hess (2013). "Low temperature Cu etching using CH4-based Plasmas." ECS Journal of Solid State Science and Technology **2**(11): P506-P514.

Chou, Pei-Wen, Jenn-Ming Song, Zong-Yu Xie, Masatake Akaike, Tadatomo Suga, Masahisa Fujino and Jing-Yuan Lin (2018). "Low temperature de-oxidation for copper surface by catalyzed formic acid vapor." Applied Surface Science **456**: 890-898.

Chu, YS, IK Robinson and Andrew A Gewirth (1999). "Comparison of aqueous and native oxide formation on Cu (111)." The Journal of chemical physics **110**(12): 5952-5959.

Chui, Stephen S-Y, Samuel M-F Lo, Jonathan PH Charmant, A Guy Orpen and Ian D Williams (1999). "A chemically functionalizable nanoporous material [Cu3 (TMA) 2 (H2O) 3] n." Science **283**(5405): 1148-1150.

Clark, R, K Tapily, K-H Yu, T Hakamata, S Consiglio, D O'Meara, C Wajda, J Smith and G Leusink (2018). "Perspective: New process technologies required for future devices and scaling." APL Materials **6**(5): 058203.

Coburn, John W and Harold F Winters (1979). "Ion‐and electron‐assisted gas‐surface chemistry—An important effect in plasma etching." Journal of Applied physics **50**(5): 3189-3196.

Deloitte (2017). Global Mobile Consumer Survey.

Donnelly, Vincent M and Avinoam Kornblit (2013). "Plasma etching: Yesterday, today, and tomorrow." Journal of Vacuum Science & Technology A: Vacuum, Surfaces, and Films **31**(5): 050825.

Dubey, P, N Kaurav, RS Devan, GS Okram and YK Kuo (2018). The effect of stoichiometry on the structural, thermal and electronic properties of thermally decomposed nickel oxide. RSC Adv 8: 5882–5890.

Dudarev, SL, GA Botton, SY Savrasov, CJ Humphreys and AP Sutton (1998). "Electron-energy-loss spectra and the structural stability of nickel oxide: An LSDA+ U study." Physical Review B **57**(3): 1505.

Edelstein, Daniel C (2017). 20 Years of Cu BEOL in manufacturing, and its future prospects. 2017 IEEE International Electron Devices Meeting (IEDM), IEEE.

Edwards, HGM and A Knowles (1992). "Vibrational spectroscopic study of nickel (II) formate, Ni (HCO2) 2, and its aqueous solution." Journal of molecular structure **268**(1-3): 13-22.

Elvers, Barbara (1991). Ullmann's encyclopedia of industrial chemistry, Verlag Chemie.

Falicov, LM, Daniel T Pierce, SD Bader, R Gronsky, Kristl B Hathaway, Herbert J Hopster, David N Lambeth, SSP Parkin, Gary Prinz and Myron Salamon (1990). "Surface, interface, and thin-film magnetism." Journal of Materials Research **5**(6): 1299-1340.

Fenn, J (2002). "Electrospray ionization mass spectrometry: How it all began." Journal of biomolecular techniques: JBT **13**(3): 101.

Fu, Nan, Yanxiang Liu, Xiaolong Ma and Zhanfeng Chen (2019). "EUV Lithography: State-of-the-Art Review." Journal of Microelectronic Manufacturing **2**(2).

Fujino, Masahisa, Masatake Akaike, Naoya Matsuoka and Tadatomo Suga (2017). "Reduction reaction analysis of nanoparticle copper oxide for copper direct bonding using formic acid." Japanese Journal of Applied Physics **56**(4S): 04CC01.

Fukumizu, Hiroyuki, Makoto Sekine, Masaru Hori, Koji Kanomaru and Takuo Kikuchi (2019). "Atomic layer etching of AlGaN using Cl2 and Ar gas chemistry and UV damage evaluation." Journal of Vacuum Science & Technology A: Vacuum, Surfaces, and Films **37**(2): 021002.

Fukushima, K., J. Chao and B. J. Zwolinski (1971). "NORMAL COORDINATE TREATMENT AND THERMODYNAMIC PROPERTIES OF CIS-TRANS ISOMERS OF FORMIC ACID AND ITS DEUTERO-ANALOG." Journal of Chemical Thermodynamics **3**(4): 553-562.

Garribba, Eugenio and Giovanni Micera (2006). "The determination of the geometry of Cu (II) complexes: an EPR spectroscopy experiment." Journal of chemical education **83**(8): 1229.

George, Steven M (2009). "Atomic layer deposition: an overview." Chemical Reviews **110**(1): 111-131.

Gonzalez, Carlos M, Rajendra Timilsina, Guoliang Li, Gerd Duscher, Philip D Rack, Winand Slingenbergh, Willem F van Dorp, Jeff TM De Hosson, Kate L Klein and Huimeng M Wu (2014). "Focused helium and neon ion beam induced etching for advanced extreme ultraviolet lithography mask repair." Journal of Vacuum Science & Technology B, Nanotechnology and Microelectronics: Materials, Processing, Measurement, and Phenomena **32**(2): 021602.

Graddon, DP (1959). "The dimerization of cupric propionate in chloroform solution." Journal of Inorganic and Nuclear Chemistry **11**(4): 337-342.

Green, J. H. S. (1961). "THERMODYNAMIC PROPERTIES OF ORGANIC OXYGEN COMPOUNDS." Quarterly Reviews **15**(2): 125-152.

Griffith, John Stanley (1964). The theory of transition-metal ions, Cambridge university press.

Grimme, S., J. Antony, S. Ehrlich and H. Krieg (2010). "A consistent and accurate ab initio parametrization of density functional dispersion correction (DFT-D) for the 94 elements H-Pu." Journal of Chemical Physics **132**(15): 154104-154101-154119.

Grimme, S., S. Ehrlich and L. Goerigk (2011). "Effect of the Damping Function in Dispersion Corrected Density Functional Theory." Journal of Computational Chemistry **32**(7): 1456-1465.

Grimme, Stefan, Jens Antony, Stephan Ehrlich and Helge Krieg (2010). "A consistent and accurate ab initio parametrization of density functional dispersion correction (DFT-D) for the 94 elements H-Pu." The Journal of chemical physics **132**(15): 154104.

Gupta, Anshul, Jürgen Bömmels, Yves Saad, Ivan Ciofi and Christopher J Wilson (2018). "Integration scheme and 3D RC extractions of three-level supervia at 16 nm half-pitch." Microelectronic Engineering **191**: 20-24.

Hagen, DJ, Martyn E Pemble and M Karppinen (2019). "Atomic layer deposition of metals: Precursors and film growth." Applied Physics Reviews **6**(4): 041309.

Hämäläinen, Jani, Timo Hatanpää, Esa Puukilainen, Leila Costelle, Tero Pilvi, Mikko Ritala and Markku Leskelä (2010). "(MeCp) Ir (CHD) and molecular oxygen as precursors in atomic layer deposition of iridium." Journal of Materials Chemistry **20**(36): 7669-7675.

Hämäläinen, Jani, Esa Puukilainen, Timo Sajavaara, Mikko Ritala and Markku Leskelä (2013). "Low temperature atomic layer deposition of noble metals using ozone and molecular hydrogen as reactants." Thin Solid Films **531**: 243-250.

Hietala, Jukka, Antti Vuori, Pekka Johnsson, Ilkka Pollari, Werner Reutemann and Heinz Kieczka (2016). Formic Acid. Ullmann’s Encyclopedia of Industrial Chemistry, Wiley‐VCH Verlag GmbH & Co. KGaA 1-22.

Ivankovits, John C (2000). Reactions of hexafluoroacetylacetone with selected metal oxides, metal films, and metallic contaminants on copper, tin-lead solder, and silicon surfaces. Master of Science, Lehigh University.

Jezewski, Christopher, WA Lanford, Christopher J Wiegand, JP Singh, Pei-I Wang, Jay J Senkevich and Toh-Ming Lu (2005). "Inductively coupled hydrogen plasma-assisted Cu ALD on metallic and dielectric surfaces." Journal of the Electrochemical Society **152**(2): C60.

Jin, Guangxi, Kun Cao, Guang-Can Guo and Lixin He (2012). "Origin of ferroelectricity in high-T c magnetic ferroelectric CuO." Physical Review Letters **108**(18): 187205.

Johnson, Nicholas R and Steven M George (2017). "WO3 and W Thermal Atomic Layer Etching Using “Conversion-Fluorination” and “Oxidation-Conversion-Fluorination” Mechanisms." ACS Applied Materials & Interfaces **9**(39): 34435-34447.

Johnson, Nicholas R, Jennifer K Hite, Michael A Mastro, Charles R Eddy Jr and Steven M George (2019). "Thermal atomic layer etching of crystalline GaN using sequential exposures of XeF2 and BCl3." Applied Physics Letters **114**(24): 243103.

Kanarik, Keren J, Thorsten Lill, Eric A Hudson, Saravanapriyan Sriraman, Samantha Tan, Jeffrey Marks, Vahid Vahedi and Richard A Gottscho (2015). "Overview of atomic layer etching in the semiconductor industry." Journal of Vacuum Science & Technology A: Vacuum, Surfaces, and Films **33**(2): 020802.

Kanarik, Keren J, Samantha Tan and Richard A Gottscho (2018). "Atomic Layer Etching: Rethinking the Art of Etch." The Journal of Physical Chemistry Letters **9**(16): 4814-4821.

Karaffa, Linda S (2013). The Merck index: an encyclopedia of chemicals, drugs, and biologicals, RSC Publishing.

Karahashi, Kazuhiro and Satoshi Hamaguchi (2014). "Ion beam experiments for the study of plasma–surface interactions." Journal of Physics D: Applied Physics **47**(22): 224008.

Kauppinen, Christoffer, Sabbir Ahmed Khan, Jonas Sundqvist, Dmitry B Suyatin, Sami Suihkonen, Esko I Kauppinen and Markku Sopanen (2017). "Atomic layer etching of gallium nitride (0001)." Journal of Vacuum Science & Technology A: Vacuum, Surfaces, and Films **35**(6): 060603.

Kerrigan, Marissa M, Joseph P Klesko, Kyle J Blakeney and Charles H Winter (2018). "Low Temperature, Selective Atomic Layer Deposition of Nickel Metal Thin Films." ACS applied materials & interfaces **10**(16): 14200-14208.

Kim, Ja-Yong, Deok-Sin Kil, Jin-Hyock Kim, Se-Hun Kwon, Ji-Hoon Ahn, Jae-Sung Roh and Sung-Ki Park (2012). "Ru films from bis (ethylcyclopentadienyl) ruthenium using ozone as a reactant by atomic layer deposition for capacitor electrodes." Journal of The Electrochemical Society **159**(6): H560.

Kim, Taeseung, Jack Kun-Chieh Chen, Jane P %J Journal of Vacuum Science Chang, Surfaces Technology A: Vacuum and Films (2014). "Thermodynamic assessment and experimental verification of reactive ion etching of magnetic metal elements." **32**(4): 041305.

Kirfel, A. and K. Eichhorn (1990). "ACCURATE STRUCTURE-ANALYSIS WITH SYNCHROTRON RADIATION - THE ELECTRON-DENSITY IN AL2O3 AND CU2O." Acta Crystallographica Section A **46**: 271-284.

Kirfel, Armin and K Eichhorn (1990). "Accurate structure analysis with synchrotron radiation. The electron density in Al2O3 and Cu2O." Acta Crystallographica Section A: Foundations of Crystallography **46**(4): 271-284.

Köhler, Frank H (2007). "Paramagnetic complexes in solution: The NMR approach." eMagRes.

Konh, Mahsa, Chuan He, Xi Lin, Xiangyu Guo, Venkateswara Pallem, Robert L Opila, Andrew V Teplyakov, Zijian Wang and Bo Yuan (2019). "Molecular mechanisms of atomic layer etching of cobalt with sequential exposure to molecular chlorine and diketones." Journal of Vacuum Science & Technology A: Vacuum, Surfaces, and Films **37**(2): 021004.

Kresse, Georg and Jürgen Furthmüller (1996). "Efficiency of ab-initio total energy calculations for metals and semiconductors using a plane-wave basis set." Computational materials science **6**(1): 15-50.

Kresse, Georg and Jürgen Furthmüller (1996). "Efficient iterative schemes for ab initio total-energy calculations using a plane-wave basis set." Physical review B **54**(16): 11169.

Kresse, Georg and Daniel Joubert (1999). "From ultrasoft pseudopotentials to the projector augmented-wave method." Physical review b **59**(3): 1758.

Krishnan, M and MF Lofaro (2016). Copper chemical mechanical planarization (Cu CMP) challenges in 22 nm back-end-of-line (BEOL) and beyond. Advances in Chemical Mechanical Planarization (CMP), Elsevier**:** 27-46.

Kudriavtsev, Yu, A Villegas, A Godines and R Asomoza (2005). "Calculation of the surface binding energy for ion sputtered particles." Applied surface science **239**(3-4): 273-278.

Laegreid, Nils and GK Wehner (1961). "Sputtering yields of metals for Ar+ and Ne+ ions with energies from 50 to 600 eV." Journal of Applied Physics **32**(3): 365-369.

Lambers, Eric S, CN Dykstal, Jae M Seo, Jack E Rowe and Paul H Holloway (1996). "Room-temerature oxidation of Ni (110) at low and atmospheric oxygen pressures." Oxidation of metals **45**(3-4): 301-321.

Larin, GM, AN Gusev, Yu V Trush, KV Rabotyagov, VF Shul'gin, GG Aleksandrov and IL Eremenko (2007). "EPR spectra and structures of dinuclear copper (II) complexes with acyldihydrazones of benzenedicarboxylic acids." Russian Chemical Bulletin **56**(10): 1964-1971.

Larsen, Ask Hjorth, Jens Jørgen Mortensen, Jakob Blomqvist, Ivano E Castelli, Rune Christensen, Marcin Dułak, Jesper Friis, Michael N Groves, Bjørk Hammer and Cory Hargus (2017). "The atomic simulation environment—a Python library for working with atoms." Journal of Physics: Condensed Matter **29**(27): 273002.

Lavoie, C, FM d'Heurle, Christophe Detavernier and C Cabral Jr (2003). "Towards implementation of a nickel silicide process for CMOS technologies." Microelectronic Engineering **70**(2-4): 144-157.

Lee, Younghee and Steven M George (2015). "Atomic layer etching of Al2O3 using sequential, self-limiting thermal reactions with Sn (acac) 2 and hydrogen fluoride." ACS nano **9**(2): 2061-2070.

Lee, Younghee and Steven M George (2017). "Thermal Atomic Layer Etching of Titanium Nitride Using Sequential, Self-Limiting Reactions: Oxidation to TiO2 and Fluorination to Volatile TiF4." Chemistry of Materials **29**(19): 8202-8210.

Letzkus, F, J Butschke, M Irmscher, FM Kamm, C Koepernik, J Mathuni, J Rau and G Ruhl (2004). "Dry etch processes for the fabrication of EUV masks." Microelectronic Engineering **73**: 282-288.

Levinson, Joshua A, Eric SG Shaqfeh, Mehdi Balooch and Alex V Hamza (1997). "Ion-assisted etching and profile development of silicon in molecular chlorine." Journal of Vacuum Science & Technology A: Vacuum, Surfaces, and Films **15**(4): 1902-1912.

Lim, WS, JB Park, JY Park, BJ Park and GY Yeom (2009). "Low damage atomic layer etching of ZrO2 by using BCl3 gas and ar neutral beam." Journal of nanoscience and nanotechnology **9**(12): 7379-7382.

Lin, Xi, Meixi Chen, Anderson Janotti and Robert Opila (2018). "In situ XPS study on atomic layer etching of Fe thin film using Cl2 and acetylacetone." Journal of Vacuum Science & Technology A: Vacuum, Surfaces, and Films **36**(5): 051401.

Luong, Vu, Vicky Philipsen, Eric Hendrickx, Karl Opsomer, Christophe Detavernier, Christian Laubis, Frank Scholze and Marc Heyns (2018). "Ni-Al Alloys as Alternative EUV Mask Absorber." Applied Sciences **8**(4): 521.

Mackus, Adriaan JM, Noémi Leick, Layton Baker and Wilhelmus MM Kessels (2012). "Catalytic combustion and dehydrogenation reactions during atomic layer deposition of platinum." Chemistry of Materials **24**(10): 1752-1761.

Makov, G and MC Payne (1995). "Periodic boundary conditions in ab initio calculations." Physical Review B **51**(7): 4014.

Malcolm, W and JR Chase (1998). "NIST-JANAF thermochemical tables." J. Phys. Chem. Ref. Data **9**.

Mameli, Alfredo, Marcel A Verheijen, Adriaan JM Mackus, Wilhelmus MM Kessels and Fred Roozeboom (2018). "Isotropic atomic layer etching of ZnO using Acetylacetone and O2 plasma." ACS applied materials & interfaces **10**(44): 38588-38595.

Mangat, Pawitter JS, Scott Daniel Hector, Stewart Rose, Gregory Frank Cardinale, Edita Tejnil and Alan R Stivers (2000). EUV mask fabrication with Cr absorber. Emerging Lithographic Technologies IV, International Society for Optics and Photonics.

Matsui, N, K Mashimo, A Egami, A Konishi, O Okada and T Tsukada (2002). "Etching characteristics of magnetic materials (Co, Fe, Ni) using CO/NH3 gas plasma for hardening mask etching." Vacuum **66**(3-4): 479-485.

Matsunami, Noriaki, Yasunori Yamamura, Yukikazu Itikawa, Noriaki Itoh, Yukio Kazumata, Soji Miyagawa, Kenji Morita, Ryuichi Shimizu and Hiroyuki Tawara (1984). "Energy dependence of

the ion-induced sputtering yields of monatomic solids." Atomic Data & Nuclear Data Tables **31**(1): 1-80.

Matsuura, Takashi, Yasuhiko Honda and Junichi Murota (1999). "Atomic-order layer-by-layer role-share etching of silicon nitride using an electron cyclotron resonance plasma." Applied physics letters **74**(23): 3573-3575.

Matsuura, Takashi, Junichi Murota, Yasuji Sawada and Tadahiro Ohmi (1993). "Self‐limited layer‐by‐layer etching of Si by alternated chlorine adsorption and Ar+ ion irradiation." Applied physics letters **63**(20): 2803-2805.

Meguro, Takashi, Masashi Ishii, Hirokazu Kodama, Manabu Hamagaki, Tamio Hara, Yasuhiro Yamamoto and Yoshinobu Aoyagi (1990). "Layer-by-layer controlled digital etching by means of an electron-beam-excited plasma system." Japanese journal of applied physics **29**(10R): 2216.

Metzler, Dominik, Chen Li, Sebastian Engelmann, Robert L Bruce, Eric A Joseph and Gottlieb S Oehrlein (2016). "Fluorocarbon assisted atomic layer etching of SiO2 and Si using cyclic Ar/C4F8 and Ar/CHF3 plasma." Journal of Vacuum Science & Technology A: Vacuum, Surfaces, and Films **34**(1): 01B101.

Miessler, Gary L (2008). Inorganic chemistry, Pearson Education India.

Miyoshi, Nobuya, Hiroyuki Kobayashi, Kazunori Shinoda, Masaru Kurihara, Tomoyuki Watanabe, Yutaka Kouzuma, Kenetsu Yokogawa, Satoshi Sakai and Masaru Izawa (2017). "Atomic layer etching of silicon nitride using infrared annealing for short desorption time of ammonium fluorosilicate." Japanese Journal of Applied Physics **56**(6S2): 06HB01.

Mohimi, Elham, Xiaoqing I Chu, Brian B Trinh, Shaista Babar, Gregory S Girolami and John R Abelson (2018). "Thermal Atomic Layer Etching of Copper by Sequential Steps Involving Oxidation and Exposure to Hexafluoroacetylacetone." ECS Journal of Solid State Science and Technology **7**(9): P491-P495.

Montaser, Akbar (1998). Inductively coupled plasma mass spectrometry, John Wiley & Sons.

Moore, Gordon E (1965). Cramming more components onto integrated circuits, McGraw-Hill New York.

Moretti, Giuliano (1998). "Auger parameter and Wagner plot in the characterization of chemical states by X-ray photoelectron spectroscopy: a review." Journal of electron spectroscopy and related phenomena **95**(2-3): 95-144.

Neisser, Mark and Stefan Wurm (2013). Overview of Next Generation Lithography, Advanced Patterning, EUV and Self Assembly.

Neugebauer, Jörg and Matthias Scheffler (1992). "Adsorbate-substrate and adsorbate-adsorbate interactions of Na and K adlayers on Al (111)." Physical Review B **46**(24): 16067.

Nogami, T, M He, X Zhang, K Tanwar, R Patlolla, J Kelly, D Rath, M Krishnan, X Lin and O Straten (2013). CVD-Co/Cu (Mn) integration and reliability for 10 nm node. 2013 IEEE International Interconnect Technology Conference-IITC, IEEE.

Nojiri, Kazuo (2015). Dry etching technology for semiconductors, Springer.

Oehrlein, GS, D Metzler and C Li (2015). "Atomic layer etching at the tipping point: an overview." ECS Journal of Solid State Science and Technology **4**(6): N5041-N5053.

Oswald, H.R.; Reller, A.; Schmalle, H.W.; Dubler, E. (1990). "Structure of copper(II) hydroxide, Cu(OH)2." Acta Crystallographica Section C: Crystal Structure Communications **46**: 2279-2284.

Paranjpe, Ajit, Boris Druz, Katrina Rook and Narasimhan Srinivasan (2018). Ion beam etching of STT-RAM structures, Google Patents.

Park, Jin Woo, Doo San Kim, Mu Kyeom Mun, Won Oh Lee, Ki Seok Kim and Geun Young Yeom (2017). "Atomic layer etching of InGaAs by controlled ion beam." Journal of Physics D: Applied Physics **50**(25): 254007.

Park, SD, WS Lim, BJ Park, HC Lee, JW Bae and GY Yeom (2008). "Precise depth control and low-damage atomic-layer etching of HfO2 using BCl3 and Ar neutral beam." Electrochemical and Solid-State Letters **11**(4): H71-H73.

Park, SD, CK Oh, JW Bae, GY Yeom, TW Kim, JI Song and JH Jang (2006). "Atomic layer etching of InP using a low angle forward reflected Ne neutral beam." Applied physics letters **89**(4): 043109.

Pascher, Tobias F, Milan Ončák, Christian van der Linde and Martin K Beyer (2019). "Decomposition of copper formate clusters: insight into elementary steps of calcination and carbon dioxide activation." ChemistryOpen **8**(12): 1453-1459.

Patmore, Nathan J (2010). Recent developments in the chemistry of metal-metal multiply bonded paddlewheel compounds. Organometallic Chemistry**:** 77-92.

Perdew, John P, Kieron Burke and Matthias Ernzerhof (1996). "Generalized gradient approximation made simple." Physical review letters **77**(18): 3865.

Pettersson, Mika, Ermelinda MS Maçôas, Leonid Khriachtchev, Rui Fausto and Markku Räsänen (2003). "Conformational isomerization of formic acid by vibrational excitation at energies below the torsional barrier." Journal of the American Chemical Society **125**(14): 4058-4059.

Philipsen, Vicky, Kim Vu Luong, Karl Opsomer, Christophe Detavernier, Eric Hendrickx, Andreas Erdmann, Peter Evanschitzky, Robbert WE Van De Kruijs, Zahra Heidarnia-Fathabad and Frank Scholze (2018). Novel EUV mask absorber evaluation in support of next-generation EUV imaging. Photomask Technology 2018, International Society for Optics and Photonics.

Poulston, S, E Rowbotham, P Stone, P Parlett and M Bowker (1998). "Temperature-programmed desorption studies of methanol and formic acid decomposition on copper oxide surfaces." Catalysis letters **52**(1): 63-67.

Quirk, Michael and Julian Serda (2001). Semiconductor manufacturing technology, Prentice Hall Upper Saddle River, NJ.

Rugar, Daniel and Paul Hansma (1990). "Atomic force microscopy." Physics today **43**(10): 23-30.

Rungtaweevoranit, Bunyarat, Christian S Diercks, Markus J Kalmutzki and Omar M Yaghi (2017). "Spiers Memorial Lecture: Progress and prospects of reticular chemistry." Faraday discussions **201**: 9-45.

Salahuddin, Sayeef, Kai Ni and Suman Datta (2018). "The era of hyper-scaling in electronics." Nature Electronics **1**(8): 442-450.

Scholze, Frank, Christian Laubis, Kim Vu Luong and Vicky Philipsen (2017). Update on optical material properties for alternative EUV mask absorber materials. 33rd European Mask and Lithography Conference, International Society for Optics and Photonics.

Seah, MP and TS Nunney (2010). "Sputtering yields of compounds using argon ions." Journal of Physics D: Applied Physics **43**(25): 253001.

Setter, N, D Damjanovic, L Eng, G Fox, Spartak Gevorgian, S Hong, A Kingon, H Kohlstedt, NY Park and GB Stephenson (2006). "Ferroelectric thin films: Review of materials, properties, and applications." Journal of applied physics **100**(5): 051606.

Shattuck, Thomas W. (2011). "ABC Rotational Constant Calculator." 2020, from http://www.colby.edu/chemistry/PChem/scripts/ABC.html.

Shen, Meihua, Thorsten Lill, Nick Altieri, John Hoang, Steven Chiou, Jim Sims, Andrew McKerrow, Rafal Dylewicz, Ernest Chen and Hamid Razavi (2020). "Review on recent progress in patterning phase change materials." Journal of Vacuum Science & Technology A: Vacuum, Surfaces, and Films **38**(6): 060802.

Shoki, Tsutomu, Morio Hosoya, Takeru Kinoshita, Hideo Kobayashi, Youichi Usui, Ryo Ohkubo, Shinichi Ishibashi and Osamu Nagarekawa (2002). Process development of 6-in EUV mask with TaBN absorber. Photomask and Next-Generation Lithography Mask Technology IX, International Society for Optics and Photonics.

Shushanyan, Artem D, Nataliya S Nikolaeva, Evgeniia S Vikulova, Ludmila N Zelenina, Sergey V Trubin, Sergey V Sysoev, Svetlana I Dorovskikh and Natalya B Morozova (2019). "Thermochemical study of new volatile palladium (II) and copper (II) β-ketohydrazonates for CVD application." Journal of Thermal Analysis and Calorimetry **136**(6): 2341-2352.

Smith, Henry I, J Melngailis, RC Williamson and WT Brogan (1973). Ion-beam etching of surface gratings. 1973 Ultrasonics Symposium, IEEE.

Standards, National Institute of and Technology (2018). NIST Chemistry WebBook, SRD 69.

Sugiura, Kuniaki, Shigeki Takahashi, Minoru Amano, Takeshi Kajiyama, Masayoshi Iwayama, Yoshiaki Asao, Naoharu Shimomura, Tatsuya Kishi, Sumio Ikegawa and Hiroaki Yoda (2009). "Ion beam etching technology for high-density spin transfer torque magnetic random access memory." Japanese Journal of Applied Physics **48**(8S1): 08HD02.

Sugiyama, Takayuki, Takashi Matsuura and Junichi Murota (1997). "Atomic-layer etching of Ge using an ultraclean ECR plasma." Applied surface science **112**: 187-190.

Tappmeyer, WP and Arthur W Davidson (1963). "Cobalt and nickel acetates in anhydrous acetic acid." Inorganic Chemistry **2**(4): 823-825.

Thissen, Peter, Oliver Seitz and Yves J Chabal (2012). "Wet chemical surface functionalization of oxide-free silicon." Progress in surface science **87**(9-12): 272-290.

Togo, Atsushi and Isao Tanaka (2015). "First principles phonon calculations in materials science." Scripta Materialia **108**: 1-5.

Trucks, GW, Krishnan Raghavachari, GS Higashi and YJ Chabal (1990). "Mechanism of HF etching of silicon surfaces: A theoretical understanding of hydrogen passivation." Physical Review Letters **65**(4): 504.

Ubara, H, T Imura and A Hiraki (1984). "Formation of Si-H bonds on the surface of microcrystalline silicon covered with SiOx by HF treatment." Solid State Communications **50**(7): 673-675.

Van Niekerk, JN and FRL Schoening (1953). "X-ray evidence for metal-to-metal bonds in cupric and chromous acetate." Nature **171**(4340): 36-37.

Walker, Perrin and William H Tarn (1990). CRC handbook of metal etchants, CRC press.

Weiss, Theodor, Volkmar Zielasek and Marcus Bäumer (2015). "Influence of Water on Chemical Vapor Deposition of Ni and Co thin films from ethanol solutions of acetylacetonate precursors." Scientific reports **5**: 18194.

Williams, Kirt R, Kishan Gupta and Matthew Wasilik (2003). "Etch rates for micromachining processing-Part II." Journal of Microelectromechanical Systems **12**(6): 761-778.

Wu, Fangyu, Galit Levitin and Dennis W Hess (2011). "Temperature effects and optical emission spectroscopy studies of hydrogen-based plasma etching of copper." Journal of The Electrochemical Society **159**(2): H121.

Yan, Pei-yang, Guojing Zhang, Patrick Kofron, Jeffrey E Powers, Mark Tran, Ted Liang, Alan R Stivers and Fu-Chang Lo (2000). EUV mask absorber characterization and selection. Photomask and Next-Generation Lithography Mask Technology VII, International Society for Optics and Photonics.

Yan, Pei-yang, Guojing Zhang, Andy Ma and Ted Liang (2001). TaN EUVL mask fabrication and characterization. Emerging Lithographic Technologies V, International Society for Optics and Photonics.

Yang, BX, JM Tranquada and G Shirane (1988). "Neutron scattering studies of the magnetic structure of cupric oxide." Physical Review B **38**(1): 174.

Yeoh, A, A Madhavan, N Kybert, S Anand, J Shin, M Asoro, S Samarajeewa, J Steigerwald, C Ganpule and M Buehler (2018). Interconnect Stack using Self-Aligned Quad and Double Patterning for 10nm High Volume Manufacturing. 2018 IEEE International Interconnect Technology Conference (IITC), IEEE.

Yeom, Geun Young (2009). "Etch characteristics of TiO2 etched by using an atomic layer etching technique with BCl3 gas and an Ar neutral beam." Journal of the Korean Physical Society **54**(3).

Yu, Kuang and Emily A Carter (2014). "Communication: Comparing ab initio methods of obtaining effective U parameters for closed-shell materials." The Journal of Chemical Physics **140**(12): 121105.